Optics, Photonics and Lasers:

Proceedings of the 6th International Conference on Optics, Photonics and Lasers (OPAL' 2023)

17-19 May 2023

Funchal (Madeira Island), Portugal

Edited by Sergey Y. Yurish

IFSA Publishing

Sergey Y. Yurish, *Editor*
Optics, Photonics and Lasers
OPAL' 2023 Conference Proceedings

E-mail (for orders and customer service enquires): ifsa.books@sensorsportal.com

Visit our Home Page on http://www.sensorsportal.com

ISBN: 978-84-09-48335-8
BN-20230511-XX
BIC: TTB

Contents

Foreword

On behalf of the OPAL' 2023 Organizing Committee, I introduce with pleasure these proceedings devoted to contributions from the *6th International Conference on Optics, Photonics and Lasers (OPAL' 2023)*. The conference is organized by the International Frequency Sensor Association (IFSA) in technical cooperation with our media partners: Institute of Physics (IOP), UK, *MDPI Photonics* (ISSN 2304-6732) and *MDPI Sensors* (ISSN 1424-8220) journals, Switzerland.

In keeping with tradition begun in 2018 in Barcelona, Spain the Series of Conference attracts researchers and practitioners in the related fields, from around the world including well-known experts and invited speakers. The conference program provides an opportunity for researchers interested in optics, photonics and lasers to discuss their latest results and exchange ideas on the new trends and challenges.

All submitted papers have been preliminary peer reviewed by international reviewers. The authors have revised papers after review, and resubmitted it for the second round of review by the technical committee. All published papers have been presented at the OPAL' 2023 conference and opened for discussion.

We thank all authors for submitting their latest work, thus contributing to the excellent technical contents of the Conference. Especially, we would like to thank the individuals and organizations that worked together diligently to make this Conference a success, and to the members of the International Program Committee for the thorough and careful review of the papers. It is important to point out that the great majority of the efforts in organizing the technical program of the Conference came from volunteers.

Prof., Dr. Sergey Y. Yurish
OPAL' 2023 Chairman

(0107)

Building Homogenous and Heterogenous Shells around $LiLuF_4:Ln^{3+}$ Nanothermometers – Problems, Benefits, and Lessons Learned

M. Lederer [1], H. Rijckaert [2] and A. M. Kaczmarek [1]
[1] Ghent University, NanoSensing Group, 281-S3 Krijgslaan, 9000 Gent, Belgium
[2] Ghent University, SCRiPTS, 281-S3 Krijgslaan, 9000 Gent, Belgium
E-mail: anna.kaczmarek@ugent.be

Summary: Lanthanide-doped nanoparticles are popular candidates for obtaining luminescence properties, including being used as a luminescent thermometer. Their temperature sensitive luminescence allows remote measurements of temperature, even in working environment or hard to reach areas. To enhance luminescence properties of lanthanide-doped nanoparticles a common practice is constructing core-shell structures, where the emissive ions are doped only in the core and are protected by an un-doped (inert) shell. That way the emissive ions are protected from the quenching influence of the environment. Our on-going work however shows that not all nanoparticle host matrixes behave in the same way upon building core-shell structures. We have investigated $LiLuF_4$ nanoparticles doped with lanthanide ions extensively and show that unlike in host such as $NaYF_4$, homogenous core-shell structures suffer extensive ion migration processes and therefore only heterogenous shells can offer sufficient protection from the environment.

Keywords: Lanthanides, Nanoparticles, Luminescence thermometry, Core-shell structures, Ion migration.

1. Introduction

Nanothermometry is a fast-developing field of research due to the possibility of remote, precise, reliable, and noninvasive temperature sensing in real time [1, 2]. Among some, the most studied materials suitable for luminescence thermometry are lanthanide (Ln)-based nanoparticles. Doped core-inert shell nanoparticles are a common approach to enhance emission intensity and improve the performance of the Ln^{3+}-doped nanoparticles [3]. The inert shell shields the dopants against coupling with water overtones on the surface of the nanoparticles. This however only works if there is no migration of the emissive ions into the shell/outer surface of the nanoparticles [4]. A wide range of core−shell nanoparticle structures have been reported up to date [3]. The core material can be the same as the shell material (homogeneous) or a different material can be chosen for the core and the shell (heterogeneous) [5]. Though obtaining such heterogeneous structures can be synthetically quite challenging. Some materials, such as the $NaYF_4$, have already been quite extensively studied, and it is known that hardly any ion migration is observed in such geometries, although it is dependent on the size of the nanoparticles and synthesis route [4]. We have found that $LiLuF_4$ is much more prone to ion migration, and this cannot be prevented by changing the synthesis route, but only by designing a heterogenous shell.

2. Experimental Section

For the development of the $LiLuF_4$:Ln and $LiLuF_4$:Ln@Li(Lu,Y)F_4 core-shell structures two synthesis routes were employed: the decomposition route and the co-precipitation route [6, 7]. They could both be used to grow either the lanthanide doped core particles or the inert shell.

3. Results and Discussion

The core-shell nanoparticles were developed using the $LiLuF_4$ and $LiYF_4$ host matrixes, with the combinations presented in Scheme 1.

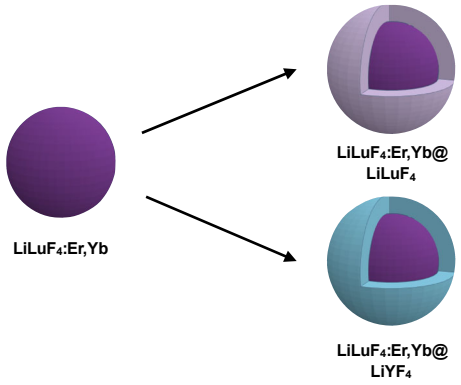

Scheme 1. Schematic overview of the most important core-shell structures presented in this work.

The morphology of the samples was first analyzed by TEM (Fig. 1) and later the formation of the right material was confirmed using PXRD. The core-shell nanoparticles could be made by either using the co-precipitation or decomposition route. Also, a mixed synthesis, where the core is made using one approach, and the shell using the second approach, was investigated. The decomposition route is without doubt the easiest to control and yields most regular nanoparticles. To fully assess if a shell has formed

EDX maps were recorded for all materials. This allowed to visualize in which cases ion migration was taking place in the core-shell nanoparticles. In all homogenous core-shell $LiLuF_4$ nanoparticles a clear migration of the emissive Er^{3+} and Yb^{3+} could be observed, which of course has a strong consequence on all further optical properties.

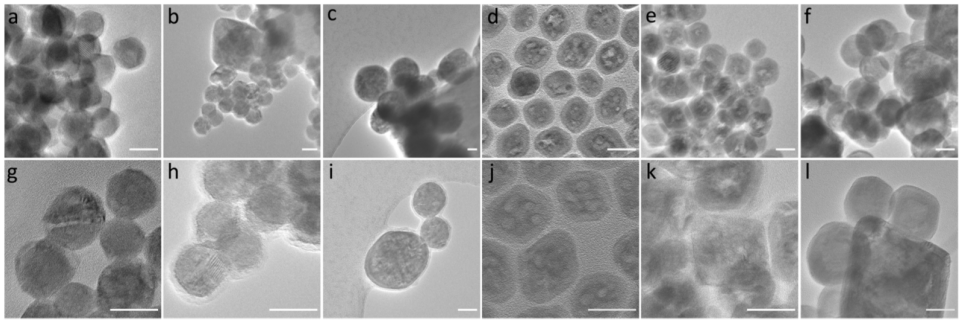

Fig. 1. Overview and magnified TEM images of (a, g) Er,Yb:$LiLuF_4$@$LiLuF_4$ where both the core and shell were obtained in the thermal decomposition route; (b, h) Er,Yb:$LiLuF_4$@$LiLuF_4$ where both the core and shell were obtained in the coprecipitation route; (c, i) $LiLuF_4$@ Er,Yb:$LiLuF_4$ where both the core and shell were obtained in the coprecipitation route; (d, j) Er,Yb:$LiLuF_4$@$LiYF_4$ with the core from the thermal decomposition route and the shell from the coprecipitation route; (e, k) $LiLuF_4$@Er,Yb:$LiYF_4$ with both the core and shell from the coprecipitation route; (f, l) $LiYF_4$@Er,Yb:$LiLuF_4$ with both the core and shell from the coprecipitation route. The scale bar is 25 nm for all images.

After detailed characterization of the materials, their room temperature and temperature dependent luminescence properties were investigated in detail. To confirm the observations of ion migration based on EDX maps, we have also carried out high temperature luminescence studies. The intensities of the Er^{3+} green emission peaks were compared at different temperatures (Fig. 2). The emission of $NaYF_4$:Er,Yb@$NaYF_4$ shows a linear drop in luminescence intensity from 280 to 480 K for all peaks. Fig. 2 shows that the intensity, normalized to 280 K, does not vary greatly with increasing temperature. This behavior was expected and indicates that the $NaYF_4$ core−shell nanoparticles show no (significant) ion migration from the core to the surface of the core-shell particles, where the luminescence of the emissive ions could get quenched by water molecules at room temperature. On the other hand, $LiLuF_4$:Er,Yb@$LiLuF_4$ shows a slight drop in luminescence intensity from 280 to 320 K followed by a sharp increase in intensity around the expected temperature of water evaporation at an onset of 340 K until 450 K where it reaches a saturation that is continued to 480 K. This behavior indicates that indeed emissive ions migrate from the core to the outer surface (shell) of the core−shell particles, where their luminescence is quenched by water molecules at room temperature. At elevated temperatures, the water starts to evaporate, leading to thermal enhancement due to weaker-intensity quenching of the emissive ions. When heterogenous core-shell structures are formed for this type of host materials ($LiLuF_4$:Er,Yb@$LiYF_4$) a linear drop in luminescence intensity from 280 to 480 K is observed for all peaks. This behavior was expected since significantly less ion migration was observed in the STEM and EDX maps. It is therefore observed that $LiYF_4$ shell is able to significantly hinder ion migration for $LiLuF_4$ core. We have additionally observed the intensity change for homogenous core-shell nanoparticles built of $LiYF_4$ ($LiYF_4$:Er,Yb@$LiYF_4$) and observed very similar behavior to that of $LiLuF_4$, therefore suggesting that lithium based host matrixes were less stable against ion migration then the well explored $NaYF_4$.

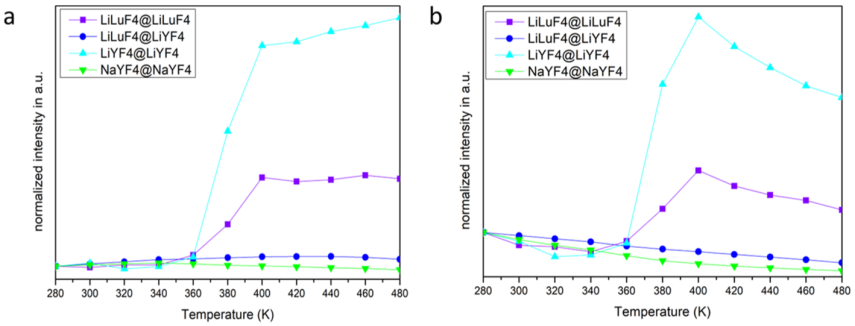

Fig. 2. Intensity of (a) $^2H_{11/2} \rightarrow {}^4I_{15/2}$ (520 nm) transition and (b). $^4S_{3/2} \rightarrow {}^4I_{15/2}$ (550 nm) transition for $LiLuF_4$:Er,Yb@$LiLuF_4$, $LiLuF_4$:Er,Yb@$LiYF_4$, $LiYF_4$:Er,Yb@$LiYF_4$, and $NaYF_4$:Er,Yb@$NaYF_4$. The intensities are normalized to the 280 K intensity of each sample. The highest intensity is reached around 380-400 K, where water evaporation from the surface of the sample is completed.

4. Conclusions

Our study shows that in Li-based host matrixes lanthanide dopants show a tendency to migrate between the core and the shell. Synthesis routes do not have an influence on this. The only way to overcome (or minimalize) the issue is by growing a heterogenous core-shell structure. Although luminescence enhancement after building a shell around a nanoparticle can be observed, this might solely be due to size increase only, and not the presence of an actual inert shell. This obviously has an impact of further optical properties and potential applications. Considering these findings, the importance of careful analysis of every new nanomaterial is highlighted.

Acknowledgements

These results are part of a project that has received funding from the European Research Council (ERC) under the European Union's Horizon 2020 research and innovation programme (Grant Agreement No. 945945).

References

[1]. D. Jaque, F. Vetrone, Luminescence nanothermometry. *Nanoscale*, Vol. 4, 2012, pp. 4301-4326.

[2]. S. Yatsyshyn, B. Stadnyk, Ya. Lutsyk, L. Buniak, Handbook of Thermometry and Nanothermometry, *IFSA Publishing*, 2014.

[3]. D. Hudry, I. A. Howard, R. Popescu, D. Gerthsen, B. S. Richards, Structure-property relationship in lanthanide-doped upconverting nanocrystals: Recent advances in understanding core-shell structures, *Advanced Materials*, Vol. 21, 2019, 1900623.

[4]. D. Hudry, A. M. M. Abeykoon, E. Dooryhee, D. Nykypanchuk, J. H. Dickerson, Probing the crystal structure and formation mechanism of lanthanide-doped upconverting nanocrystals, *Chemistry of Materials*, Vol. 28, 2016, pp. 8752-8763.

[5]. D. Hudry, R. Popescu, D. Busko, M. Diaz-Lopez, M. Abeykoon, P. Bordet, D. Gerthsen, I. A. Howard, B. S. Richards, Interface disorder in large single- and multi-shell upconverting nanocrystals, *Journal of Materials Chemistry C*, Vol. 7, 2019, pp. 1164-1172.

[6]. Q. Zou, C. Marcelot, N. Ratel-Ramond, X. Yi, P. Roblin, F. Frenzel, U. Resch-Genger, A. Eftekhari, A. Bouchet, C. Coudret, M. Verelst, X. Chen, R. Mauricot, C. Roux, Heterogenous Oxysulfide@FluorideCore / Shell Nanocrystals for Upconversion-Based Nanothermometry, *ACS Nano*, Vol. 16, 2022, pp. 12107-12117.

[7]. A. M. Kaczmarek, M. Suta, H. Rijckaert, T. van Swieten, I. Van Driessche, M. K. Kaczmarek, A. Meijerink, High temperature (nano)thermometers based on $LiLuF_4:Er^{3+},Yb^{3+}$ nano- and micro-crystals, *Journal of Materials Chemistry C*, Vol. 9, 2021, pp. 3589-3600.

[8]. M. Lederer, H. Rijckaert, A. M. Kaczmarek, Understanding and hindering ion migration in $Er,Yb:LiLuF_4$ core-shell nanoparticles for nanothermometers with enhanced photoluminescence, *ACS Applied Nano Materials*, Vol. 6, 2023, pp. 2438-2449.

(0122)

Photobiomodulation in Dentistry

Arasappan Rajakumaran and Lakshmi Balaji
Department of Conservative Dentistry & Endodontics,
Sri Ramachandra Institute of Higher Education & Research, Porur, Chennai, Tamil Nadu, India
E-mail: arasappan@sriramachandra.edu.in, lakshmifeb5@gmail.com

Summary: Photobiomodulation is defined as "a principle of inducing a biological response through energy transfer, in that the photonic energy delivered into the tissue by the LASER, modulates the biological processes within that tissue and within the biological system of which that tissue is a part. The term photobiomodulation being correlated to the mechanism underlying light therapy is replacing the different acronyms correlated to laser therapy, such as low-level laser therapy (LLLT), low-power laser therapy (LPLT), low-energy laser therapy (LELT), low-intensity laser therapy (LILT), high-intensity laser therapy (HILT). In this presentation, 215 published articles from PubMed and 118 published articles from Google Scholar database are reviewed to elaborate the application of "Photobiomodulation in dentistry".

Keywords: Photobiomodulation, low level laser therapy, application in dentistry, non-invasive therapy, photonic energy.

1. Introduction

One of the main goals of modern medicine is to reduce invasive aspects of therapeutic pathways, from diagnosis to surgery and to physical or pharmacological treatments. the invasiveness of a procedure depends not only on the procedure itself or on its secondary pharmacological treatment. Light can be considered as a one of the most crucial minimal invasive therapies [1].

2. Historical Background

The beneficial and therapeutic properties of light have been acknowledged since antiquity, and ancient peoples have identified the light and its power with deities [2]. At the end of the nineteenth century, after some sporadic observations about the bactericidal properties of sunlight, Ryberg Finsen invented a device for the treatment of lupus vulgaris and awarded a Nobel Prize [3]. In 1960 Theodore Maiman realized the first laser – a ruby laser (694 nm) and the surgical possibilities of laser use were first investigated within the field of medicine. In Hungary the physician Andrè Mester was studying the use of a ruby laser in oncology. He observed the regression of a skin melanoma after irradiation with a defective device, delivering insufficient energy for a surgical action. After he implanted cancer cells under the shaved skin of lab rats and irradiated the implantation area of some of them with a common ruby laser. Surprisingly the healing of the surgical incision and the hair regrowth were faster in the irradiated mice Andrè Mester is considered as the father of photobiomodulation, He gave the elaborate definition for photobiomodulation as "a principle of inducing a biological response through energy transfer, in that the photonic energy delivered into the tissue by the LASER, modulates the biological processes within that tissue and within the biological system of which that tissue is a part [4].

3. Mechanism of Action

The interaction of light with living matter is photo physical. The light of a given wavelength is absorbed by specific molecular chromophores that consequently become excited. If no absorption occurs, no photobiological and no phototherapeutic effects will be observed (first law of photobiology). The natural tendency to return to a more stable state (ground state) is satisfied through different possible pathways, non-radiative when the stored energy is released as heat (vibrational relaxation and internal conversion) or radiative (fluorescence). We may have a transition from the excited state (singlet) to a more stable and long-lived one (triplet state, with a change in the spin state, having unpaired electrons). The residual energy can be released through radiative processes (phosphorescence or delayed fluorescence) or used to trigger photochemical reactions, favoured by the long life of the triplet state, transferring electrons to molecular targets [5].

The literature evidence shows that there are series of reaction starts from a biophysical event (the absorption of the light by an intracellular chromophore) and continues with biochemical effects at cellular level and subsequent biological effects at tissue level, responsible for the clinical performances of LLLT: anti-inflammatory effects, analgesia, biostimulation, and bactericidal effects [6]. Arndt-Schulz law explains well regarding the dosage related biological effect on the tissue. [Fig 1].

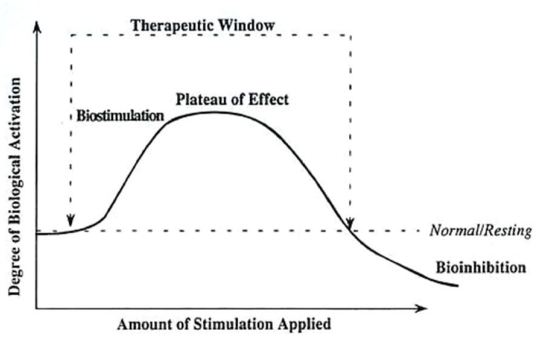

Fig. 1. Arndt-Schulz law.

4. Clinical Steps in Photobiomodulation

The sequence of events in clinical approach includes the following steps,

4.1 Diagnosis
4.2 Protocol
4.3 Safety
4.4 Power setting
4.5 Treatment
4.6 Follow up.

4.1. Diagnosis

Sonis et al in 2016 see things in the same light, suggesting an investigational strategy to ensure that the positive effect of the LLLT on the oral mucositis in head and neck cancer patients is independent from every effect on the speeding up of the neoplastic disease. The number of variables at stake is so high that a comparison among the articles is very difficult. It is also possible to combine different strategies in the attempt to find the best therapeutic options.

In 2015 Barasch et al. in a study on leukemic cells found that a pre-irradiation with a red laser was able to render the cells more sensitive to a treatment with ionizing radiations.

In the absence of a universal consensus, caution is necessary, studying carefully the clinical history of the patients before the treatment and avoiding irradiation if there are doubts about the differential diagnosis.

4.2. Protocol

The therapy of every pathology is performed following guidelines or recommendations based on scientific evidence or on the most extended consensus. LLLT finds its indications in its minimal invasiveness compared to other therapies or in its support to other elective treatments.

If there are no indications provided by scientific associations or academies, the most recent and accredited scientific literature will help in defining an acceptable protocol.

To define a protocol, it is necessary to evaluate and choose several parameters as follows:

- Wavelength
- Dose (fluence – energy density)
- Power density – intensity
- Emission mode
- Irradiation technique
- Number and timetable of the sessions
- Duration of the therapeutic treatment

4.3. Safety

Most of the contraindications and precautions arise from the possibility that the biostimulating and immunomodulating effects of LLLT could interfere with some physiological and pathological conditions or from the possibility of electromagnetic interferences with some obsolete implantable devices, such as pacemakers or implantable cardiac defibrillators (ICD).

4.4. Power Setting

Before treating it's necessary to set the laser equipment according to clinical parameters and to irradiation technique, checking carefully that the setting matches the data calculated in advance.

4.5. Treatment & Follow up.

When all the procedures relative to the choice of the protocol suitable for the diagnosed clinical condition (to laser setting; to safety) are concluded, the treatment can be performed.

During and after the application, the patient reactions must be detected, and the outcomes must be evaluated in order to verify the efficacy of the treatment and to intercept possible, although rare, side or adverse effects.

5. Conclusion

The photobiomodulation offers to the practitioners in every field of medicine and in every branch of dentistry the opportunity to interact with patients, with the maximum respect of their physical and psychological integrity, perfectly adhering to the new concept of health.

References

[1]. Donald J. Coluzzi, Steven P.A. Parker, Lasers in Dentistry – Current Concepts, *Springer Publications,* 2017.
[2]. Karu T., Is it time to consider photobiomodulation as a drug equivalent? *Photomed Laser Surg.*, 31, 5, 2013, pp. 189–191.
[3]. Gotzsche P., Niels Finsen's treatment for lupus vulgaris, *JRSM,* 104, 1, 2011, pp. 41–42.

[4]. Gaspar L., Professor Endre Mester, the father of photobiomodulation, *J Laser Dent.*, 17, 2009, pp. 146–148.
[5]. Jenkins P. A., Carrol J. D., How to report low-level laser therapy (LLLT)/photomedicine dose and beam parameters in clinical and laboratory studies, *Photomed Laser Surg*., 29, 12, 2011, pp. 785–787.
[6]. Hamblin M. R., Demidova T. N., Mechanisms of low-level light therapy, in Biomedical optics 2006, *International Society for Optics and Photonics,* 2006, 614001-614001-12.

(0435)

Advanced Laser Systems at the Extreme Light Infrastructure Beamlines Facility

R. Antipenkov, J. Novák, J. T. Green, J. Cupal, P. Trojek, B. Plötzeneder, P. Bakule, D. Kramer, D. Margarone, J. Andreasson and B. Rus
The Extreme Light Infrastructure ERIC, ELI Beamlines facility,
Za Radnicí 835, 252 41 Dolní Břežany, Czech Republic
E-mail: roman.antipenkov@eli-beams.eu

Summary: The mission of the Extreme Light Infrastructure (ELI) is to provide scientists with the access to the state-of-the-art high energy and high peak intensity laser systems for excellent research. ELI Beamlines facility is one of the ELI sites and it hosts four unique laser systems, which are designed to reach unprecedented parameters. The lasers operate at relatively high repetition rates given the delivered femtosecond pulse energy: from 1 kHz repletion rate for >50 mJ system to 1 shot/minute for the >1 kJ output system. These ultra-high intensity lasers are driving the experiments in the fields ranging from high-harmonics generation to laser driven particle acceleration and high energy density physics. These lasers together with the experimental stations and diagnostics are available to the scientific community as part of the open user access. In this contribution we are going to cover the current state and the parameters of the main laser systems, overview the specific challenges and give a detailed description of the available secondary sources and diagnostics.

Keywords: High-intensity lasers, Ultrashort pulse generation, Non-linear optics, Petawatt-class lasers, Laser particle acceleration.

1. Introduction

The ELI Beamlines laser facility provides scientists from across the world with an opportunity to perform unique experiments on laser-matter interaction, high repetition rate particle acceleration and explore high energy plasma states. Some of the instruments are already available for the open user access, the others will be offered soon after careful testing and characterization.

There are four state-of-the-art femtosecond laser systems that are covering a whole range of the performance parameters: from TW to PW peak powers and repetition rates from 1 kHz to 1 shot per minute.

2. Current Status of the Laser Systems

2.1. L1-Allegra kHz OPCPA System

The first laser system commissioned at ELI is the L1-Allegra laser, which is based entirely on OPCPA (optical parametric chirped pulse amplification) pumped by Yb-doped thin disk lasers. The system operates at 1 kHz repetition rate with an option to run in the 200 Hz regime. The minimum output pulse duration is 15 fs and the maximum output energy used for experiments is 50 mJ. The energy stability is ~1.6 % RMS over 10 minutes (see Fig. 1.). The laser is routinely operated for more than 20 weeks a year for a variety of user and in-house experiments, which include high-harmonic generation (HHG), driving the plasma X-ray source (PXS) or laser wakefield acceleration (LWFA) stations.

In addition to the main laser system, an auxiliary lower power laser with the same pulse duration is being developed. The auxiliary system is fully synchronized with the main L1-Allegra both through electronic and optical locking loops. It can be used for pump-probe experiments with very long time delays, as the auxiliary output can be shifted by an arbitrary time offset of up to 1 ms relative to the main pulse.

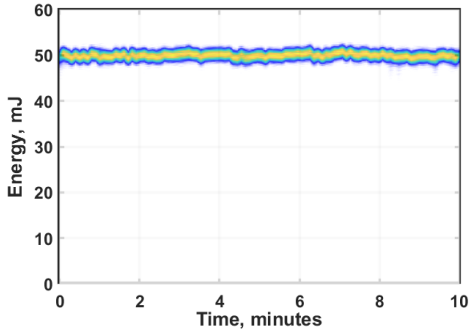

Fig. 1. The performance of the L1-Allegra laser at the maximum 50 mJ output energy.

2.2. L2-DUHA Laser

The L2-DUHA laser system is designed to operate at 20 Hz repetition rate with the possible upgrade to 50 Hz. It is a 100 TW femtosecond OPCPA system pumped by the helium-cooled multi-slab Yb:YAG laser. The architecture of the nanosecond pump laser is similar in design to DiPOLE laser system [1]. The output of the OPCPA will be compressed using grating compressor to 30 fs duration. The output of this laser

is mainly dedicated to drive laser particle acceleration experiments.

2.3. L3-HAPLS High Rep-rate PW System

The L3-HAPLS laser was developed at Lawrence Livermore National Laboratory and it can boast being a fully diode pumped system. Its nominal parameters are the operation at 10 Hz repetition rate providing 30 fs pulses at 1 PW peak power. It is a Ti:Sa system which employs two Nd-doped glass amplifiers pumped by high power laser diode arrays [2]. The design of the multi-slab amplifier cooled by room temperature, high flow speed helium gas [3] enables for the efficient heat removal in both the pump laser and the main amplifier. The system can currently deliver up to 13 J in about 27 fs at a repetition rate of 3.3 Hz for the experimental campaigns.

2.4. 10 PW L4-ATON Laser

The L4-ATON system architecture is based on an OPCPA front-end, followed by the direct amplification in the flash-lamp pumped multi-slab modules with two types of Nd:glass. Innovative technologies, such as liquid cooling of laser modules, allow for the operation of the system at the repetition rate of up to 1 shot per minute. The demonstrated maximum energy reaches 1.5 kJ, and the diagnostics compressor [4] has been used to prove the compressibility of the pulses to below 150 fs. Currently, the assembly of the full aperture compressor is in progress. After commissioning it will enable the operation in the 10 PW regime.

The L4-ATON laser also has a non-CPA mode of operation, when the power amplifier chain is seeded by a narrowband nanosecond pulse instead of the broadband OPCPA frond-end output. The narrowband pulse can be temporally shaped in a wide range of pulse durations. This mode of operation at a kJ-level is already available for the experiments [5].

3. Integration with the Experiments

The current development at ELI Beamlines facility is now aimed at exploiting the full potential of such high repetition rate systems. The implemented data archiving system is capable of storing thousands of measured parameters and system variables with a facility-wide synchronized timestamp. This way the collection of the experimental data can be significantly automated. In addition, such large amount of stored data allows for development and using of AI algorithms to interpret the results.

The recently commissioned beam transport enables the beam delivery from laser floor either to the plasma physics research hall, or to the stations dedicated to high-repetition rate ion acceleration. The beam path switching is automated and repeatable, thus allowing for the versatile use of the laser.

In addition, a lot of attention is dedicated to the synchronization and stabilization of the laser systems to ensure reliable performance. For the kHz system, multiple feedback loops are installed that are stabilizing the beam pointing, temperature and temporal overlap of the pulses. The centralized timing system provides the reference clock for synchronization of the independent lasers together. This, together with a sophisticated beam transport, opens the possibility of the multibeam experiments.

4. Conclusions

In this contribution we will cover the current state of the systems mentioned above with the focus on the recently introduced upgrades and new features. We will also briefly present the technology and tools that are already available through the ELI open access user programme.

Acknowledgements

A portion of the presented work was supported by European Regional Development Fund (ADONIS, CZ.02.1.01/0.0/0.0/16–019/0000789) and Ministry of Education, Youth and Sports of the Czech Republic (NPS II Project No. LQ1606).

References

[1]. S. Banerjee, et al., DiPOLE: a 10 J, 10 Hz cryogenic gas cooled multi-slab nanosecond Yb:YAG laser, *Optics Express*, Vol. 23, Issue 15, 2015, pp. 19542-19551.

[2]. C. L. Haefner, et al., High average power, diode pumped petawatt laser systems: a new generation of lasers enabling precision science and commercial applications, *Proceedings of SPIE*, Vol. 10241, 2017, 1024102.

[3]. A. Bayramian, et al., The Mercury project: A high average power, gas-cooled laser for inertial fusion energy development, *Fusion Science and Technology*, Vol. 52, Issue 3, 2007, pp. 383-387.

[4]. Š. Vyhlídka, et al., Temporal diagnostics for kJ class laser using object-image-grating self-tiling compressor, *Proceedings of SPIE*, Vol. 11034, 2019, 1103409.

[5]. F. P. Condamine, et al., Commissioning results from the high-repetition rate nanosecond-kilojoule laser beamline at the extreme light infrastructure, *Plasma Physics and Controlled Fusion*, Vol. 65, Issue 1, 2023, 015004.

(0460)

High-gain and Low-noise-figure Quantum-dash Semiconductor Optical Amplifier over Wide Temperature Rang

Youxin Mao [1], Chun-Ying Song [1], Zhenguo Lu [1], Philip J. Poole [1], Jiaren Liu [1], Guocheng Liu [1], Pedro Barrios [1], Daniel Poitras [1], John Weber [1], Ping Zhao [1], Martin Vachon [1], Xiaoran Xie [1] and Ahmad Atieh [2]

[1] Advanced Electronics and Photonics Research Centre, National Research Council Canada, Ottawa, ON, Canada

[2] Optiwave Systems, 7 Capella Court, Suite 300, Ottawa, ON, Canada

Tel.: + 613-993-7331

E-mail: youxin.mao@nrc-cnrc.gc.ca

Summary: A advanced C- and L-band InAs/InP quantum dash optical amplifiers (Qdash SOA) is presented. A chip gain of 31 dB and 3 dB output saturated power of 18 dBm were achieved at CW bias current 400 mA and temperature 17 °C. The value of NF is less than 6 dB in the whole temperature range from 17 to 80 °C and it is almost constant across small-signal gain region. The range of 3 dB amplified spontaneous emission (ASE) bandwidth achieved is from 50 to 80 nm, and the peak wavelength covers from 1516 to 1581 nm at 100-450 mA and 17-80 °C. To our knowledge, the overall performance of our Qdash SOA is better than the reported so far.

Keywords: Quantum dash, Semiconductor optical amplifier, Chip gain, Noise figure.

1. Introduction

Quantum dot or dash semiconductor optical amplifiers (QD-SOA) [1, 2] are key components in compact integrated optical circuits, optical communications, and all-optical signal processing. QD-SOAs have many advantages over quantum well (QW) SOAs including a much broad bandwidth due to the gain inhomogeneity, ultra-fast recovery time within a few picoseconds [3] that ensures distortion-less amplification of high speed signals, low bias and noise figure (NF), and the ability to amplify multi-wavelength signals with no crosstalk. The most important characteristics of QD gain media is great temperature stability and other properties that distinguishes them from QW devices [4]. In this presentation, we report an overall high performance C- and L-band InAs/InP quantum dash (QDash) SOA fabricated in NRC Canada. 31-17 dB chip gain and 1-6 dB NF are achieved in the small signal gain range within the 17-80 °C temperature range. A 3 dB ASE bandwidth of 80 nm is obtained at 300 mA and 80 °C. These performances make it a promising solution for applications in all-optical signal processing, and high-speed optical and wireless networks to replace bulked and high cost EDFA and Raman amplifiers.

2. Materials and Devices

QDash gain material was grown on a n-InP substrate with an InP buffer and lattice matched cladding (1.15Q) as shown in Fig. 1(a). The core consists of five-stack-layers of InAs QDashes as shown by a cross-sectional SEM image in Fig. 1(b) and the inset shows SEM image of the top view of the QDash. The average density in each layer is around $3.5 \times 10^{10}\ cm^{-2}$. This core structure provides both carrier and optical confinement in the active region emitting in C- and L-band range. The waveguide was fixed at an angle of 7° to the normal of the cleaved facet to reduce reflection. The cleaved facets were coated with anti-reflective dielectric materials with $<10^{-4}$ mode reflectivity for further reducing reflection.

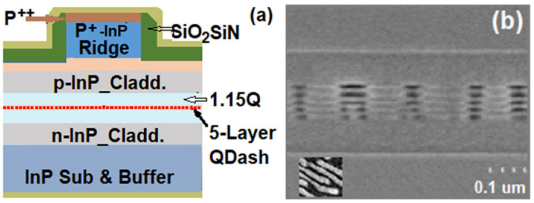

Fig. 1. (a) Schematic diagram of grown structure for an InAs/InP QDash SOA. (b) Cross-section SEM image of five QDash layers in the active region. Inset: the top view of a QDash layer.

3. Experimental Setup

Fig. 2 shows a test setup for a QDash SOA, where blue and black boxes are for ASE and gain/NF measurements, respectively. The SOA chip was mounted on the station driven with an ILX controller for CW bias and temperature. For calibration of the fiber coupling powers from the tilted output beams, total output ASE powers at the difference biases and temperatures were first measured by using a large-area-photodetector. The output of SOA waveguide was then aligned by a lensed PM fiber on the output facet, then connected to a double-stage

isolator and a 1×2 90/10 optical coupler. The measured coupling losses are between 12 and 18.5 dB depending on the conditions. The average of these values equals to 15.25 dB, which is a good match to the 15 dB reported in [5]. The coupling loss plus the insertion/excess losses of the isolator and 90/10 coupler are used for the calibration of the SOA input and output powers, therefore for SOA chip gain, saturation output power, and noise figure.

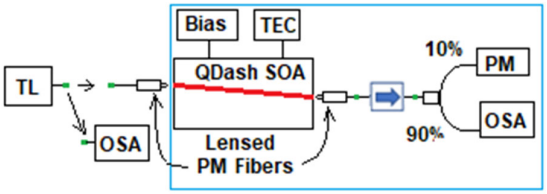

Fig. 2. Block diagram of test setup used for characterizing the QDash SOA. TL: Tunable Laser, PM: Power Meter, OSA: Optical spectrum Analyzer. All fibers used are polarization maintaining (PM) fibers.

4. Results and Discussion

ASE spectra of an QDash SOA in temperature of 17-80 ºC at CW 300 and 400 mA are presented in Fig. 3(a). The ASE peak wavelength λ_p, (left) and 3 dB bandwidth $\Delta\lambda$ (right) versus bias and temperature are shown in Fig. 3(b). They show that the ASE intensity decreases and the peak shifts to longer wavelength when temperature increases. The range of λ_p of 1515.7 to 1581.3 nm was obtained with covering the whole C-band and part of L-band. The $\Delta\lambda$ increases with both bias and temperature increases. The $\Delta\lambda$ of 80 nm is obtained at CW 450 mA and 80 ºC.

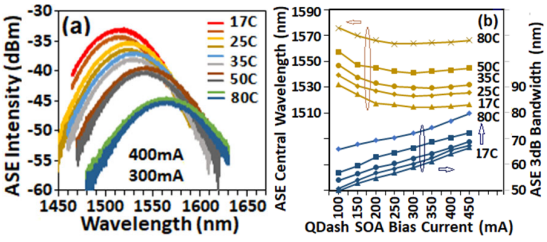

Fig. 3 (a) ASE spectra of QDash-SOA at the temperature from 17-80C and CW currents at 400 mA and 300-mA. (b) ASE peak wavelength and 3 dB bandwidth versus bias current and temperature.

From Fig. 4(a), the maximum small signal gain G_{max} of 31 dB is obtained at 400 mA and 17 ºC. Fig. 4(b) shows, as temperature increases from 17 to 80 ºC at 300 mA, the G_{max} decreases from 30 to 17 dB, wavelength at G_{max} shifts from 1530 to 1562 nm, and the output saturated power $P_{0\text{-}sat}$ decreases from 18.0 to 14.8 dBm.

Due to achieved high SOA gain and low source spontaneous emission P_{SSE} (<-70 dBm from the Agilent TL), NF mainly depends on signal-spontaneous beat noise for our QDash SOA, which can be expressed as $NF = 2 \cdot P_{in}/(\Delta\nu h\nu OSNR_{out})$ as described in Ref [3]. Fig. 5(a) shows, at all 17-80 ºC, the values of NF are <6 dB and keep constant across the small-signal gain region, but increase in the saturated region, which is due to the linearity of $OSNR_{out}$ over low inputs and saturated after. The lowest NF value is at 25 ºC temperature and -12 dBm input power as shown in Fig. 5(b).

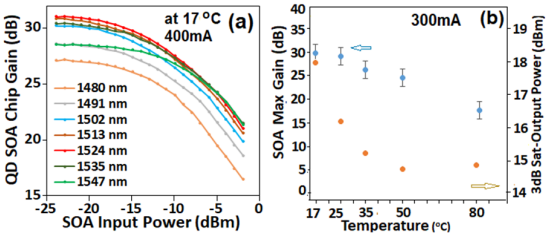

Fig. 4. (a) Chip Gain as a function of input power for different wavelengths at CW 400 mA and 17 ºC. (b) Max gain (left) and 3 dB saturated output power (right) vs. temperature at CW 300 mA.

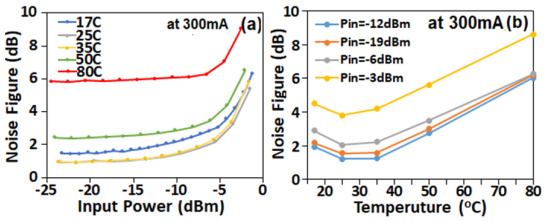

Fig. 5. (a) Noise figure as a function of input power for different temperatures at 300 mA. (b) Noise figure as a function of temperature for different inputs at 300 mA.

4. Conclusions

High performance C- and L-band QDash semiconductor optical amplifier (SOA) is demonstrated. High small-signal chip gain of 31-17 dB and low noise figure less than 6 dB are achieved within the 17-80 ºC temperature range. A wide 3 dB bandwidth of 80 nm is obtained at 80 ºC. These results may lead to an important step towards small size, cost-efficient, high gain, low noise figure, broad bandwidth, and a high temperature property SOA for advanced systems such as compact integrated optical circuits, optical communications, and all-optical signal processing.

Acknowledgements

The authors would like to acknowledge the support of National Research Council Canada's High Throughput and Secure Networks (HTSN) challenge research program.

References

[1]. T. Akiyama, M. Sugawara, Y. Arakawa, Quantum-dot semiconductor optical amplifiers, *Proceedings of IEEE,* Vol. 95, 2007, pp. 1757-1766.

[2]. S. Liu, et al., High-performance o-band quantum-dot semiconductor optical amplifiers directly grown on a CMOS compatible silicon substrate, *ACS Photonics*, Vol. 6, Issue 10, 2019, pp. 2523-2529.

[3]. B. Boriboon, et al*.,* Performances of conventional SOAs versus QD-SOA in 1530-nm upstream transmission of 40 Gb/s access network, *IEEE Photonics Journal,* Vol. 14, Issue 1, 2022, pp. 1-12.

[4]. K. Akahane, T. Umezawa, A. Matsumoto, Y. Yoshida, N. Yamamoto, High temperature operation of quantum dot semiconductor optical amplifier for uncooled 80 Gbps data transmission, in *Proceedings of the Conference on Lasers and Electro-Optics (CLEO'20)*, 2020, p. AW3M.2.

[5]. B. Boriboon, D. Worasucheep, A. Matsumoto, K. Akahane, N. Yamamoto, N. Wada, Optimized design of QD-LD toward QD-SOA to achieve 35-dB maximum chip gain with 400-mA injected current, *Opt. Commun*., Vol. 475, 2020, 126238.

(0884)

Terahertz Four-wave Mixing in Fluorides

D. Lorenc [1], E. Noskovicova [1,2] and M. Jerigova [1,2]
[1] International Laser Centre, Ilkovicova 3, 84104 Bratislava, Slovakia
[2] Faculty of Natural Sciences, Comenius University, Ilkovicova 6, 84104 Bratislava, Slovakia
Tel.: + 421265421575, fax: + 421265423244
E-mail: dusan.lorenc@gmail.com

Summary: Toxic industrial chemicals/materials (TICs/TIMs) play an important role from an environmental and safety point of view. One of the areas of intensive research is the use of THz spectroscopic techniques in the identification of TIC/TIM type substances in the gas phase however current THz spectrometers are costly and cumbersome. Four-wave mixing (FWM) in chi(3) media offers the possibility of converting the THz signal into the optical domain. In this contribution, we studied the interaction of intense broadband THz pulses with an optical pump at ω_p = 800 nm in the co-propagating geometry, while observing properties of the generated signal with a wavelength of ω_s = 400 nm – Ω_{THz}. A number of samples has been tested but the THz-FWM signal was only observed in fluorides and is both well collimated and temporally localized. We conclude that the THz-FWM signal observed in CaF_2, BaF_2 and MgF_2 is due to resonantly amplified FWM process. The presented method has prospective use in THz sensorics.

Keywords: THz-FWM, Terahertz nonlinear optics.

1. Introduction

Rapid and sensitive THz-frequency gas- and molecule- detectors – typically operating in the range of 0.1-10 THz – are at the forefront of current research effort as they would ideally allow an unambiguous identification of chemicals and compounds at extremely low concentration levels – potentially down to the single molecule scale. THz based gas detection, for example, shows great promise toward both environmental and security related applications [1]. For instance, under normal working conditions toxic industrial materials (TIMs) may pose even a greater threat than chemical warfare agents (CWA), since such chemicals are more commonly found than CWAs. The THz frequency domain is ideally suited for sensing small molecules and larger hydrocarbons, since they typically show strong response within this spectral range [2]. However, current THz spectrometers are typically cumbersome and costly, since they either rely on mechanical delay stages, or coupled/synchronized femtosecond laser sources. Here we explore THz-FWM [4-6] in fluorides as a mean of converting the THz signal into the optical domain. Experimentally our approach follows that of Clerici *et. al.* [3] but instead of diamond, we apply fluorides (CaF_2, MgF_2 and BaF_2) and show resonant enhancement of the FWM.

2. Experiment

The output beam of an amplified Ti:Sapphire system (COHERENT Legend DUO) was split into two with the main output of 3 mJ at 120 fs acting as a pump for 2-colour plasma based THz source [7] and the remaining 0.5 mJ used as an optical pump for the FWM. Both the pump and THz pulses were overlapped inside of the fluoride sample and a combination of low-pass filter and fiber coupled spectrometer (Flame-T, Ocean Optics) was used to sample the THz-FWM optical signal. A set of optical grade microscopic cover slips was used to tune the pump power and a combination of two wire-grid polarizers (Pure-wave polarizers) was employed as a variable attenuator for the THz idler beam.
For an efficient FWM to occur, phase matching condition has to be satisfied:

$$2k_{\omega_p} = k_{\omega_s} + k_{\Omega_{THz}},$$

where ω_p, ω_s and Ω_{THz} are respective frequencies of pump, signal and the terahertz waves as schematically depicted in Fig. 1a. This condition is generally difficult to be satisfied given the broad range of frequencies involved (10^{12}-10^{15} Hz) although some benefits can be gained in the counterpropagating geometry [3]. In our case a substantial signal ω_s has been observed in case of co-propagating geometry and fluoride samples as shown in Fig. 1b.

We identify the actual detuning Ω_{THz} to correspond to a strong resonance in BaF_2 [8] hence the lower level as marked by the dotted green line in Fig. 1a corresponds to a real level of the system. Also note, that we have performed a separate OPTP (optical-pump THz-probe) experiment proving the THz-FWM signal to be temporally localized thereby excluding any long lasting effects in the system.

Although the THz-FWM signal (ω_s) intensity follows the expected linear scaling as a function of the THz intensity as seen in Fig. 2, there is a stark

difference to the expected parabolic scaling with respect to pump intensity and instead we observe activated behavior.

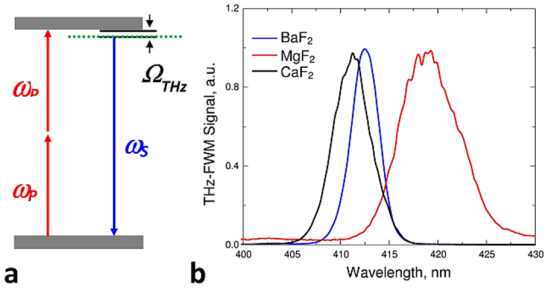

Fig. 1. Schematics of the THz-FWM (a). THz-FWM signal (ω_s) as obtained in CaF_2, BaF_2 and MgF_2 samples (b).

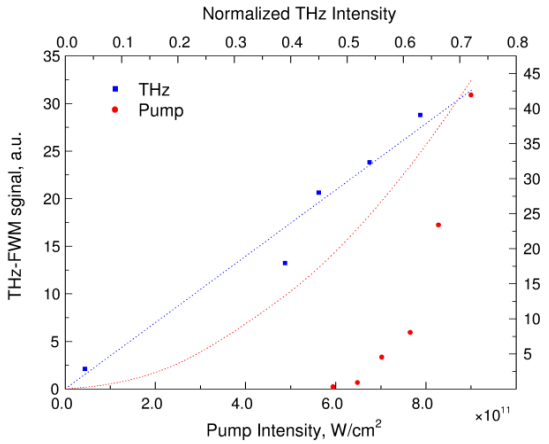

Fig. 2. THz-FWM scaling with the THz intensity (blue) and pump intensity (red). Blue dotted line is the actual linear fit, while red dotted line represents the expected parabolic scaling.

Note that this significantly different from the previous findings in diamond [3] as they were proving the parabolic scaling. We believe that the activated scaling supports our finding of the resonantly enhanced THz-FWM in fluorides.

4. Conclusions

We have demonstrated THz-FWM in selected fluorides and identified the effect to be due to resonant enhancement. Our approach shows potential toward THz detection by optical means.

Acknowledgements

This research is sponsored by NATO's Emerging Security Challenges Division in the framework of the Science for Peace and Security Programme.

References

[1]. M. F. Pereira, O. Shulika (Eds.), Terahertz and Mid Infrared Radiation: Detection of Explosives and CBRN (Using Terahertz), *Springer Science+Business Media*, Dordrecht, 2014.

[2]. H. Pickett, R. Poynter, E. Cohen, et al., Submillimeter, millimeter, and microwave spectral line catalog, *J. Quant. Spectrosc. & Rad. Transfer*, Vol. 60, Issue 5, 1998, pp. 883-890.

[3]. M. Clerici, L. Caspani, E. Rubino, M. Peccianti, M. Cassataro, A. Busacca, T. Ozaki, D. Faccio, R. Morandotti, Counterpropagating frequency mixing with terahertz waves in diamond, *Opt. Lett*., Vol. 38, Issue 2, 2013, pp. 178-180.

[4]. M. Koys, E. Noskovicova, D. Velic, D. Lorenc, Nonphasematched broadband THz amplification and reshaping in a dispersive chi(3) medium, *Opt. Express*, Vol. 25, Issue 12, 2017, pp. 13872-13882.

[5]. V. Kumar, R. K. Varshney, S. Kumar, Terahertz generation by four-wave mixing and guidance in diatomic Teflon photonic crystal fibers, *Opt. Comm.,* Vol. 454, 2020, 124460.

[6]. T. Christopoulos, O. Tsilipakos, E. E. Kriezis, Degenerate four-wave mixing in the THz regime with standing-wave graphene resonators, *J. Opt. Soc. Am. B*, Vol. 37, Issue 9, 2020, pp. 2626-2636.

[7]. X.-C. Zhang, J. Xu, Introduction to THz Wave Photonics, *Springer,* New York, 2010.

[8]. W. Kaiser, W. G. Spitzer, R. H. Kaiser, L. E. Howarth, Infrared properties of CaF_2, SrF_2, BaF_2, *Phys. Rev.*, Vol. 127, Issue 6, 1962, pp. 1950-1954.

(1161)

UV Stability of Femtosecond Laser Textured Stainless Steel Surfaces

O. Myronyuk [1], A. M. Rodin [2] and D. Baklan [1]
[1] Igor Sikorsky Kyiv Polytechnic Institute, Department of Chemical Technology of Composite Materials, Peremohy Ave. 37, 03056 Kyiv, Ukraine
[2] Center for Physical Sciences and Technology, Solid State Laser Laboratory, Savanoriu Ave. 231, 02300 Vilnius, Lithuania
Tel.: + (370)60140057
E-mail: aleksej.rodin@ftmc.lt

Summary: The use of femtosecond lasers for texturing metal surfaces at both micro- and submicron levels is a promising way for imparting superhydrophobic properties. Although the effect of self-hydrophobization, based on a gradual increase in the water repellency of such surfaces after microprocessing, is well known, their resistance to one of the main environmental factors – ultraviolet, has not been studied in detail. This effect was investigated here on a femtosecond laser textured surface of ANSI 304 stainless steel. The microtexture alone provided a water contact angle of 159°, and in combination with the LIPSS nanotexture – from 140° to 155°, depending on the grating pitch. Although the combination of nano- and microtexture proved to be more resistant to UV exposure, the water repellency due to self-hydrophobization was still not sufficiently stable.

Keywords: Functional materials, Superhydrophobic surface, Ultrafast laser-matter interaction, Laser micro-texturing, Laser-induced periodic surface structures (LIPSS), UV resistance.

1. Introduction

Femtosecond laser texturing is a promising way to obtain superhydrophobic metal surfaces, and in some cases these surfaces, initially hydrophilic after micromachining, subsequently become superhydrophobic without any additional treatment. This transition, called "wettability conversion", has found several explanations for its nature. It was shown [1] that the resulting surface has two types of roughness at the micro- and nanolevels, and the amount of carbon on the surface increases with time after texturing. The increase in the content of C may be due to the interaction with CO_2 in the air. It has been shown that the transition occurs faster in a CO_2 atmosphere than in air, and as a result, higher water contact angles were obtained [2]. Another explanation is the interaction with organic compounds and the appearance of nonpolar carbon groups on the surface after treatment [3]. The formation of hydrophobic properties in vacuum is also reported, which may be associated with internal chemical processes in the material [4]. However, it has been shown that superhydrophobic properties can change, for example, upon interaction with water [2]. In this work, we study the resistance of the water-repellent properties of a stainless-steel surface to UV exposure depending on the type of laser texture.

2. Materials and Methods

Both nanopatterns and microtextures were machined using “Carbide” laser (Light Conversion) with an average power of 6 W at a wavelength of 1030 nm, a pulse width of ~360 fs and a repetition rate of 60 kHz. Samples with a polished surface of 20×20 mm^2 and a thickness of 2 mm were made from AISI 304 series stainless steel. To form LIPPS nanopatterns, the samples were moved at a speed of 60 mm/s using X-Y stages (Aerotech). The energy of the laser pulse on the sample reached ~46 μJ, and the spot diameter of the focused laser beam was ~80 μm (at $1/e^2$ level). The laser spots overlapped on the sample by ~60 % with continuous scanning and a step between adjacent lines of 30 μm. To engrave microtextures, the laser beam was expanded to a diameter of ~7 mm (at $1/e^2$ level) in front of a lens with a focal length of 1 inch for a sharper focus of ~5 μm. The energy of the laser pulse on the sample varied from ~21 μJ to ~35 μJ at 60 kHz and the samples moved at the same speed.

UV exposure testing was performed using the procedures defined in ASTM D4329. A 400 W 340 UVA fluorescent lamp was used to simulate mid-to-short UV sunlight with an uninsulated black panel at a controlled temperature of 60 ± 3 °C. The surface of the samples was recorded with a TESCAN MIRA3 scanning electron microscope, and the water contact angle (WCA) was determined by the sessile drop technique using an optical microscope and a Delta Optical HCDE-50 digital camera.

3. Results

WCA obtained on the surface of stainless steel after laser texturing after 120 days of exposure to the ambient air are given in Tab. 1. Reducing the pitch of the grooves allows the WCA to be increased to 155° for pattern *K* compared to 140° for sample *J*. Notably, sample *L*, which does not contain LIPSS but has a microtexture like sample *K*, has an even larger WAC of 159°.

Table 1. WCA according to laser textured pattern.

Sample	Laser textured pattern	WCA
Plain steel	-	62
J	LIPPS and microgrooves with a pitch of 100 µm and a width of 30 µm	140
K	LIPPS and microgrooves with a pitch of 60 µm and a width of 45 µm	155
L	Plain top, grooves with a pitch of 60 µm and a width of 45 µm	159

SEM shows a nanotexture (Fig. 1a) at the top of micrograting protrusions (Fig. 1b).

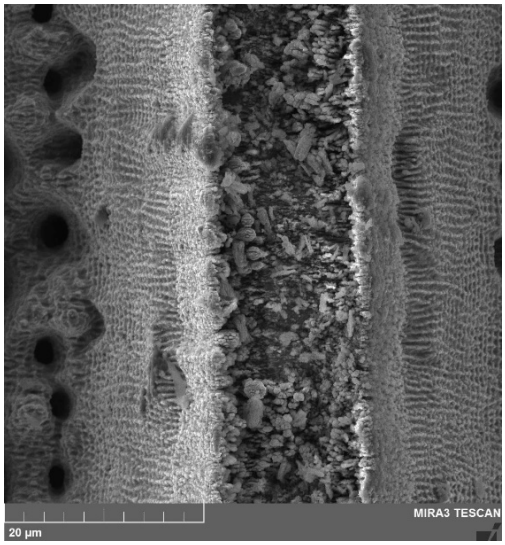

a

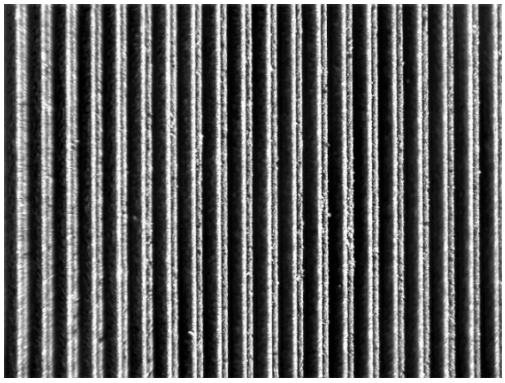

b

Fig. 1. Surface texture of sample "*L*" seen under SEM (a) and under optical microscope (b).

Under the influence of UV irradiation, a decrease in WCA was observed (Fig. 2), which indicates an increase in the surface polarity. The most resistant to UV radiation was sample *L*, which becomes hydrophilic only after 90 min of exposure. For samples *K* and *J*, the transition to hydrophilic properties occurs after 45 min and ~30 min, respectively. Some WCA changes are observed even on a plain steel sample.

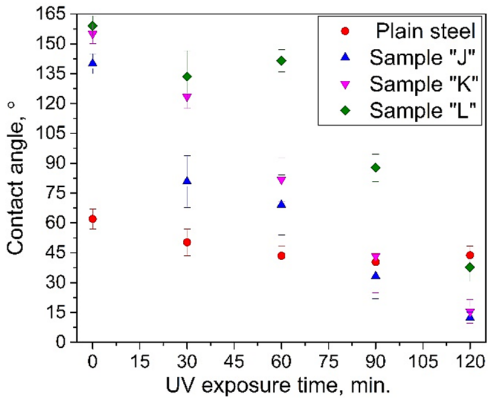

Fig. 2. WCA change with UV exposure.

4. Conclusions

The effect of UV irradiation on the water repellency of a laser-textured 304 stainless steel surface is considered. It has been shown that the water repellency of such surfaces is highly unstable when exposed to UV radiation and needs to be improved, for example using chemical post-treatment.

Acknowledgements

This project has received funding from the Research Council of Lithuania, agreement S-LU-22-3 and Ministry of Education and Science of Ukraine, agreement No. 28, reg. No. 0122U002645.

References

[1]. A. M. Kietzig, S. G. Hatzikiriakos, P. Englezos, Patterned superhydrophobic metallic surfaces, *Langmuir*, Vol. 25, 2009, pp. 4821-4827.

[2]. S. Basset, G. Heisbourg, A. Pascale-Hamri, S. Benayoun, S. Valette, Effect of texturing environment on wetting of biomimetic superhydrophobic surfaces designed by femtosecond laser texturing, *Nanomaterials*, Vol. 12, 2022, 3099.

[3]. P. Bizi-Bandoki, S. Valette, E. Audouard, S. Benayoun, Time dependency of the hydrophilicity and hydrophobicity of metallic alloys subjected to femtosecond laser irradiations, *Applied Surface Science*, Vol. 273, 2013, pp. 399-407.

[4]. R. Fürbacher, G. Liedl, A. Otto, Fast transition from hydrophilic to superhydrophobic, icephobic properties of stainless steel samples after femtosecond laser processing and exposure to hydrocarbons, *Procedia CIRP*, Vol. 111, 2022, pp. 643-647.

(1251)

Dissimilar Laser Beam Welding of Titanium to Stainless Steel Using Pure Niobium as Filler Material in Lap Joint Configuration

M. Wiegand [1], A. Kimm [1], N. Sommer [1], L. Marks [2] and S. Böhm [1]
[1] Department for Cutting and Joining Manufacturing Processes, Institute for Production Technologies and Logistics, University of Kassel, Kurt-Wolters-Str. 3, Kassel, Germany
[2] NMI Natural and Medical Sciences Institute at the University of Tübingen, Markwiesenstr. 55, Reutlingen, Germany
Tel.: +49561804-3863, fax: +49561804-2045
E-mail: m.wiegand@uni-kassel.de

Summary: In the present investigation, commercially-pure titanium is welded to AISI 316L stainless steel by intermixing niobium as filler material in lap joint configuration. For this purpose, a pulsed Nd:YAG laser with various pulse durations and pulse peak powers is employed in order to obtain different mixing conditions of the materials. It will be demonstrated that, despite the implementation of the filler material, the weld seams are characterized by a high affinity for cracking, which in turn can be attributed to the formation of hard intermetallic compounds. Nevertheless, utilization of optimized process parameters can yield crack-free specimens in a reproducible manner. Tensile forces of up to 140 N can be achieved with a single weld seam. By increasing the joint area with four adjacent weld seams, tensile forces up to 320 N are attained, thus exceeding the yield strength of the stainless steel.

Keywords: Pulsed laser beam welding, Dissimilar welding, Intermetallic compounds, Titanium, Medical technology.

1. Introduction

Dissimilar welded joints provide the potential to combine the individual properties of metals and, thus, generate various functional and economic advantages. In particular, hybrid parts made of commercially-pure titanium (cp-Ti) and stainless steel are of high relevance in many industrial sectors, as for example chemical, energy and medical technology industries [1, 2]. However, dissimilar fusion welding of cp-Ti to stainless steel is limited by thermophysical and chemical incompatibilities. The Fe-Ti phase diagram visualizes that fusion welding of cp-Ti to stainless steel is restricted by a very low solubility in solid state as well as the formation of intermetallic compounds (IMC) [1, 3]. These IMC are extremely brittle and consequently severely restrict the weldability and mechanical properties of fusion welded joints. Further limitations arise from different melting temperatures, thermal conductivities and thermal expansions of the materials, resulting in considerably increased stress conditions during cooling [1].

Previous studies on autogenous beam welding of titanium to stainless steel have consequently achieved comparatively poor joining properties [4-6]. However, by using filler materials, it is possible to substantially increase the chemical compatibility of the joint. Previously investigated filler materials, e.g., copper [7, 8], vanadium [8-10], nickel [8] as well as multilayer configurations such as Nb/Cu [9, 11, 12], Nb/Ni [13] and Ta/Va/Fe [14] showed substantially enhanced properties for dissimilar welded joints of titanium and stainless steel. However, the aforementioned material combinations are unsuitable for medical technology applications, as they do not exclusively involve biocompatible materials. In a recent study by Wiegand et al. [2], pure niobium (Nb) was also found to be a promising filler material if used as an interlayer between cp-Ti and stainless steel in butt-joint configuration. In addition to the comparatively high tensile strength achieved in this study, pure Nb is biocompatible, allowing the welded parts to potentially be used in medical applications.

The present investigation builds on this study and addresses intermixing of a Nb foil into a cp-Ti / stainless steel dissimilar weld in lap joint configuration. Different pulse durations as well as pulse peak powers were applied to control the welding depth into the substrate sheet, the time for intermixing processes to occur and, thus, tailor the chemical composition of the respective weld metal. It can be demonstrated that crack-free weldments can be generated in a reproducible manner if optimized process parameters are applied.

2. Materials and Methods

Thin sheet geometries measuring $12.5 \times 25 \times 0.25$ mm^3 were used as base materials. Nb-foil with a thickness of 0.1 mm was inserted as an interlayer between both base materials. The welding tests were performed on a pulsed Nd:YAG laser SLS 200 CL 8 (Coherent Switzerland AG, formerly ROFIN-LASAG AG, Belp, Switzerland) with a beam diameter of approximately 38 µm. The welding system offers a maximum laser output power of 1 kW and the option to perform free-form pulse-shaping. The

applied process parameters are summarized in Table 1. In order to achieve varying welding depths, the pulse peak power was increased in increments of 25 W, resulting in a total of 5 weld seams for each pulse duration. In addition, a customized pulse shape was implemented. Hence, the power was continuously reduced within the individual pulses and, consequently, provided more homogeneous cooling conditions. The beam was focused on the surface of the top sheet.

Table 1. Overview of the applied welding parameters.

Pulse Duration [ms]	Pulse Peak Power [W]	Traverse Speed [mm/s]	Pulse Frequency [Hz]
1	700-800	0.15	3
3	400-500	0.3	
7	300-400		
10	250-350		

The welding tests were carried out using titanium as the top sheet with stainless steel as the substrate sheet and vice versa. The welding configuration is schematically illustrated in Fig. 1. In order to ensure a virtually gap-free positioning, the specimens were clamped in a special fixture. Furthermore, the welding processes were conducted using argon 4.8 as shielding gas to obtain an optimal protection of the highly reactive materials.

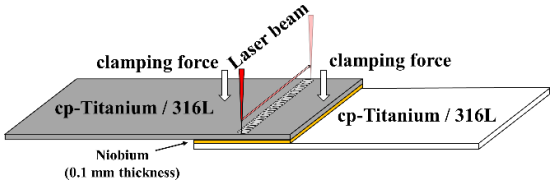

Fig. 1. Schematic illustration of the welding configuration.

The welded samples were characterized by means of optical light microscopy, hardness mappings as well as tensile tests.

3. Results and Discussion

The welding tests performed reveal that the investigated material combination is mostly characterized by severe crack formation in longitudinal direction along the welding trajectory, as exemplified in Fig. 2. The observed poor weldability can ultimately be attributed to the presence of brittle IMC, which form due to the mixing of stainless steel with cp-Ti and Nb, respectively [2]. As can be derived from the hardness mapping of an exemplary sample in Fig. 3a, the cracked specimens are characterized by extreme hardness values, which partly exceed 1000 HV. These values correspond very well to the findings of previous studies on autogenous welding of titanium with stainless and indicate a pronounced formation of Fe_2Ti IMC [1, 4].

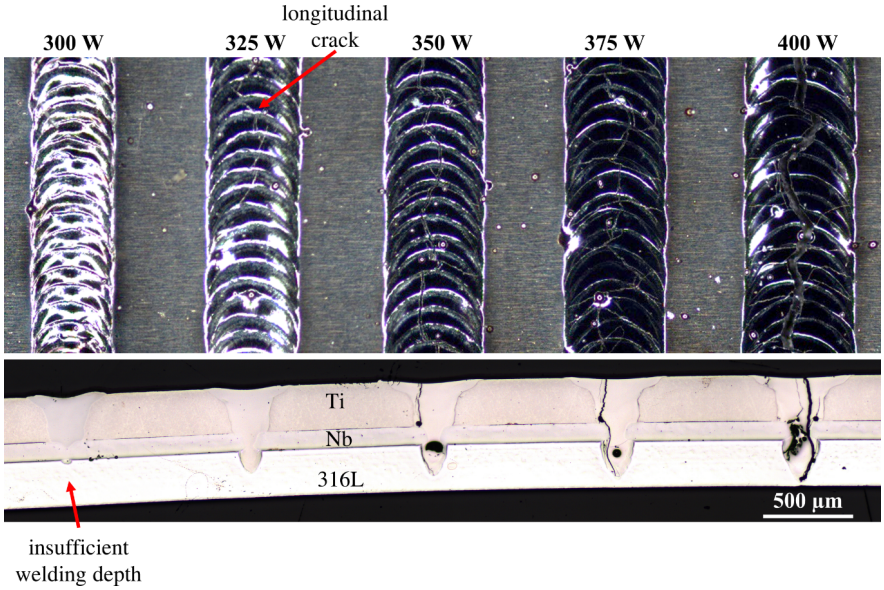

Fig. 2. Weld seam surfaces and cross-sections of a sample welded with 7 ms pulse duration and pulse peak powers of 300 to 400 W.

Furthermore, it can be observed that the hardness distribution in the weld metal of the presented sample is rather inhomogeneous, as the exceptionally high hardness values are particularly concentrated in the lower area of the weld metal. This can be attributed to the comparatively short pulse duration of 3 ms leading to faster solidification of the weld metal and insufficient time for intermixing processes to take effect. Consequently, a higher proportion of stainless steel, which ultimately leads to a pronounced segregation of critical IMC, can be anticipated in the area of the weld seam root.

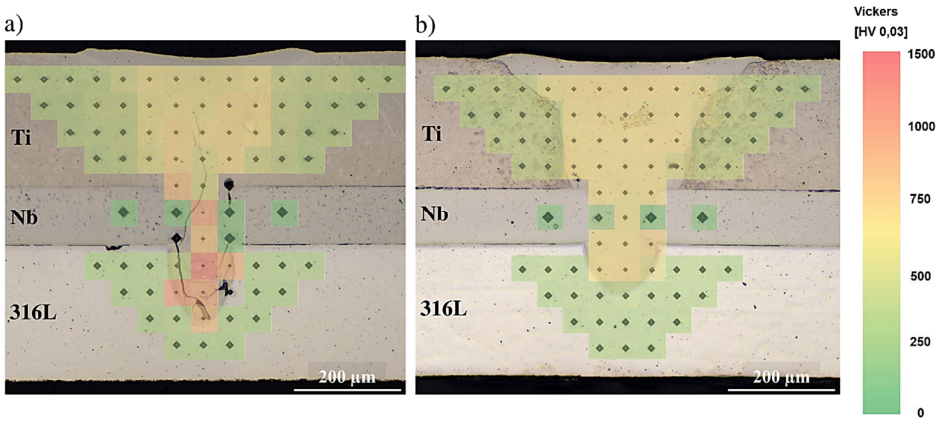

Fig. 3. Hardness mappings of specimens welded with: (a) 3 ms pulse duration and 500 W pulse peak power (b) 10 ms pulse duration and 325 W pulse peak power.

Despite the high affinity for cracking of the investigated material combination, it was possible to identify a parameter set which not only generated defect-free weld seams in a reproducible manner but also achieved superior mechanical properties. As illustrated by the hardness mapping in Fig. 3b, the corresponding sample exhibits significantly lower hardness values in the weld metal averaging at approximately 520 HV. This can eventually be attributed to the deviating process parameters and their impact on the chemical composition. The penetration depth in the substrate sheet is relatively low compared to the sample in Fig. 3a, which results in a reduced proportion of molten and intermixed 316L. According to the findings of previous studies, limiting the intermixing of stainless steel in dissimilar weldments with titanium is expedient in order to obtain improved weldability and mechanical properties [1, 4]. Furthermore, the comparatively long pulse duration of 10 ms applied in this parameter set enables a prolonged timeframe for intermixing processes to take effect. Consequently, the low proportion of molten 316L is distributed more homogenously within the weld metal, which eventually leads to an uncritical chemical composition. This finding is also reflected by the more uniform distribution of hardness in the weld metal.

The tensile specimens for this parameter set, which measure a width of 2.5 mm, can withstand tensile forces of up to 140 N. By increasing the joint area using four adjacent weld seams, the bond strength was increased, reaching a tensile force of up to 320 N, which corresponds to approx. 78 % of the strength of the 316L base material while maintaining the aforementioned absence of cracking. In conjunction with the biocompatibility of the filler material used, the results of this work provide the foundation for this material combination to be used within future medical technology applications.

4. Conclusions

The investigation at hand demonstrates that dissimilar joints between cp-Ti and 316L can be welded crack-free with good mechanical properties by using Nb as filler material in lap joint configuration. However, the weldability is significantly influenced by the applied process parameters, which consequently require a systematic optimization in order to produce non-critical chemical compositions. The experimental results reveal that a limitation of the intermixed proportion of 316L as well as a homogeneous material distribution in the weld metal should be aimed for.

Acknowledgements

The shown results were achieved in the project “MeTiWeld” (reference IGF 21.601 N), which is supervised by the Forschungsvereinigung Schweißen und verwandte Verfahren e.V. of the German Welding Society and funded by the German Federation of Industrial Research Associations (AiF) by means of the Federal Ministry for Economic Affairs and Climate Action (BMWK) on the basis of a decision by the German Bundestag.

References

[1]. M. M. Quazi, M. Ishak, M. A. Fazal, A. Arslan, S. Rubaiee, A. Qaban, M. H. Aiman, T. Sultan, M. M. Ali, S. M. Manladan, Current research and development status of dissimilar materials laser welding of titanium and its alloys, *Optics & Laser Technology*, Vol. 126, 2020, 106090.

[2]. M. Wiegand, L. Marks, N. Sommer, S. Böhm, Dissimilar micro beam welding of titanium to Nitinol and stainless steel using biocompatible filler materials for medical applications, *Welding in the World*, Vol. 67, Issue 1, 2023, pp. 77-88.

[3]. G. Cacciamani, J. de Keyzer, R. Ferro, U. E. Klotz, J. Lacaze, P. Wollants, Critical evaluation of the Fe-Ni, Fe-Ti and Fe-Ni-Ti alloy systems, *Intermetallics*, Vol. 14, Issues 10-11, 2006, pp. 1312-1325.

[4]. S. Chen, M. Zhang, J. Huang, C. Cui, H. Zhang, X. Zhao, Microstructures and mechanical property of laser butt welding of titanium alloy to stainless steel, *Materials & Design*, Vol. 53, 2014, pp. 504-511.

[5]. G. Satoh, Y. L. Yao, C. Qiu, Strength and microstructure of laser fusion-welded Ti-SS dissimilar material pair, *The International Journal of Advanced Manufacturing Technology*, Vol. 66, Issues 1-4, 2013, pp. 469-479.

[6]. B. Shanmugarajan, G. Padmanabham, Fusion welding studies using laser on Ti-SS dissimilar combination, *Optics and Lasers in Engineering*, Vol. 50, Issue 11, 2012, pp. 1621-1627.

[7]. Y. Zhang, D. Q. Sun, X. Y. Gu, Y. J. Liu, Nd/YAG pulsed laser welding of TC4 titanium alloy to 301L stainless steel via pure copper interlayer, *The International Journal of Advanced Manufacturing Technology*, Vol. 90, Issues 1-4, 2017, pp. 953-961.

[8]. T. Wang, B. Zhang, J. Feng, Influences of different filler metals on electron beam welding of titanium alloy to stainless steel, *Transactions of Nonferrous Metals Society of China*, Vol. 24, Issue 1, 2014, pp. 108-114.

[9]. A. Mannucci, I. Tomashchuk, A. Mathieu, R. Bolot, E. Cicala, S. Lafaye, C. Roudeix, Use of pure vanadium and niobium/copper inserts for laser welding of titanium to stainless steel, *Journal of Advanced Joining Processes*, Vol. 1, 2020, 100022.

[10]. Y. Zhang, J. Zhou, D. Sun, H. Li, Two pass laser welding of TC4 Titanium alloy to 301L stainless steel via pure V interlayer, *Journal of Materials Research and Technology*, Vol. 9, Issue 2, 2020, pp. 1400-1404.

[11]. Y. Fang, X. Jiang, T. Song, D. Mo, Z. Luo, Pulsed laser welding of Ti-6Al-4V titanium alloy to AISI 316L stainless steel using Cu/Nb bilayer, *Materials Letters*, Vol. 244, 2019, pp. 163-166.

[12]. J. Li, Y. Liu, Y. Gao, P. Jin, Q. Sun, J. Feng, Benefits of interfacial regulation with interlayers in laser welding Ti6Al4V/316L steel, *Optics & Laser Technology*, Vol. 125, 2020, 106007.

[13]. Y. Zhang, J. Zhou, D. Sun, H. Li, Three-pass laser welding of Ti alloy-stainless steel using Nb and Ni interlayers, *Journal of Materials Research and Technology*, Vol. 9, Issue 2, 2020, pp. 1780-1784.

[14]. Y. Zhang, D. Q. Sun, X. Y. Gu, Z. Z. Duan, H. M. Li, Nd:YAG pulsed laser welding of TC4 Ti alloy to 301L stainless steel using Ta/V/Fe composite interlayer, *Materials Letters*, Vol. 212, 2018, pp. 54-57.

(1328)

Smart Composite Material Microphone Using a Grating Fiber Optic Sensor

M. I. Rusu [1], D. Savastru [1], R. Savastru [1], M. Tautan [1] and I. I. Lancranjan [1]
[1] National Institute for R&D of Optoelectronics - INOE 2000,
409 Atomistilor St., Magurele, Ilfov, RO-077125, Romania
Tel.: + 40 214575757, fax: + 40 214574522
E-mail: J_J_F_L@yahoo.com

Summary: The main scope of the paper consists of presenting the photonic quantum computation and simulation results obtained in optimization of a smart polymer composite material application as microphone sensing element. The composite material became of a smart type by the grating optic fiber sensor which is embedded into its polymer matrix. The main investigated grating optic fiber sensor, namely the Long Period Grating Fiber Sensor (LPGFS) with Long Period diffraction Grating (LPG) was manufactured in standard communication Single Mode (SM) optic fiber. LPG's were induced into (SM) optic fiber by various methods which are briefly commented. In the simulation process there were investigated the functional limits of a smart polymer composite material applications microphone imposed by delamination of the composite.

Keywords: Long period grating fiber sensor, Fiber Bragg grating, Smart polymer composite material applications microphone, Delamination effects.

1. Introduction

The main scope of the paper consists of presenting the results obtained using photonic quantum computation and simulations performed in order to optimize of a smart polymer composite material as microphone sensing element.

Smart composite materials can be used as microphone sensing element. A composite material is transformed into a smart one by embedding an optical fiber grating sensor into its polymer matrix. System simulations were performed to optimize a smart polymer composite material as microphone sensing element. Operational limits imposed by delamination or the separation of layers were identified as a common failure mode in laminated composite materials under applied vibration effects.

2. Long Period Grating Fiber Sensor

A Long Period Grating Fiber Sensor is used to measure the vibrations effect on composites such as initiation and propagation of the delamination process, basing on determination of the spectral shifts of the absorption spectra. Long Period Grating Fiber Sensor is composed of a single mode optical fiber into which, along a length of 50 mm, a Bragg diffraction grating is created. The Fig. 1 presents the transmission spectrum characterizing the investigated Long Period Grating Fiber Sensor with 775 μm grating period. Absorption bands with peak wavelengths situated at grating Bragg resonance wave. In the transmission spectrum of the grating sensor there could be observed absorption lines corresponding resonance Bragg wavelength.

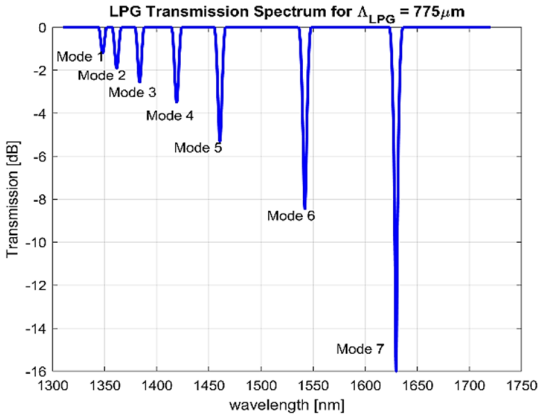

Fig. 1. The transmission spectrum of the investigated LPG.

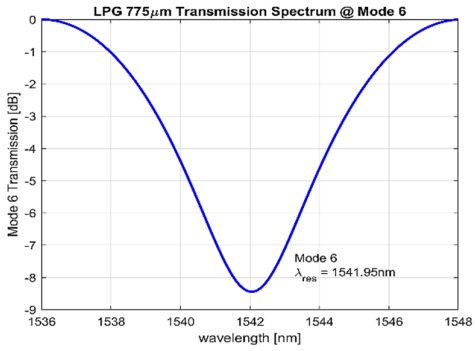

Fig. 2. The transmission spectrum of Mode 6 of the investigated LPG.

Among the peaks of the Bragg resonances the was chosen one denoted as Mode 6. Mode 6 was chosen because its resonance wavelength is placed near the

middle of the fiber interrogator input spectral domain. Its peak Bragg resonance wavelength is situated at 1541.95 nm.

The microphone sensing element consist in three layers with different relative orientation of fiber 3-5 mm length and 2-3 mm width or a 3-5 mm diameter plate with the grating optic fiber embedded into a central position of the plate. The polymer matrix of the investigated composite material was composed of PVC or PDMS polymer.

There were considered that applied vibrations induce into a smart polymer composite material two main types of applied mechanical loads: bending and twisting when an external bending mechanical load is applied. In Figs. 3 and 5 there are presented applied bending (Fig. 3) and twisting (Fig. 5) mechanical loads.

In Figs. 4 and 6 there are presented Mode 6 resonance wavelength spectral shift variation vs bending (Fig. 4) and twisting (Fig. 6) induced strain.

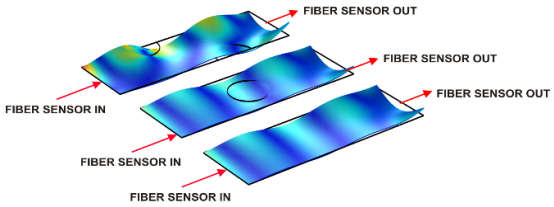

Fig. 3. Representation of applied bending mechanical load.

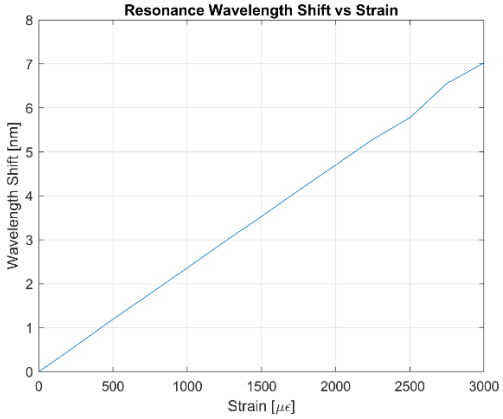

Fig. 4. The variation of Mode 6 resonance wavelength spectral shift vs bending induced strain.

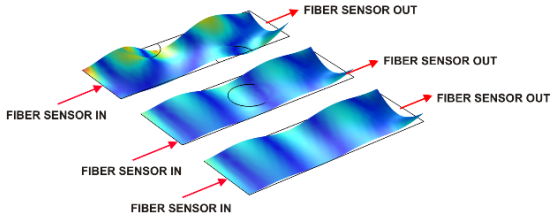

Fig. 5. Representation of applied twisting mechanical load.

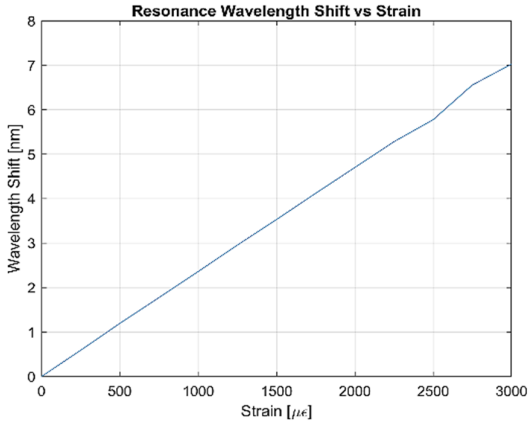

Fig. 6. The variation of Mode 6 resonance wavelength spectral shift vs twisting induced strain.

3. Conclusions

An analysis of possible application of smart composite materials based on an optical fiber grating sensor embedded in the polymer matrix of the smart composite material used as microphone operated in vibration fields was developed.

Acknowledgements

This work was supported by the Core Program within the National Research Development and Innovation Plan 2022-2027, carried out with the support of MCID, project no. PN 23 05, the Romanian Ministry of Research, Innovation and Digitalization, through Program 1- Development of the national research-development system, Subprogram 1.2 – Institutional performance – Projects to finance the excellent RDI, Contract no. 18PFE/30.12.2021 and a grant of the Ministry of Research, Innovation and digitalization, CNSC-UEFISCDI, project number PN-III-P4-PCE-2021-0585, within PNCDI III.

References

[1]. A. Mironov, A. Kovalovs, A. Chate, A. Safonovs, Static loads influence on modal properties of the composite cylindrical shells with integrated sensor network, *Sensors*, Vol. 23, Issue 6, 2023, 3327.
[2]. Y. Zhang, Y. Feng, X. Rui, L. Xu, L. Qi, Z. Yang, C. Hu, P. Liu, H. Zhang, Acoustic source localization in CFRP composite plate based on wave velocity-direction function fitting, *Sensors*, Vol. 23, Issue 6, 2023, 3052.
[3]. B. Degamber, G. F. Fernando, Process monitoring of fiber-reinforced polymer composites, *MRS Bulletin*, Vol. 27, Issue 5, 2002, pp. 370-380.

(1541)

Adjustable Refractive Index Materials for Precision Optical Filters Fabrication

V. Torres-Costa [1], E. Pérez-Picazo [1], I. Sardaña-Ortega [1] and R. J. Martín-Palma [1]
[1] Universidad Autónoma de Madrid, Applied Physics Department, Faculty of Sciences,
Francisco Tomás y Valiente 7, 28049 Cantoblanco, Madrid, Spain
E-mail: vicente.torres@uam.es

Summary: In this work it is shown how porous materials may be fabricated with a predetermined effective refractive index within a wide range of values. In particular electrochemical etching of silicon wafers results in porous silicon films with a refractive index that can range from 1.4 to 2.1, while grazing angle electron beam evaporation can produce porous germanium films with indexes between 1.4 to 4. Moreover, both techniques allow the fabrication of layered structures where the refractive index changes following a predesigned profile, resulting in a monolithic structure with a tailored interference effect. These porous materials and fabrication processes are very promising for the fabrication of precise monolithic optical filters for application in the VIS, NIR and SWIR wavelength ranges.

Keywords: Effective refractive index, Porous silicon, Grazing angle deposition, Optical filters, Interference, Multilayer.

1. Introduction

Porous semiconductors such as Si and Ge are very attractive materials for the fabrication of optical filters due to the possibility of adjusting their effective refractive index within a wide range of values. Moreover, by using the appropriate growth technique, a predefined in-depth profile of refractive index can be achieved, resulting in a monolithic multilayer structure showing a tailored interference effect.

Porous silicon layered structures can be easily fabricated by electrochemical etch of Si wafers suitable for the near infrared and visible wavelength ranges. This process, however, may present some drawbacks, such as mechanical stress in high porosity layers or in-depth gradients due to electrolyte depletion inside low porosity structures.[1] Grazing angle deposition (GRAD), in which a material is evaporated onto a substrate at a very low (grazing) incidence angle overcomes those drawbacks. Because the structure is grown bottom-up in a vacuum, no electrolyte is present.[2], while multilayer structures can be obtained by varying the substrate's tilt angle during the deposition.

2. Experimental

Porous Si was produced electrochemically etching (100) p-type silicon wafers (0.01-0.02 Ohm·cm) applying between 10 and 150 mA/cm^2 in an electrolyte composed of hydrofluoric acid (48 % wt.) and ethanol in 1:1 and 2:1 ratios. To obtain layered structures the applied current was alternatively switched from 10 to 150 mA/cm^2 during the etching process.[3]

Porous Ge was grown onto Si by electron beam evaporation in the grazing angle configuration in which the substrate was tilted between 0º (flat deposition) and 85º respect to the incoming particle flux. Substrates rotated at 10 rpm during deposition to ensure isotropy.

Optical properties of the obtained films were studied by UV-VIS and FTIR spectroscopy, and the effective refractive index was derived from those measurements using a specifically developed software package.[4]

3. Results and Discussion

Fig. 1 shows the effective refractive index of porous silicon layers etched with current densities from 10 to 150 mA/cm^2 in an HF (48 %wt) and ethanol 2:1 and 1:1 ratio electrolytes. As it can be expected, a higher etching current induces a more aggressive etching, resulting in higher porosity films with a lower optical density. In this case, the effective refractive index can be adjusted between 1.384 and 2.125 using an 1:1 electrolyte. The influence of the etching current can be reduced using an electrolyte with a higher HF content: as it can be observed, for the same applied current interval, the resulting refractive index ranges only from 2.08 to 2.19 when using the 2:1 electrolyte.

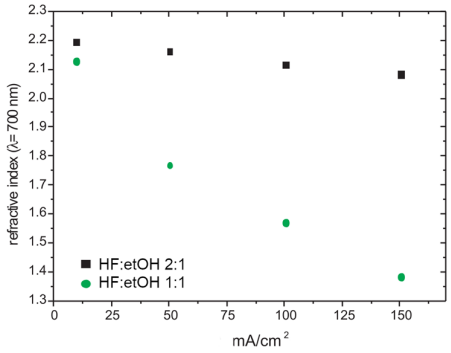

Fig. 1. Refractive index at 700 nm of porous Si films etched in HF:ethanol 2:1 and 1:1 electrolytes.

This effect is attributed to the higher viscosity of the 2:1 electrolyte, which hinders its ability to efficiently infiltrate the porous network during etching. Hence, an electrolyte with a 1:1 electrolyte provides a wider range of refractive index values than the 2:1 formula ($\Delta n = 0.74$ instead of $\Delta n = 0.11$), while on the other hand, the 2:1 electrolyte provides a much higher control for fine tuning the resulting index in a narrower interval.

With the electrochemical etching process, layered structures can be achieved by varying the applied current during etching, which results in a stack of layers with well-defined boundaries, as shown in Fig. 2. This process also allows the fabrication of rugated profiles if the current is varied gradually.

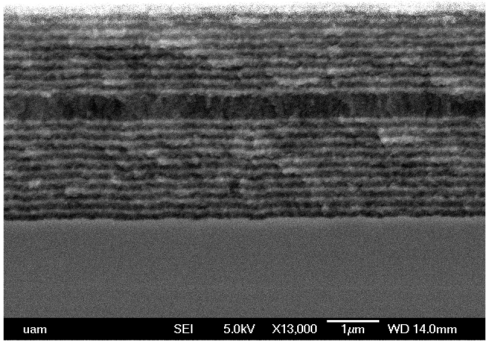

Fig. 2. Cross-section SEM image of a porous Si multilayer.

FTIR spectroscopy was used to determine the refractive index in the short-wave infrared (SWIR) range of porous Ge films grown by GRAD at different angles. Results summarized in Fig. 3 show that the effective refractive index decreases with tilt angle, almost neglectable at tilt angles below 30º, moderately up to 60º, and above 70º even a small variation in deposition angle results in a large change in the measured refractive index [5]. Optical characterization revealed that an effective refractive index as low as 1.4 can be achieved by GRAD while the porous films remain mechanically stable. On the other hand, low porosity values with a high refractive index can also be achieved by GRAD, as there is no electrolyte that needs to diffuse through the porous structure.

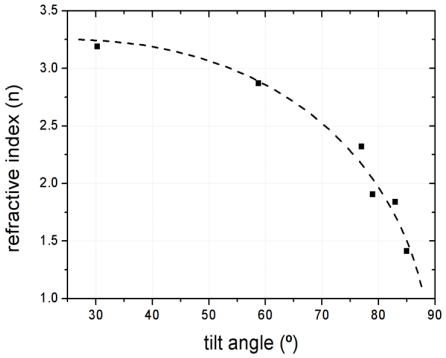

Fig. 3. Refractive index in SWIR of porous Ge films grown by GRAD at increasing tilt angles.

Such a wide range of refractive index offers a very high flexibility for the design of precision optical filters. As an example, a GRAD porous Ge filter tuned to detect the presence of ethanol was designed adjusting the filter's bandpass to match the 3000 cm^{-1} absorption peak of ethanol. The filter structure is BABAABABAAB/Si, where B is a 320 nm low index layer (n = 1.4, 85º GRAD) and A is a 240 nm high index layer (n = 4.03, 0º GRAD). The grown structure is shown in Fig. 4, and its transmittance spectrum of the filter is shown in Fig. 5.

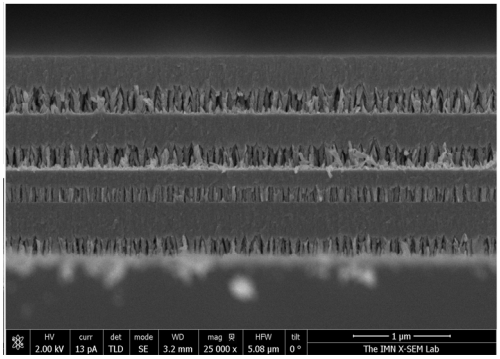

Fig. 4. Cross-section SEM image of a porous Gemultilayer.

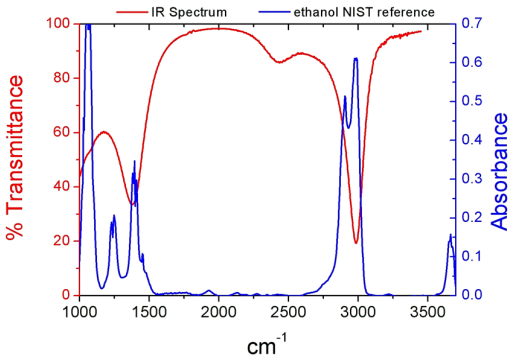

Fig. 5. Transmittance spectrum of a porous Ge SWIR filter tuned to detect ethanol.

4. Conclusions

Porous Si and Ge films can be fabricated with a wide range of predefined effective refractive indexes. By changing the current density during etching or the substrate's tilt angle during GRAD growth, porous multilayer structures can also be achieved with a precisely tailored refractive index profile that result in optical interference devices for applications in the VIS, NIR and SWIR ranges.

Acknowledgements

This research was sponsored by the NATO Science for Peace and Security Programme under grant G5734. and the Community of Madrid within the framework of the agreement with Universidad Autonoma de

Madrid in item "Excellence of University Professorate"

References

[1]. M. G. Berger, C. Dieker, M. Thönissen, L. Vescan, H. Lüth, H. Münder, Porosity superlattices: A new class of Si heterostructures, *Journal of Physics D*, Vol. 27, Issue 6, 1994, 1333.

[2]. L. Abelmann, C. Lodder, Oblique evaporation and surface diffusion, *Thin Solid Films*, Vol. 305, 1997, pp. 1-21.

[3]. V. Torres-Costa, R. J. Martín-Palma, J. M. Martínez-Duart, Optical characterization of porous silicon films and multilayer filters, *Applied Physics A*, Vol. 79, 2004, pp. 1919-1923,

[4]. V. Torres-Costa, R. J. Martín-Palma, J. M. Martínez-Duart, Optical constants of porous silicon films and multilayers determined by genetic algorithms, *Journal of Applied Physics*, 96, 2004, pp. 4197-4203.

[5]. A. Barranco, A. Borras, A. R. Gonzalez-Elipe, A. Palmero, Perspectives on oblique angle deposition of thin films: From fundamentals to devices, *Progress in Materials Science*, Vol. 76, 2016, pp. 59-153.

(2009)

Structure and Luminescent Properties of Niobium Modified $ZnO-B_2O_3:Eu^{3+}$ Glass

M. Milanova [1], A. Yordanova [1], L. Aleksandrov [1], R. Iordanova [1], N. Nedyalkov [2] and P. Petrova [3]

[1] Institute of General and Inorganic Chemistry, Bulgarian Academy of Sciences, G. Bonchev, str., bld. 11, 1113 Sofia, Bulgaria

[2] Institute of Electronics, Bulgarian Academy of Sciences, Tzarigradsko shousse 72, Sofia 1784, Bulgaria

[3] Institute of Optical Materials and Technologies "Acad. Jordan Malinowski", blvd. Akad. G. Bonchev 109, Sofia 1113, Bulgaria

Tel.: +3592979 3588, fax:+3592870 50 24

E-mail: margi@svr.igic.bas.bg

Summary: In this study we have investigated the effect of the addition of Nb_2O_5 (up to 5 mol%) on the structure and luminescent properties of $ZnO-B_2O_3$ glass doped with 0.5 mol % Eu_2O_3 by using of infrared (IR), and photoluminescence (PL) spectroscopy. Physical properties as molar volume, oxygen packing density and glass transition temperature were determined using the results of differential scanning calorimetry (DSC) and Archimedes principle for density. IR spectra revealed that niobium ions incorporate into the base zinc borate glass as NbO_6 octahedra, interconnected by corners and edges in chains and in 3D clusters. The higher Eu^{3+} luminescence emission observed in zinc borate glasses containing 1÷5 mol% Nb_2O_5 compared to the Nb_2O_5-free zinc borate glass evidences that Nb_2O_5 is suitable component for modification of host glass structure and improving the emission intensity. The overall results show that these Eu^{3+} doped glasses could be potential candidates for red emitting phosphors.

Keywords: Glasses, Structure, Europium, IR spectra, Density.

1. Introduction

Niobium containing glasses are suitable matrices for doping with active Eu^{3+} ions since Nb^{5+} ions can modify the environment around the rare earth ions due to their higher polarizability [1]. Also Nb_2O_5 has important optical characteristics as low phonon energy, high refractive index (n = 2.4), NIR and visible transparency, that are directly related to the luminescence properties [2].

This work reports for the preparation, structure and photoluminescence properties of glasses $50ZnO:(50-x)B_2O_3:0.5Eu_2O_3:xNb_2O_5$, (x = 0, 1, 3 and 5 mol %). The aim is to investigate the effect of the addition of Nb_2O_5 to the binary $50ZnO:50B_2O_3$ glass, on the glass structure and photoluminescence properties of the active Eu^{3+} ions doped in this host glass matrix.

2. Experimental

Glasses with the composition in mol% of $50ZnO:(50-x)B_2O_3:xNb_2O_5:0.5Eu_2O_3$, (x = 0, 1, 3 and 5 mol %) were prepared by melt quenching method using reagent grade ZnO, WO_3, H_3BO_3 and Eu_2O_3 as starting compounds and studied by X-ray diffraction (XRD), differential scanning calorimetry (DSC), infrared (IR) spectroscopy, photoluminescence (PL) spectroscopy and density measurements.

3. Results and Discussion

Yellowish, transparent, bulk glasses (insets, Fig. 1) were obtained and their x-ray diffraction patterns are shown on Fig. 1. The absence of sharp peaks in the x-ray diffraction spectra showed that prepared samples are glassy in nature.

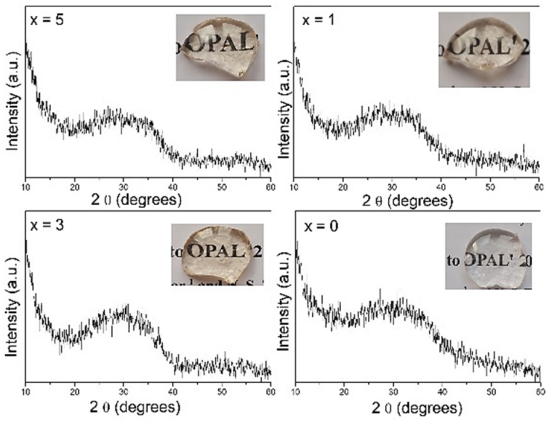

Fig. 1. XRD patterns and photographs (insets) of glasses $50ZnO:(50-x)B_2O_3:xNb_2O_5:0.5Eu_2O_3$, (x = 0, 1, 3 and 5 mol %)

A deconvolution process was performed to determine the vibrational bands associated with the various structural units constituting the glass network

(Fig. 3). In this way, presence of several structural groups have been established as: highly distorted NbO_6; Nb-O-Eu bonding; $[BØ_4]^-$ tetrahedral units involved in various superstructural groups; pyroborate dimers, $[B_2O_5]^{4-}$; metaborate units $BØ_2O^-$ (Ø = bridging oxygen, O^- = nonbridging oxygen); B-O-B bridges, connecting superstructural groups through three-fold coordinated boron centers. The detailed bands assignment is listed in Table 1. IR spectra revealed that niobium ions incorporate into the base zinc borate glass matrix as highly distorted NbO_6 octahedra interconnected by corners and edges in chains and in 3D clusters (band 13 and band 15 in glasses
x = 1, 3, 5). At the lowest Nb_2O_5 content (x = 1), niobium oxygen polyhedral enter into the base zinc borate glass network by breaking the B-O-B bonds in the superstructural borate units (disappearance of the bands 4-6, and decreased intensity of the band 8 in the spectra of glasses x = 1, 3) and favours formation of metaborate $BØ_2O^-$ groups and new mixed Nb-O-B bonds (decrease in frequency of the B-O^- stretching in $BØ_2O^-$ units (1387-1370 cm^{-1} (band 10) and 1472-1459 (band 11) for glass x = 0 and for glass x = 1 respectively). With increasing Nb_2O_5 content (x = 3 and 5), niobium ions start to link with Eu^{3+} ions and formation of Nb-O-Eu took place (band 19 at 629 cm^{-1}) evidencing that in these glass compositions NbO_6 groups are closely associated to the Eu^{3+} ions [3].Thus the inclusion of Nb_2O_5 into the base zinc borate glass leads to the formation of more disordered and reticulated glass networks.

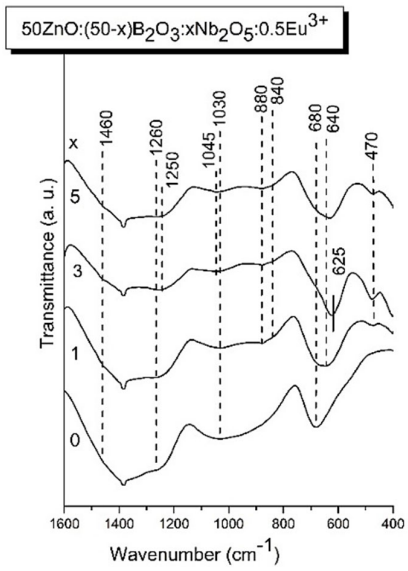

Fig. 2. Infrared spectra of glasses $50ZnO:(50-x)B_2O_3$: $xNb_2O_5:0.5Eu_2O_3$, (x = 0, 1, 3 and 5 mol %).

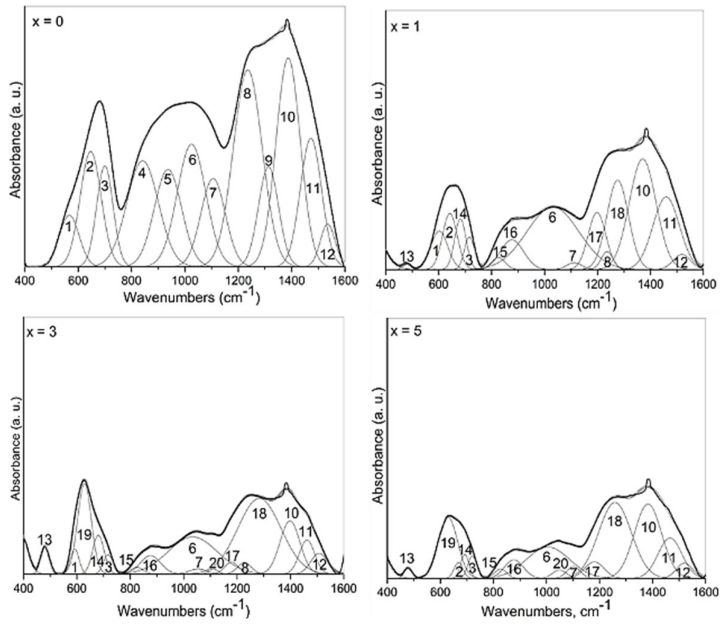

Fig. 3. Deconvolution into Gaussian component bands of the infrared spectra of glasses $50ZnO:(50-x)B_2O_3$: $xNb_2O_5:0.5Eu_2O_3$, (x = 0, 1, 3 and 5 mol %). Black solid lines represent the experimental spectra and circle symbols (○) the simulated spectra.

The spectral observations for the effect of Nb_2O_5 on the structure of the Eu^{3+}-doped zinc borate base glass are confirmed by the physical parameters: density (ρ), molar volume (V_m), oxygen molar volume (V_o) and oxygen packing density (OPD) of x = 0 and x = 0.5 glasses established, which are listed in Table 2. As it is seen the Nb_2O_5 containing glasses are characterized with higher density and OPD values, also evidencing that the addition of Nb_2O_5 into the zinc borate glass leads to the formation of highly cross-linked and connected networks [4]. In addition, the lowest value of OPD of the glass having the highest Nb_2O_5 content (x = 5) as compared with the OPD values of other Nb_2O_5-containing glasses indicates

decreasing cross-link efficiency of niobium ions as NbO_6 start to link each other with Nb_2O_5 loading (increased number of Nb-O-Nb bonds and decreased number of Nb-O-B and Nb-O- Eu linkages).

Table 1. Infrared bands (in cm^{-1}) and their assignments for the studied glasses.

Band center, cm^{-1}/ Band number	Assignment	Ref.
480/13	(NbO_6) edge shared/	4
566-602/1	In-plane band of BO_3 units	5
646-668/2; 700-720/3	Out-of-plane band of BO_3 units	4, 5
628/19	ν (Nb-O-Eu)	3
680-692/14	ν_3 (NbO_6) 3D corner shared	4
825-827/15	(NbO_6) corner shared in chain, ν (Nb-O-Nb)	4
876/16	(NbO_6) ν_1 (Nb-O short bonds)	4
841/4, 936/5; 1006-1034/6; 1049-1054/20	ν_{as} $[B\O_4]^-$ in various superstructural groups	4
1236/8	ν_{as}(B-O-B) bridges connect BO_3 units	4
1105-1012/7	(B-O-B) stretch in pyroborate units, $[B_2O_5]^{4-}$	6
1313/9	B-O^- stretch in pyroborate units, $[B_2O_5]^{4-}$	6
1370-1398/10	B-O^- stretch in metaborate units, $B\O_2O^-$	4, 6
1459-1472/11	B-O^- stretch in metaborate units, $B\O_2O^-$	4, 6

Table 2. Various physical parameters of glasses 50ZnO: (50-x)B_2O_3: xNb_2O_5:0.5Eu_2O_3, (x = 0, 1, 3 and 5 mol %): density, ρ (g/cm^3); molar volume (cm^3/mol); oxygen molar volume Vo (cm^3/mol); oxygen packing density, OPD (g atom/l).

Sample ID	ρ ±0.001	V_m	V_o	(OPD)
x = 0	3.413	22.634	11.261	88.804
x = 1	3.567	22.208	10.940	91.408
x = 3	3.663	22.697	10.965	91.201
x = 5	3.665	23.755	11.258	88.823

The emission spectra of Eu^{3+} doped 50ZnO: (50-x)B_2O_3: xNb_2O_5:0.5Eu_2O_3, x = 0, 1, 3 and 5 mol% glasses upon excitation into the most intensive $^7F_0 \rightarrow {}^5L_6$ transition of Eu^{3+} at 395 nm are shown in Fig. 4.

All spectra consist of emission peaks attributed to $^5D_0 \rightarrow {}^7F_J$ transitions of the Eu^{3+} ion [7]. By comparing the emission spectra, it can be observed that the peak intensities increase with increasing Nb_2O_5 content and reach a maximum at about 3 mol %. Further increase in Nb_2O_5 concentration up to 5 mol% leads to decrease in luminescence intensity.

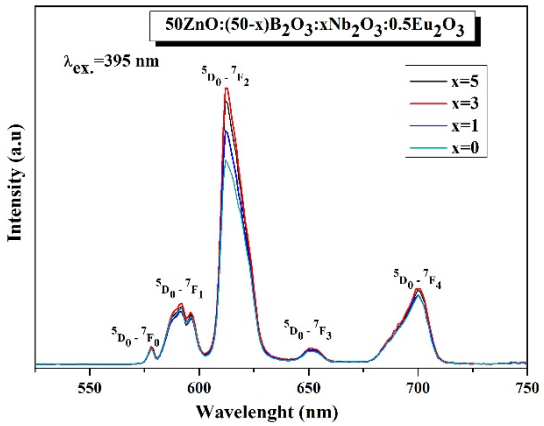

Fig. 4. Emission spectra of glasses 50ZnO:(50-x)B_2O_3: xNb_2O_5:0.5Eu_2O_3, (x = 0, 1, 3 and 5 mol %).

4. Conclusions

IR data revealed that the inclusion of Nb_2O_5 into the base zinc borate glass modify borate network resulting in decrease in the number of $B\O_4^-$ tetrahedral units involved in various superstructural groups and increasing amount of metaborate species $B\O_2O^-$ ($BO_4 \rightarrow BO_3$ transformation). The spectral analysis and the physical parameters established evidenced that the addition of Nb_2O_5 into the zinc borate glass leads to the formation of highly cross-linked and connected networks containing high number Nb-O-B an Nb-O-Eu bonds, that are very suitable for incorporating the active Eu^{3+} ions. The glasses obtained presented strong 613 nm red luminescence with excitation at 395 nm that was found to be the most intense for host glass composition having 3 mol% Nb_2O_5 due to the more homogeneous distribution of niobium ions in the host glass structure ensuring more even distribution of the active Eu^{3+} ions.

Acknowledgements

This work is supported by the Bulgarian National Science Fund at the Ministry of Education and Science under project КП-06-Н29/7.

References

[1]. G. Bilir, H. Ertap, L. Ma, B. Di Bartoli, Infrared to visible upconversion emission in Nb_2O_5 modified tellurite glasses triply doped with rare earth ions, *Materials Research Express*, Vol. 6, 2019, pp. 085203-0852214.

[2]. L. M. Marcondes, S. Maestri, B. Sousa, R. R. Gonçalves, F. C. Cassanjes, G. Y. Poirier, High niobium oxide content in germanate glasses: Thermal,

structural, and optical properties, *Journal of the American Ceramic Society*, Vol. 101, Issue 1, 2018, pp. 220-230.

[3]. M. Ptak, B. Polarek, A Watras, P. Godlewska, I. Szczygiel, J. Hanuza, Vibrational and optical properties of Eu^{3+}-doped Gd_3NbO_7 niobates – The mechanism of their structural phase transition, *Journal of Alloys and Compounds*, Vol. 810, 2019, 15189211.

[4]. R. Iordanova, M. Milanova, L. Aleksandrov, K. Shinozaki, T. Komatsu, Structural study of WO_3-La_2O_3-B_2O_3-Nb_2O_5 glasses, *Journal of Non-Crystlline Solids*, Vol. 543, 2020, 120132.

[5]. C. P. E. Varsamis, N. Makris, C. Valvi, E. I. Kamitsos, Short-range structure, the role of bismuth and property-structure correlations in bismuth borate glasses, *Physical Chemistry Chemical Physics*, Vol. 23, 2021, pp. 10006-10020.

[6]. R. Iordanova, M. Milanova, L. Aleksandrov, A. Khanna, Structural study of glasses in the system B_2O_3-Bi_2O_3-La_2O_3-WO_3, *Journal of Non-Crystlline Solids*, Vol. 481, 2018, pp. 254-259.

[7]. K. Binnemans, Interpretation of europium (III) spectra, *Coordination Chemistry Reviews*, Vol. 295, 2015, pp. 1-45.

(2289)

Adding Twist to Polymer Optical Fibers

J. Preizal [1,2], L. Bilro [1] and R. Oliveira [2]
[1] Instituto de Telecomunicações and University of Aveiro, Campus de Santiago, 3810-1938 Aveiro, Portugal
[2] Physics Department, University of Aveiro, Campus de Santiago, 3810-193 Aveiro, Portugal
Tel.: + 351 234377900, fax: + 351 234377901
E-mail: joaopreizal@.ua.pt

Summary: In this work, we report, for the first time, the fabrication of a permanent helically twisted polymethylmethacrylate microstructured polymer optical fiber through a fiber post-processing technique. The fabrication of this structure allowed the creation of spectral resonances at the low-loss region of the fiber. This novel structure will allow the creation of new smart flexible devices with fields of application in sensors and short-range communications. Although the repetition of several torsions under the same conditions demonstrated the possibility of replicating this technology, a torsion test was also performed, showing that it is sensitive to this type of deformation.

Keywords: microstructured polymer optical fiber, helically twisted optical fiber, torsion sensing.

1. Introduction

Helically twisted optical fibers (HTOF) have aroused interest in the scientific community thanks to their advantages over other existing optical components. Among all their qualities, the generation of orbital angular momentum [1], polarization control, the suppression of high-order laser modes, long-period grating couplers, and the ability to measure torsion with directionality [2], gives this component a great interest in research. Specifically talking about sensor applications, HTOFs can be used to measure parameters commonly measured by other optical fiber sensors (OFS), such as, deformation [2], temperature [3], and transverse load [4]. However, HTOFs distinguish from conventional OFS, namely in torsion applications, thanks to the way the structures are engraved. This behavior has already been reported in literature for different types of fibers, such as in photonic crystal fibers (PCFs), double-helix chiral structures, concentric rectangular core fiber, single-helix structure in an off-center core fiber, etc. [5].

Unfortunately, this type of structure has never been reported in polymer optical fibers (POFs), however, POFs can be a plus in certain situations. POF is an optical fiber cable normally made of polymethylmethacrylate (PMMA) and operates in the visible wavelength region. This fiber has several advantages when compared to commonly used glass optical fibers (GOFs), namely due to its biological compatibility, lower Young's modulus, higher elastic limits and higher flexibility making them very interesting for the application in soft stretchable skins. Furthermore, POFs have low processing temperatures (~110 ºC vs. 1200 ºC), and thus, conventional methods used for post-process GOFs, such as CO_2 [1], electric arc, and hydrogen-oxygen flame [4] are not needed, and simpler heating elements can be used.

In this work we will induce a permanent twist in a microstructured POF (mPOF) and we will check its spectral response after fabrication and in torsion sensor applications.

2. Fabrication and Characterization of HTOFs

The mPOF used in this work was a PMMA mPOF composed of 6 layers of air holes hexagonally arranged, and with one central hole missing. To induce a permanent twist to the mPOF, we build a dedicated setup composed by 3 linear and 1 rotational positioners as seen in Fig. 1.

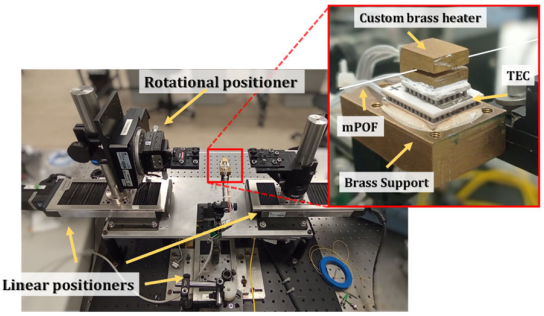

Fig. 1. Experimental setup used to induce a permanent twist in the mPOF. The inset shows the heating region.

The linear positioners found at the left and right sides of Fig. 1 were used to longitudinally move the fiber related to the heat source found in the middle. The velocity of these positioners was adjusted to 0.8 mm/s, being one of the positioners with a slightly higher velocity, allowing to keep the fiber tension during the process. As shown in Fig. 1, the heating zone is composed of a brass block which is used to support a dual-stage thermoelectric cooler (TEC), (TECD2,

Thorlabs®). Furthermore, on top of the TEC, a smaller brass block containing a 0.8 mm through hole, is used to keep ~10 mm of the mPOF in a homogeneous constant temperature, namely at the softening point of the PMMA mPOF ~ (110 ºC). This was done through a temperature controller (model 3040, Newport®). The mPOF was permanently deformed with a helical pitch of 650 µm, and with a total of 100 periods. To verify the repeatability of the process, we repeated the fabrication 3 times and record the final spectra.

To characterize the helically twisted mPOF to torsion, we secured the fiber structure between a fixed stage and a rotational stage, as shown in Fig. 2.

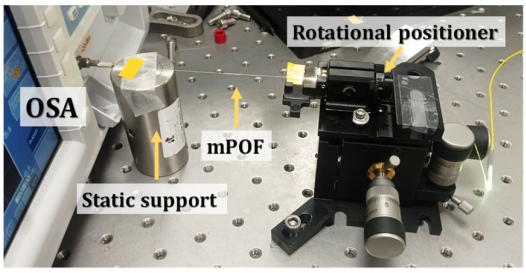

Fig. 2. Setup used to characterize the HTOF to torsion.

The distance in which the fiber was kept secured was 8.9 cm. The characterization was done in steps of 30º.

To record the optical spectra, light from a supercontinuum source was coupled into the mPOF by splicing it to a silica pigtail fiber. This splice was done manually through a dedicated setup, using a photosensitivity UV resin between the fiber terminals. On the other mPOF terminal, it was used an optical spectrum analyzer (OSA), to record the spectra for each rotation step.

3. Results and Discussion

The spectra taken for 3 different mPOFs after the permanent twist are shown in Fig. 3. In the same figure, it is also shown a microscope image of one of those HTOFs, showing a periodic pattern of ~116 µm. This pattern was associated to the rotation of the air holes sitting along the 6 sides of the hexagon that forms the POF microstructure, and thus, we estimate an experimental helical pitch (Λ) of ~ 696 µm, which is close but deviates slightly.

The spectra shown at Fig. 3, show a series of spectral dips found at the low loss region of PMMA. Each of these dips correspond to the coupling of the fundamental guided mode to one of the modes allowed to propagate in the air hole cladding region of the mPOF. The results were similar to the ones obtained in [1] for PCFs with similar fiber structure. The spectra obtained for 3 different HTOF have some similarities, however we stress out that these are very preliminary results, which will require refining of the process to maintain the repeatability. Despite this, each of the spectral resonances shown in Fig. 3, can be used to monitor external parameters as is the case used in this work for torsion sensing. As an example, we recorded the spectral dip that appears at 451 nm for each torsion step. The results, concerning the spectra shift and dip wavelength shift, are shown in Fig. 4(a) and (b), respectively.

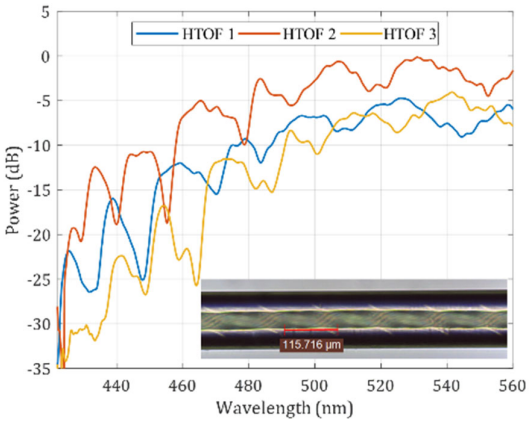

Fig. 3. Spectra obtained for 3 HTOF with Λ = 650 µm.

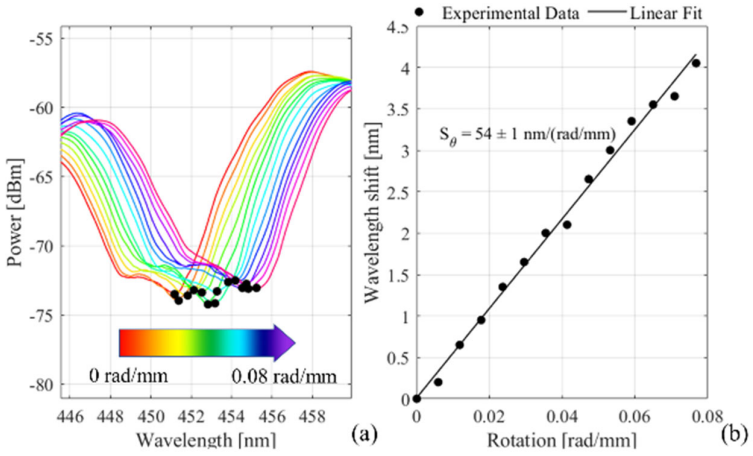

Fig. 4. (a) Resonance dip found at ~451 nm, obtained for different twist rates. (b) Corresponding wavelength shift.

As observed from Fig. 4(a), the spectra are shifted to the right with increasing twist rate as in accordance with theory. The corresponding dip wavelength shifts shown in Fig. 4(b), show a linear tendency and a linear fit to the data produced a sensitivity of 54±1 nm/(rad/mm). This value is similar to the one found in [2]. Despite the similar results, we stress out that the soft nature of the POF allows reaching a much higher twist rate, permitting their use in extended ranges when compared to their silica counterparts.

4. Conclusion

We successfully produced for the first time helically twisted polymer optical fibers. Furthermore, the low post-processing temperature used to shape the fiber make it much more attractive when compared to their silica counterparts. The preliminary results shown in this work will pave the way for a variety of fiber optic devices with high flexibility and elasticity.

Acknowledgements

This work was funded by Fundação para a Ciência e a Tecnologia (FCT) and FEDER funds through the COMPETE 2020 Programme and under the projects UIDB/50008/2020-UIDP/50008/2020 and by FCT/MEC under the project (PTDC/EEI-TEL/1511/2020). R. Oliveira acknowledges the FCT contract CEECIND2021.01066.

References

[1]. G. K. L. Wong, *et al.*, Excitation of orbital angular momentum resonances in helically twisted photonic crystal fiber, *Science*, Vol. 337, Issue 6093, Jul. 2012, pp. 446-449.

[2]. X. Xi, G. K. L. Wong, T. Weiss, P. S. J. Russell, Measuring mechanical strain and twist using helical photonic crystal fiber, *Opt. Lett.*, Vol. 38, Issue 24, 2013, pp. 5401-5404.

[3]. V. M. Churikov, V. I. Kopp, A. Z. Genack, Chiral diffraction gratings in twisted microstructured fibers, *Opt. Lett.*, Vol. 35, Issue 3, 2010, pp. 342-344.

[4]. C. Fu, *et al.*, Transverse-load, strain, temperature, and torsion sensors based on a helical photonic crystal fiber, *Opt. Lett.*, Vol. 44, Issue 8, Apr. 2019, pp. 1984-1987.

[5]. V. I. Kopp, A. Z. Genack, Adding twist, *Nat. Photonics*, Vol. 5, Issue 8, Aug. 2011, pp. 470-472.

(2494)

Synthesis, Optical Properties and Effect of Heat Treatment on ZnSe Quantum Dots in Borosilicate Glass

Nilanjana Shasmal [1], Andrea Simone Stucchi de Camargo [2] and Ana Candida Martins Rodrigues [1]

[1] Universidade Federal de São Carlos, Departamento de Engenharia de Materiais, LaMaV – Laboratório de Materiais Vítreos, Rod. Washington Luiz, km 235, 13565-905 – São Carlos – SP – Brazil

[2] São Carlos Institute of Physics, LEMAF – Laboratório de Espectroscopia de Materiais Funcionais, University of São Paulo, Avenida Trabalhador São-carlense, n 400 Parque Arnold Schimidt – CEP 13566-590, São Carlos – SP- Brazil

E-mail: nilanjana@ufscar.br

Summary: ZnSe quantum dots (QDs) have been generated in borosilicate glass matrix using one-step convention melt-quenching method via in-situ process. TEM studies confirm the generation of ZnSe QDs, with size below 10 nm, during the glass preparation steps. Absorption spectra of ZnSe-doped glasses show broad bands around 367, 498 and 760 nm indicating the presence of different sizes of ZnSe NPs. The variation in calculated E_{opt} values confirms the quantum confinement effect in nano-dimension. The glasses were heat treated for different times up to 60 h at 650 °C. With increasing heat treatment duration, enlargement of previously existing QDs and generation of new QDs were observed. Thus, PL emission from the glasses rapidly increased up to 20 h of heat treatment and then gradually decreased as a result of the rise in non-radiative loss between the enlarged particles.

Keywords: ZnSe quantum dots, ZnSe-doped glasses, Semiconductor doped glasses, Quantum confinement, Photoluminescence, Heat treatment.

1. Introduction

Semiconductor QDs having sizes comparable to the exciton Bohr radius show three-dimensional quantum confinement effect. They present tunable optical properties due to the discretization of the energy levels [1-2]. Particularly, the II-VI semiconductors (ZnS, ZnSe, CdS, CdSe, etc.) show maximum response to the size related properties within 1-100 nm size range [3]. Zinc selenide (ZnSe) is one of the first discovered and most important II-VI semiconductors materials with several applications in different electronic and optoelectronic areas like nonlinear optical devices, flat panel displays, light emitting diodes (LEDs), laser diodes (LDs) operating under the blue or ultra violet spectral excitation, logic gates, transistors, etc. [4].

In the present study we have successfully generated ZnSe QDs in borosilicate glasses by conventional melt-quenching method, measured absorption and emission properties, and studied how it varies with heat treatment.

2. Experimental Procedure

2.1. Preparation

The raw materials were quartz, SiO_2, boric acid, H_3BO_3, barium carbonate, $BaCO_3$, potassium carbonate, K_2CO_3, aluminum oxide, Al_2O_3, erbium oxide, Er_2O_3 and zinc selenide, ZnSe (all from AR, Sigma Aldrich). Glasses batches of 70 g, were prepared by melting the well-mixed powders of calculated composition in a high-purity alumina crucible at 1250 °C for 1.5 h with intermittent stirring with silica rod for 0.5 min in air in a raising hearth electric furnace. All the molten samples were cast into an iron plate in air and annealed at 600 °C for 6 h followed by slow cooling down to room temperature. The glass blocks were cut and polished for optical characterizations.

2.2. Characterization

Glass samples were analyzed by Differential Scanning Calorimetry (DSC-Netzsch 404) to find out the glass transition (Tg) temperature. Microstructures were analyzed by transmission electron microscopy (TEM), energy dispersive X-Ray analysis (EDX) and selected area electron diffraction (SAED) using MEV XL30 FEG instrument. For absorption spectra, Perkin-Elmer Lambda 950 UV-Vis-NIR spectrophotometer, was used. The PL excitation and emission spectra were collected in a HORIBA Jobin Yvon spectrofluorometer model Fluorolog FL3-221, equipped with CW xenon flash lamp and a photomultiplier detector (HORIBA PPD-850), and in a fiber optic spectrometer (AvaSpec-3648-USB2, Avantes) and diode laser source of wavelength 447 nm.

3. Results and Discussion

3.1. Differential Scanning Calorimetry

T_g of a representative glass sample was found at about 600 ºC. No crystallization peak was observed at the measured temperature range. As the dopant contents are very low in the glasses, no significant change was observed in Tg for the other glasses of the series.

3.2. TEM and SAED

TEM image of the representative BZ06 sample, showed tiny particles of average size less than 10 nm distributed over the glass matrix. However, very few particles were observed to be very small, below 2 nm. SAED showed multiple rings representing different crystal planes of the nanocrystals. The d-spacing values have been calculated and they match with the d-spacings of different crystal planes of ZnSe crystal (JCPDS no. 15-0105). These results confirm the presence of ZnSe QDs in the glass.

3.3. UV-Vis Absorption Spectra

The UV-V is absorption spectra shows multiple absorption bands peaking at 367, 498 and 760 nm due to the presence of ZnSe QDs of different sizes. The most prominent band being at 367 nm indicates that the majority of ZnSe NPs are of smaller sizes. The intensity of the absorption bands increases with increasing ZnSe content and the bands become more and more prominent with rising ZnSe concentration. The lowering of the band gap with increasing ZnSe content, confirms the quantum confinement effect in nano-dimension [5].

3.4. Emission Spectra

When they are excited at 367 and 498 nm, they exhibit bright red emission. The emission spectra show a broad band in the range of 600 to 800 nm centered around 696 nm. The PL intensity was found to increase with increasing ZnSe content, at both excitations. As both the number and size of ZnSe NPs increase with increasing ZnSe content, increase in the PL intensity is expected and usual [3-5].

4. Heat Treatment Results

4.1. XRD and TEM

X-ray diffraction analysis was conducted for all the as-prepared and heat-treated samples. None of the glass samples exhibit any sign of crystallization, even after being subjected to the longest heat treatment time. TEM images were taken for glasses heat treated at different times. Gradual enlargement of the QDs were observed as well as formation of new QDs. The size varies from <10 nm in as-prepared glasses to >100 nm at 60 h of heat treatment.

4.2. Absorption Spectra

The effect of this enlargement was observed in the UV-*Vis* absorption spectra. The broadness and intensities of all the bands rise slightly with increasing heat treatment duration because of the formation of new ZnSe QDs as well as the growth of already existing QDs.

4.3. Emission Spectra

The PL intensity shows an initial sharp increase up to 1 h of heat-treatment, followed by a smoother increase up to 20 h, and then a steady decrease. The initial sharp increase is attributed to the formation of new ZnSe NPs, as well as to the growth of the previously existing NPs over the heat treatment. In this glass, minute ZnSe QDs begin to form at elevated temperature during the heat treatment. These small QDs contribute to the overall PL emission of the glass, leading to the steep increase in PL intensity up to a certain heat treatment time (2 h in this case). After that, the rate of formation of ZnSe QDs slows down and the existing particles continue to grow, which leads to a slow increase in PL intensity. Eventually, it reaches a maximum level where the enhancement effect of the QDs emission is at its maximum. After that, crowding of the glass matrix with larger QDs results in decreased inter-particle distance and the overall emission intensity decreases due to increased non-radiative relaxation among the ZnSe QDs, leading to reduced radiative emission intensity.

5. Conclusions

ZnSe QDs (of size <10 nm) have been successfully generated in borosilicate glasses. They show characteristic broad absorption and (red) emission bands of ZnSe which are due to the overlap of emissions from QDs (electron-hole recombination) and from defect to traps, formed owing to Se and Zn vacancies. With heat treatment a significant enhancement in emission intensity was observed due to the generation and growth of ZnSe QDs up to a certain time, then it decreases due to radiative damping from enlarged particles.

Acknowledgements

Authors would like to acknowledge the funding of this work by Fundação de Amparo a Pesquisa do Estado de São Paulo – FAPESP, through the Cepid Project No. 2013/07793-6 (CeRTEV – Center for

Research, Technology and Education in Vitreous Materials). NS is particularly thankful to FAPESP for the postdoctoral fellowship (process No. 2018/04113-8).

References

[1]. A. P. Alivisatos, Perspectives on the physical chemistry of semiconductor nanocrystals, *J. Phys. Chem*., Vol. 100, 1996, pp. 13226-13239.

[2]. L. Manna, et. al., Controlled growth of tetrapod-branched inorganic nanocrystals, *Nature Mat*., Vol. 2, 2003, pp. 382-385.

[3]. C. Dey, et. al., Single-step in-situ synthesis and optical properties of ZnSe nanostructured dielectric nanocomposites, *J. Appl. Phys*., Vol. 115, 2014, 134309.

[4]. Q. Zhang, H. Li, Y. Ma, T. Zhai, ZnSe nanostructures: Synthesis, properties and applications, *Prog. Mater. Sci*., Vol. 83, 2016, pp. 472-535.

[5]. N. Shasmal, W. J. Faria, A. S. S. Camargo, A. C. M. Rodrigues, Enhancement in green and NIR emissions of Er^{3+} by energy transfer from ZnSe nanoparticles in borosilicate glass, *J. Alloys Compd*., Vol. 863, 2021, 15842.

(2551)

Sensitive Photothermal Gas Detection Using a Mode-locked Laser and Self-heterodyne Harmonic Amplification

K. Krzempek and Piotr Jaworski
Laser Spectroscopy Group, Faculty of Electronics, Photonics and Microsystems,
Wroclaw University of Science and Technology Wyb. Wyspianskiego 27, 50-370 Wroclaw, Poland
E-mail: karol.krzempek@pwr.edu.pl

Summary: A novel method for photothermal gas detection will be presented. Our approach utilizes a custom-built fiber-based mode-locked laser with a gas cell integrated into its cavity. The gas molecules are excited via an auxiliary *pump* laser in that cell. Therefore, the photothermal-induced gas refractive index modulation is directly translated into a shift in the mode-locked laser cavity path-length and, as a result, in its pulse repetition frequency. This approach encodes the spectroscopic signal into frequency deviations, providing significant advantages. We have exploited the special features of mode-locked lasers, such as the distinctive RF beat-note signal, to maximize the potential of our method. We were able to increase the sensor's sensitivity by a factor of 22 by simply demodulating the spectroscopic signal at higher harmonics of the fundamental beatnote. A 9.6 ppbv limit of detection for nitric oxide was achieved at 5.26 μm with an averaging time of 136 s.

Keywords: Laser spectroscopy, Laser gas detection, Photothermal effects, Photothermal gas detection, Mode-locked laser.

1. Introduction

Photothermal gas spectroscopy (PTS) is a powerful nondirected spectroscopic technique that, when combined with the proper sensor configuration, can outperform sensors relying on classical direct-absorption-based approaches. In principle, PTS is similar to photoacoustic spectroscopy (PAS). The gas sample is illuminated with a laser, called a pump, whose wavelength is chosen to match the absorption profile of the gas under test. The illuminated gas molecules absorb the photons, and the resulting energy is partially released through nonradiative processes, such as collision transfer to other gas molecules and the surroundings. This heats up the gas sample along the path length of the pump laser, generating a photothermal effect that produces a pressure wave and modulates the refractive index (RI) of the gas.

In contrast to PAS, the sensor in PTS is constructed to monitor the RI modulation. Due to the small amplitude of the induced changes, interferometric methods such as Mach-Zehnder (MZI) and Fabry-Perot (FPI) interferometers are commonly used to extract the spectroscopic signal from the photothermal effect. These interferometers are constructed around the area where the gas sample is excited [1].

Although providing excellent sensitivities, MZI and FPI-based sensors require acousto-optical modulators or piezoceramic transducers to operate properly for long periods of time [2]. Our research has resulted in the development of a novel spectroscopic technique known as self-heterodyne harmonic amplification (SHHA). This cutting-edge technique leverages the unique characteristics of a mode-locked fiber laser to amplify the photothermal gas spectroscopy signal.

2. Sensor Setup

The sensor setup is summarized in Fig. 1.

The sensor comprises a home-built SESAM-based mode-locked (ML) fiber laser operating at 1.55 μm. The all-polarization-maintaining (PM) fiber configuration ensures self-starting pulsed operation at a pulse repetition frequency of 23.66 MHz when the 980 nm pump laser delivers 120 mW of optical power to the active fiber. The gas absorption cell (GAC), integrated into the ML laser linear cavity, consists of a 20-cm-long chamber filled with gas samples during measurements. Gas particles in the GAC are excited using an auxiliary pump laser, while the ML laser beam travels through the GAC in both directions. A 5.26 μm quantum cascade laser (QCL) is used to target a strong transition of nitric oxide (NO) at this wavelength, and its beam is co-linearly aligned in the GAC with the oscillating beam of the ML laser. The resulting photothermal effect modulates the refractive index (RI) of the gas sample, inducing a change in the ML's cavity optical pathlength and, as a result, the pulse repetition frequency. This encodes the amplitude of the PTS signal directly into frequency deviations of the ML's beatnotes. To simplify signal extraction, the QCL's wavelength is modulated with a sinewave signal (f_0 = 300 Hz) and swept through the NO absorption line, if necessary. An RF signal analyzer with a custom application demodulates the electrical signal from the photodiode (PD) at a chosen beatnote frequency to monitor the pulse repetition frequency. The self-heterodyne harmonic amplification (SHHA) technique employed in this sensor allows for further multiplication of the observed frequency deviation by demodulating the signal at higher beatnotes of the ML laser, which are clearly observable in its RF spectrum.

The value of the frequency change can be calculated as:

$$\Delta f_{harm} = -H \frac{\Delta n \cdot c}{2L \cdot n^2}, \quad (1)$$

where Δf_{harm} is the change in the repetition frequency, H is the harmonic number at which the signal is demodulated, Δn is PTS-induced RI change of the gas sample, c is the speed of light in vacuum, n is the refractive index and L is the length of the laser cavity.

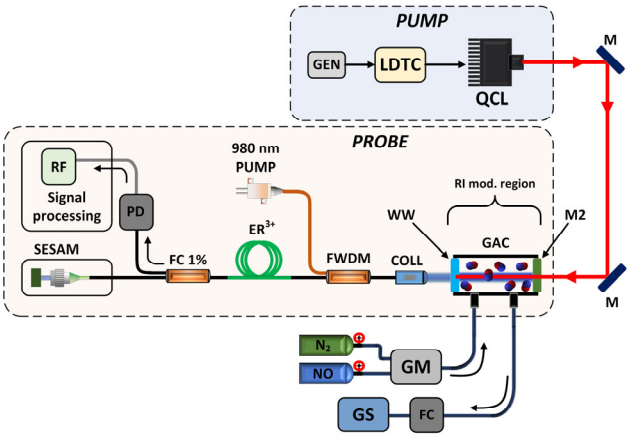

Fig. 1. Experimental setup. SESAM – fiber pigtailed semiconductor saturable absorber mirror, RF – RF spectrum analyzer, PD – photodiode, FC – fiber coupler, Er^{3+} - erbium-doped fiber, FWDM –wavelength division multiplexer, COLL – fiber collimator, WW – wedged window, M – mirror, M2 – CaF_2 HR coated window, GAC – 20 cm-long gas absorption cell, GM – gas mixer, FC – flow controller, GS - gas scrubber. QCL – mid-IR *pump* laser, LDTC – laser controller, GEN – signal generator.

3. Sensor Performance

Wavelength modulation spectroscopy (WMS) approach to signal processing is used, thus the $2\times f_0$ amplitude component is monitored in the demodulated signal via FFT processing. The performance of our sensor was optimized by varying crucial parameters, including: modulation depth, modulation frequency, and pump optical power. Once the optimal values were determined, we conducted experiments using a gas mixture of 1000 ppmv NO in N_2 and a pump power of 100 mW. We then measured the full 2f spectra to register the maximum amplitude of the signal. Fig. 2 depicts the measured signal while demodulating at the 1st and 315th harmonics of the ML laser beatnote, clearly illustrating the significant increase in registered signal amplitude achievable through our SHHA technique. Finally, based on the Allan deviation plot (Fig. 3), we calculated a limit of detection of 6.9 ppbv for a 136 s integration time, underscoring the impressive sensitivity of our approach.

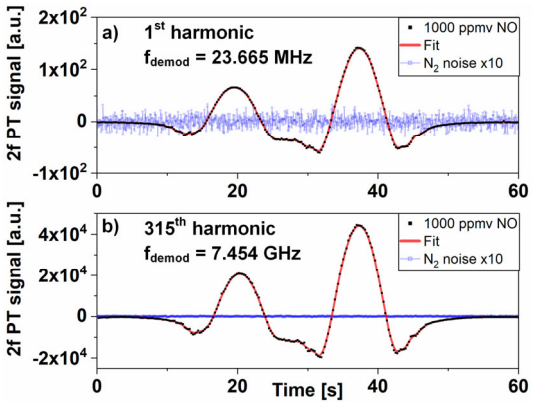

Fig. 2. Full 2f spectra of the transition doublet registered for 1000 ppmv NO in the gas cell, for the 1st and the 315th harmonic. The blue trace shows the background noise registered for pure N_2 in the GAC (magnified 10×).

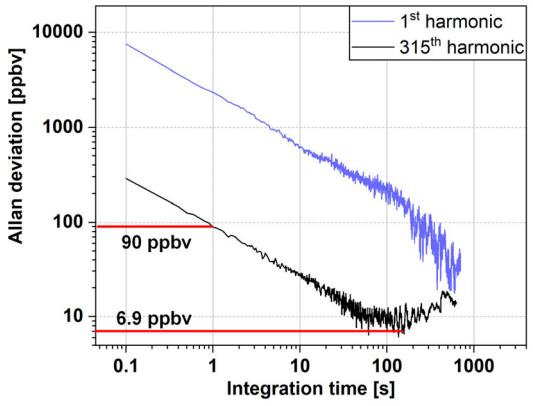

Fig. 3. Allan plots registered for N_2 in the GAC.

4. Conclusions

The novel technique we propose allows the encoding of spectroscopic signals into frequency deviations, providing an advantage over amplitude-based signal readout. Furthermore, our sensor is versatile and capable of measuring any gas sample by simply changing the pump laser to target the desired absorption line. Overall, our innovative gas detection method based on the photothermal effect, in combination with mode-locked lasers, offers substantial enhancements in sensitivity and precision.

Acknowledgements

This work was supported by the National Science Centre, Poland under "M-ERA.NET 2 Call 2019" grant number 2019/01/Y/ST7/00088 and under "SONATA15" grant number 2019/35/D/ST7/04436.

References

[1]. C. C. Davis, S. J. Petuchowski, Phase fluctuation optical heterodyne spectroscopy of gases, *Applied Optics*, Vol. 20, Issue 14, 1981, pp. 2539-2554.

[2]. K. Krzempek, P. Jaworski, P. Kozioł, W. Belardi, Antiresonant hollow core fiber-assisted photothermal spectroscopy of nitric oxide at 5.26 μm with parts-per-billion sensitivity, *Sensors and Actuators B: Chemical*, Vol. 345, 2021, 130374.

(2680)

Brain Tumor Segmentation by Generalized Optical Scanning Holography (GOSH) Based Active Contour (AC)

Anass Cherkaoui [1], Abdennacer El-Ouarzadi [1], Abdenbi Bouzid [1], Younes Achaoui [1], and Abdelaziz Essadike [2]

[1] Moulay Ismail University, Faculty of Sciences, Department of physics,
BP 11201 Zitoune, Meknes, Morocco

[2] Hassan First University of Settat, Higher Institute of Health Sciences, Laboratory Health Sciences and Technologies, B. P. 26000, mdical physicist. Settat, Morocco

E-mail: an.cherkaoui@edu.umi.ac.ma

Summary: This paper aims to develop a fully automatic MRI Brain tumor segmentation and detection to tackle the problem of manual segmentation, which is an error-prone, sensitive, and time-absorbing process. We enhance our previous framework [1] for optical scanning holography (OSH) to detect abnormal tissue regions in MRI in terms of acquisition speed, precision, and data size we present our latest work on improving Eq. (10), which has led to significant enhancements in the segmentation metrics and the computation time, as shown in (Table 1 and 2). The proposed method combines the in-line holography setup, performed by a heterodyne fringe pattern, and an MRI display assured by a spatial light modulator. The extraction of the maximum peaks In-phase component of the scanned current gives a reliable precision to the tumor's position. Simultaneously, this position is applied in an Active Contour Model (ACM) to perform a fast segmentation of the region corresponding to the tumors. Various images of brain tumors from the BRATS database, which have different contrast and shape, are used to test the proposed method. The suggested method achieves high accurate detection of tumor tissue by returned parameters (L, c) by the GOSH method. Besides, compared with active contour-based methods, the proposed method gives a more reliable performance with the averages of sensitivity = 0.98, Dice coefficient = 0.98, Hausdorff distance = 2.10, specificity = 0.99, and more rapidly with computation time averaging 0.19 seconds per frame.

Keywords: Optical Scanning Holography (OSH), Brain tumor detection, Active contour, Segmentation, In-phase component.

1. Introduction

Optical biomedical imaging has emerged these last years as an important area of research and development in diagnostic medicine driven by the need for safe, affordable, non-invasive modalities to detect and diagnose cellular abnormalities in the human body. The optical image processing field has undergone tremendous development and has found various applications ranging from optical image encryption [2], ophthalmological cancer detection [3], brain tumor detection and Magnetic Resonance Imaging (MRI) image segmentation [4], to biometric applications [5]. Its high-speed parallel processing makes it promising for the next generation of image processing techniques, replacing traditional numerical algorithms. There are four main aspects of optical image processing systems tackled; image pre-processing techniques to filter out noise and extracting specific regions of interest through new segmentation techniques, object feature extraction and detection techniques for locating areas of interest or altering scene conditions, image processing applications that create intelligent instrumentation systems, and image encryption techniques to ensure security and safety of data communication [6].

The segmentation is the final process after having images of the biological agent through medical imaging modalities as optical imaging, radionuclide imaging, and MRI. For example, optical imaging is a scattering light-based technique. In this type of technique, the base methods can be classified into two modalities; one is a direct observation of the light rays passing through the structure tissue, and the other uses fluorescent contrast agents [7]. In addition, the new automatic segmentation methods for identifying and measuring volumetric structures with magnetic resonance imaging (MRI) [8, 9], CT dose optimization [10], automatic reconstruction and segmentation for structural characterization of scanning electron microscopy images [11], and image-guided radiation therapy [12]. The proposed method solves the segmentation task in a way adapted to current needs, including in surface analysis like skin diseases [13], tumor localization in the human breast [14], eye diseases [15] and dosimetry planning in brain radiotherapy [16]. Radiotherapy aims to provide a curative and precise dose of radiation delivered to the target volume, i.e., the brain tumor, whilst sparing the surrounding risk organs. Given the problem's sensitivity, tumor segmentation is usually manually performed by neuroradiologists or using methods characterized by a lack of entirely automatic detection. The main disadvantage of these limitations directly affects the expected results in terms of accuracy and time-consuming.

Segmentation of the "brain" area of interest is a common preprocessing of MRI images. Unfortunately,

this technique isolates the "brain" component from the initial data volume to limit the work areas during subsequent segmentation and thus improve the quality of the results obtained and reduce the computational complexity (in time and space) [3, 5, 15]. Recently, optical methods opened a new field to tackle this technological challenge due to the specificities of the constraints of different natures. This paper proposes a new architecture that extracts phase information corresponding to the tumor position by the enhanced optical scanning holography (OSH). Concurrently, an active contour model (ACM) is applied to this position to perform a faster segmentation of the region corresponding to the tumors in each slice. The underlying physics of this automatic extraction is driven by the In-phase component of the image scan current, which can also facilitate the calculation of the active contour energy terms and therefore alleviate the segmentation of the tumor tissue by rendering the segmentation as an energy minimization problem.

Optical scanning holography is a Realtime Holographic Recording technique wherein holographic information about a 3D three-dimensional object is collected using a single active optical scan in two dimensions. Implementations of this technique include optical scanning microscopy, 3D holographic display, pattern recognition, and optical remote sensing [17-20]. Following our previous work [1], we explored the use of Optical Scanning Holography (OSH) in automatizing tumor tissue detection in MRI. This paper proposes an enhanced framework for optical scanning holography (OSH) to detect abnormal tissue regions. The proposed method combines the in-line digital holography setup, a heterodyne fringe pattern, and an MR image display assured by a spatial light modulator SLM. We improve [1] in terms of acquisition speed, accuracy, and data size. In addition, This technique GOSH of recording holographic information is advantageous as two on-axis holograms are acquired simultaneously, unlike standard phase-shifting holography where their holograms are acquired sequentially. Hence, we can construct a complex hologram that does not create a double image in reconstruction from the two on-axis holograms [21-26].

2. Method

This section presents the scanning image process used, based on a typically two-pupil optical heterodyne. Since we consider that the automatic tumor detection is based on the In-phase component of the scanned current, we require to use a system to preserve this In-phase component throughout the data acquisition. From our investigation, the practical solution to this problem is using optical heterodyning.

For example, switching the laser beam frequency can be achieved through acousto-optic modulators [27]. The dual laser beams are combined with a beam splitter (BS) and projected by the x-y scanner towards a 3D object at a distance $z + z_0$ from the back focal plane of the L1 lens. We set the object in a spatial light modulator. An amplitude transmittance T(x,y,z) represents each slice of the object.

The SLM displays the brain tumor image, I(x,y,z), located at a distance $z + z_0$ away from the back focal plane of the lens L1, Furthermore, the first attempts to develop SLMs suffer from a diffraction efficiency problem arising from phase shift loss. In this case, as the MRI image is a binary image, the SLM used can achieve an offset range approaching 2π, which results in excellent diffraction efficiency. Besides, the SLM is a recent device allowing modulating the blazing functions to achieve maximum grating efficiency and high diffraction performance.

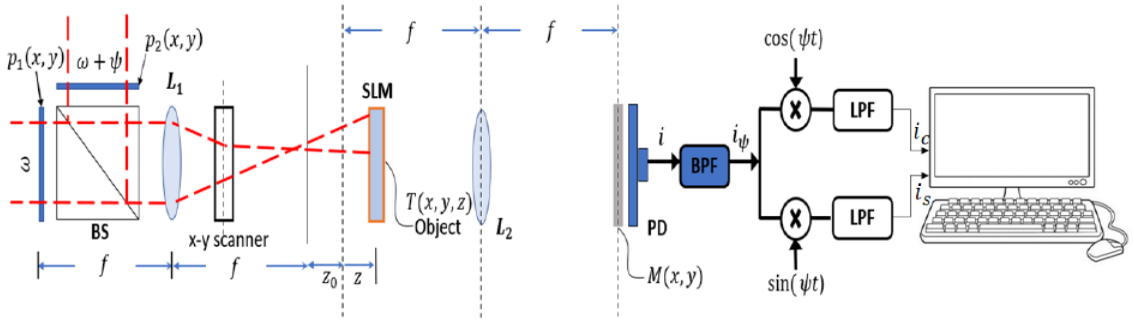

Fig. 1. Generalized two-pupil heterodyne scanning image processing system for the In-phase component extraction of brain tumor.

We place the object in front of the lens L_2 of the Fourier transform. The amplitude distributions of the two laser beams before the object slice at the $z + z_0$ position is mathematically given by:

$$P(x,y,z+z_0) = P^1_{z+z_0}\left(\frac{k_0 x}{f},\frac{k_0 y}{f}\right)e^{j\omega t} + \\ +P^2_{z+z_0}\left(\frac{k_0 x}{f},\frac{k_0 y}{f}\right)e^{j(\omega+\psi)t}, \quad (1)$$

where

$$P^i_{z+z_0}\left(\frac{k_0 x}{f},\frac{k_0 y}{f}\right) = P^i\left(\frac{k_0 x}{f},\frac{k_0 y}{f}\right) * \\ * h(x,y,z+z_0) = F\{P^i(x,y)\}_{k_x,k_y} * \\ * h(x,y,z+z_0), \quad (2)$$

with i = 1,2 and

$$F\{P^i(x,y)\}_{k_x,k_y} = \\ = \iint_{-\infty}^{+\infty} P^i(x,y)e^{j(k_x x+k_y y)}dxdy \quad (3)$$

Eq. (3) is the Fourier transform of P_i (x, y), where in k_x and k_y designate the spatial frequencies associated with the variables x and y, accordingly, in Eq. (1).

$$h(x,y,z+z_0) = \\ = e^{-jk_0(z+z_0)}\frac{jk_0}{2\pi(z+z_0)}e^{\frac{-jk_0}{2(z+z_0)}(x^2+y^2)} \quad (4)$$

Equation (4) is the free space spatial impulse response in Fourier optics [20], where in k_0 is the wave number of the laser beam; The field right after the object is:

$$i_\psi(t) = Re\big(\int\big[P^2_{z+z'}(x',y')T(x'+x,y'+y,z')\,dx'\big]\times\int\big[P^{1\,*}_{z+z'}(x',y')\,T^*(x''+x,y''+y,z'')\,dx''\,dy''\,dz''\big]e^{j\psi t}\big), \quad (5)$$

where x = x(t) and y = y(t) representing the current 2D Position of the object in terms of the distribution of the light amplitude. This field propagates across the lens L2 of the Fourier transform and reaches the mask, M(x,y), located in the back focal plane of the lens L_2. The distribution of the field coming out of the mask, from all slices of the object T(x,y,z), is as follows:

$$A(x,y;x_M,y_M) \propto \{P^1_{z+z_0}(x',y')e^{j\omega t} + P^2_{z+z_0}(x',y')e^{j(\omega+\psi)t}\}T(x'+x,y'+y,z')\times \\ \times\Big\{\exp\big(\tfrac{jk_0}{f}(x'x_M+y'y_M)\big)\,dx'\Big\}\Big\{\exp\big(-\tfrac{jk_0 z}{2f}({x_M}^2+{y_M}^2)\big)\,dz\Big\}, \quad (6)$$

wherein x_M and y_M are the coordinates in the mask plane, and z is the distance to the slice of the object that is located at SLM, measured from the front focal plane of the lens L_2. Following the integration on z represents the volumetric e_ect due to the 3D object. Finally, the photodetector (PD), which is sensitive to the intensity, yields the output current i(t) through spatial integration of the intensity:

$$i(t) \propto \int|A(x,y;x_M,y_M)|^2 dx_M dy_M, \quad (7)$$

i(t) is composed of a base-band current and a heterodyne current at the frequency ψ. After several manipulations, the current heterodyne i(t), coming out of the bandpass filter (see Fig. 1), is yielded by [23]:

$$i_{\psi_Q}(x,y,z+z_0) = \\ = P^1_{z+z_0}\left(\frac{k_0x'}{f},\frac{k_0y'}{f}\right)P^{2\,*}_{z+z_0}\left(\frac{k_0x'}{f},\frac{k_0y'}{f}\right)\otimes \\ \otimes|O(x,y,z+z_0)|^2 \quad (8)$$

Afterward, we are able to define the optical transfer function (OTF) of the system by:

$$OTF_\psi(k_x,k_y,z+z_0) = \frac{F\{i_{\psi_Q}(x,y,z+z_0)\}}{F\{|O(x,y,z+z_0)|^2\}} \quad (9)$$

As a result, we obtain the following equations:

$$i_c(x,y) = Re\{\int F^{-1}\{F\{|O(x,y,z+ \\ +z_0)|^2\}.OTF_\psi\}\,dz\}, \quad (10)$$

$$i_s(x,y) = \\ = Im\Big\{\int F^{-1}\{F\{|O(x,y,z+z_0)|^2\}.OTF_\psi\}\,dz\Big\} \quad (11)$$

These two currents are respectively representing the In-phase component i_c (x,y) and the quadrature component i_s (x,y) of the extracted heterodyne current from the scanned MR image. the temporal frequency shift is inserted between the two pupils by assuming $P^1{}_{z+z0}$ (x,y) = 1 and $P^2{}_{z+z0}$(x,y) = δ(x,y) Thus, the optical transfer function becomes:

$$OTF_\psi(k_x,k_y,z+z_0) = exp\left[\tfrac{-j(z+z_0)}{2k_0}({k_x}^2+{k_y}^2)\right], \quad (12)$$

and the two streams become:

$$i_c(x,y) = \int\Big\{|O(x,y,z+z_0)|^2 * \frac{k_0}{2\pi(z+z_0)}\,sin\,sin\,\left[\frac{k_0}{2(z+z_0)}(x^2+y^2)\right]\Big\}dz, \quad (13)$$

$$i_s(x,y) = \int\Big\{|O(x,y,z+z_0)|^2 * \frac{k_0}{2\pi(z+z_0)}\,cos\,cos\,\left[\frac{k_0}{2(z+z_0)}(x^2+y^2)\right]\Big\}dz \quad (14)$$

The proposed approach's basic idea is to use the In-phase component ic(x,y) for detecting abnormal tissue in MR images. The optical system in Fig. 1 gives an output that shows the distribution of the In-phase component of the heterodyne current. Maximum values characterize this output called the In-phase component peaks. Fig. 2 shows examples of the In-phase component peaks given by the GOSH method.

Therefore, determining the brain tumor's position by searching the peaks given by the maximum values of the In-phase component distribution. With the peaks position of the In-phase component, as shown in Fig. 3, we extract the initial contour C_i of the tumor segmentation within the tumor tissue. The proposed method can be adapted to detect multimodal tumors by detecting the two maxima's two positions of the In-phase component peaks.

In a digital system, the OSH optical process results are used for extracting the following parameters: c the center of the tumor, L the amplitude of the In-phase component peak, and C_i the initial contour formed using the principal in Fig. 3. the suggested method detects tumor tissue and facilitates the energy calculation of active contours. Using the initially detected contour C_i, we calculate the averages of the image I(x,y) inside C_i and outside C_i to define the active contour model:

$$E_{i,j} = \alpha . C_{i,j} + \beta . \left| I - M_{i,j} \right|^2 + \\ + \gamma . \left| I - m_{i,j} \right|^2, \quad (15)$$

where, $\alpha = \beta = \gamma = 1$ are fixed parameters. $C_{i,j}$ is the initial contour detected by the proposed method. mi,j is the average of the input RM image I(x,y) inside the initial contour $C_{i,j}$. $M_{i,j}$ is the average of the input RM image I(x,y) outside the initial contour $C_{i,j}$. Besides, the evolution of the initial contour detected by the GOSH system is realized through the programming of the proposed active contour pattern, based on finite differences obtained after linearization and discretization of Eq's energy 15. The lecturer can find more details about applying the active contour model proposed in our previous work in [16]. Fig. 4 shows examples of tumor segmentation through the proposed GOSH method.

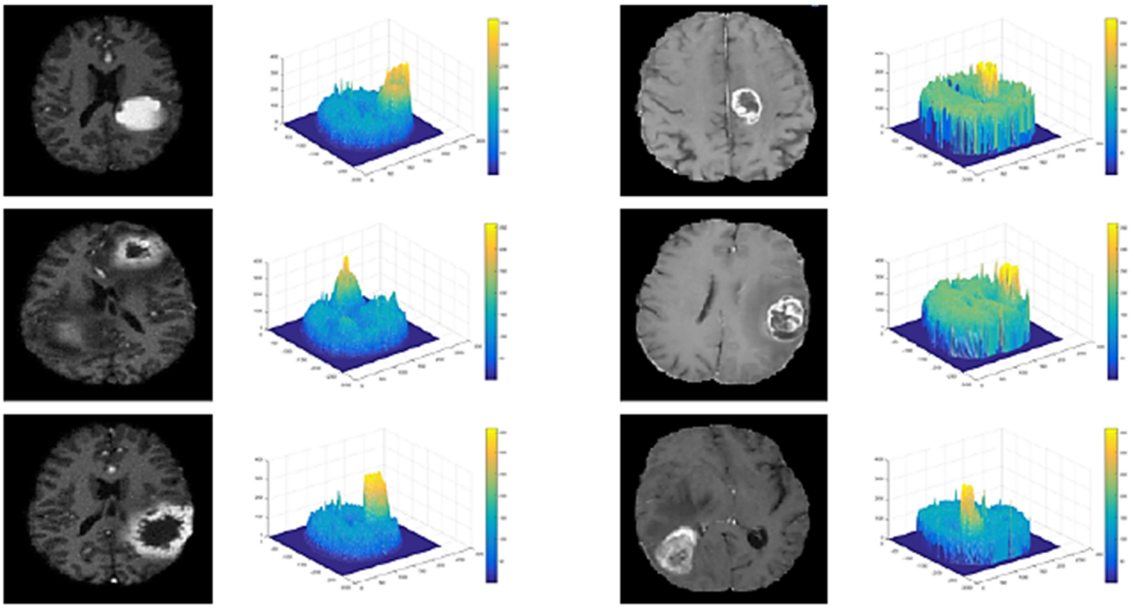

Fig. 2. In-phase component peaks at the tumor position according to the proposed method GOSH: BRATS 2012 and BRATS 2013 database images.

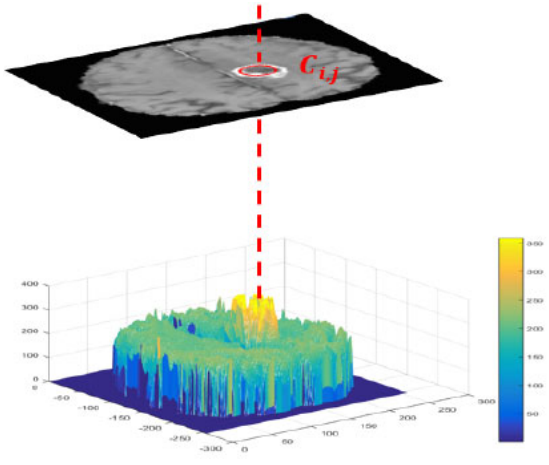

Fig. 3. Principle of extracting the initial contour C_i within the tumor tissue, by GOSH method based on In-phase component peaks.

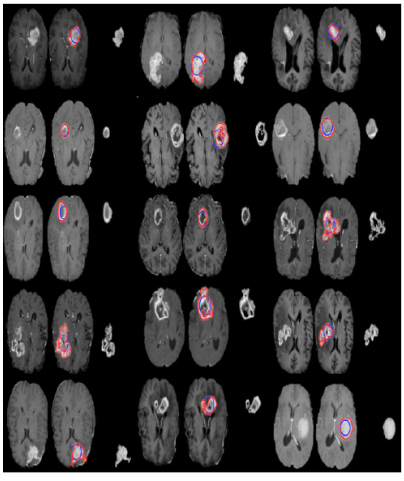

Fig. 4. Segmentation results collected from the BRATS 2012 and 2013 databases. ■: Initial contours detected through the GOSH method, ■: Definitive contours after the GOSH method evolution.

3. Experimental Results

In this part, we first evaluate the performance of the proposed method concerning brain tumor detection. For that, we assess the two-parameter returned by the GOSH: the center of tumor c and the maximum peak value of the In-phase component L. Two databases, BRATS 2012 and BRATS 2013 (https://www.smir.ch/BRATS/Start2016), were used for all the tests due to ground truths' availability [28]. In order to evaluate the methods used, four similarity criteria were considered: the Sensitivity Sen, the Dice coefficient D, the Hausdorff distance H_d, and the Specificity Spe calculated as below:

$$0 \leq Sen = \frac{TP}{TP+FN} \leq 1, \quad (16)$$

$$0 \leq D = \frac{TP}{TP+\frac{FP+FN}{2}} \leq 1, \quad (17)$$

$$0 \leq Sep = \frac{TN}{TN+FP} \leq 1, \quad (18)$$

where in TP is the true positive (pixels correctly classified as a tumor tissue), TN is the true negative (pixels correctly classified as healthy tissue), FP is the false positive (normal tissue incorrectly classified as tumor region), and FN is the false negative (undetected tumor tissue).

$$H_d(G,S) = \max\left\{\begin{matrix}\max\limits_{a\in G}\min\limits_{b\in S}\|a-b\| \\ \max\limits_{b\in S}\min\limits_{a\in G}\|b-a\|\end{matrix}\right\}, \quad (19)$$

where G is the ground truth or gold standard and S is the automatically obtained result. The perfect correspondence is obtained when the metrics Sen, D, and Spe are equal to 1 and the ideal value of H_d(G, S) is 0.

3.1. Brain Tumor Detection

Research in the area of dosimetry planning and radiotherapy is progressing at a staggering pace. Since the first surveys, it has been widely used to inject a curative and precise dose of radiation, mainly through automatic detection and segmentation methods. Such methods are unfortunately limited in real life as they suffer a lack of full automaticity in terms of tumor detection. Our method solved this limitation by using the maximum peaks of In-phase components extracted by the GOSH process.

As the decision of the existence of a brain tumor on an MR image is based on the parameter L, we have studied L values for MR images of healthy and tumor brains. Fig. 5 represents the statistical distribution of the L parameter in the two cases mentioned. Evidently, in the case of the tumor, L values are large compared to the healthy brain. In the images of healthy brains, the average L in the images used was 110, and in the images of brain tumors was 325. It should be noted that the maximum peaks of In-phase components given by the GOSH process, which localized the tumors, were within the margin of [300; 350]. This margin increases to over 255 due to the multiplication of the MRI images in equation 10. Moreover, due to the uniform distribution of pixel intensity in images of the healthy brain, all of the maximum peaks of the In-phase component in cases of healthy brains being within [100 120]. Therefore, the parameter L given by the GOSH process is a reliable parameter to decide the existence of a tumor in the MR images.

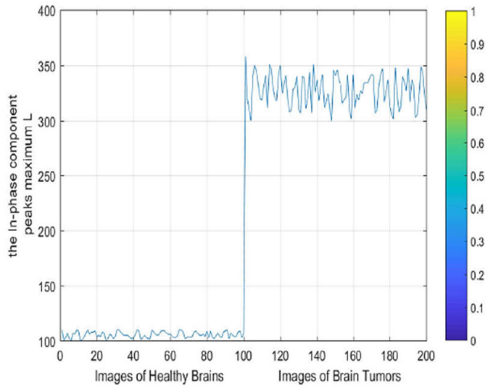

Fig. 5. Distribution of the L parameter in the healthy and tumorous brain images.

Similarly, the brain tumor position's decision is based on the parameter c given by the GOSH. Therefore, we have estimated the precision of the proposed method regarding the detection of c inside of the tumor tissue. As a comparison, we have also calculated the percentage rate of the potential field segmentation (PFS) algorithm [29] regarding tumor centers' detection. This approach is founded on potential field analogy in detecting brain tumors by assuming the intensity of a pixel as a mass, creating a potential field.

It should be pointed out that the center used is obtained from the maximum peaks of the In-phase component. Table 1 reveals the high accuracy of detecting the center of the tumor tissue by the proposed method. In 98.5 % of the patients (from both databases), the maximum peaks of In-phase components given by the proposed method are located in the tumor tissue center. In the remaining 1.5 %, the GOSH returned parameter c to the border of this tumor. Two principal reasons explain these results; firstly, owing to the modalities used in MR images to separate tumors from healthier tissue, contrast provides an almost unique signature for each type of tissue, particularly the type of tumor, which appears in most cases with the white color. Secondly, the high value of the maximum peaks of the In-phase component in tumoral regions. Therefore, the proposed method is a promising technique for detecting anomalous tissue in MR images, comparing with recently published methods. The proposed method is more accurate and quicker. It should be noted that the center used is

determined by the maximum peak of the In-phase component.

3.2. Brain Tumor Segmentation

Once the GOSH technique has automatically and quickly detected the tumor tissue, we can discuss OSH's advantages in part devoted to segmentation. For this purpose, we have investigated several active contour models (ACM) based on the GOSH. All the ACM processes have been initialized with the proposed GOSH's initial contours for relevant comparison.

Table 1. Percentage of the proposed method in terms of the c parameter return within the tumor tissue and the meantime, comparing to the method of [29].

Method	Accuracy (%)			Time average (s)
	Inside tumor	Edge tumor	Outside tumor	
Potential Field [29]	95 %	0	5 %	38.1643
Proposed method	98.5 %	1.5 %	0 %	0.2009

To test the proposed method in a very demanding way and link it to clinical imaging applications, we have used 20 images of patients with the most challenging segmentation conditions. These images contain different shapes, sizes, and contrasts of tumors, Tables 2-3 compare the performance reported from these 20 images and reached by the GOSH method with the GAC (Geodesic Active Contour model) [30], the LAC (Localized Active Contour) [31], the Active Contours by Cuckoo Search (ACCS) [32] and our previous work OSH-ACM [1]. Compared to other ACMs, the proposed method performs better in terms of Sen, D, H, and Spe parameters. For evidence, the sensitivity value of 0.9961 reached by the proposed method was the highest obtained, and its Hausdorff distance of 2.0000 was the lowest. Besides, its highest average specificity value of Spe = 1:0000 indicates that it can correctly classify healthy tissue more than other ACM-based methods. It should be noted that the highly efficient performance of all methods in terms of the Spe parameter is explained by the fact that all the initial contours detected by the proposed GOSH technique are located inside the tumor tissue. Following these methods' development, the optimal segmentation contours remain inside the tumor tissue, making the FP parameter very close to zero. Also, it can be observed from Tables 2 and 3 that the proposed method reduces the calculation time (in seconds).

The proposed GOSH method detects the initial contour inside the tumor in real-time, making it possible to calculate the time required for the active contour to evolve. Therefore, the proposed method is the quickest approach. Overall, the proposed GOSH-AC method is a technique for automatic detection and fast segmentation of brain tumors. It solves the manual segmentation of tumors performed by experts and error-prone, sensitive, and time-absorbing process. The GOSH process is a fully automatic process offering an accuracy of 100 % in detecting all tumor types. Besides, its returned parameter L is a trustworthy parameter for deciding the MR images tumor position. Moreover, the proposed method is more efficient in terms of segmentation.

Table 2. Sensitivity, Dice, Hausdorff distance, Specificity, and elapsed time rates obtained from the optimal contour of the BRATS 2012 database images reached by using the Geodesic Active Contour (GAC), the Localized Active Contour (LAC), the Active Contour driven by Cuckoo Search (ACCS), our previous work (OSH-ACM) and the proposed method (Proposed).

Patients	Method	Sen	D (AVG±SDx10^{-4})	H_d	Spe	Time (s)
Patient 1 (BRATS 2012)	GAC	0.7194 ±1.2	0.7650±6.3	4.1200 ±2.6	0.9945±0.0	14.9945±1.2
	LAC	0.9016 ±2.6	0.9482±3.3	2.7488 ±2.6	0.9975±2.3	14.2406±1.9
	ACCS	0.9502 ±7.5	0.9495±9.0	2.6488 ±5.2	0.9980±1.0	48.1200±2.0
	OSH-ACM	0.9772 ±0.5	0.9838±0.3	2.0458 ±0.0	0.9987±4.5	0.2937±3.1
	Proposed	**0.9809** ±0.7	**0.9896**±0.1	**2.0402**±0.1	**0.9989**±2.5	**0.2463**±2.1
Patient 2 (BRATS 2012)	GAC	0.7844 ±0.0	0.7377 ±4.2	4.3589 ±6.1	0.9903 ±4.5	26.1737 ±2.5
	LAC	0.8250 ±5.4	0.9041 ±4.8	4.0010 ±2.0	0.9957 ±2.8	17.1943 ±9.5
	ACCS	0.9347 ±1.5	0.9605 ±0.8	3.0050 ±2.5	0.9989 ±1.1	46.9430 ±9.0
	OSH-ACM	0.9752 ±0.2	0.9753 ±0.1	2.1623 ±0.0	0.9980 ±0.0	0.3540 ±7.2
	Proposed	**0.9879** ±0.4	**0.9802** ±0.6	**2.1597** ±0.2	**0.9987** ±0.1	**0.3232** ±8.2
Patient 3 (BRATS 2012)	GAC	0.6804 ±6.3	0.7489 ±5.6	5.7823 ±2.4	0.9902 ±0.3	27.7494 ±2.8
	LAC	0.6715 ±2.3	0.8417 ±5.3	4.8990 ±7.5	0.9914 ±0.0	17.3898 ±7.0
	ACCS	0.9274 ±3.8	0.9410 ±4.1	3.5560 ±7.1	0.9992 ±0.9	59.2705 ±2.7
	OSH-ACM	0.9898 ±0.1	0.9897 ±0.1	2.0623 ±1.0	1.0000 ±0.1	**0.2530 ±3.8**
	Proposed	**0.9899** ± 0.0	**0.9898 ±0.0**	**2.0596 ±3.0**	**1.0000 ±0.1**	**0.2498 ±2.4**
Patient 4 (BRATS 2012)	GAC	0.5751 ±3.7	0.6456 ±0.1	4.1231 ±8.7	0.9976 ±1.7	37.9528 ±8.7
	LAC	0.6346 ±2.0	0.7765 ±1.0	4.3589 ±5.7	0.9950 ±4.6	17.6072 ±8.0
	ACCS	0.8892 ±3.9	0.9395 ±1.0	3.3940 ±3.3	0.9989 ±7.4	25.7492 ±5.4
	OSH-ACM	0.9867 ±0.1	0.9834 ±0.1	2.0056 ±1.0	0.9997 ±0.7	0.2212 ±1.5
	Proposed	**0.9884 ±0.0**	**0.9905 ±0.6**	**2.0024 ±5.0**	**0.9999 ±0.2**	**0.2200 ±1.0**

Table 2. (Continued).

Patients	Method	Sen	D (AVG±SDx10^{-4})	H_d	Spe	Time (s)
Patient 5 (BRATS 2012)	GAC	0.7247 ±3.4	0.6902 ±2.8	5.7958 ±3.9	0.9906 ±5.5	22.1867 ±9.6
	LAC	0.7678 ±2.0	0.7243 ±0.0	4.0001 ±1.0	0.9907 ±0.5	16.6965 ±0.8
	ACCS	0.9192 ±2.1	0.9380 ±0.2	3.5437 ±1.0	0.9984 ±6.6	18.4792 ±0.8
	OSH-ACM	0.9894 ±0.2	0.9757 ±0.1	2.5826 ±1.0	0.9997 ±4.4	0.2165 ±2.6
	Proposed	**0.9899 ±0.1**	**0.9864 ±0.2**	**2.459 ±3.0**	**0.9997 ±0.3**	**0.2130 ±0.6**
Patient 6 (BRATS 2012)	GAC	0.7800 ±5.4	0.8096 ±1.7	3.0010 ±2.0	0.9950 ±2.2	9.3899 ±7.4
	LAC	0.7473 ±0.3	0.7181 ±0.1	3.0000 ±0.0	0.9975 ±7.9	10.5313 ±0.9
	ACCS	0.9247 ±2.0	0.9400 ±2.3	2.8947 ±9.7	0.9998 ±2.3	15.3692 ±5.0
	OSH-ACM	0.9898 ±1.7	0.9887 ±1.2	2.0620 ±0.0	0.9995 ±3.8	0.1730 ±2.6
	Proposed	**0.9902 ±0.8**	**0.9942 ±5.8**	**2.0329 ±0.5**	**0.9998 ±9.7**	**0.1710 ±4.6**
Patient 7 (BRATS 2012)	GAC	0.5154 ±0.4	0.6069 ±0.4	5.3852 ±0.0	0.9963 ±2.7	26.4020 ±4.0
	LAC	0.6850 ±0.4	0.6436 ±0.2	4.9904 ±0.3	0.9975 ±7.0	14.1543 ±6.6
	ACCS	0.8995 ±1.2	0.9364 ±5.6	2.9634 ±2.3	0.9986 ±0.9	28.3751 ±5.9
	OSH-ACM	0.9789 ±1.5	0.9871 ±1.1	2.0458 ±0.0	0.9997 ±0.0	0.1356 ±1.8
	Proposed	0.9808 ±5.6	0.9894 ±6.2	2.0389 ±1.0	0.9996 ±0.0	0.1310 ±2.9
Patient 8 (BRATS 2012)	GAC	0.5471 ±0.4	0.5565 ±0.3	5.8990 ±1.0	0.9904 ±0.5	24.9600 ±1.3
	LAC	0.7693 ±0.6	0.7895 ±0.5	4.3852 ±1.0	0.9985 ±2.8	16.8878 ±1.0
	ACCS	0.9599 ±0.6	0.9601 ±4.0	2.7945 ±0.0	0.9950 ±3.3	36.7810 ±1.8
	OSH-ACM	0.9886 ±2.4	0.9749 ±1.0	2.0827 ±1.1	0.9987 ±4.6	0.1321 ±3.6
	Proposed	0.9888 ±1.4	0.9780 ±2.0	2.0684 ±2.5	0.9996 ±2.4	0.1329 ±4.7
Patient 9 (BRATS 2012)	GAC	0.6878 ±0.2	0.6558 ±0.0	5.0915 ±0.2	0.9967 ±0.0	15.7585 ±4.5
	LAC	0.8095 ±0.0	0.8947 ±0.1	3.1623 ±2.0	0.9974 ±7.7	8.5422 ±8.9
	ACCS	0.9097 ±3.0	0.8997 ±0.4	3.1597 ±5.3	0.9988 ±9.6	17.1467 ±2.4
	OSH-ACM	0.9877 ±1.4	0.9782 ±0.5	2.1284 ±0.0	0.9996 ±0.8	0.1879 ±0.3
	Proposed	0.9899 ±0.9	0.9842 ±0.2	2.0084 ±0.2	0.9997 ±1.5	0.1479 ±1.9
Patient 10 (BRATS 2012)	GAC	0.5499 ±0.3	0.4998 ±0.1	6.7823 ±0.0	0.9945 ±9.1	20.8182 ±6.2
	LAC	0.6867 ±0.3	0.6577 ±0.1	5.1644 ±0.1	0.9959 ±2.2	8.0357 ±9.8
	ACCS	0.9002 ±4.2	0.9147 ±2.5	2.9846 ±7.3	0.9979 ±0.4	18.7666 ±0.0
	OSH-ACM	0.9868 ±1.0	0.9786 ±0.2	2.0628 ±1.0	0.9997 ±2.0	0.2429 ±4.7
	Proposed	0.9961 ±6.0	0.9882 ±4.2	2.0304 ±9.0	0.9997 ±0.0	0.2099 ±8.2

Table 2. Sensitivity, Dice, Hausdorff distance, Specificity, and elapsed time rates obtained from the optimal contour of the BRATS 2013 database images reached by using the Geodesic Active Contour (GAC), the Localized Active Contour (LAC), the Active Contour driven by Cuckoo Search (ACCS), our previous work (OSH-ACM) and the proposed method (Proposed).

Patients	Method	Sen	D (AVG±SDx10^{-4})	H_d	Spe	Time (s)
Patient 11 (BRATS 2013)	GAC	**0.7607 ±0.2**	**0.7185 ±0.0**	**3.1623 ±0.1**	**0.9933 ±1.8**	**12.3015 ±8.9**
	LAC	**0.8068 ±0.1**	**0.8931 ±1.8**	**2.8361 ±0.6**	**0.9964 ±2.8**	**8.2133 ±8.7**
	ACCS	**0.9547 ±0.0**	**0.9328 ±4.4**	**2.5138 ±9.7**	**0.9973 ±0.7**	**22.8520 ±3.3**
	OSH-ACM	**0.9876 ±1.5**	**0.9882 ±0.8**	**2.1166 ±1.0**	**0.9987 ±1.0**	**0.2820 ±4.3**
	Proposed	**0.9896 ±0.0**	**0.9893 ±0.2**	**2.1040 ±0.0**	**0.9989 ±0.0**	**0.2095 ±7.2**
Patient 12 (BRATS 2013)	GAC	**0.6573 ±0.4**	**0.6718 ±0.5**	**6.4721 ±2.0**	**0.9934 ±6.3**	**37.0503 ±5.1**
	LAC	**0.7185 ±4.0**	**0.7832 ±0.3**	**3.7417 ±0.0**	**0.9967 ±4.9**	**6.2981 ±8.1**
	ACCS	**0.9009 ±3.7**	**0.9343 ±2.4**	**2.9987 ±0.0**	**0.9972 ±0.4**	**19.7351 ±0.8**
	OSH-ACM	**0.9898 ± 0.1**	**0.9847 ±0.0**	**2.0495 ±0.0**	**0.9989 ±5.5**	**0.1013 ±1.5**
	Proposed	**0.9900 ±9.0**	**0.9904 ±5.2**	**2.0398 ±5.0**	**0.9997 ±4.2**	**0.1010 ±2.9**
Patient 13 (BRATS 2013)	GAC	**0.5080 ±0.3**	**0.5443 ±0.2**	**5.7446 ±0.5**	**0.9930 ±2.0**	**36.8782 ±4.7**
	LAC	**0.6304 ±0.5**	**0.6307 ±0.4**	**4.4721 ±0.0**	**0.9911 ±0.9**	**8.6424 ±1.3**
	ACCS	**0.8975 ±0.7**	**0.9051 ±6.6**	**3.3001 ±3.3**	**0.9970 ±1.0**	**28.4568 ±9.6**
	OSH-ACM	**0.9887 ±0.1**	**0.9865 ±0.1**	**2.1417 ±1.0**	**0.9987 ±2.2**	**0.1468 ±0.2**
	Proposed	**0.9890 ±2.0**	**0.9894 ±1.2**	**2.1314 ±9.0**	**0.9996 ±3.1**	**0.1316 ±8.1**
Patient 14 (BRATS 2013)	GAC	**0.7040 ±0.3**	**0.7755 ±0.7**	**3.4495 ±0.0**	**0.9900 ±3.2**	**10.4806 ±6.4**
	LAC	**0.8897 ±0.1**	**0.8825 ±0.0**	**3.1200 ±1.12**	**0.9956 ±7.9**	**3.9965 ±8.0**
	ACCS	**0.9110 ±3.3**	**0.8997 ±2.2**	**3.2546 ±6.9**	**0.9967 ±0.7**	**44.3490 ±3.7**
	OSH-ACM	**0.9769 ±1.4**	**0.9769 ±1.2**	**2.0000 ±0.0**	**0.9987 ±2.3**	**0.2164 ±1.3**
	Proposed	**0.9802 ±5.6**	**0.9890 ±3.2**	**2.0000 ±0.0**	**0.9996 ±8.4**	**0.2030 ±5.2**
Patient 15 (BRATS 2013)	GAC	**0.6699 ±0.3**	**0.5401 ±0.0**	**4.2426 ±0.5**	**0.9963 ±2.7**	**20.9238 ±7.3**
	LAC	**0.6436 ±0.1**	**0.7043 ±0.0**	**3.4641 ±0.0**	**0.9977 ±2.7**	**3.4695 ±0.2**
	ACCS	**0.9567 ±0.0**	**0.9476 ±1.2**	**2.7640 ±2.8**	**0.9976 ±2.4**	**30.2648 ±4.5**
	OSH-ACM	**0.9887 ±0.1**	**0.9887 ±1.0**	**2.0458 ±1.1**	**0.9997 ±0.0**	**0.1357 ±0.7**
	Proposed	**0.9899 ±2.5**	**0.9904 ±9.0**	**2.0053 ±9.1**	**0.9997 ±0.0**	**0.1300 ±0.9**
Patient 16 (BRATS 2013)	GAC	0.6917 ±0.4	0.6517 ±0.2	5.6569 ±5.5	0.9955 ±4.8	36.9248 ±7.2
	LAC	0.8937 ±0.1	0.8850 ±0.0	3.6904 ±1.0	0.9971 ±3.8	6.0861 ±8.3
	ACCS	0.9379 ±9.8	0.9471 ±2.7	2.8000 ±0.0	0.9989 ±4.4	34.7982 ±0.8
	OSH-ACM	0.9886 ±0.2	0.9891 ±0.1	2.1056 ±1.0	0.9990 ±0.0	0.2294 ±3.8
	Proposed	0.9902 ±8.1	0.9900 ±5.2	2.1009 ±9.0	0.9996 ±0.0	0.2064 ±5.2

Table 3. (Continued).

Patients	Method	Sen	D (AVG±SDx10^{-4})	H_d	Spe	Time (s)
Patient 17 (BRATS 2013)	GAC	0.5269 ±0.4	0.5252 ±0.3	6.4807 ±0.0	0.9945 ±1.4	38.9236 ±8.6
	LAC	0.6864 ±0.4	0.7052 ±0.3	3.7417 ±0.0	0.9958 ±2.2	13.6119 ±0.8
	ACCS	0.9007 ±2.1	0.9111 ±2.8	3.5781 ±5.5	0.9973 ±2.2	34.2876 ±2.2
	OSH-ACM	0.9839 ±0.1	0.9712 ±0.0	2.1024 ±1.0	0.9987 ±0.7	0.2165 ±2.4
	Proposed	0.9902 ±4.2	0.9890 ±0.8	2.1000 ±3.0	0.9997 ±1.9	0.1990 ±8.7
Patient 18 (BRATS 2013)	GAC	0.5748 ±2.3	0.5180 ±7.5	6.7727 ±2.0	0.9910 ±4.5	44.1824 ±5.9
	LAC	0.8753 ±0.0	0.8935 ±1.7	3.9990 ±0.1	0.9928 ±6.3	15.1849 ±7.4
	ACCS	0.9018 ±3.7	0.9124 ±8.6	3.3179 ±2.4	0.9979 ±5.8	38.7530 ±0.2
	OSH-ACM	0.9850 ±0.1	0.9760 ±0.0	2.0361 ±0.0	0.9987 ±2.4	0.1834 ±0.5
	Proposed	0.9902 ±4.2	0.9801 ±2.0	2.0254 ±0.0	0.9996 ±2.0	0.1664 ±0.1
Patient 19 (BRATS 2013)	GAC	0.7629 ±0.0	0.7655 ±0.1	3.2361 ±1.0	0.9986 ±6.7	20.4650 ±0.4
	LAC	0.7279 ±0.2	0.6910 ±0.0	4.8759 ±0.2	0.9984 ±0.8	6.3258 ±8.4
	ACCS	0.8974 ±4.7	0.9046 ±2.7	3.7000 ±0.0	0.9990 ±0.2	33.4758 ±0.4
	OSH-ACM	0.9815 ±1.3	0.9720 ±0.4	2.0730 ±1.0	1.0000 ±0.0	0.2100 ±0.0
	Proposed	0.9900 ±8.0	0.9924 ±8.1	2.0345 ±5.0	1.0000 ±0.0	0.1600 ±0.0
Patient 20 (BRATS 2013)	GAC	0.8193 ±0.0	0.9007 ±0.0	3.6458 ±1.0	0.9980 ±3.4	11.2779 ±4.9
	LAC	0.8467 ±0.0	0.9170 ±0.0	3.0458 ±1.6	0.9985 ±9.7	3.2656 ±5.3
	ACCS	0.9544 ±2.4	0.9590 ±2.4	3.0001 ±9.7	0.9995 ±2.4	27.2486 ±0.4
	OSH-ACM	0.9779 ±1.0	0.9823 ±0.4	2.0475 ±0.2	0.9997 ±3.1	0.1547 ±3.2
	Proposed	0.9800 ±2.0	0.989192 ±8.2	2.0362 ±4.1	0.9997 ±0.0	0.1377 ±8.2

4. Conclusions

In this paper, we enhance our previous research [1] in terms of acquisition speed, precision, and data size. The proposed method detects the brain tumor's position using two parameters (L, c) returned by the GOSH technique. The underlying physics behind the obtained results (Tables 2 and 3) is the fast computation of the extraction of In-phase components' peaks maximums in the MR image. Besides, this approach's main advantage is the short computation time, the automaticity, and the reliable precision of segmentation. Hence, we have reached a principal aim to move the active contour theory from semi-automatic to automatic status by the reliable detection of Brain tumors by the Generalised Optical Scanning Holography (GOSH).

Acknowledgements

The authors would like to express thankfulness to Professor Ivan Cabria, Departamento de FsicaTerica, Universidad de Valladolid, Valladolid, Spain, for the details about the source code of his work on the Potential Field Segmentation algorithm. Further, the Authors thank Raphael Meier, Medical Image Analysis Institute for Surgical Technology and Biomechanics, University of Bern, Switzerland, for providing access to the BRATS database.

References

[1]. A. Essadike, E. Ouabida, A. Bouzid, Optical scanning holography for tumor extraction from brain magnetic resonance images, *Optics & Laser Technology*, Vol. 127, 2020, 106158.

[2]. S. Dou, X. Shen, B. Zhou, L. Wang, C. Lin, Experimental research on optical image encryption system based on joint Fresnel transform correlator, *Optics & Laser Technology*, Vol. 112, 2019, pp. 56-64.

[3]. E. Ouabida, A. Essadike, A. Bouzid, Automated segmentation of ophthalmological images by an optical based approach for early detection of eye tumor growing, *Physica Medica*, Vol. 48, 2018, pp. 37-46.

[4]. J. Chaki, Brain Tumor MRI Image Segmentation Using Deep Learning Techniques. *Elsevier*, 2021.

[5]. E. Ouabida, A. Essadike, A. Bouzid, Optical approach for iris segmentation and tracking, in *Proceedings of the 4th IEEE International Colloquium on Information Science and Technology (CiSt'16)*, 2016, pp. 476-480.

[6]. V. K. Asari, M. Nazrul Islam, Special issue on optical image processing, *Optics Laser Technology*, Vol. 57, 2014, pp. 227-229.

[7]. J. E Bugaj, S. I. Achilefu, R. B. Dorshow, R. Rajagopalan, Novel fluorescent contrast agents for optical imaging of in vivo tumors based on a receptor-targeted dye-peptide conjugate platform, *Journal of Biomedical Optics*, Vol. 6, Issue 2, 2001, pp. 122-133.

[8]. P. S. Jorgensen, K. Vels Hansen, R. Larsen, J. R. Bowen, A framework for automatic segmentation in three dimensions of microstructural tomography data, *Ultramicroscopy*, Vol. 110, Issue 3, 2010, pp. 216-228.

[9]. X. Y. Wang, R. Lockwood, M. Malac, H. Furukawa, P. Li, A. Meldrum, Reconstruction and visualization of nanoparticle composites by transmission electron tomography, *Ultramicroscopy*, Vol. 113, 2012, pp. 96-105.

[10]. J. Amorim, B. Mendes, E. Ribau, M. Gouvêa, S. Sarmento, Image processing as a potential tool for CT dose optimization, *Physica Medica*, Vol. 32, 2016, 316.

[11]. D. Roldan, C. Redenbach, K. Schladitz, M. Klingele, M. Godehardt, Reconstructing porous structures from _b-sem image data, Optimizing sampling scheme and image processing, *Ultramicroscopy*, Vol. 226, 2021, 113291.

[12]. Y. Kawata, H. Arimura, K. Ikushima, Z. Jin, K. Morita, C. Tokunaga, H. Yabu-Uchi, Y. Shioyama, T. Sasaki, H. Honda, et al., Impact of pixel-based machine-learning techniques on automated frameworks for delineation of gross tumor volume

regions for stereotactic body radiation therapy, *Physica Medica*, Vol. 42, 2017, pp. 141-149.

[13]. M. A. Mahjoub, G. Monier, L. Bideux, B. Gruzza, C. Robert-Goumet, Multi-mode elastic peak electron microscopy (mm-epem): A new imaging technique with an ultimate in-depth resolution for surface analysis, *Ultramicroscopy*, Vol. 188, 2018, pp. 13-18.

[14]. B. Wu, M. Alrubaiee, S. K. Gayen, Time reversal optical tomography: Detecting and locating tumors in an ex vivo model human breast, *Optics & Laser Technology*, Vol. 77, 2016, pp. 229-235.

[15]. Z. Chen, D. Li, H. Shen, H. Mo, Z. Zeng, H. Wei, Automated segmentation of UID regions in optical coherence tomography b-scan images of age-related macular degeneration, *Optics & Laser Technology*, Vol. 122, 2020, 105830.

[16]. A. Essadike, E. Ouabida, A. Bouzid, Brain tumor segmentation with Vander Lugt correlator based active contour, *Computer Methods and Programs in Biomedicine*, Vol. 160, 2018, pp. 103-117.

[17]. T.-C. Poon, Scanning holography and two-dimensional image processing by acoustooptic two-pupil synthesis, *JOSA A*, Vol. 2, Issue 4, 1985, pp. 521-527.

[18]. T.-C. Poon, M. H. Wu, K. Shinoda, Y. Suzuki, Optical scanning holography, *Proceedings of the IEEE*, Vol. 84, Issue 5, 1996, pp. 753-764.

[19]. T.-C. Poon, R. Juday, T. Hara, Spatial light modulators research, development, and applications: Introduction to the feature issue, *Applied Optics*, Vol. 37, Issue 32, 1998, pp. 7471-7471.

[20]. T.-C. Poon, P. P. Banerjee, Contemporary Optical Image Processing with MATLAB, *Elsevier*, 2001.

[21]. I. Yamaguchi, Phase-shifting digital holography, in Digital Holography and Three-Dimensional Display, *Springer*, 2006, pp. 145-171.

[22]. T.-C. Poon, Optical scanning holography-a review of recent progress, *Journal of the Optical Society of Korea*, Vol. 13, Issue 4, 2009, pp. 406-415.

[23]. T.-C. Poon, G. Indebetouw, Three-dimensional point spread functions of an optical heterodyne scanning image processor, *Applied Optics*, Vol. 42, Issue 8, 2003, pp. 1485-1492.

[24]. T.-C. Poon, Recent progress in optical scanning holography, *Journal of Holography and Speckle*, Vol. 1, Issue 1, 2004, pp. 6-25.

[25]. T.-C. Poon, Optical Scanning Holography with MATLAB, Vol. 21, *Springer*, 2007.

[26]. T.-C. Poon, On the fundamentals of optical scanning holography, *American Journal of Physics*, Vol. 76, Issue 8, 2008, pp. 738-745.

[27]. P. P. Banerjee, D. Cao, T.-C. Poon, Basic image-processing operations by use of acousto-optics, *Applied Optics*, Vol. 36, Issue 14, 1997, pp. 3086-3089.

[28]. M. Kistler, S. Bonaretti, M. Pfahrer, R. Niklaus, P. Bûchler, The virtual skeleton database: An open access repository for biomedical research and collaboration, *Journal of Medical Internet Research*, Vol. 15, Issue 11, 2013, e245.

[29]. I. Cabria, I. Gondra, MRI segmentation fusion for brain tumor detection, *Information Fusion*, Vol. 36, 2017, pp. 1-9.

[30]. V. Caselles, R. Kimmel, G. Sapiro, Geodesic active contours, *International Journal of Computer Vision*, Vol. 22, Issue 1, 1997, pp. 61-79.

[31]. E. Ilunga-Mbuyamba, J. G. Avina-Cervantes, A. Garcia-Perez, R. de Jesus Romero-Troncoso, H. Aguirre-Ramos, I. Cruz-Aceves, C. Chalopin, Localized active contour model with background intensity compensation applied on automatic MR brain tumor segmentation, *Neurocomputing*, Vol. 220, 2017, pp. 84-97.

[32]. E. Ilunga-Mbuyamba, J. M. Cruz-Duarte, J. G. Avina-Cervantes, C. R. Correa-Cely, D. Lindner, C. Chalopin, Active contours driven by cuckoo search strategy for brain tumour images segmentation, *Expert Systems with Applications*, Vol. 56, 2016, pp. 59-68.

(2798)

Speckle-learned Orbital Angular Momentum De-multiplexing

Trishita Das, Manas Ranjan Pandit, Purnesh Singh Badavath and Vijay Kumar
Department of Physics, National Institute of Technology Warangal, Telangana-506004, India
E-mail: tdph20150@student.nitw.ac.in, vijay@nitw.ac.in

Summary: Orbital Angular Momentum (OAM) multiplexing is a promising technique for enhancing optical communication capacity. Here we present a deep learning model to demultiplex the encoded OAM superposition modes using their corresponding speckle patterns. We employed a speckle-learned demultiplexing technique to accurately recognize the encoded OAM modes. A Convolutional Neural Network (CNN) is trained to recognize superimposed Laguree-Gaussian modes through their far-field intensity speckle patterns. Our approach allows for accurate recognition of encoded OAM modes through speckle-learned classification. The trained CNN achieved a classification accuracy of > 99 % in reconstructing a 4-bit grey image of 100×100 pixels.

Keywords: Orbital Angular Momentum, Laguerre-Gaussian beam, Speckle patterns, Deep Learning, CNN.

1. Introduction

The OAM beams with helical phase-front can increase the information-carrying capacity of communication channel links. OAM beams introduce a new degree of freedom to encode information in free space optical (FSO) communication [1]. Each beam serves as a distinct channel carrier due to the orthogonality between OAM beams of a different order. The traditional machine learning methods utilizing the direct mode intensity images are very sensitive to alignment and need to capture the whole mode for their classification making it challenging to accurately identify the original modes and decode the encoded information [2]. Using the far-field speckle patterns, the OAM modes can be easily classified as it is more stable and robust to noise and alignment [3-7].

This paper uses Laguerre-Gaussian ($LG_{m,l}$) modes as the OAM beams and exploits their far-field speckle patterns for efficient classification. Our research focuses on the development of a speckle-learned demultiplexing technique for OAM modes, leveraging a well-trained Convolutional Neural Network to accurately decode the speckle encoded information. We demonstrated the information encoded and decoded for a 4-bit grey-level image using multiplexed Laguerre-Gaussian modes (with $p = 0$ and $l = 1 - 4$) for increased capacity and information-carrying potential in optical communication.

2. Concept and Methodology

The Laguerre- Gaussian beams are the solutions to the paraxial Helmholtz equation in the cylindrical coordinates system. The mathematical expression of the $LG_{m,l}$ beams is given by,

$$LG_{m,l}(r,\phi,z) = A_{l,m}\left[\frac{W_0}{W(z)}\right]\left(\frac{\rho}{W(z)}\right)^{l} L_m^l\left(\frac{2\rho^2}{W^2(z)}\right)\exp\left(-\frac{\rho^2}{W^2(z)}\right)\times \\ \times \exp\left[-ikz - ik\frac{\rho^2}{2R(z)} \mp il\phi + i(l+2m+1)\zeta(z)\right] \quad (1)$$

Here L_p^l, represent the Laguerre polynomial, p (non-negative integer) is the radial mode index and l (integer) is an azimuthal mode index. The $LG_{m,l}$ beams for $l = 1 - 4$ are superimposed to form a total of sixteen orthogonal beams.

To realize a 4-bit demultiplexing scheme, we had considered only four $LG_{p,}$ beams ($p = 0, l = 1 - 4$ (4 modes) and constructed sixteen superposed beams. A 4-bit grey-level image is encoded in sixteen $LG_{p,}$ superposed beams, where each grey level is assigned to one $LG_{p,}$ superposed beam as shown in Fig. 1. The encoded information is recovered by using the far-field speckle patterns of these beams and feeding them to a trained Convolutional Neural Network (CNN).

The far-field speckle patterns $U(r)$ of the sixteen $LG_{p,}$ superposed beams are generated by multiplying uniformly distributed random phase mask $\phi_R(\boldsymbol{r})$ and performing FFT: $U(r) = \mathcal{F}\{LG(r)e^{i\phi_R}\}$. The intensity images of these speckle patterns $I(\boldsymbol{r}) = U^*(\boldsymbol{r})\,U(\boldsymbol{r})$ are used for developing the deep learning model.

A custom Convolutional Neural Network (CNN) was used for classification, offering greater performance and control as the model could be specifically designed and optimized for the task at hand, while also providing greater privacy. The CNN was designed with five convolutional layers, one flatten layer, and two dense layers. The relu and SoftMax activation functions were used with Adam as the optimizer (learning rate 0.0001).

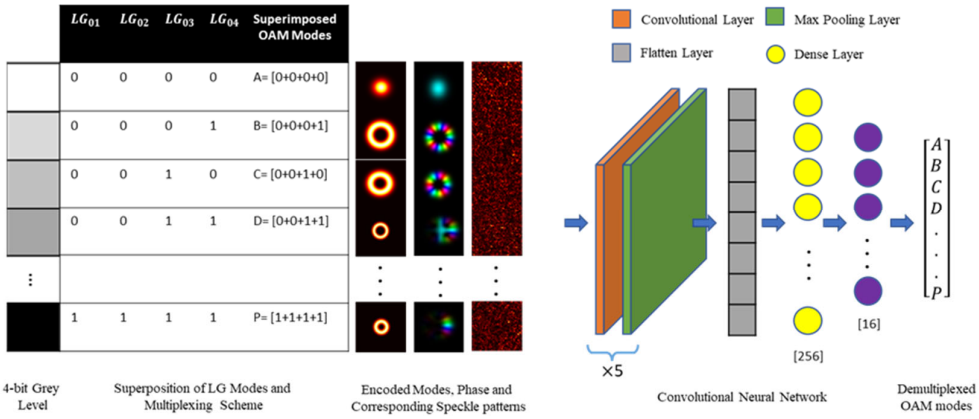

Fig. 1. OAM encoding scheme and speckle-based demultiplexing using CNN.

The designed CNN is trained on a total of 16,000 speckle images, 80 % of the image data was randomly selected for training and validation, and the remaining 20 % for evaluation. The network learned the complex relationships between the input image data and the corresponding LG_p, superposition beams by extracting features of the images in the training set. The trained CNN was then evaluated on the test data, achieving a classification accuracy > 99 %. The Fig. 2. is the confusion matrix showing the true modes vs the predicted modes.

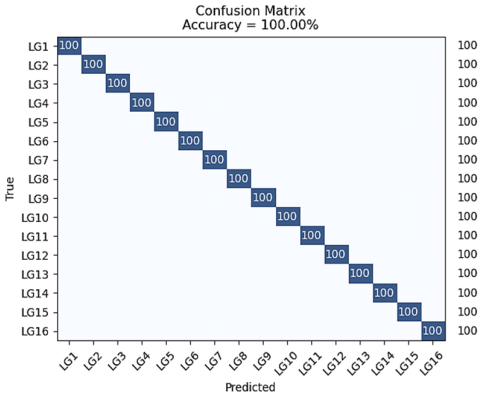

Fig. 2. Confusion matrix of the OAM classification.

4. Conclusion

We have trained a custom build CNN to identify $LG_{p,l}$ superposition beams through their far-field speckle patterns. to implement the concept for its practical application, we have proposed an optical communication link where a 4-bit grayscale image is transmitted through sixteen $LG_{p,l}$ superposition beams and the image can be faithfully reconstructed with the help of trained CNN.

In conclusion, speckle-based learned demultiplexing techniques can also improve the performance of free-space communication systems by enabling the transmission of multiple data channels through a single laser beam, increasing the spectral efficiency of the system and reducing the effects of atmospheric turbulence that can cause signal degradation and loss. The combination of speckle-based demultiplexing and deep learning algorithms has opened up new possibilities for improving the efficiency and reliability of optical communication systems. As research in this area continues to progress, we can expect to see even more advanced and innovative applications of this technology in the future.

References

[1]. J. Wang, J. Liu, S. Li, Y. Zhao, J. Du, L. Long, Orbital angular momentum and beyond in free-space optical communications, *Nanophotonics*, Vol. 11, Issue 4, 2022, pp. 645-680.

[2]. B. Li, H. Luan, K. Li, Q. Chen, W. Meng, K. Cheng, M. Gu, X. Fang, Orbital angular momentum optical communications enhanced by artificial intelligence. *Journal of Optics*, Vol. 24, Issue 9, 2022, 094003.

[3]. V. Raskatla, B. P. Singh, S. Patil, V. Kumar, R. P. Singh, Speckle-based deep learning approach for classification of orbital angular momentum modes, *J. Opt. Soc. of Am. A,* Vol. 39, Issue 4, 2022, pp. 759-765.

[4]. V. Raskatla, B. P. Singh, S. Patil, V. Kumar, R. P. Singh, Speckle-based recognition of OAM modes, *Optics and Photonics News*, Vol. 51, December 2022.

[5]. V. Raskatla, B. P. Singh, V. Kumar, Convolutional networks for speckle-based orbital angular momentum modes classification, *Optical Engineering,* Vol. 61, Issue 3, 2022, 036114.

[6]. V. Raskatla, B. P. Singh, V. Kumar, Speckle-learned convolutional neural network for the recognition of intensity degenerate orbital angular momentum modes, *Optical Engineering*, Vol. 62, Issue 3, 2022, 036104.

[7]. B. P. Singh, V. Raskatla, P. Chakravarthy, V. Kumar, Speckle-based structured light shift-keying for non-line-of-sight optical communication, *App. Opt.*, Vol. 62, Issue 20, 2023 (Accepted).

(2857)

Grating Optic Fiber Sensors Detection of Smart Polymer Composite Delamination

R. Savastru [1], D. Savastru [1], M. I. Rusu [1], M. Tautan, V. Savu [1] and I. I. Lancranjan [1]
[1] National Institute for R&D of Optoelectronics – INOE 2000,
409 Atomistilor St., Magurele, Ilfov, RO-077125, Romania
Tel.: + 40 214575757, fax: + 40 214574522
E-mail: J_J_F_L@yahoo.com, madalin@inoe.ro

Summary: The paper presents the results obtained in simulation of a Smart Composite Polymer Material (SCPM) interfacial failure or delamination detection using a Long Period Grating Fibre Sensor (LPGFS) embedded into polymer matrix and operated directly in a simple transmission setup. The SCPM delamination is analysed using a FEM based cohesive zone model (CZM). The modification of the LPGFS transmission spectrum induced as a delamination collateral effect are observed and used for delamination detection. The LPGFS constitutes the feedback loop of the SCPM to be used in system automatized irreparable failure. The simulation results are compared with experimental ones and a good agreement between the two kinds of data being observed. The paper is pointing to an improved simulation/design method of smart composite polymer materials and their applications in various fields such as aeronautics, industry, medicine and defense.

Keywords: Smart composite polymer material, Optical fibre composite delamination sensor, Long period grating fibre sensor.

1. Introduction

Polymer composite materials have numerous applications in aircraft construction, in industry, in manufacturing parts of the mechanical structures and parts such as pipes used in chemistry, in agriculture and in medical devices. In all these kinds of applications the failure caused by delamination is an important issue to be considered for an improved design of reliable mechanical parts made of polymer composite materials. The main purpose of the paper consists of presenting simulation results obtained with a finite element method (FEM) analysis of smart composite materials based on a grating optic fiber sensor embedded in the polymer matrix of such composite, composite which are used for construction of mechanical structures and parts. The composite material is transformed into a smart one by using the grating optic fiber sensor signal as input into a feedback loop of an automatization system. There were analyzed the short period diffraction grating (Fiber Bragg Grating - FBG) and the long period grating (LPG) versions of the optic fiber sensor. Both grating versions are induced into a single mode (SM) optic fiber by various methods which are briefly characterized. The composite delamination process is analyzed using the cohesive zone model (CZM). CZM implies the traction-separation law that describes the softening in the cohesive zone near the delamination point, zone. In the performed analysis a bilinear traction-separation law in a laminated composite using the layered shell interface (LSI) was used for description of mixed-mode softening and delamination propagation. The simulations were performed considering a composite material plate of 1.5 mm thickness with PVC or PDMS matrix. The grating optic fiber sensor is analyzed as embedded in the polymer matrix being used as stress detector.

A composite plate made of two layers each of 1.5 mm thickness suffers a delamination process. The composite plate has dimensions 50 mm × 75 mm. The delamination initiation and propagation into the investigated composite plate can be noticed.

A Long Period Grating Fiber Sensor (LPGFS) is used to detect the initiation and propagation of the delamination process. LPGFS is composed of a Single Mode optical fiber into which, along length L = 50 mm, a Bragg diffraction grating is created with a 775 μm grating period. In the first stage of the simulation process, the transmission spectrum characterizing the LPGFS was simulated. Absorption bands with peak wavelengths situated at grating Bragg resonance wavelengths can be noticed. The LPGFS use is based on determining the spectral shifts of the absorption spectra. Among the absorption peaks of the LPGFS transmission spectrum it was chosen Mode 6 which has the peak Bragg resonance wavelength is situated at λ_{res} = 1541.95 nm. Mode 6 was chosen because its λ_{res} is placed near the middle of the LPGFS interrogator input spectral domain. The Mode 6 spectral shift appears as a result of bending or stress or induced by the delamination process.

In Figs. 1 and 2 are represented the delamination induced stress and the variation of Mode 6 resonance wave length spectral shift versus the delamination induced stress.

In Figs. 3 and 4 are represented the interface health associated stress and the variation of Mode 6 resonance wave length spectral shift versus health associated stress.

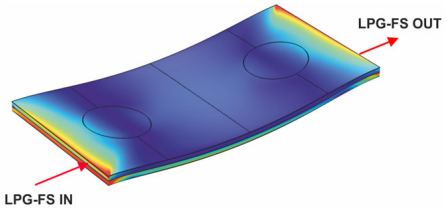

Fig. 1. Representation of Delamination stress.

Fig. 2. Mode 6 resonance wavelength spectral shift vs delamination induced stress.

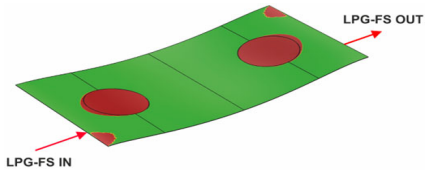

Fig. 3. Representation of interface health.

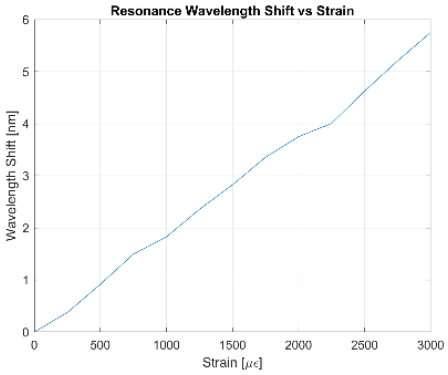

Fig. 4. Mode 6 resonance wavelength spectral shift vs interface health associated stress.

In Figs. 5 and 6 are represented the adhesive stress and the variation of Mode 6 resonance wave length spectral shift versus health associated stress. The table example is shown below.

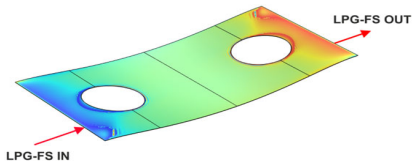

Fig. 5. Example of figure. (maximal possible width for single-column figures is 7.6 cm).

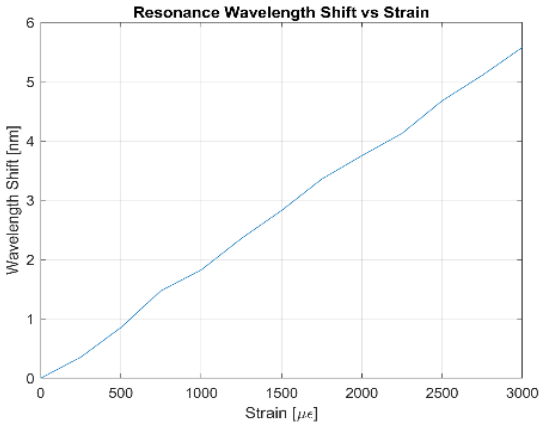

Fig. 6. Mode 6 resonance wavelength spectral shift vs adhesive associated stress.

2. Conclusions

A finite element method analysis of smart composite materials based on an optical fiber grating sensor embedded in the polymer matrix of the smart composite material was developed. These smart composite materials are intended to be used in mechanical structures and parts construction. The composite material is transformed into a smart one by using the optical fiber grating sensor signal as input into a feedback loop of an automatization system. These smart composite materials are intended to be used in mechanical structures and parts construction. The composite material is transformed into a smart one by using the optical fiber grating sensor signal as input into a feedback loop of an automatization system.

Acknowledgements

This work was supported by the Core Program within the National Research Development and Innovation Plan 2022-2027, carried out with the support of MCID, project no. PN 23 05, the Romanian Ministry of Research, Innovation and Digitalization, through Program 1 – Development of the national research-development system, Subprogram 1.2 – Institutional performance – Projects to finance the excellent RDI, Contract no. 18PFE/30.12.2021 and a grant of the Ministry of Research, Innovation and digitalization, CNSC-UEFISCDI, project number PN-III-P4-PCE-2021-0585, within PNCDI III.

References

[1]. A. Mironov, A. Kovalovs, A. Chate, A. Safonovs, Static loads influence on modal properties of the composite cylindrical shells with integrated sensor network, *Sensors*, Vol. 23, Issue 6, 2023, 3327.
[2]. S. W. James, R. P. Tatam, Optical fibre long-period grating sensors: characteristics and application, *Meas. Sci. Technol.*, Vol. 14, 2003, pp. R49-R61.

(2974)

Spectroscopic Characterization of Laser-induced Fluorescence for Environmental Thermometry

H. Mustafa, H. Bartholomeus and L. Kooistra
Laboratory of Geo-Information Science and Remote Sensing, Wageningen University and Research,
6708 PB Wageningen, The Netherlands
E-mail: hasib.mustafa@wur.nl

Summary: Using soft, biodegradable, miniaturized seed-like robots endowed with fluorescence tags, the EU H2020 I-Seed project aims for sustainable environmental monitoring of topsoil and air above soil environments. Reaction with relevant environmental parameters and process of biodegradation will induce a change of fluorescence in the artificial seeds, which will be recorded from an airborne platform with sufficient signal-to-noise ratio to identify the concentration of targeted soil parameters, such as mercury, carbon dioxide, humidity and temperature. Here we present the results of lab-scale spectroscopic characterization to realize an active laser-induced fluorescence system on Unmanned Aerial Vehicle (UAV) platform.

Keywords: Laser-induced fluorescence, Near-infrared laser, Ratiometric spectroscopy, Temporal spectroscopy, Environmental thermometry.

1. Introduction

Plant seeds are one of the significant examples of morphological computation in natural world with optimized features such as, passive take-off, flying, landing, and drilling, to name a few. Taking inspiration from plant seeds' morphology and dispersion capabilities, the EU H2020 I-Seed project aims to develop biodegradable and self-deployable soft miniaturized artificial seeds with fluorescence sensors (termed 'I-Seeds') for monitoring environmental parameters, such as temperature, humidity, carbon dioxide, and mercury in topsoil and the air above soil [1]. Within the project, winged seeds such as Samara (length 4-5 cm, width 1-2 cm) are one of the selected species for biomimicking [2]. Initially, these artificial seeds will be dispersed using UAVs, and the seeds will be spread over the target area following their natural-like pathways. The artificial seeds need to be detected and localized in real time for the subsequent activity of read-out of the sensors. For remote read-out of in situ sensor information, an active laser-induced fluorescence observation system onboard UAV will excite the I-Seeds for fluorescence emission that is the function of measured environmental parameters [3].

An airborne active laser-induced fluorescence observation system should be capable of three functions – measurement of fluorescence emission (spectroscopy), localization of the emission in spatial coordinates (geo-localization) and estimation of the altitude of the emission (ranging), as well as needs to meet several requirements in terms of weight, resolution, and SNR. Lab-scale design can adapt to various design requirements. Generally, characterization of various biotic and abiotic components of the environment is tested in the lab to assess the efficacy of the detection system [4-7]. Here, we present the lab-scale characterization of artificial seed material that will serve as benchmark for UAV payload construction and measurement.

2. Experimental Setup

Lab scale experiments were carried out using commercially available off-the-shelf (COTS) products including a continuous-wave near-infrared diode laser, read-out optics, back-thinned CCD spectrometer, progressive scan CCD cameras, Avalanche photodiodes and air-to-plate heat pump assembly. The samples were PolyLactic Acid (PLA) polymer discs embedded with fluorescencing lanthanide particles. The schematic of experimental setup is shown in Fig. 1.

The laser beam was line-shaped having a Gaussian intensity profile along the fast and slow axis (divergence 6.4 and 0.2 mrad respectively). A half wave plate (HWP) along with a polarizing beam splitter (PBS) cube was used to control the output power of the laser, as well as to polarize the randomly polarized beam linearly with an extinction ratio of 13.7 dB. A pyroelectric detector was used to measure the average laser power after the beam passed through the HWP-PBS arrangement with an error less than 5 %.

The samples were PolyLactic Acid (PLA) polymer discs embedded with fluorescencing lanthanide particles (15 wt%), having a diameter of 1.7 cm and a thickness of 2.5 cm. The samples were placed at varying distances up to 4 m from the laser source and the beam was directed perpendicular to the sample surface. The samples were irradiated at controlled room temperature (21 ± 1 °C), as well as at temperatures of 5 ± 1 °C and 40 ± 1 °C to account for the probable temperature variation range in the agricultural fields or representative outside environment/conditions. For controlling the sample

temperature above or below the room temperature, the samples were placed on an air to plate heat pump assembly using clamping arms. The luminescence lifetime was analyzed by modulating the laser source using a function generator, and recording the filtered luminescence response using a Si-APD photodiode. The spectrographs and the RGB images were recorded using a CCD spectrometer and camera respectively. The integration and exposure time was adjusted as per the requirements of the experiments.

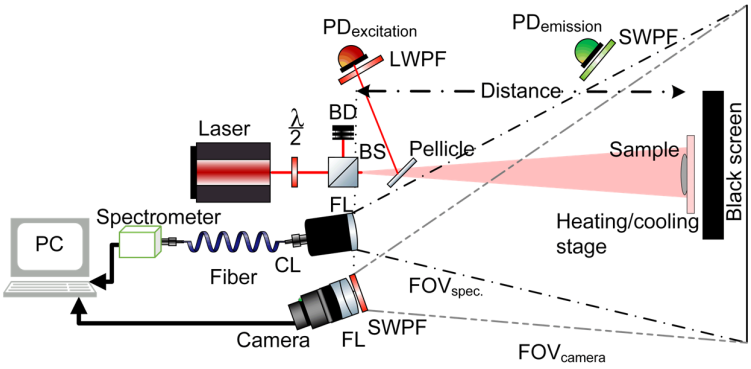

Fig. 1. Schematic of experimental setup (BS – beam splitter, BD – beam dump, CL- collimating lens, FL – focusing lens, FOV – field-of-view, SWPF – shortwave pass filter, LWPF – longwave pass filter, PD -photodiode).

3. Results

The fluorescence emission from the samples were measured at a distance of 4 m for varying excitation intensities at an integration time of 3 s and temperatures ranging from 5 to 40 C. With increasing sample temperature, the ratio of peaks changes, and therefore, can be utilized to sense temperature of the sample (see Fig. 2(a)). Similar behavior can also be observed for modulated excitation, where the fluorescence lifetime changes with temperature (see Fig. 2(b)).

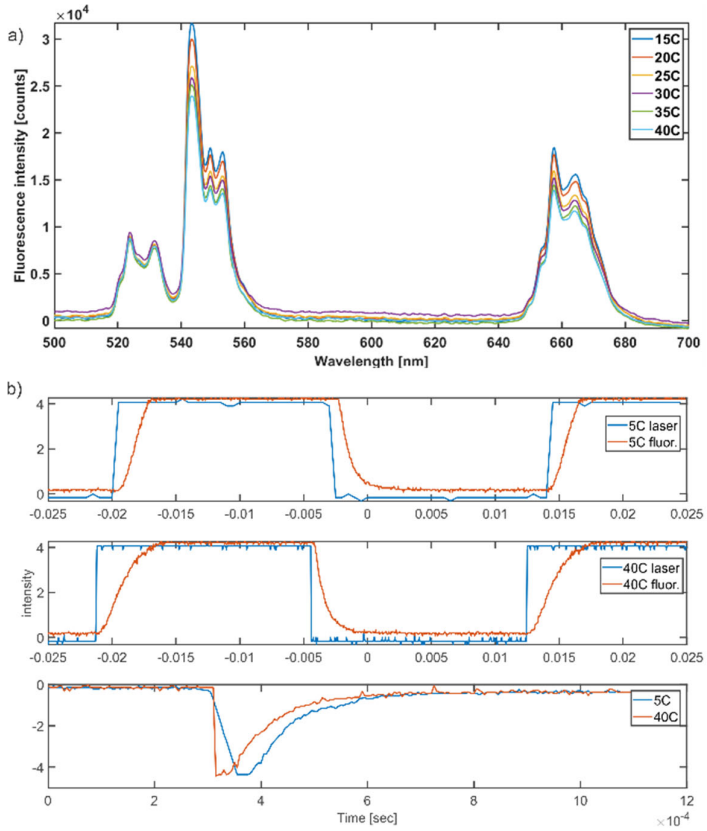

Fig. 2. (a) change in spectra of fluoresceing samples with sample temperature at a distance of 4 m for an excitation laser power of 2.8 W; (b) lifetime of fluorescence response at different sample temperature.

Along with spectroscopy, imaging of the sample was carried out from a distance of 4 m to assess the capabilities of localization from RGB imagery during laser excitation. This ensures the precise positioning of the samples in the ground during optical read-out, which may get shifted by wind or animals. Within the limits of exposure time for non-saturated pixels, 8-bit RAW data of R, G, and B pixels provides some insight on the sample temperature as well (see Fig. 3).

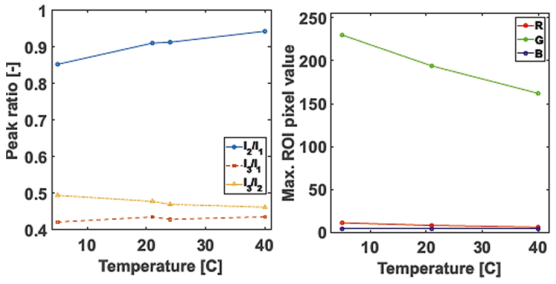

Fig. 3. Ratio of spectral peaks (left) and maximum intensity of R, G, and B pixels from RAW8 image (right) as a function of sample temperature.

4. Conclusions

In context to the I-Seed scenario, quantification of the emitted fluorescence signal strength from I-Seeds is important as it indicates the concentration or level of monitored environmental parameter. Several factors can affect the system's signal-to-noise ratio (SNR), and thereby, the actual development of the system will start from a laboratory-based setup to achieve a complete understanding of the level of influence of these parameters for real-world field applications. We demonstrated the read-out of stable signal with good SNR up to a distance of 4 m in controlled condition. Critical environmental conditions and sample behavior were assessed to evaluate their effect on signal read-out. Proof of principle for temperature read-out using both ratiometric and temporal approach have been realized. Development of lightweight prototype for field testing is well under way, followed by the miniaturization for UAV deployment.

Acknowledgements

This project has received funding from the European Union's Horizon 2020 research and innovation programme under grant agreement No 101017940. The content of this publication is the sole responsibility of the authors. The Commission cannot be held responsible for any use that may be made of the information it contains.

References

[1]. B. Mazzolai, T. Kraus, N. Pirrone, L. Kooistra, A. De Simone, A. Cottin, L. Margheri, Towards new frontiers for distributed environmental monitoring based on an ecosystem of plant seed-like soft robots, in *Proceedings of the Conference on Information Technology for Social Good (GoodIT'21)*, Rome, Italy, 9-11 September 2021, pp. 221-224.

[2]. G. K. Nave Jr., N. Hall, K. Somers, B. Davis, H. Gruszewski, C. Powers, M. Collver, D. G. Schmale III, S. D. Ross, Wind dispersal of natural and biomimetic maple samaras, *Biomimetics*, Vol. 6, Issue 2, 2021, 23.

[3]. H. Mustafa, H. A. Khan, H. Bartholomeus, L. Kooistra, Design of an active laser-induced fluorescence observation system from unmanned aerial vehicles for artificial seed-like structures, *Proceeding of SPIE*, Vol. 12262, 2022, 1226205.

[4]. L. Palombi, D. Alderighi, G. Cecchi, V. Raimondi, G. Toci, D. Lognoli, A fluorescence LIDAR sensor for hyper-spectral time-resolved remote sensing and mapping, *Optics Express*, Vol. 21, Issue 12, 2013, pp. 14736-14746.

[5]. O. Bukin, D. Proschenko, C. Alexey, D. Korovetskiy, I. Bukin, V. Yurchik, I. Sokolova, A. Nadezhkin, New solutions of laser-induced fluorescence for oil pollution monitoring at sea, *Photonics*, Vol. 7, Issue 2, 2020, 36.

[6]. X. Zhao, S. Shi, J. Yang, W. Gong, J. Sun, B. Chen, K. Guo, B. Chen, Active 3D imaging of vegetation based on multi-wavelength fluorescence lidar, *Sensors*, Vol 20, Issue 3, 2020, 935.

[7]. V. N. Lednev, A. F. Bunkin, S. M. Pershin, M. Y. Grishin, D. G. Artemova, V. A. Zavozin, P. A. Sdvizhenskii, R. A. Nunes, remote laser induced fluorescence of soils and rocks, *Photonics*, Vol. 8, Issue 10, 2021, 411.

(2987)

A Multiwavelength Vacuum Environment Laser Calorimetry System

Can Gözönünde, Semih Yurtseven, Damla Şendoğdu,
Humbat Nasibov * and Ramiz Hamid
[1] National Metrology Institute, The Scientific and Technological Research Council of Türkiye
(TÜBİTAK- UME, Ulusal Metroloji Enstitüsü), Gebze, Kocaeli, Türkiye
Tel.: + 902626795000, fax: + 902626795010
E-mail: humbet.nasibli@tubitak.gov.tr, humbat.nasibov@gmail.com

Summary: In the current work, we describe a process of optimizing of a laser calorimeter system to characterize the thermal performance of optical glasses and thin films in a vacuum environment. The system is adapted from its predecessor, working in the atmospheric environment, and adapted for the qualification of space-based optics. The new system is capable of operating in vacuum and atmosphere environments. It can perform optical absorption measurements at five different wavelengths by uncoherent combining of five single-mode continuous-wave lasers working at 461 nm, 532 nm, 640 nm, 1064 nm, and 1070 nm wavelengths. Besides, the experimental setup includes a thermally-isolated chamber, power meter, and NTC sensors, where the sample geometry and thermometer positions can be varied by demand. The measurements are performed according to methods, regulated by ISO-11551 series standards. To control the calorimetry system and the whole measurement procedure, homemade software based on the LabVIEW programming package was developed.

Keywords: Absorption coefficient, Laser calorimetry, Optical absorption, ISO 11551, Space-grade optics.

1. Introduction

The development of high-power laser applications over the last few decades has increased the demand for sensitive optical absorption measurements of optical materials and thin films. Therefore, many sensitive and accurate techniques have been developed for optical absorption measurements. For example, the photothermal common-path interferometer-based methods can reveal the ultra-weak optical absorption coefficient value of about sub-ppm level. However, only laser calorimetry methods for the optical absorption measurements are currently only a laser calorimetry methods for the optical absorption measurements are standardized and described in ISO/DIS 11551 standard [1-3]. Currently, at TUBITAK-UME, in the scope of the ongoing CAS-121N767 project, a laser calorimeter operating in the vacuum environment was developed and verified. This work presents a comparative study of this system with its counterpart working in the atmospheric environment.

2. Brief Description of the Method

A laser calorimetry method determines the optical absorption coefficient of optical components by analyzing the temperature versus time curvature of the material during and after laser irradiation. The homogeneous model described in ISO 11551 makes the following assumptions: (1) the sample is in thermal equilibrium with the environment; (2) thermal energy caused by absorption is distributed uniformly throughout the sample because the sample's thermal conductivity is assumed to be infinite [3, 4]:

$$\dot{\vartheta} = \frac{\alpha d P}{m c_p} - \gamma\vartheta \Rightarrow \vartheta\left(T_{sample} - T_{enviroment}\right) \qquad (1)$$

where P is the laser power, α is the absorption coefficient, m is the mass, c_p is the specific heat capacity under constant pressure, d is the thickness of the sample and γ is the temperature loss coefficient, which is known from previous measurements or can be calculated from the below equation:

$$\gamma = \frac{h}{m\, c_p} * 2\pi r\,(r + d) \qquad (2)$$

where h is the heat loss coefficient, r is the radius of the sample. The solution of equation (1) is as follows:

$$\vartheta(t) = \begin{cases} 0, t < t_0 \\ \dfrac{\alpha d P}{\gamma m c_p}\left(1 - e^{-\gamma(t-t_0)}\right), t_0 < t < t_1 \\ \dfrac{\alpha d P}{\gamma m c_p}\left(e^{-\gamma(t-t_1)} - e^{-\gamma(t-t_0)}\right), t > t_1 \end{cases} \qquad (3)$$

with irradiation occurring between t_0 and t_1.

3. The Design

The design of both calorimeters (working in vacuum and atmospheric environments) is based on the ISO/DIS 11551 standard. A representative block schematic of the systems is shown in Fig. 1.

Both benchmarks consist of a laser system, a power meter to measure the power of the laser, a focusing optical arrangement to focus the laser beam onto a specimen, a couple of contact thermometers, a system for the holding of a sample, and beam dumps. Fig. 2 shows photographs of the developed systems. The

main difference between the two systems is the environment for the sample: a thermally isolated chamber to obtain a high-stable temperature uniformity in an atmospheric environment and a vacuum chamber to perform the measurements in vacuum conditions.

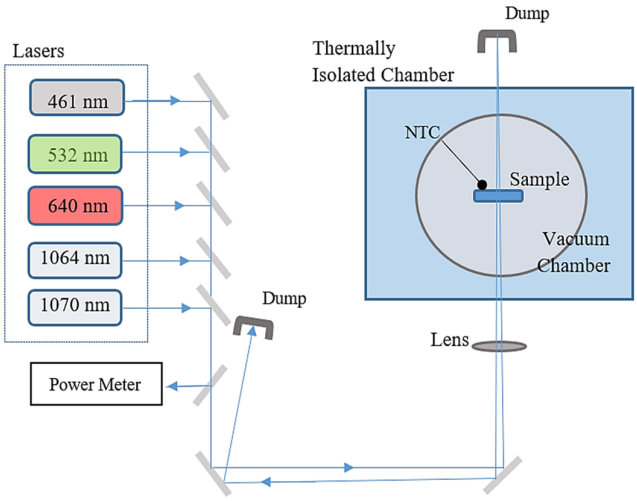

Fig. 1. Schematic diagram of the laser calorimeter.

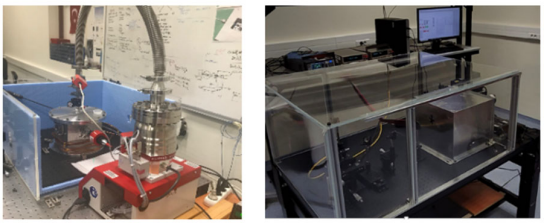

(a) (b)

Fig. 2. Images of the laser calorimeter systems working in (a) vacuum, (b) in atmospheric conditions.

The laser system consists of a set of four single-mode continuous-wave lasers working at 461 nm, 532 nm, 640 nm, 1064 nm, and 1070 nm wavelengths and uncoherent combined by using a set of mirrors. The laser beams are focused onto the surface of the sample with a spot of about 500 μm diameter at $1/e^2$. Special attention was paid to figuring out the chromatic aberration as well as locating the beam spot of different laser lines on the same point on the sample surface.

A couple of high-precision and small-size temperature sensors (thermistors) are used to monitor the sample surface temperature by direct contact with the surface. To reduce possible distortions by scattered radiation and secondary reflections, two pinholes are placed on the optical path on both sides of the holder, as it is shown in Fig. 3.

A special holder is designed and manufactured to hold the sample under test (Fig. 4). Two pieces of thermistors are contacted to the rear side of the sample surface. To increase thermal contact, the thermistors are pressed onto the surface by using PZT controller stage. The other axis of PZT controller stage can change the thermistor positions remotely with a resolution of 0.1 mm. In order to adjust the sample surface with respect to the impinging laser beam, three axis controlling stage is placed on the bottom side.

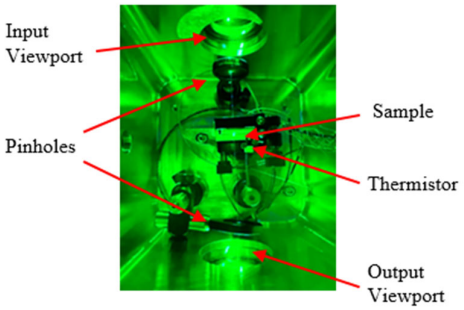

Fig 3. The view of the vacuum chamber inside.

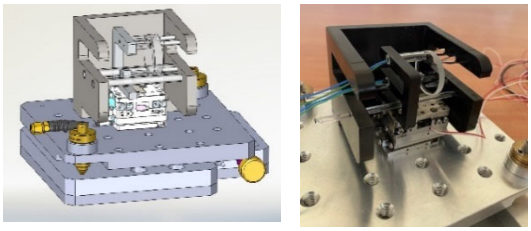

(a) (b)

Fig. 4. (a) SolidWorks drawing, and (b) being manufactured of sample holder.

For effective stabilization of the environmental temperature in the atmospheric measurement setup, an external thermally isolated chamber, whose temperature uniformity is controlled with a specially developed PID temperature control system is used. The greatest temperature drift obtained by these controlling methods is 10 mk/h. The linear temperature drift is calculated from the temperature data before the

irradiation began and it should be extrapolated and subtracted from the whole temperature data. Prior to the irradiation, the temperature data is started to record for several minutes (at least for 60 s).

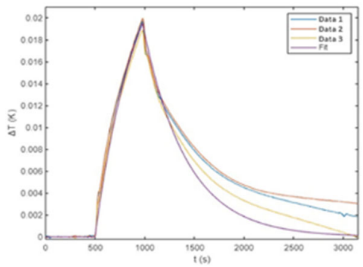

(a)

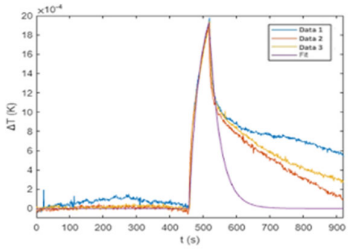

(b)

Fig. 5. (a) 3 Consecutive uncoated Fused silica measurement (R=19 mm, d=6mm) and fit in vacuum environment (330 ppm/cm) (b) 3 Consecutive uncoated Fused silica measurement (R=25.4 mm, d=6 mm) and fit in atmospheric environment (33 ppm/cm).

Each time a sample is inserted or an optical adjustment is made, 3 measurements are made in a row to guarantee measurement consistency. Uncoated Fused silica samples were taken in both an atmospheric and vacuum environment, as shown by the measurement results in Figs. 5a and 5b. A laser with an output of 8.7 W at 1070 nm was used to measure the experiment conducted in an atmosphere, while a laser with an output of 1.5 W at 532 nm was used to measure the experiment conducted in a vacuum. The measurements' repeatability in both situations is around 1 ppm/cm. However, because to the lack of convection, there is a 10-fold difference between the two measurements taken in a vacuum and an atmospheric environment. Utilizing the absolute calibration described in [5] will solve this issue.

4. Evaluation Methods

The temperature data obtained during absorption measurement is analyzed by using two different fitting methods [3, 5].

Exponential Method: In this method, by applying Equation 4 to the heating $(A_h - B_h e^{-c_h t})$ or cooling $(A_c - B_c e^{-C_c t})$ curves, the absorption coefficient was calculated (Fig 6(a)) as follows:

$$\alpha = \frac{A_h\, c_h m\, c_p}{dP}\, \gamma{\sim}c_c \cong c_h \tag{4}$$

Pulse Method: By applying exponential fitting to the cooling curve and extrapolating the fitted function to the half irradiation time (t_p) it is possible to obtain the absorption coefficient (Fig 6(b)):

$$\alpha = \frac{\vartheta_{pulse} c_c\, m\, c_p}{dP}\left(1 - e^{-c_c t_p}\right) e^{\frac{c_c t_p}{2}} \tag{5}$$

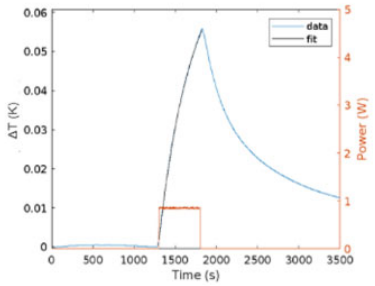

(a)

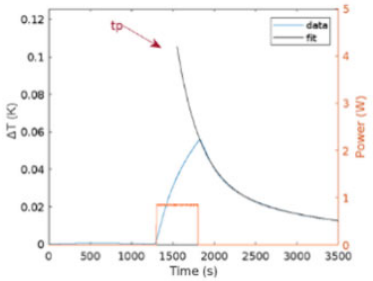

(b)

Fig. 6. An example of (a) the exponential fitting (3020 ppm/cm) (b) the pulse fitting (3061 ppm/cm) for an optical window made from uncoated BK7 glass (R=25.4 mm, d=4 mm).

The pulse method only fits the cooling part of the temperature curve, whereas the exponential method fits both the heating and cooling parts of the temperature curve. However, when applied to the heating curve, the exponential technique typically produces more precise results. The two procedures produced different results, with a difference of about 10 %.

5. Conclusions

Two multi-wavelength laser calorimeters (one working in a vacuum, the other - in an atmospheric environment), capable of assessing the optical absorption of optical components at five different laser lines were developed and tested. Several measurements of different specimens (dielectric and metallic coatings, and uncoated bulk materials (fused silica, HK9, BK7, etc.) were performed in both systems and then compared.

Acknowledgements

This paper has been written through funding received from the TUBİTAK-ARDEB project CAS-121N767

References

[1]. D. J. Gallant, Computer automated laser absorption calorimeter, *Review of Scientific Instruments*, Vol 59, 1988, pp. 2241-2246.

[2]. ISO. Optics and photonics-Lasers and laser-related equipment-Test method for absorptance of optical laser components: ISO 11551: 2019[S]. *ISO*, 2019.

[3]. U. Willamowski, T. Grob, D. Ristau, H. Welling, Calorimetric Measurements of Optical Abs. at 532 nm and 1064 nm according to ISO/FDIS 11551, *SPIE*, Vol. 2817, 2016, pp. 483-494.

[4]. Y. Wang and B. Li, Accurate Temperature model for Absorptance Determination of Optical Components with Laser Calorimetry, *Applied Optics*, Vol. 50, No. 9, 2011, pp. 264-273.

[5]. Y. Willer, L. Hao, I. Balasa and D. Ristau, Calibration Accuracy of Laser Calorimetry for Common Crystal Geometries, in *Proceedings of the SPIE Conference on Laser-Induced Damage in Optical Materials*, Colorado, United States, 24-27 September 2017.

(3382)

Radially Polarized Electromagnetic Wave Focused by a Segment of a Parabolic Mirror

Zerihun T. Godana [1, 2], János Hebling [1, 2, 3] and László Pálfalvi [1, 2]
[1] Institute of Physics, University of Pécs, 7624 Pécs, Hungary
[2] Szentagothai Research Centre, University of Pécs, Pécs 7624, Hungary
[3] MTA-PTE High-Field Terahertz Research Group, Pécs 7624, Hungary
E-mails: godanaze@gamma.ttk.pte.hu, zerihunta@du.edu.et

Summary: A strong longitudinal electric field and a small spot size at the focal point are observed when radially polarized beams are tightly focused using a high numerical aperture parabolic mirror. The longitudinal electric field component can accelerate electrons along the propagation axis at high intensities in the focal region, which opens an application in particle acceleration. In this paper, we present a theoretical calculation of the diffracted vector field focused by a segment of a parabolic mirror with an incident radially polarized electromagnetic waves using the Stratton-Chu integral, a rigorous electromagnetic wave diffraction theory. The derived integral representations accurately describe the diffracted vector field and satisfy Maxwell's equations. The calculation method can be improved for Gaussian beams as well and the model is suitable for multicycle pulses as well.

Keywords: Focusing, Parabolic mirror, Radially polarized beams, Stratton-Chu integral.

1. Introduction

The paraboloid mirror can focus light nearly within a 4π solid angle [1-3]. For high-intensity laser systems, which make a lot of effort to obtain the greatest laser intensities feasible, the investigation of the vector field focusing characteristics is of special interest [4]. By tightly focusing the beam on a vacuum using an off-axis parabolic mirror (OAP), it is possible to obtain this intense laser light, which opens a variety of fascinating possibilities for particle acceleration [5], materials processing, and the study of the basic forces in nature. Beginning with a study by Ignatovsky in 1920, a detailed diffraction theory of focused light from parabolic mirrors has been developed over the period of nearly a century. Richards and Wolf provided another theoretical approach in which strongly focused beams were accurately described [6, 7]. There are different approaches for evaluating tightly focused beams based on the Stratton-Chu formulation of Green's theorem [8], which incorporates both the electric and magnetic fields after substituting values from Maxwell's equations [6, 7]. In 2000, Varga and Török derived a solution to the problem of a linearly polarized electromagnetic wave focused by a parabolic mirror using Stratton-Chu integral by solving a boundary-value problem [6]. When a radially polarized beam is tightly focused, the electromagnetic fields' radial symmetry produces a perfectly symmetric focal spot with a strong longitudinal electric field component centered on the optical axis, reducing the focal region's area. Using a high numerical aperture parabolic mirror with a radially polarized beam is ideal for achieving a small focal spot size, which opens an application in particle acceleration [3]. This paper deals with a theoretical calculation of the diffracted vector field focused by a segment of a parabolic mirror with an incident radially polarized electromagnetic waves using the Stratton-Chu integral. We first derived general formulas for parabolic mirrors, then calculated the field on the parabolic surface, and finally, used this result as a boundary value in the Stratton-Chu integral.

2. General Formulas of the Parabolic Mirror

Consider a parabolic mirror with a focus at the origin O of a Cartesian coordinate system and a rotation axis that coincides with the z-axis, as shown in Fig. 1. The paraboloid equation is given by:

$$z_s = \frac{{x_s}^2 + {y_s}^2}{4f} - f, \tag{1}$$

where x_s, y_s and z_s are points on the paraboloidal surface S and f is the focal length of the parabolic mirror. Let ρ_s is the distance between point S and the focus F. Eq. (1) becomes,

$$\rho_s = z_s + 2f \tag{2}$$

The unit vector inward normal to the paraboloidal surface is written as:

$$\hat{\boldsymbol{n}}(x_s, y_s) = \frac{-\frac{1}{2f}(x_s\hat{e}_x + y_s\hat{e}_y) + \hat{e}_z}{\sqrt{1 + \frac{{x_s}^2 + {y_s}^2}{4f^2}}} \tag{3}$$

Using the spherical coordinate components, $(\rho_s \sin\theta \cos\emptyset\,, \rho_s\, sin\,\theta \sin\emptyset\,, \rho_s \cos\theta)$, Eq. (2) becomes,

$$\rho_s = \frac{2f}{1 - cos\,\theta_s} \tag{4}$$

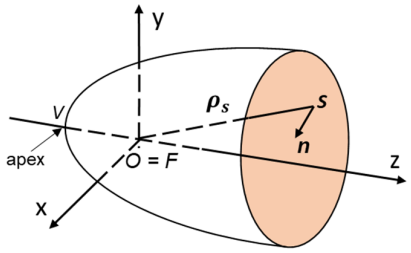

Fig. 1. Schematic diagram for the parabolic mirror.

3. A Rigorous Diffraction Theory to Focus Radially Polarized Waves by a Parabolic Mirror

In this section, we consider how the electric and magnetic field is reflected by the surface of the parabolic mirror. Let us use $\boldsymbol{E}_i$ and $\boldsymbol{H}_i$ to represent the incident electric and magnetic fields, respectively. Based on the electromagnetic boundary conditions, up on reflection the tangential components of the electric field, $\boldsymbol{E}_{r,t}$ and the normal components of the magnetic field, $\boldsymbol{H}_{r,n}$ change sign, but the normal components of the electric field, $\boldsymbol{E}_{r,n}$ and the tangential components of the magnetic field, $\boldsymbol{H}_{r,t}$ remain unchanged [6]. Hence, the reflected fields are written as:

$$\boldsymbol{E}_{r,n} = \boldsymbol{E}_{i,n} = \hat{\boldsymbol{n}}(\boldsymbol{E}_i \cdot \hat{\boldsymbol{n}}), \tag{5}$$

$$\boldsymbol{H}_{r,t} = \boldsymbol{H}_{i,t} = \boldsymbol{H}_i - \boldsymbol{H}_{i,n}, \tag{6}$$

$$\boldsymbol{E}_{r,t} = -\boldsymbol{E}_{i,t} = -\big(\boldsymbol{E}_i - \boldsymbol{E}_{i,n}\big), \tag{7}$$

$$\boldsymbol{H}_{r,n} = -\boldsymbol{H}_{i,n} = -\hat{\boldsymbol{n}}(\boldsymbol{H}_i \cdot \hat{\boldsymbol{n}}), \tag{8}$$

where $\boldsymbol{E}_{i,n}$ and $\boldsymbol{H}_{i,n}$ are the normal components of the incident electric and magnetic fields, respectively. $\boldsymbol{E}_{i,t}$ and $\boldsymbol{H}_{i,t}$ are the tangential components of the incident electric and magnetic fields, respectively.

Therefore, the total reflected fields are expressed as:

$$\boldsymbol{E}_r = \boldsymbol{E}_{r,n} + \boldsymbol{E}_{r,t} = 2\hat{\boldsymbol{n}}(\boldsymbol{E}_i \cdot \hat{\boldsymbol{n}}) - \boldsymbol{E}_i \tag{9}$$

$$\boldsymbol{H}_r = \boldsymbol{H}_{r,n} + \boldsymbol{H}_{r,t} = \boldsymbol{H}_i - 2\hat{\boldsymbol{n}}(\boldsymbol{H}_i \cdot \hat{\boldsymbol{n}}) \tag{10}$$

The total field is given as the sum of the incident and reflected fields:

$$\boldsymbol{E} = \boldsymbol{E}_i + \boldsymbol{E}_r = 2\hat{\boldsymbol{n}}(\boldsymbol{E}_i \cdot \hat{\boldsymbol{n}}), \tag{11}$$

$$\boldsymbol{H} = \boldsymbol{H}_i + \boldsymbol{H}_r = 2\boldsymbol{H}_i - 2\hat{\boldsymbol{n}}(\boldsymbol{H}_i \cdot \hat{\boldsymbol{n}}) \tag{12}$$

Next, we suppose that a surface limited by the apex V and a plane perpendicular to the optical axis form the segment of the paraboloid. The plane is positioned in such a way that $z \le 0$, as shown in Fig. 2. The polar angle α, for which $\pi/2 \le \alpha < \pi$, determines the segment of the paraboloid [6].

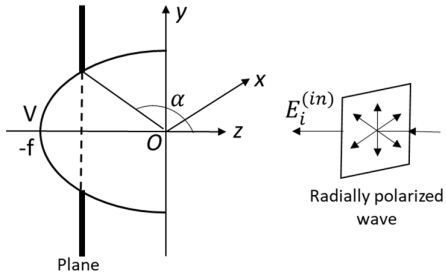

Fig. 2. Schematic diagram for radially polarized waves focused by a segment of the parabolic mirror.

Again, we use the Stratton-Chu integral formula to derive an expression for the vector diffraction electric field focused by a segment of a parabolic mirror [8].

$$\boldsymbol{E}(P) = \frac{1}{4\pi}\oint_S \Big[\begin{matrix} ik(\hat{\boldsymbol{n}} \times \boldsymbol{H})G + \\ +(\hat{\boldsymbol{n}} \times \boldsymbol{E})\nabla G + (\hat{\boldsymbol{n}} \cdot \boldsymbol{E})\nabla G\end{matrix}\Big] dA + \\ + \frac{1}{4\pi ik}\oint_C \nabla G\,(\boldsymbol{H} \cdot d\boldsymbol{s}), \tag{13}$$

with,

$$G(u) = \frac{\exp(iku)}{u}, \tag{14}$$

where, $k = 2\pi/\lambda$ is wave number, λ is the wavelength of the incident beam and u is the distance between a point $S(x_s, y_s, z_s)$ on the surface of the paraboloid and a point $P(x_p, y_p, z_p)$ on the observation plane. Hence,

$$u = \left[(x_s - x_p)^2 + (y_s - y_p)^2 + (z_s - z_p)^2\right]^{1/2} \tag{15}$$

The first integral in Eq. (13) represents the surface integral of a closed surface, whereas the second integral represents the contour integral of a discontinuous surface [8].

The ∇G should be calculated at the point $S(x_s, y_s, z_s)$ on the surface of the paraboloid [6]. The ∇G can be expressed as:

$$\nabla G(u) = ik\left(1 - \frac{1}{iku}\right)\frac{G(u)}{u} \times \\ \times \left(\Delta x\hat{e}_x + \Delta y\hat{e}_y + \Delta z\hat{e}_z\right), \tag{16}$$

where, $(\Delta x, \Delta y, \Delta z) = (x_s - x_p, y_s - y_p, z_s - z_p)$.

The paraboloid surface element dA is given by:

$$dA = \left[1 + \left(\frac{\partial z_S}{\partial x_S}\right)^2 + \left(\frac{\partial z_S}{\partial y_S}\right)^2\right]^{1/2} dx_S dy_S, \\ dA = \frac{{\rho_S}^2}{n_z}\sin\theta_s\, d\theta_s d\emptyset_s \tag{17}$$

To determine the diffracted vector field from a segment of a parabolic mirror, we assume that a radially polarized incident electromagnetic wave

propagates in the negative z direction. Considering cylindrical coordinate system (ρ, ϕ, z), the radially polarized wave has an electric field in the radial direction with respect to propagation axis while magnetic field is aligned in an azimuthal orientation. There are no longitudinal components in the electric and magnetic fields. The incident electromagnetic field can be written as:

$$\boldsymbol{E}_i = \left(\boldsymbol{E}_\rho, \boldsymbol{E}_\emptyset, \boldsymbol{E}_z\right) = \left(\boldsymbol{E}_\rho, 0, 0\right) = aexp(-ikz)\hat{e}_\rho,$$
$$\boldsymbol{H}_i = \left(\boldsymbol{H}_\rho, \boldsymbol{H}_\emptyset, \boldsymbol{H}_z\right) = (0, \boldsymbol{H}_\emptyset, 0) = -aexp(-ikz)\hat{e}_\emptyset,$$

$$\boldsymbol{E}_i = a\exp(-ikz)\left[\cos\emptyset\,\hat{e}_x + \sin\emptyset\,\hat{e}_y\right], \quad (18)$$

$$\boldsymbol{H}_i = a\exp(-ikz)\left[\sin\emptyset\,\hat{e}_x - \cos\emptyset\,\hat{e}_y\right], \quad (19)$$

where, $a = \exp[-i(\pi/2 - kf)]$.

First, we discuss the surface integral for electric field distributions in the Stratton-Chu integral formula in Eq. (10). Using Eqs. (11), (12), (18) and (19), we can write quantities in Eq. (13) as:

$$\hat{\boldsymbol{n}} \times \boldsymbol{H} = 2a\left[\cos\emptyset\,\hat{e}_x + \sin\emptyset\,\hat{e}_y - \left(\frac{n_x}{n_z}\cos\emptyset + \frac{n_y}{n_z}\sin\emptyset\right)\hat{e}_z\right]\exp(-ikz), \quad (20)$$

$$(\hat{\boldsymbol{n}} \times \boldsymbol{E}) = 0, \quad (21)$$

$$\hat{\boldsymbol{n}} \cdot \boldsymbol{E} = 2a\left(n_x\cos\emptyset + n_y\sin\emptyset\right)\exp(-ikz) \quad (22)$$

Substituting Eqs. (2), (14), (16), (17) and (20)-(22) into (13), we obtain the surface integral for the vector diffraction electric field distributions formed by a segment of a parabolic mirror based on the Stratton-Chu integral:

$$\boldsymbol{E}_S(P;\,\alpha,\pi) = a\frac{\exp(2ikf)}{2\pi}ik\int_\alpha^\pi\int_0^{2\pi} d\theta_s\,d\emptyset_s \times \frac{\exp[ik(u-\rho_s)]}{u}{\rho_s}^2\sin\theta_s\left\{\left[\cos\emptyset_s - \tan\left(\frac{\theta_s}{2}\right)\left(1-\frac{1}{iku}\right)\frac{\Delta x}{u}\right]\hat{e}_x + \right.$$
$$\left. + \left[\sin\emptyset_s - \tan\left(\frac{\theta_s}{2}\right)\left(1-\frac{1}{iku}\right)\frac{\Delta y}{u}\right]\hat{e}_y + \tan\left(\frac{\theta_s}{2}\right)\left[1-\left(1-\frac{1}{iku}\right)\frac{\Delta z}{u}\right]\hat{e}_z\right\}, \quad (23)$$

where, $\pi/2 \le \alpha < \pi$.

Eq. (23) is easily evaluated to determine the diffracted electric field from a segment of a parabolic mirror. It matches the boundary condition at the closed surface and perfectly obeys Maxwell's equations.

Next, we discuss the contour integral for electric field distributions in the Stratton-Chu integral formula in Eq. (10). Let the paraboloid be intersected by a plane perpendicular to the optical axis at $z(\delta_s) = \rho(\delta_s)\cos\delta_s$, with $\rho(\delta_s) = 2\mathrm{f}/1 - \cos\delta_s$, follow from Eq. (4). [6]. The radius of the circle formed at the plane-paraboloid intersection is $r = \rho(\delta_s)\sin\delta_s$, and hence the small vector line element for the circumference of a paraboloid is given by:

$$d\boldsymbol{s} = rd\emptyset_s\hat{e}_\emptyset = r\left(-\sin\emptyset_s\,\hat{e}_x + \cos\emptyset_s\,\hat{e}_y\right)d\emptyset_s,$$
$$d\boldsymbol{s} = 2f\tan\left(\frac{\delta_s}{2}\right)\left(-\sin\emptyset_s\,\hat{e}_x + \cos\emptyset_s\,\hat{e}_y\right)d\emptyset_s \quad (24)$$

From Eqs. (12) and (19), the Cartesian coordinate components of the total magnetic field, $\left(H_x, H_y, H_z\right)$ can be written as:

$$H_x = 2a\left[\begin{matrix}(1-n_x^2)\sin\emptyset_s + \\ +n_xn_y\cos\emptyset_s\end{matrix}\right]\exp(-ikz),$$

$$H_y = 2a\left[\begin{matrix}(n_x^2-1)\cos\emptyset_s - \\ -n_xn_y\sin\emptyset_s\end{matrix}\right]\exp(-ikz),$$

$$H_z = 2a\left(\begin{matrix}n_yn_z\cos\emptyset_s - \\ -n_xn_z\sin\emptyset_s\end{matrix}\right)\exp(-ikz),$$

where, from Eq. (3) and the spherical coordinate system $(\rho_s, \delta_s, \emptyset_s)$, the coordinate components of the unit vector normal to paraboloid surface are given by:

$$n_x = -\frac{\sin\delta_s\cos\emptyset_s}{[2(1-\cos\delta_s)]^{1/2}},$$
$$n_y = -\frac{\sin\delta_s\sin\emptyset_s}{[2(1-\cos\delta_s)]^{1/2}}, \quad (25)$$
$$n_z = \left(\frac{1-\cos\delta_s}{2}\right)^{1/2}$$

Thus, the Cartesian coordinate components of the total magnetic field, $\left(H_x, H_y, H_z\right)$ becomes,

$$H_x = 2a\sin\emptyset_s\exp(-ikz), \quad (26)$$

$$H_y = 2a\cos\emptyset_s\exp(-ikz), \quad (27)$$

$$H_z = 0 \quad (28)$$

Using Eqs. (24), (26), (27) and (28), we obtain,

$$\boldsymbol{H} \cdot d\boldsymbol{s} = -4af\tan\left(\frac{\delta_s}{2}\right)\exp(-ikz)d\emptyset_s \quad (29)$$

Substituting Eqs. (14), (16) and (29) into (13), we obtain the contour integral for the vector diffraction electric field distributions formed by a segment of a parabolic mirror based on the Stratton-Chu integral:

$$\boldsymbol{E}_C(P;\,\delta_s) = -\frac{af\exp(2ikf)}{\pi}\tan\left(\frac{\delta_s}{2}\right) \times \int_0^{2\pi}\frac{\exp[ik(u-\rho(\delta_s))]}{u} \times \left(1-\frac{1}{iku}\right)\left(\frac{\Delta x}{u}\hat{e}_x + \frac{\Delta y}{u}\hat{e}_y + \frac{\Delta z}{u}\hat{e}_z\right)d\emptyset_s, \quad (30)$$

where, $\delta_s = \alpha$ is defined by the position of the plane perpendicular to the optical axis intersecting the paraboloid.

Eq. (30) implies that the electric field distributions on a discontinuous surface change in passing across closed contour *C* and obeys Maxwell's equations exactly.

4. Conclusions

Focusing light on a very small spot is an important topic in optical research and applications. A radially polarized beam can achieve smaller focal spot sizes than a linearly polarized beam. Focusing a radially polarized beam with a parabolic mirror is very well suited to achieving minimum focal spot size. In this paper, we used the Stratton-Chu integral formula, a rigorous electromagnetic wave diffraction theory to describe focusing of radially polarized electromagnetic wave by a segment of a parabolic mirror. To determine the diffracted electric field distributions from a segment of a parabolic mirror, we assumed that the plane intersects the paraboloid between the focus and the apex *V* is positioned in such a way that $z \leq 0$, and a radially polarized incident electromagnetic wave propagates in the negative z direction. The derived surface and contour integrals for electric field distributions at closed and discontinuous surfaces, respectively, have been obtained as boundary-value problems from the Stratton-Chu integral. It provides a more accurate description of the diffracted vector field and perfectly obeys Maxwell's equations.

References

[1]. N. Bokor, N. Davidson, 4π focusing with single paraboloid mirror, *Optics Communications,* Vol. 281, Issue 22, 2008, pp. 5499-5503.

[2]. A. April, M. Piché, 4π Focusing of TM 01 beams under nonparaxial conditions, *Optics Express,* Vol. 18, Issue 21, 2010, pp. 22128-22140.

[3]. A. April, P. Bilodeau, M. Piché, Focusing a TM 01 beam with a slightly tilted parabolic mirror, *Optics Express,* Vol. 19, Issue 10, 2011, pp. 9201-9212.

[4]. T. M. Jeong, S. Weber, B. Le Garrec, D. Margarone, T. Mocek, G. Korn, Spatio-temporal modification of femtosecond focal spot under tight focusing condition, *Optics Express,* Vol. 23, Issue 9, 2015, pp. 11641-11656.

[5]. K. Popov, V. Y. Bychenkov, W. Rozmus, R. Sydora, Electron vacuum acceleration by a tightly focused laser pulse, *Physics of Plasmas,* Vol. 15, Issue 1, 2008, 013108.

[6]. P. Varga, P. Török, Focusing of electromagnetic waves by paraboloid mirrors. I. Theory, *JOSA A,* Vol. 17, Issue 11, 2000, pp. 2081-2089.

[7]. X. Zeng, X. Chen, Characterization of tightly focused vector fields formed by off-axis parabolic mirror," *Optics Express,* Vol. 27, Issue 2, 2019, pp. 1179-1198.

[8]. J. A. Stratton, L. Chu, Diffraction theory of electromagnetic waves, *Physical Review,* Vol. 56, Issue 1, 1939, 99.

(3592)

A Facile Route of Manufacturing and Improvement of Plasmonic Nanostructures towards Magnetic Resonance Applications

M. Flimelová [1], Y. V. Ryabchikov [1], N. M. Bulgakova [1] and J. Behrends [2]
[1] HiLASE Centre, Institute of Physics of the Czech Academy of Sciences,
Za Radnicí 828, 25241 Dolní Břežany, Czech Republic
[2] Berlin Joint EPR Lab, Fachbereich Physik, Freie Universität Berlin,
Arnimallee 14, 14195 Berlin, Germany
Tel.: + 420 314 00 77 54
E-mail: flimelova@fzu.cz

Summary: Multicomponent nanostructures consisting of several elements have attracted a broad research interest being served for various aspects in the field of biosensing, catalysis, photovoltaics and biomedicine. Their synthesis by a pulsed laser ablation in a water enables eliminating various side effects originated from chemical contamination. Variable experimental conditions lead to tuning plasmonic and magnetic features influenced by physicochemical reactions during synthesis, thus enhancing their functionality. In this work, we performed synthesis of hybrid AuSi nanoparticles (NPs) with novel modalities by ultrashort laser ablation of bulk gold in water containing silicon NPs. The Au/Si atomic ratio in the nanohybrids was finely varied from 0.5 to 3.5 when changing the initial Si NPs concentration in water from 70 μg/mL to 10 μg/mL respectively. It has been found that the laser-fluence-insensitive silicon content depends on the mass of nanohybrids. A high concentration of paramagnetic defects ($2.2 \cdot 10^{18}$ spin/g) in polycrystalline plasmonic NPs has been achieved. Our findings can open further prospects for plasmonic nanostructures as contrast agents in optical and magnetic resonance imaging techniques, biosensing and cancer theranostics.

Keywords: Ultrashort pulse laser ablation in liquid, Hybrid nanomaterials, Gold-silicon nanoparticles, Plasmonic nanomaterials, Magnetic resonance.

1. Introduction

Plasmonic nanomaterials attract a great research interest in the multifaceted upcoming field of nanomedicine [1, 2]. To improve nanomaterials' functionality, many efforts are made by chemical means for merging plasmonic, magnetic and semiconductor materials in one multifunctional nanoplatform. Combining different elements in a one nanoparticle can easily vary their physicochemical properties in a wide range adjusting their functionality and wide their applications in many fields such as sensor drug delivery, imaging and therapeutic application [3]. Using chemical-based methods for synthesis of NPs can considerably obstruct their applications in biomedical fields due to their contamination by chemical residuals. To overcome the aforementioned issues a versatile method of pulsed laser ablation in liquids is widely employed for the synthesis of multicomponent nanostructures. However, pulsed laser ablation method is still challenging being at the early stage of its development. Nevertheless, laser-synthesized metallic-semiconductor nanocomposites have already shown promising perspectives for molecule detection using surface-enhanced Raman scattering (SERS) or infrared absorption techniques (SEIRA) having tracking features as Raman modality or paramagnetic defect labels at the same time [4].

2. Experimental

Yb:KGW femtosecond (250 fs) laser (Pharos, Light Conversion) operated at 1030 nm wavelength with 1000 Hz repetition rate is used. Laser radiation of (fluence 100 and 150 μJ/pulse) is focused by a galvanoscanner on a solid target surface (162 mm focal distance) into a spot of 50 μm size. Scanning speed of galvanoscanner was 2 m/s within the irradiation area of 10×10 mm^2. To improve the functionality of plasmonic nanoparticles, we employed the PLAL technique by irradiation of a gold target in water-based environment with 30 nm spherical Si NPs whose concentration was varied in the range of 0-70 mg/L. Bare Au NPs were obtained by PLAL without Si NPs while the presence of Si NPs in water led to the formation of hybrid nanostructures. The gold samples placed under 10-mm water level were irradiated for 20 minutes (Fig. 1).

To estimate the size distribution and the chemical composition of the Au-based NPs, a high-resolution transmission electron microscope (HR-TEM) with energy-dispersive X-ray spectrometer (EDX) was used. Prior to the investigation, a drop of a freshly prepared NP suspension was deposited on a carbon-coated copper grid and dried under ambient conditions. The chemical composition of the gold-silicon nanohybrids (AuSi NHs) was studied by inspecting a single isolated nanoparticle of a given size. The nanoparticle size distribution was calculated

by means of the ImageJ software using approximately 1000 particles for each sample. To study the structural properties of the produced nanohybrids, X-ray diffraction (XRD) and X-ray Photoelectron Spectroscopy (XPS) methods were used. An electron paramagnetic resonance (EPR) method was employed to investigate their paramagnetic defect labels with unpaired electrons. Optical properties were studied using a UV-Vis.

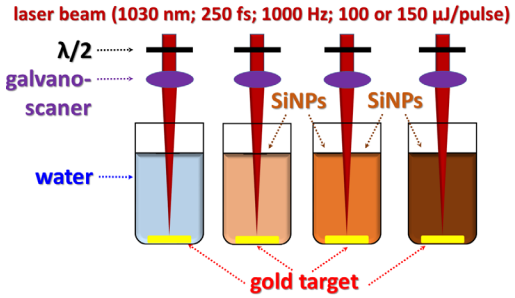

Fig. 1. A scheme of PLAL synthesis of gold-based nanoparticles.

3. Results and Discussion

It was found that a laser impact on metal targets immersed in a colloidal solution of semiconductor nanoparticles provokes considerable changes of their properties. We have found a strong impact of Si NPs suspended in the ablation medium on the size of nearly round-shaped hybrid NPs ranged from several to hundred nanometers. Much more homogeneous size dispersion of hybrid AuSi NPs compared to bare ones was observed.

This treatment also leads to a significant variation of their chemical composition influencing structural and optoelectronic features of NPs. It can be seen that size distribution is significantly reduced compared to that of initial NPs. Bare Au NPs exhibit bimodal size distributions. Their full width at half maximum (FWHM) showed broadening > 30 % when the irradiation energy was increased by 50 %. The presence of two peaks in the size distributions may indicate that different mechanisms of nanoparticles formation upon laser ablation in the case of bare Au NPs. Indeed, hybrid AuSi NPs exhibit only one peak in the size distribution, which is narrower as compared to bare Au NPs. The FWHM is found to be almost fluence-independent for hybrid nanostructures (Fig. 2).

From chemical composition analysis it shows that Large NPs (>25 nm) revealed a major gold contribution (~98 % of mass) independent on the laser fluence. Decreasing the diameter below 25 nm leads to a change of the gold content from 98 % of mass for 25 nm to 63 % of mass for 5 nm of hybrid NPs. The size-dependent chemical composition was not affected by the change of the laser fluence. With increasing the concentration of the Si NPs, the ratio of numbers of gold and silicon atoms (Au/Si ratio) reduces exponentially from 3.5 (10 μg/mL) to 0.5 (70 μg/mL).

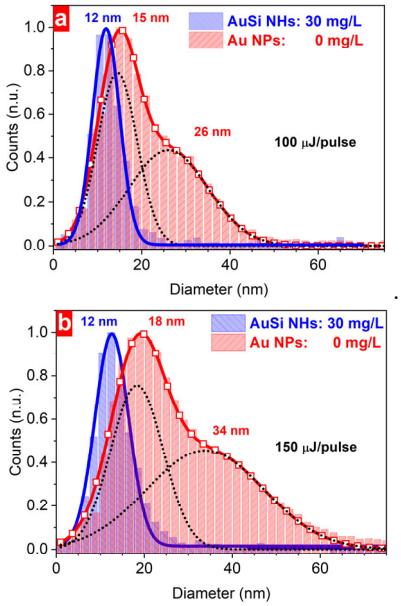

Fig. 2. Size distributions of AuSi hybrid and bare Au NPs formed at laser fluences of 100 μJ/pulse (a) and 150 μJ/pulse (b).

To confirm the combination of gold and silicon modalities in one NP, the nanohybrids were investigated by means of UV-Vis and EPR spectroscopies. Plasmonic response from both hybrid and bare NPs was found, which arises from nanostructured gold. In the absorbance spectrum of AuSi NHs, the plasmonic maximum was 18 nm blue-shifted as compared to bare Au NPs (Fig. 3).

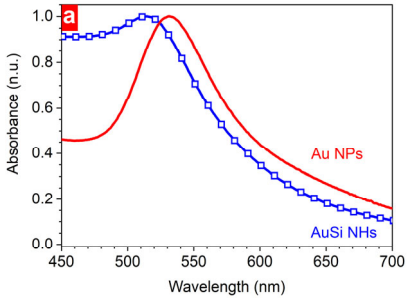

Fig. 3. Absorbance spectra of hybrid and bare NPs.

4. Conclusions

A successful combination of both plasmonic and paramagnetic modalities is achieved in hybrid nanomaterials manufactured by a “green” laser-based technique. Size distribution and chemical content can be controlled by experimental conditions. Our results indicate that the developed method extends the functionality of plasmonic metal nanostructures by laser-induced combination with semiconductor materials, thus allowing their non-invasive tracking by magnetic resonance imaging techniques. We assume that it can provide further significant extensions of the

performance of hybrid metallic-semiconductor nanoparticles by the development of multifunctional nanotools due to their combination with other elements. For instance, laser-induced incorporation of different types of radionuclides (RNs) can add new modalities to la-ser-synthesized nanostructures such as diagnostic and/or therapeutic one by choosing an appropriate type of elements. It can considerably facilitate the formation of radionuclide nanocarriers for nuclear nanomedicine that are currently performed by complexed chemical methods where RNs can play a dual role (both diagnostics and therapeutic), locally detecting or treating a malignant tumor [5].

Acknowledgements

This project was funded by the European Union's Horizon 2020 research and innovation programme under the Marie Skłodowska-Curie grant agreement No 897231 (LADENTHER)., European Regional Development Fund and the state budget of the Czech Republic (Project BIATRI: CZ.02.1.01/ 0.0/0.0/15_003/0000445), the Ministry of Education, and by Freie Universität Berlin within the Excel-lence Initiative of the German Research Foundation (0503121810).

References

[1]. J. K. Lima, S. A. Majetich, Composite magnetic – Plasmonic nanoparticles for biomedicine: Manipulation and imaging, *Nano Today*, Vol. 8, 2013, pp. 98-113.

[2]. A. Shakeri-Zadedh, H. Zareyi, R. Sheervalilou, S. Laurent, H. Ghaznavi, H. Samadin, Gold nanoparticles-mediated bubbles in cancer nanotechnology, *J. Control Release*, Vol. 330, 2021, pp. 49-60.

[3]. T. Chen, L. Su, X. Ge, W. Zhang, Q. Li, X. Zhang, J. Ye, L. Lin, J. Song, H. Yang, Dual activated NIR-II fluorescence and photoacoustic imaging-guided cancer chemo-radiotherapy using hybrid plasmonic-fluorescent assemblies, *Nano Res*., Vol. 13, 2020, pp. 3268-3277.

[4]. O. Bibikova, J. Haas, A.I. López–Lorente, A. Popov, M. Kinnunen, Yu. Ryabchikov, et al., Surface enhanced infrared absorption spectroscopy based on gold nanostars and spherical nanoparticles, *Analytica Chimica Acta*, Vol. 990, 2017, pp. 141-149.

[5]. V. M. Petriev, V. K. Tischenko, A. A. Mikhailovskaya, A. A. Popov, G. Tselikov, I. Zelepukin, S. M. Deyev, A. D. Kaprin, S. Ivanov, Y. V. Timoshenko, P. N. Prasad, I. N. Zavestovskaya, A. V. Kabashin, Nuclear nanomedicine using Si nanoparticles as safe and effective carriers of 188Re radionuclide for cancer therapy, *Sci. Rep*., Vol. 9, 2019, 2017.

(3812)

On the Possibility of Efficient Energy Transfer of Electromagnetic Radiation to Very Thin Wires

N. Kokodii [1], V. Maslov [1], D. Gurina [1], V. Timaniuk [2], S. Pogorelov [2], I. Garyachevskaya [1], M. Dubinin [1] and I. Priz [1]
[1] Karazin Kharkiv National University, 4, Svobody Sq., 61022, Kharkiv, Ukraine
[2] National University of Pharmacy, 53, Pushkinskaya str., 61002, Kharkiv, Ukraine
Tel.: +3 8 (050) 637 54 04
E-mail: kokodiy.n.g@gmail.com

Summary: Very thin conductors, hundreds of times smaller in diameter than the wavelength, can strongly absorb and scatter electromagnetic radiation. The absorption maximum is observed when the diameter of the conductor is approximately 10 times smaller than the wavelength in the substance. In experiments, electromagnetic radiation was directed to a conducting fiber. The absorbed power was determined from the change in the electrical resistance of the fiber. The method for measuring the power absorbed in a fiber has been developed. The absorption coefficient was calculated, which is equal to the ratio of the power absorbed in the fiber to the power in the radiation beam incident on it. Experiments were carried out in the microwave range (wavelength is 8 mm) and infrared range (wavelength is 10.6 μm).

Keywords: Thin fiber, Wire, Microwave range, Infrared range, Absorption, Measuring.

1. Introduction

The action of an electromagnetic wave on a cylindrical target (wire, fiber) depends on the ratio between the wavelength λ and the cylinder diameter *D*. It is usually strongest when the cylinder diameter is comparable to the wavelength. Thin cylinders are usually "not noticed" by the wave. But in [1, 2] it was found that metal wires can absorb electromagnetic radiation very strongly when their diameter is several hundred times smaller than the wavelength. It was found that the effect is observed when the wave is incident on the fiber perpendicular to its axis, and its electric vector is directed along the fiber. Then conditions arise for the excitation of currents in the fiber by the electric field of the wave. Later [3] it was found that the effect also exists when the fiber is located along the axis of the radiation beam, although in this case the electric vector of wave is perpendicular to the fiber axis, and there are no conditions for excitation of currents by the field. This is a new physical effect. It can be used to transfer energy from microwave or laser radiation to small targets without focusing and to create protective screens in the microwave and infrared ranges, when it is necessary to provide strong absorption of radiation in a wide frequency range.

This paper presents the results of measurements of the absorption of microwave and infrared laser radiation in thin conducting fibers.

2. Theory

The action of an electromagnetic wave on an object can be described using scattering efficiency factor

$$Qsca = Psca/P,$$

and absorbing efficiency factor

$$Qabs = Pabs/P,$$

where P is the power of the radiation that hit the object, $Psca$ is the power of the scattered radiation, $Pabs$ is the power of the absorbed radiation. Usually, the values of these factors lie in the range from zero to several units. But for conductors, when their diameter is several hundred times smaller than the wavelength, their values in the microwave and infrared ranges can reach several tens or hundreds. This happens with wire diameters of a few micrometers, that is, for very thin wires.

The absorption coefficient is also significant

$$Kabs = Pabs/P_0,$$

where P_0 is the total power in the radiation beam.

3. Microwave Experiment

The radiation source was a generator with the frequency range of 26-38 GHz. The radiation power was varied in the range from 20 to 40 mW. Waveguide cross section is 7.2×3.4 mm. Wave type is H10. The radiation power was measured by a thermistor receiver with a directional coupler (Fig. 1).

A graphite fiber was located at the distance of several millimeters from the horn. Fiber diameter is 11 μm. The resistance of the fiber changes when radiation is absorbed. It was measured with a digital ohmmeter.

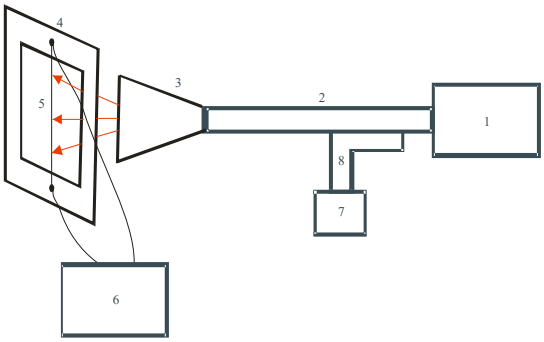

Fig. 1. Block diagram of the experimental setup
1 – generator, 2 – waveguide, 3 – horn, 4 – frame, 5 – fiber, 6 – ohmmeter, 7 – wattmeter, 8 – directional coupler.

The field configuration at the location of the fiber is the same as in the waveguide. Integrating fields over coordinates gives:

$$P_0 = \frac{1}{2} I_0 \, a \, b,$$

where I_0 is the intensity at the maximum, a = 32 mm is the wide wall of the horn, b = 22 mm is the narrow wall.
Radiation intensity at the location of the fiber is

$$I_0 = \frac{2P_0}{ab} \qquad (1)$$

Power is delivered to the fiber

$$P = I_0 D b, \qquad (2)$$

where D is the fiber diameter.

The temperature rise ΔT can be estimated from the change in fiber resistance:

$$\Delta T = \frac{\Delta R}{\alpha_R R_0}, \qquad (3)$$

where R_0 = 4308 Ohm is the initial resistance, ΔR = -1 Ohm is the change in resistance, α_R = -2.11·10^{-4} 1/K is the temperature coefficient of graphite resistance.

The power absorbed in the fiber according to Newton's law for thermal processes is:

$$P_{abs} = \alpha_p L \Delta T \qquad (4)$$

Here L is the fiber length (L = 25 mm), α_P = 0.03 W/(m·K) is the linear coefficient of heat exchange between the wire and the environment.

At the frequency of 29 GHz by the radiation power of 20 mW, the power of 13.8 μW is delivered to the fiber. The temperature rise of the fiber is 1 °C. The absorbed power in the fiber is 743 μW according to formula (4). This is much more than the power that fell on the geometric dimensions of the fiber, as the energy flow lines are bent near the fiber and it is "focused" on the fiber.

Absorption efficiency factor is

$$Q_{abs} = \frac{P_{abs}}{P_{in}} = 53.8 \qquad (5)$$

A plot of the absorption efficiency factor versus frequency is shown in Fig. 2.

The solid line shows the results of the calculation, the dots show the results of the experiment. The agreement between theory and experiment is satisfactory. The experimental values of *Qabs* are somewhat larger than the theoretical ones, but the behavior of the frequency dependence is the same.

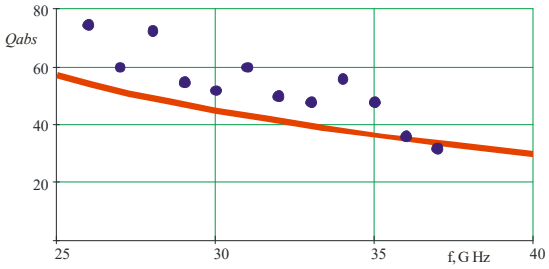

Fig. 2. Frequency dependence of absorption in graphite fiber.

The fiber absorption coefficient of the power incident on it is about 4 %, despite the fact that the fiber area is 3000 times smaller than the beam cross-sectional area, and there are no focusing lenses.

The explanation of the effect is as follows [2]. Strong absorption is observed when the conductor diameter is comparable to the thickness of the skin layer. Then the electric field fills the entire volume of the conductor, and the absorbed power is greater than the power of the radiation that hit the conductor, since the energy flow lines are bent, and the radiation is concentrated on the wire. The absorption maximum is observed when the diameter of the conductor is approximately 10 times smaller than the wavelength in the substance.

4. Laser Experiment

The source of radiation was a CO_2 laser with a wavelength of 10.6 μm. Radiation power is 10 W, beam diameter at the laser output is 3.5 mm, Gaussian beam profile, find linear vertical polarization.

The polarization attenuator *C-MA* served to changes the radiation power. The power was controlled by a *StarLab 2.40* calorimeter. It was exposed to radiation reflected from a *KRS-6 (TlBr-TlCl)* plate.

The laser radiation traveled a path of about 4 m to the focusing lens. A long path is necessary to ensure that a beam with a diameter comparable to the diameter

of the lens. Lens material is *ZnSe*, diameter is 40 mm, focal length is 400 mm. The lens has an antireflection coating.

After the lens, the beam hit the wire. Wires from various metals with diameters from 10 to 50 μm were studied. The wire was placed horizontally along the beam axis so that its middle was in the focal region at a distance of 430 mm from the lens. The wire was placed on two crosses made of nickel wire 100 μm in diameter. The length of the working part of the wire (the distance between the crosses) is 20 mm. Behind the crosspieces on each side there were another 20 mm drags. Its ends are soldered to the contacts, which simultaneously serve to tension the wire.

The wire was placed on a platform that can be moved in three mutually perpendicular directions and rotated in the horizontal and vertical planes. This is necessary in order to position the wire along the axis of the radiation beam. The wire resistance was measured with the *Picotest M3500* multimeter. The signals from the power meter and multimeter were entered into a computer.

At the location of the wire, the beam diameter varied from 0.6 mm along the edges of the region to 0.3 mm in the center of the region.

On Fig. 3 shows the profile of the radiation beam. The curve with noise interference was obtained by scanning the beam cross section. The solid line is the Gaussian function:

$$f(x) = I_0\, e^{-\frac{x^2}{r_0^2}},$$

where $I_0 = 0.135$ is the intensity at the beam center in relative units, $r_0 = 0.11$ mm is the rms beam radius. The horizontal line is drawn at the level I_0/e^2. The beam diameter at this level is 0.3 mm. The beam profile is close to Gaussian.

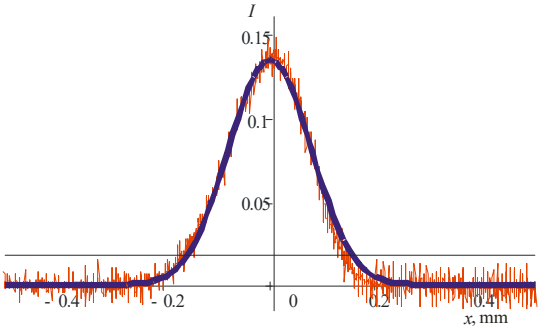

Fig. 3. Beam profile.

5. Processing of Measurement Results

1. The volt-ampere characteristic of the wire was measured. This is the dependence of the current I in it on the applied voltage U. This characteristic for the platinum wire with diameter of 20 μm is shown in Fig. 4. The abscissa shows the voltage values in volts, the ordinate shows the current in amperes. The characteristic is non-linear, since the wire was heated up to several hundred degrees.

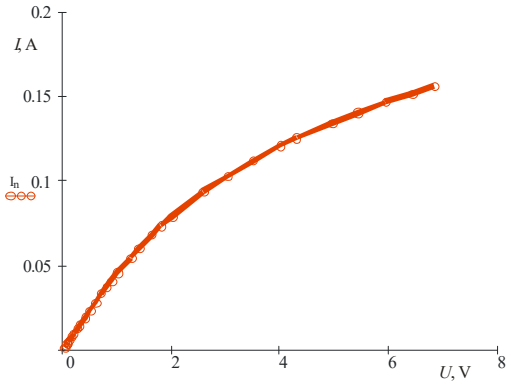

Fig. 4. Volt-ampere characteristics.

2. For each point of the characteristics the absorbed power of the electric current $P_e = U{\cdot}I$ and the corresponding resistance $R = U/I$ were calculated. A calibration curve was built, that is, the dependence $P(R)$ – Fig. 5.

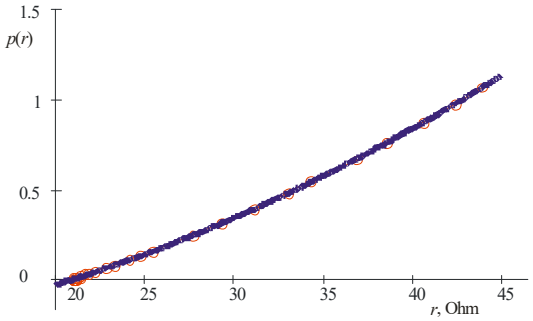

Fig. 5. Calibration curve.

3. Using the least squares method, the analytical dependence of the power p absorbed in the wire on the resistance r was determined. When the wire is strongly heated, this dependence is nonlinear. It is well approximated by a polynomial of the 2nd degree (solid line in Fig. 5):

$$p(r) = 0.000621\, r^2 + 0.00610\, r - 0.398$$

4. The power of radiation absorbed in the wire was calculated by the formula

$$P_{abs} = p(R) - p(R_0),$$

where R_0 is the resistance of the "cold" wire, R is the resistance of the "hot" wire.

5. The radiation absorption coefficient in the wire was determined as follows:

$$K_{abs} = \frac{P_{abs}}{P_0},$$

where P_0 is the power in the radiation beam.

In the experiment with a platinum wire 20 μm in diameter at the beam power of P = 1.62 W, the resistance of the wire increased from R_0 = 21.7 Ω to R = 43.0 Ω. This means that the absorption coefficient is

$$K_{abs} = 0.61$$

That is, 61 % of the energy of the laser radiation incident on wire is absorbed.

The heating temperature of the wire can be estimated using the formula:

$$T = \frac{R - R_0}{\alpha_R R_0} + T_{cp},$$

where α_R = 0.004 deg^{-1} is the temperature coefficient of resistance of platinum, T_{cp} = 20 ºC is the ambient temperature.

The calculations give T = 265 ºC.

Fig. 6 shows the target wire in the laser beam. Part of the wire is heated by radiation to a red color.

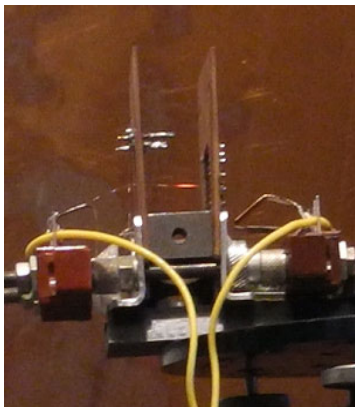

Fig. 6. Target in the laser beam.

The objects of research (targets) were:

1. Platinum wire, D = 20 μm;
2. Platinum wire, D = 50 μm;
3. Nickel wire, D = 40 μm;
4. Nickel wire, D = 50 μm;
5. Copper wire, D = 10 μm;
6. Copper wire, D = 20 μm;
7. Copper wire D = 40 μm.

The results of experiments with these targets are shown in Table 1.

1) Absorption is greater in wires with lower electrical conductivity;

2) In thin wires, absorption is greater than in thick ones.

6. Conclusions

The absorption efficiency factor of thin conductive fibers in the microwave and infrared ranges can be very large – several tens and hundreds.

Table 1. Radiation absorption in targets.

No.	Target	Kabs, %
1	Pt – 20 μm	61
2	Pt – 50 μm	25
3	Ni – 40 μm	40
4	Ni – 50 μm	13
5	Cu – 10 μm	28
6	Cu – 20 μm	7
7	Cu – 50 μm	5

By normal incidence of radiation on the fiber, the effect is observed when the electric wave vector is parallel to the fiber axis.

In the experiment, in the frequency range from 26 to 38 GHz, it varied from 60 to 30.

The effect is also observed when the fiber is located along the axis of the radiation beam.

The absorption coefficient of thin wires located along the CO_2 laser radiation beam ranged from 5 % to 60 %, depending on the diameter and material of the wire.

The effect can be used:

1) To transfer the energy of electromagnetic radiation to thin targets without focusing;
2) To create protective and masking screens in the microwave and infrared ranges.

References

[1]. A. Akhmeteli, N. Kokodii, B. Safronov, V. Balkashin, I. Priz, A. Tarasevich, Efficient non-resonant absorption of electromagnetic radiation in thin cylindrical targets: experimental evidence, *Bulletin of the American Physical Society,* Vol. 60, 2015, 237.

[2]. M. G. Kokodii, A. O. Natarova, A. V. Genzarovskiy, I. O. Priz, Interaction between thin conductive fibers and microwave radiation, *Optical and Quantum Electronics,* Vol. 55, 2023, 256.

[3]. N. G. Kokodii, M. V. Kaidash, V. A. Timaniuk, I. A. Priz, Interaction of electromagnetic radiation with a thin metal wire in the case of a glancing incident wave, *Journal of Communications Technology and Electronics,* Vol. 62, Issue 3, 2017, pp. 205-211.

(3900)

EKSPLA Tunable 1 kHz OPO Systems and Their Application Examples for the Multimodal Photoacoustic Microscopy

G. Kudaba
EKSPLA UAB, 237 Savanorių Av., 2300 Vilnius, Lithuania
Tel.: + 37052649629
E-mail: g.kudaba@ekspla.com

Summary: EKSPLA products were successfully installed for many applications, some of which were specially tailored. One of the examples is high repetition rate optical parametric oscillators (OPOs) with pump lasers and tuning in ultraviolet UV, visible VIS, near-infrared NIR, and middle infrared MIR spectral ranges suitable for photoacoustic, fluorescence and mid-infrared multimodal microscopy applications. The set of output parameters- 1 kHz repetition rate, low jitter synchronization, short laser pulse 3-5 ns, >80 nJ at 580 nm [1], >2 nJ 480 nm, > 80 nJ 532 nm [2] energy; wavelengths 224-250 nm, 3420 nm, 6050 nm, 6600 nm, with the energy 10-100 µJ [3] showed itself as very suitable for the high-resolution photoacoustic, fluorescence and ultraviolet-localized mid-infrared photoacoustic microscopy applications. The new development- 10 kHz NT262 tunable laser brings on even more benefits: better spectral resolution, faster experiment, and lower damage risk of the biological samples, so this higher repetition rate laser has the increased potential of replacing 1 kHz systems.

Keywords: OPO systems, UV, VIS, NIR, MIR wavelength ranges, Photoacoustic PAM, Fluorescence FM and ultraviolet-localized (ULM-PAM) MIR photoacoustic microscopy.

1. Introduction

EKSPLA is recognized worldwide manufacturer of high-performance solid-state Nd:YAG lasers, optical parametrical oscillators, and nonlinear spectroscopy set-ups. EKSPLA had been continuously growing its product portfolio and now is offering standard and specially designed lasers for the spectroscopy and microscopy applications. As confirmed by the "Prism Awards for Photonics Innovation" grant in the 2011 year, one of the most recognized systems are 1 kHz repetition rate OPOs (optical parametric oscillators with pump lasers) with the tuning covering almost any wavelength in ultraviolet UV, visible VIS, near infrared NIR, and middle infrared MIR ranges (Figs. 1-4):

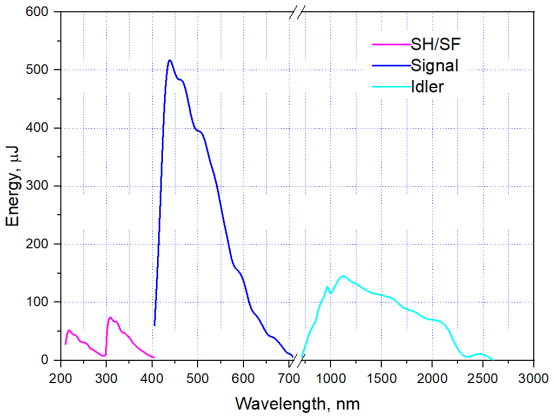

Fig. 1. The typical tuning curves of NT240 laser.

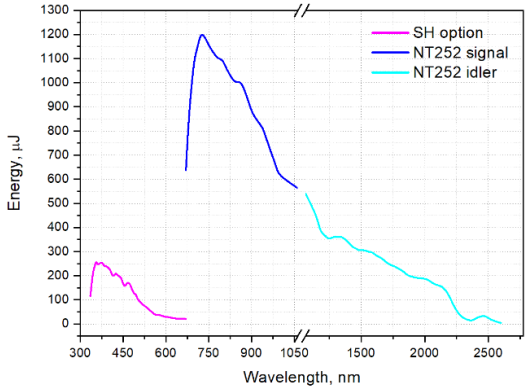

Fig. 2. The typical tuning curves of NT250 laser.

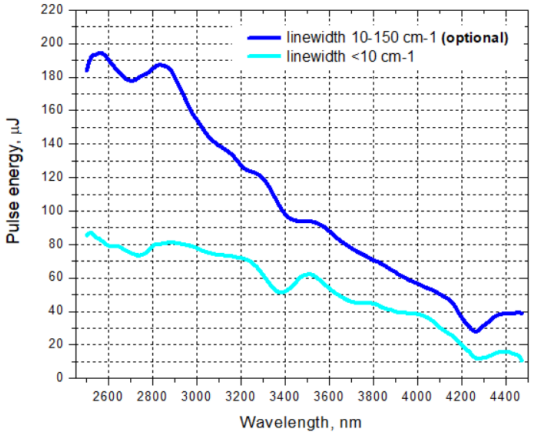

Fig. 3. The typical tuning curves of NT270 laser.

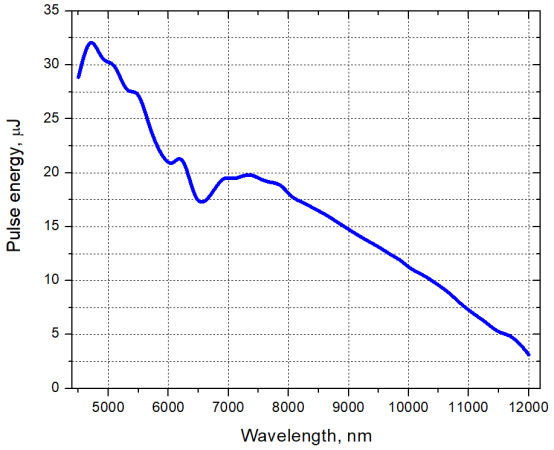

Fig. 4. The typical tuning curves of NT270 laser with XIR extension.

2. Applications

2.1. Multimodal Retinal and Choroidal Imaging System

NT240 series laser (model NT242) was successfully deployed for the multimodality retinal and choroidal imaging system with integrated spectral-domain OCT (SD-OCT), PAM, and fluorescence microscopy (FM) [2], Figs. 5, 6.

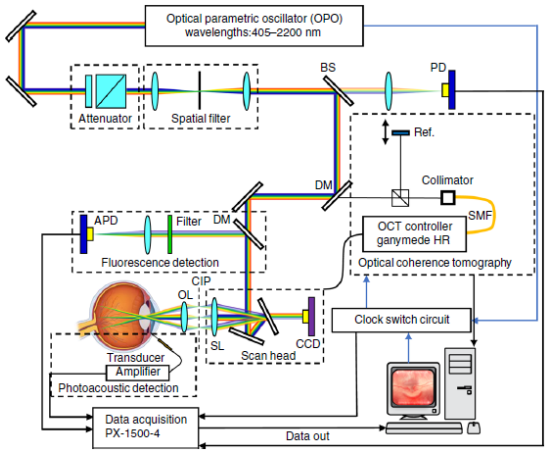

Fig. 5. Schematic of the multimodality retinal and choroidal imaging system. (OPO optical parametric oscillator; SLD super luminescent diode; BS beam splitter; DM dichroic mirror; SL scan lens; OL ophthalmic lens; CIP conjugate image planes [2]. http://creativecommons.org/licenses/by/4.0/ © 2023 Springer Nature Limited

2.2. Ultraviolet – Localized MIR Photoacoustic Microscopy

The combination of NT242 and NT270 lasers showed itself as a perfect tandem for the ultraviolet – localized MIR photoacoustic microscopy (ULM-PAM) [3], Fig. 7.

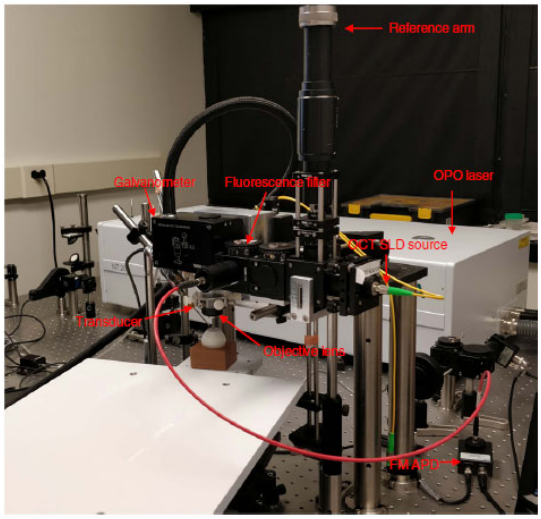

Fig. 6. Photograph of the multimodality retinal and choroidal imaging system [2]. http://creativecommons.org/licenses/by/4.0/, © 2023 Springer Nature Limited.

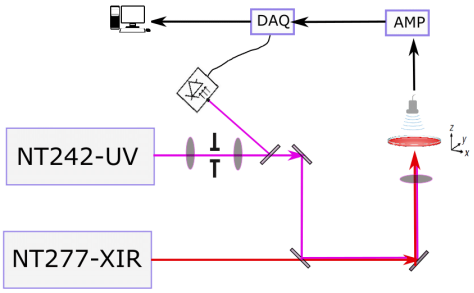

Fig. 7. Mid-infrared imaging of fresh biological samples with ultraviolet localized photoacoustic microscopy [3], simplified layout.

3. Conclusions

The set of output parameters (1 kHz repetition rate, low jitter synchronization, short laser pulse 3-5 ns, >80 nJ at 580 nm [1], >2 nJ 480 nm, > 80 nJ 532 nm [2] energy; wavelengths 224-250 nm, 3420 nm, 6050 nm, 6600 nm, with the energy 10-100 μJ [3]) showed itself as highly suitable for the mentioned above photoacoustic applications.

The new development- 10 kHz NT262 OPO laser- brings on even more benefits:

- Better resolution;
- Faster experiment;
- Lower sample damage risk.

References

[1]. V. P. Nguyen, Y. Li, W. Zhang, X. Wang, Y. M. Paulus, High-resolution multimodal photoacoustic microscopy and optical coherence

tomography image-guided laser induced branch retinal vein occlusion in living rabbits, *Scientific Reports*, Vol. 9, 2019, 10560.

[2]. W. Zhang, Y. Li, V. P. Nguyen, Z. Huang, Z. Liu, X. Wang, Y. M. Paulus, High-resolution, in vivo multimodal photoacoustic microscopy, optical coherence tomography, and fluorescence microscopy imaging of rabbit retinal neovascularization, *Light: Science & Applications*, Vol. 7, 2018, 103.

[3]. J. Shi, T. T. W. Wong, Y. He, L. Li, R. Zhang, C. S. Yung, J. Hwang, K. Maslov, L. V. Wang, High-resolution, high-contrast mid-infrared imaging of fresh biological samples with ultraviolet-localized photoacoustic microscopy, *Nature Photonics*, Vol. 13, 2019, pp. 609-615.

(3989)

Time-to-Space Ghost Imaging with Classical and Quantum Correlated Light Beams

D. B. Horoshko and M. I. Kolobov
Univ. Lille, CNRS, UMR 8523 – PhLAM – Physique des Lasers Atomes et Molécules,
F-59000 Lille, France
Tel.: + 33640108808
E-mail: dmitri.horoshko@univ-lille.fr

Summary: Temporal ghost imaging is based on temporal correlations of two optical beams and aims at forming a temporal image of a temporal object with a resolution, fundamentally limited by the photodetector resolution time and reaching 55 ps in a recent experiment. For further improvement of the temporal resolution, it is suggested to form a spatial ghost image of a temporal object relying on strong temporal-spatial correlations of two optical beams. Such correlations are known to exist between two entangled beams generated in type-I parametric downconversion. It is shown that a sub-picosecond-scale temporal resolution is accessible with a realistic source of entangled photons. It is shown also, that classical spatio-temporal correlations can also be used for realizing a time-to-space ghost imaging, but with a lower contrast, compared to using entangled beams.

Keywords: Ghost imaging, Temporal ghost imaging, Entangled beams, Spatio-temporal correlations, Parametric downconversion, Optical parametric generator.

1. Introduction

In temporal ghost imaging (TGI) [1] the image of a temporal object, whose transmittivity changes with time, is formed by detecting two temporally correlated beams: the test beam passing through the object is detected by a single-temporal-pixel detector, while the reference beam is detected by a fast detector. The image appears in the correlation function of two detection outcomes and relies on strong temporal (t-t) correlations between the test and reference beams. TGI and its spatial counterpart, relying on spatial (x-x) correlations between two beams, attract much attention since they are inherently insensitive to the distortion that may occur between the object and the single-pixel detector, allowing one to form high-resolution images in a strongly scattering medium. The temporal resolution of TGI is determined by the response time of the fast detector and its best value reported is 55 ps [1]. To improve the temporal resolution, we propose to form a spatial ghost image of a temporal object relying on strong temporal-spatial (t-x) correlations between the test and reference beams. Such a technique uses a spatial measurement of the reference beam and thus avoids the limitation of the detector speed.

2. Entangled Beams

In the first part of our work, we consider temporal-spatial correlations between two entangled beams generated in type-I parametric downconversion (PDC) explored recently experimentally [2] and theoretically [3]. The scheme of the proposed experiment is shown in Fig. 1. In the process of PDC in a nonlinear crystal with nonlinearity χ pumped by a pulsed plane-wave beam, two entangled photons are generated at phase-matched directions with anti-correlated frequencies. Two filters and two mirrors select part of the PDC radiation, corresponding to a linear angle-frequency dependence for each beam.

We propose to select a spectro-angular band where the transverse wave vector of the reference photon q depends linearly on its frequency detuning Ω from the PDC central frequency [4], as shown in Fig. 2.

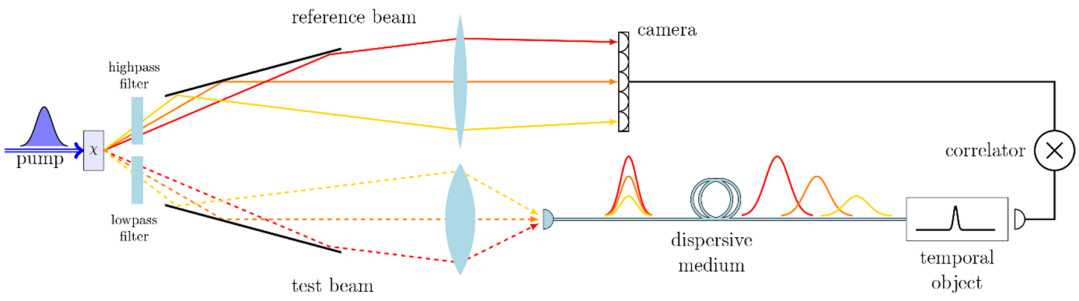

Fig. 1. Scheme of time-to-space ghost imaging.

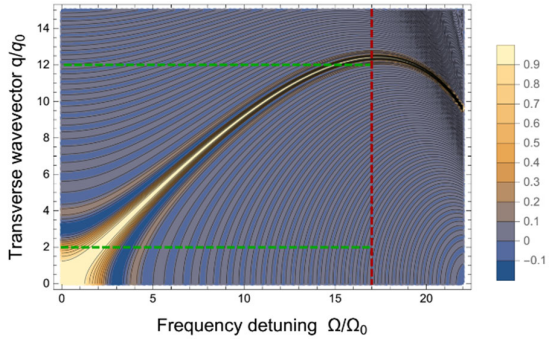

Fig. 2. Phase-matching function of a 1-mm-long BBO crystal pumped at 352 nm. Dashed lines delimit the spectro-angular band selected by the mirrors (green) and the frequency filter (red).

This photon is far-field imaged by means of a lens with the focal length f on a high-resolution camera without temporal resolution, measuring thus q. Its twin has a transverse wave vector $-q$ due to the plane-wave pump and a central frequency detuning $-\Omega$, correlated to $-q$ due to a narrow phasematching. This photon is collimated into a single-mode fibre and propagates through a dispersive medium with a group delay dispersion D, realizing a frequency-to-time mapping, then through a point temporal object, whose transmittivity changes with time, after which it is detected by a single-pixel detector. A spatial ghost image of the temporal object is formed by correlating the frames of the camera with the clicks of the single-pixel detector. The correlation function between the time of passage of the test photon through the temporal object t_2 and the detected position of the reference photon x_1 is shown in Fig. 3.

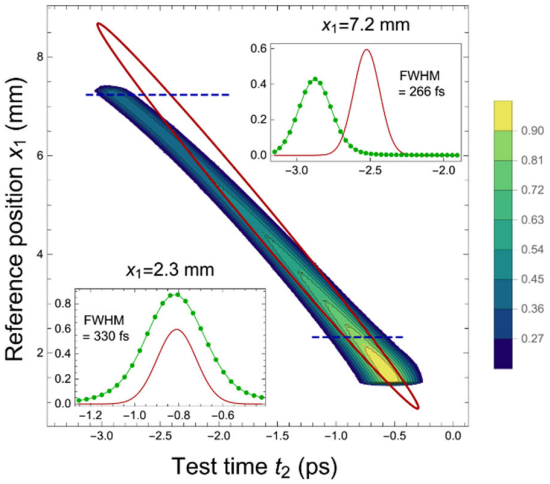

Fig. 3. Temporal-spatial cross-correlation function for two beams emitted by the crystal of Fig. 2 pumped by pulses of duration 200 fs, with D = 2268 fs^2 and f = 5 cm.

In Fig. 3, the color map shows the numerical solution, solid red line corresponds to the analytical solution being equal to 0.27. The insets show temporal numerical (green dots) and analytical (solid red line) dependencies at positions marked by dashed blue lines. This result demonstrates clearly the possibility to form a ghost image with a resolution of the order of 300 ps, more than two orders of magnitude better than in the conventional TGI [1].

3. Classically-correlated Beams

In the second part, we consider a classical source of partially coherent light with correlations described by a spatio-temporal Gauss-Shell model with a mutual coherence function

$$\begin{aligned} \Gamma_0(\boldsymbol{\xi}_1,\boldsymbol{\xi}_2) &= \langle E^*(\boldsymbol{\xi}_1)E(\boldsymbol{\xi}_2)\rangle = \\ &= I_0 \exp\left\{-\frac{1}{1-\rho_I^2}\left[\frac{x_1^2+x_2^2}{4w^2}+\frac{t_1^2+t_2^2}{4T^2}-\frac{\rho_I(x_1t_1+x_2t_2)}{2wT}\right]\right\}\times \\ &\times \exp\left\{-\frac{1}{1-\rho_\gamma^2}\left[\frac{(x_1-x_2)^2}{2\sigma^2}+\frac{(t_1-t_2)^2}{2\tau^2}-\right.\right. \\ &\left.\left.-\frac{\rho_\gamma(x_1-x_2)(t_1-t_2)}{\sigma\tau}\right]\right\}\times \exp[i\omega_0(t_1-t_2)], \end{aligned} \quad (1)$$

where, $\boldsymbol{\xi} = (x, t)$, w and T are the pulse widths and duration respectively, σ and τ are the coherence length and time respectively, ρ_I and ρ_γ are the spatio-temporal coupling parameters for the intensity and coherence, respectively. We show that light with such correlations can also be used for realizing a time-to-space ghost imaging with sub-picosecond resolution, but with a lower contrast, compared to the usage of entangled beams.

Acknowledgements

This work was funded by Agence Nationale de la Recherche, France, grant ANR-19-QUANT-0001 (QuICHE).

References

[1]. P. Ryczkowski, M. Barbier, A. T. Friberg, J. M. Dudley, G. Genty, Ghost imaging in the time domain, *Nature Photonics*, Vol. 10, 2016, pp. 167-170.

[2]. L. La Volpe, S. De, T. Kouadou, D. Horoshko, M. I. Kolobov, C. Fabre, V. Parigi, N. Treps, Spatiotemporal entanglement in a noncollinear optical parametric amplifier, *Optics Express*, Vol. 28, 2020, pp. 12385-12394.

[3]. L. La Volpe, S. De, M. Kolobov, V. Parigi, C. Fabre, N. Treps, D. Horoshko, Multimode single-pass spatio-temporal squeezing, *Physical Review Applied*, Vol. 15, 2021, 024016.

[4]. D. B. Horoshko, Time-to-space ghost imaging, *arXiv Prepress*, 2023, arXiv:2301.09184.

(4070)

Type-II GaInAsSb Based Uni-traveling Carrier Photodiodes with AlGaInAs/InP Bragg Reflectors for Improved 1.55 μm Responsivity

R. Chaudhary, A. M. Arabhavi, O. Ostinelli, M. Leich and C. R. Bolognesi
Millimeter-Wave Electronics Group (MWE)
ETH-Zürich, Zürich, Switzerland
Email: colombo@ieee.org

Summary: Uni-Travelling Carrier Photodiodes (UTC-PDs) have shown high-bandwidth and high-power performance but suffer from low responsivity due to the presence of thin absorption region. In this report, we demonstrate the use of a low period count AlGaInAs/InP Bragg reflectors to improve the 1.55 μm responsivity of top-illuminated GaInAsSb/InP based UTC-PDs. The presence of DBR mirrors positions the absorber at the constructive interference of the electric field intensity of the 1.55 μm signal to achieve maximum absorption. The 64 μm^2 device demonstrates a responsivity of 0.155 A/W, high f_{3db} cut-off of more than 65 GHz and a linear behaviour beyond 10 mA at 40 GHz.

Keywords: GaInAsSb/InP, AlGaInAs/InP, High-power, High-bandwidth, Uni-travelling carrier photodiode, UTC-PD, Bragg reflector, Responsivity improvement, Photodiodes.

1. Introduction

Uni-travelling carrier photodiodes (UTC-PDs) are attractive for high-bandwidth and high-power operations as they involve the transport of fast-moving electrons through the absorber and collector layers. Design considerations for high bandwidth UTC-PDs involve scaling down the absorption layer thickness and the device size to improve the overall bandwidth. However, higher bandwidth is necessarily traded-off against device responsivity.

To improve UTC-PD responsivity without degrading the device bandwidth and power performance, previous works include waveguide integration [1], flip-chip bonding, [2] or resonant cavity structures using gold mirror [3]. Such approaches involve non-trivial growth and fabrication processes. A previous report on UTC-PDs with GaAs based highly reflective DBRs has shown an overall responsivity improvement of 24.4 % [4]. We presently report the first resonant cavity enhanced (RCE) UTC-PD with a InP based distributed Bragg reflector (DBR) at 1.55 μm. The epitaxial design includes three pairs of quarter wavelength AlGaInAs/InP DBR layers on the bottom and one pair at the top of our standard UTC-PD epitaxial layers. As AlInGaAs and InP have low refractive index differences, AlInGaAs/InP based DBRs provide a low reflectivity but are simpler to grow and integrate with InP based photonics [5]. We observed that along with the RCE structure, the position of absorber layer is very important to achieving high responsivity. By positioning the absorber at the location of constructive interference and maximum electric field intensity between DBR mirrors, the overall measured responsivity of our UTC-PDs is improved by 55 % compared to similar devices fabricated without DBRs [6]. The epitaxial structures were lattice-matched to InP and grown by MOVPE for simpler and reproducible growth resulting in stable fabrication process and device performance. A high f_{3db} cut-off of more than 65 GHz and a linear behaviour beyond 10 mA at 40 GHz was observed for a 64 μm^2 photodiode.

2. Design, Fabrication and Results

2.1. Design

Fig. 1 shows the epitaxial structure of our RCE UTC-PDs. A resonant cavity is formed between three pairs of λ/4 AlGaInAs/InP layers on the bottom (to keep the additional thermal resistance low), and one pair at the top along with 260 nm of SiN_x. It is important to position the absorber at the constructive interference of the electric field intensity to achieve maximum absorption. Fig. 2 shows the real refractive index and the electric field intensity profile through our standard and RCE UTC-PDs, respectively. By judiciously adding the DBRs, the constructive interference peak shifts to the absorber region in the RCE UTC-PDs.

Material	Doping	Thickness
AlGaInAs	n.i.d	50 nm
InP	n.i.d	150 nm
$GaAs_{0.49}Sb_{0.51}$	C: 1.304E20	20 nm
AlGaAsSb	C:4.96E19	20 nm
$Ga_{0.81}In_{0.19}As_{0.65}Sb_{0.35}$	C:1.06E18	100 nm
InP	Si:5.96E16	200 nm
InP	n.i.d	25 nm
InP	Si:3.07E19	50 nm
$In_{0.5}Ga_{0.5}As$	Si:4.0E19	25 nm
InP	Si:3.07E19	245 nm
AlGaInAs	n.i.d	105 nm
InP	n.i.d	125 nm
AlGaInAs	n.i.d	105 nm
InP	n.i.d	125 nm
AlGaInAs	n.i.d	105 nm
InP semi-insulating substrate	n.i.d	350 µm

Fig. 1. Epitaxial layer structure of RCE UTC-PDs.

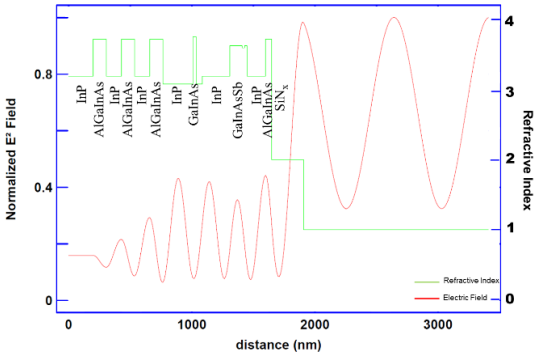

Fig. 2. The real refractive index and the electric field intensity profile of RCE UTC-PD showing peak of interference of electric field at the absorber.

2.2. Fabrication

Photodiodes of various sizes were fabricated by optical lithography and wet etching per [6]. For improved responsivity, the active device area was coated with SiN_x to serve as a single layer anti-reflection coating for top-illuminated photodiodes. DC and RF characterization were performed using an HP4156B semiconductor parameter analyzer, a PNA-X vector network analyzer, a HP power meter up to 50 GHz and a Thorlabs MX70G electrical-to-optical converter. An Er-Doped Fiber Amplifier (EDFA) was used to amplify the optical power up to 20 dBm.

2.3. Results

The measured responsivity of top-illuminated RCE-PDs is 0.155 A/W. Figs. 3(a) and (b) show the UTC-PD and a FIB cross-section with the different layers of RCE UTC-PD.

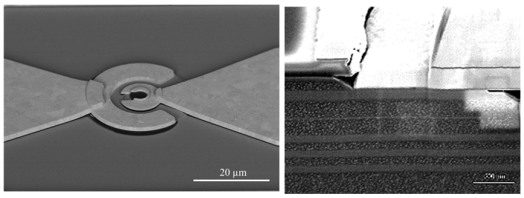

(a) (b)

Fig. 3. (a) SEM image of a fabricated UTC-PD and (b) FIB cross-section of a RCE UTC-PD to show the DBRs.

Fig. 4 shows the relative S_{21} photoresponse plotted against frequency of a 64 μm^2 device at a reverse bias of 2.5 V. It shows a f_{3dB} cutoff of more than 65 GHz, which is beyond the capabilities of our measurement setup. Fig. 5 shows the measured photogenerated RF output power versus the photocurrent. The RF power of 64 μm^2 device is plotted at -3 V at 40 GHz with a modulation depth of 40 %. The devices show a linear response up to a high photocurrent of 10 mA and an RF power over 0 dBm. Clearly, the saturation photocurrent is well beyond 10 mA and was beyond the measurement setup capability.

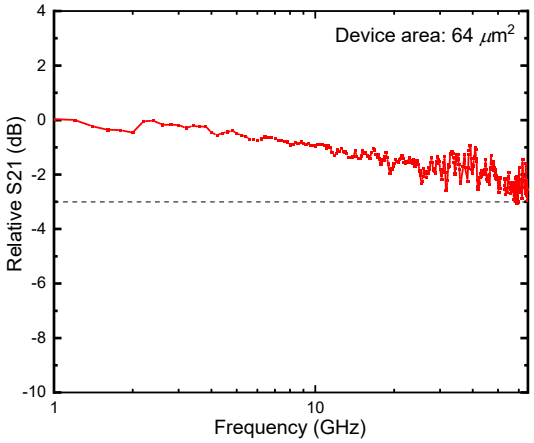

Fig. 4. Measure frequency response of a 64 μm^2 device at a reverse bias of 2.5 V.

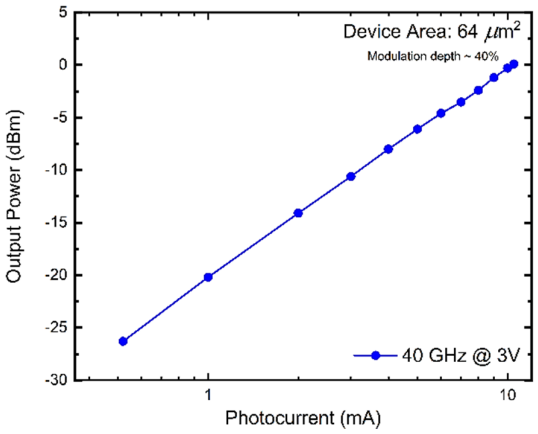

Fig. 5. The RF output power dependence of photocurrent at 40 GHz for UTC-PD at -3 V at 40% modulation depth.

3. Conclusions

The present work highlights the interest of AlInGaAs/InP based DBR mirrors for InP based photodiodes to improve DC performance without degrading the device bandwidth and power performance. We report the first UTC-PD operating at 1.55 μm with InP based DBR mirrors for improved responsivity. Future work will include RF and power performance comparison of RCE UTC-PDs with our standard devices. Further improvements in responsivity is possible with higher DBR period counts but the DBR impact on thermal must be balanced against reflectivity since UTC-PDs are often used under high-power conditions. With the present 3-period bottom DBR stack our UTC-PDs still manifest no heating related degradation with respect to UTC-PDs fabricated without DBRs and shows a high

f_{3db} cutoff of beyond 65 GHz and a linear response beyond 10 mA.

References

[1]. C. C. Renaud, M. Robertson, D. Rogers, R. Firth, P. J. Cannard, R. Moore, A. J. Seeds, A high responsivity, broadband waveguide uni-travelling carrier photodiode, *Proceedings of SPIE*, Vol. 6194, 2006, 61940C.

[2]. J. Wun, R. Chao, Y. Wang, Y. Chen, J. Shi, Type-II GaAsb0.5Sb0.5/InP uni-traveling carrier photodiodes with sub-terahertz bandwidth and highpower performance under zero-bias operation, *J. Lightw. Technol*., Vol. 35, Issue 4, Feb. 2017, pp. 711-716.

[3]. P. Latzel, et al., Generation of mW level in the 300-GHz band using resonant-cavity-enhanced unitraveling carrier photodiodes, *IEEE Transactions on Terahertz Science and Technology*, Vol. 7, Issue 6, Nov. 2017, pp. 800-807.

[4]. Q. Chen, et al., Uni-traveling-carrier photodetector with high-reflectivity DBR mirrors, *IEEE Photonics Technology Letters*, Vol. 29, Issue 14, 2017, pp. 1203-1206.

[5]. M. S. Ünlü, S. Strite, Resonant cavity enhanced photonic devices, *Journal of Applied Physics*, Vol. 78, Issue 2, 1995, pp. 607-639.

[6]. A. M. Arabhavi, et al., Type-II GaInAsSb/InP uniform absorber high speed uni-traveling carrier photodiodes, *Journal of Lightwave Technology*, Vol. 39, Issue 7, 2021, pp. 2171-2176.

(4084)

Optical Sensing of Cerebral Hemodynamics from Within the Skull

M. Balberg [1], N. Rein [2], Y. Avni [1], R. Shechter [1] and M. Medvedovsky [2,3]
[1] Holon Institute of Technology, 52 Golomb st. 5810502 Holon, Israel
[2] Department of Neurology and Agnes Ginges Center for Human Neurogenetics, Hadassah Medical Organization, Jerusalem, Israel
[3] The Faculty of Medicine, Hebrew University of Jerusalem, Jerusalem, Israel
Tel.: +97235026812, fax: +87654321
E-mail: balbergm@hit.ac.il

Summary: Functional infrared spectroscopy (fNIRS) is primarily used for non-invasive sensing of changes in cerebral hemodynamics. A novel optical sensing platform for tracking such changes in a more robust way, that improves sensitivity to cerebral blood flow, and reduces extracerebral contamination is presented. The sensors are designed as an adaptation of existing intraosseous bolts that are inserted into the skull for routine clinical monitoring of patients. Optical fibers (optodes) are introduced through openings within the bolts that reach the bottom layer of the skull. Consequently, light passage to cerebral layers is not contaminated by superficial blood flow from within the scalp. Measurements from a brain-mimicking phantom (that includes a skull) demonstrate the feasibility and benefits of using such novel intra-osseous fNIRS (ifNIRS) sensors. A sensitivity to changes in optical absorption from layers as deep as 2 cm below the skull is demonstrated.

Keywords: fNIRS, Epilepsy, Intraosseous sensing, Cerebral hemodynamics.

1. Introduction

Optical sensing of changes in cerebral blood flow and oxygenation is key for extracting information about brain health and function. Functional near infrared spectroscopy (fNIRS) has been used as an important tool in assessment of changes in neuronal activation that elicit a hemodynamic response [1]. Conventional fNIRS sensing is based on non-invasive placement of optodes (including light emitters and detectors) over the scalp. A current review of the state of the art of this technology is provided by Ayaz et al. [2]. This sensing arrangement suffers from contamination of the cerebral related signal by extracerebral blood flow, mainly through the scalp. In most cases, it is impossible to avoid this contamination, as light passes through the scalp on its way into and out of the brain's vasculature.

However, in clinical situations where an intra-osseous device is placed in the skull as an accepted practice, it is possible to use this device as an anchor for the optodes and provide a path into the brain without passing through the scalp's vasculature. Such intraosseous devices include intracranial pressure bolts, deep brain stimulation electrodes and bolts for stereo-EEG (SEEG) depth electrodes.

SEEG depth electrodes are inserted into the brain of patients with epilepsy in order to map the electric field inside the brain, improve source localization of the electric fields and determine the epileptogenic zone for a future resection [3]. Integrating fNIRS with SEEG is expected to provide multi-modal sensing of both electrical and hemodynamic activity within the brain and enable better mapping of the sources or foci of activity in epileptic seizures.

Integrating optical fibers into the bolt of a SEEG depth electrode provides several benefits, including:

1. Elimination of scalp blood flow contamination;
2. Deeper penetration for hemodynamic changes;
3. Reduction of motion artifacts.

We have designed a new intraosseous fNIRS sensor (ifNIRS), that integrates optical fibers (optodes) within the bolt of a SEEG depth electrode and tested its sensitivity to changes of optical absorption in a brain mimicking phantom.

2. Methods

2.1. fNIRS System

An fNIRS system comprising laser light sources (at 785 nm and 830 nm), was designed to operate at a 6-8 Hz scanning frequency when two ifNIRS sensors, (each comprising 4 emitter and 4 detector optodes) are active. The system includes 4 laser sources (two at each wavelength) (IPS, USA), four 4X1 optical switches (Lightwaves Link, China) and 8 avalanche photo diodes (APDs) (Hamamatsu, Japan). The optical switches are controlled using a multi-purpose digital controller (Measurement Computing Corporation, USA), and the analog to digital conversion of the detected light signals is performed using the same system. Multimode optical fibers (62.5 μm diameter), connected to the output of the optical switches, are used as emitter optodes, and 3 multi-mode fibers with a diameter of 200 μm are arranged in a bundle and used as detector optodes, and coupled to the APDs.

2.2. ifNIRS Sensor

The sensor comprises an SEEG depth electrode with a modified bolt. The bolt was manufactured from PEEK© to allow fixation through the bone and includes a superficial optode support part and an

intraosseous optode support part. Some optodes are positioned inside the superficial support, providing non-invasive readings through the scalp, and some optodes are positioned inside the skull. We note that the bolt terminates inside the skull and does not penetrate the dura. This reduces the odds of bleeding and obstruction of the fiber tips. A schematic diagram of the ifNIRS sensor is presented in Fig. 1. The depth electrode is inserted through an opening in the center of the bolt.

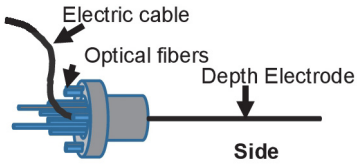

Fig. 1. A schematic design of an ifNIRS sensor with emitter and detector optodes.

2.3. Tissue Mimicking Phantom

A tissue mimicking phantom, schematically presented in Fig. 2, was constructed from Silicon rubber (RTV) mixed with scattering particles of TiO_2 [4]. Water mixed with Indian Ink, simulating the absorption of blood, was introduced through tubes simulating "capillaries" with a diameter of 1.75 mm at different depths from the surface of an artificial skull (15-25 mm). The artificial skull (with a thickness of 7 mm) was 3D printed using white PLA with a fill factor of 99 %. A transparent gel applied between the layers allowed for optical coupling.

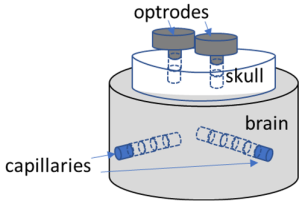

Fig. 3. A schematic diagram of the tissue mimicking phantom.

3. Results

The phantom, including 3 ifNIRS sensors with several optodes, is shown in Fig. 4. The distances between the different sensors were 2,3 and 4 cm respectively.

Measurements of the optical attenuation by the blood simulating fluid were conducted for different distances between the ifNIRS sensors. Emitter fibers were placed either superficially or within the skull.

As demonstrated in Table 1, when the fibers are inserted into the skull (inside skull), a better sensitivity for the deep "capillaries" was demonstrated, for a 3 cm distance between emitter and detector, compared to the superficial/ non-invasive placement. As can be seen a 12.5 % drop was observed for optodes placed in the superficial layer, compared to a 20 % drop in the intra-skull measurement.

Table 1. Measurements of light intensity detected from different source locations.

Location of emitter	"Capillary 1" filled with Ink [V]	Capillary 1&2 filled with ink [V]
Superficial	0.8±0.03	0.7±0.02
Inside skull	1.2±0.04	0.95±0.03

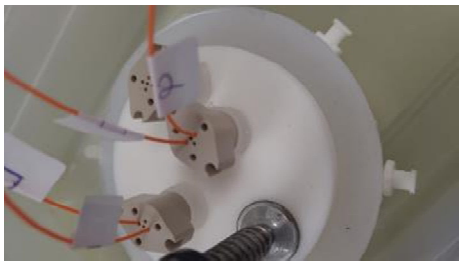

Fig. 4. A tissue mimicking phantom with three ifNIRS sensors.

4. Discussions and Conclusions

Positioning of optical fibers inside the skull, not penetrating the brain, allows for deeper light penetration and reduces contamination by superficial layers compared to non-invasive optical sensing. In this work we have demonstrated that using such an approach results in an improved sensitivity to changes in optical absorption as deep as 2 cm below an artificial skull.

We believe that the benefits of the ifNIRS sensors presented here will allow for deeper sensing of hemodynamic changes during epileptic seizure and improve the localization of epileptogenic zone in the future.

Acknowledgements

This research was funded by the Israeli Innovation Authority. The authors would like to thank Gidon Levi and Rotem Duek for developing the fNIRS system.

References

[1]. F. Scholkmann, *et al.*, A review on continuous wave functional near-infrared spectroscopy and imaging instrumentation and methodology, *Neuroimage*, Vol. 85, 2014, pp. 6-27.

[2]. H. Ayaz, *et al.*, Optical imaging and spectroscopy for the study of the human brain: Status report, *Neurophotonics*, Vol. 9, Issue S2, 2022, pp. 1-65.

[3]. J. Gonzalez-Martinez, *et al.*, Stereotactic placement of depth electrodes in medically intractable epilepsy: Technical note, *Journal of Neurosurg.*, Vol. 120, Issue 3, 2014, pp. 639-644.

[4]. M. Izzetoglu, *et al.*, Multilayer, Dynamic, Mixed solid/liquid human head models for the evaluation of near infrared spectroscopy systems, *IEEE Transactions of Instrumentation Measurements*, Vol. 69, Issue 10, 2020, pp. 8441-8451.

(4150)

Ultrafast Thulium-doped Fiber Laser with Nonlinear Optical Loop Mirror

M. Michalska, P. Grzes and J. Swiderski
Military University of Technology, Institute of Optoelectronics,
2 S. Kaliskiego St., 00-908 Warsaw, Poland Tel.: + 48261837332
E-mail: maria.michalska@wat.edu.pl

Summary: We report on a passively mode-locked thulium-doped fiber laser with an intracavity dispersion management. The all-fiber oscillator was based on a nonlinear optical loop mirror (NOLM) saturable absorber. Fundamental soliton, stretched-pulse and noise-like pulse generation were demonstrated, when the oscillator operated with the anomalous net dispersion. In soliton mode-locking regime the oscillator delivering optical solitons with a duration of 675 fs and a 3 dB spectral bandwidth of 7.96 nm with characteristic Kelly sidebands. Next, for a dispersion compensation an ultra-high numerical aperture fiber with a normal dispersion at 2 µm was utilized. Near-zero net cavity dispersion of -0.016 ps^2, stretched-pulses with a duration of 253 fs and 26.4 nm spectral bandwidth centered at wavelength of 1967 nm were generated with a fundamental pulse repetition frequency of ~15.8 MHz. For higher pump power level noise-like pulse generation, tunable over 35 nm from 1943.5 to 1978 nm, was presented in the same laser setup configuration. The maximum NLP packet energy was 2.91 nJ.

Keywords: Thulium-doped fiber, Mode-locking, Fiber-laser, NOLM, Dispersion compensation.

1. Introduction

The broadband emission bandwidth of thulium-doped fibers ranging from 1.8 to 2.1 µm makes them an excellent choice for the generation of ultrafast mode-locked pulses in the mid-infrared spectral region. Compact and environmentally stable lasers which can generate femtosecond optical pulses are very attractive in the wide range of applications including medicine, material processing, spectroscopy, remote sensing, and fundamental sciences [1-3].

Many different configurations for passively mode-locked thulium-doped fiber lasers (TDFLs) with various saturable absorbers (SA) have been proposed. However, materials SA have usually a low damage threshold and sometimes exhibit degradation of their optical property over time. Moreover, ultrafast lasers based on materials SA are sensitive to mechanical and thermal disturbances. An alternative approach for ultrashort pulse generation, involving all-fiber lasers, is mode-locking by utilizing artificial SA. In this case, the modulation of losses inside a laser cavity is induced by the nonlinear polarization evolution (NPE) or the Kerr effect, using a nonlinear fiber loop mirrors – nonlinear optical/amplifying loop mirror (NOLM/NALM) [4].

In this paper we describe operation of TDFL mode-locked by a fiber loop mirror. Generation of fundamental soliton in all-PM fiber laser setup was presented. Next, an intracavity dispersion management using an optical fiber with normal dispersion at 2 µm was described and stretched-pulse and noise-like pulse (NLP) generation were presented.

2. Experimental Setup

The experimental setup of the all-fiber TDFL is depicted in Fig. 1. The oscillator was arranged in the "figure of eight" configuration, where the right loop acts as a saturable absorber (NOLM).

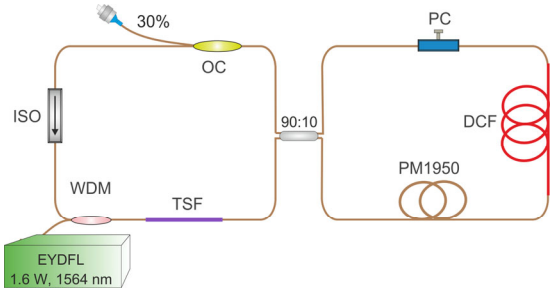

Fig. 1. Experimental setup of the mode-locked TDFL with NOLM; EYDFL – Er/Yb-co-doped ring fiber laser, WDM – 1560/2000 wavelength division multiplexer, TSF –PM single-mode thulium-doped fiber, OC – output coupler, ISO – fiber optic isolator, PM1950 – PM passive fiber, DCF – dispersion compensating fiber, PC – polarization controller.

A brief description of this experimental setup can be found in our previous paper [5]. For a dispersion compensation an ultra-high numerical-aperture fiber (UHNA4) with a core/clad diameter of 2.2/125 µm, numerical aperture of NA = 0.35 and group velocity dispersion of $\beta_2 = 93$ ps^2/km^{-1} was utilized. Almost the whole laser setup (excluding only the DCF) was built using all-PM-fiber technology.

3. Results and Discussion

Using different lengths of DCF in NOLM loop, an intracavity dispersion management was performed. In the experiment the DCF length is varied between 5.58 m and 4.57 m resulting in a total group delay dispersion value ranging from -0.016 ps^2 to -0.330 ps^2. For TDFL without DCF the arranged NOLM consists

of 10 m of PM1950 fiber and net dispersion was calculated to be -1.149 ps^2. The optical output spectrum (Fig. 2a) was centered at 1991.8 nm and had FWHM bandwidth of 7.96 nm. Fundamental solitons were generated with repetition frequency of 12.79 MHz, an average output power of 0.98 mW and the pulse duration was determined to be 675 fs using a sech^2-pulse profile assumption.

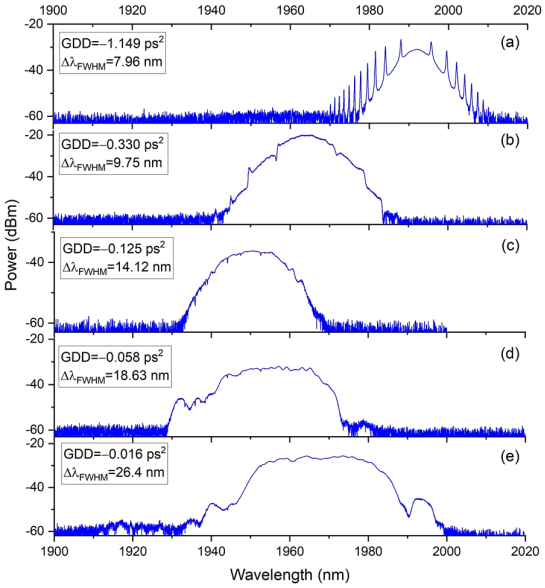

Fig. 2. Evolution of the output spectrum by varying the intracavity dispersion.

When DCF was spliced inside the fiber loop mirror, the optical spectrum expanded with decreasing the intracavity dispersion, up to laser spectrum with 3 dB bandwidth of 26.4 nm (Fig. 2e) for net dispersion of -0.016 ps^2. The developed TDFL generated stretched-pulses with repetition frequency of 15.795 MHz and an average power of 0.85 mW. The calculated energy of the single laser pulse was 54 pJ. The laser performance, when the broadest optical spectrum was generated, is presented in Fig. 3. At the laser output, generated pulses were compressed in the piece of PM1950 fiber from 1.56 ps to 253 fs. The compressed pulse duration corresponds to the time-bandwidth product of 0.516 for the Gaussian pulse.

By adjusting the PC at a higher pump power level an NLP operation mode was achieved in the developed TDFL. The maximum average output power during NLP generation was 46 mW at launched pump power of 1.59 W. NLPs were generated with the same fundamental pulse repetition frequency of 15.795 MHz and calculated maximum energy of NLP bunch was 2.9 nJ.

Fig. 4 presents continuous tuning of the NLP spectrum for a constant pump power level. The output spectrum could be tuned by 35 nm, from 1943.5 to 1978 nm, only by adjusting the PC position. The 3 dB spectral bandwidth of 12.9-18.5 nm was maintained throughout the tuning range in NLP mode-locking operation. The broadest NLP spectrum with a 3 dB spectral bandwidth of 17.4 nm was centered at a wavelength of 1961.4 nm.

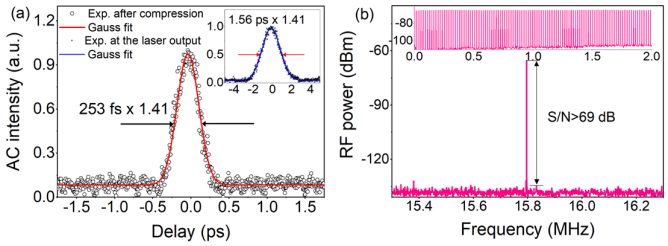

Fig. 3. Performance of the laser at -0.016 ps^2 estimated net dispersion: autocorrelation traces of the compressed and uncompressed (inset) pulse (a), RF spectrum at fundamental repetition rate and wide span RF spectrum (inset).

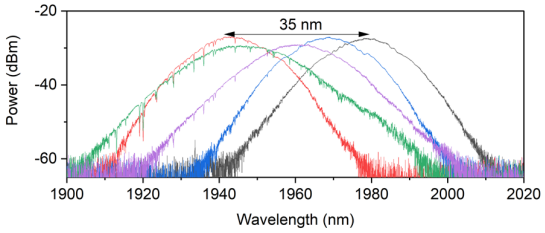

Fig. 4. Noise-like pulse output spectra at a pump power of 1.3 W.

4. Conclusions

In summary, we have demonstrated the intracavity dispersion management in TDFL based on the nonlinear loop mirror saturable absorber. Generation of dispersion-managed solitons and noise-like pulses with near-zero net dispersion were presented. The oscillator was capable of generating over 26 nm broad stretched-pulses centered at the wavelength of 1967 nm with pulse duration compressible to 253 fs.

Acknowledgements

This research was co-financed by Military University of Technology under research project no. UGB/22-878/2023/WAT.

References

[1]. K. Scholle, S. Lamrini, P. Koopmann, P. Fuhrberg, 2 μm laser sources and their possible applications, in

Frontiers in Guided Wave Optics and Optoelectronics (B. Pal, Ed.), *InTech*, 2010, pp. 471-500.

[2]. D. C. Kirsch, S. Chen, R. Sidharthan, Y. Chen, S. Yoo, M. Chernysheva, Short-wave IR ultrafast fiber laser systems: Current challenges and prospective applications, *Journal of Applied Physics,* Vol. 128, Issue 18, 2020, 180906.

[3]. C. W. Rudy, M. J. F. Digonnet, R. L. Byer, Advances in 2-μm Tm-doped mode-locked fiber lasers, *Optical Fiber Technology*, Vol. 20, Issue 6, 2014, pp. 642-649.

[4]. N. J. Doran, D. Wood, Nonlinear-optical loop mirror, *Optics Letters,* Vol. 13, Issue 1, 1988, pp. 56-58.

[5]. M. Michalska, Dispersion managed thulium-doped fiber laser mode-locked by the nonlinear loop mirror, *Optics & Laser Technology,* Vol. 138, 2021, 106923.

(4195)

Quantum-dot/dash Semiconductor Multi-wavelength Lasers for State-of-the-art Optical and Wireless Networks

Youxin Mao, Zhenguo Lu, Jiaren Liu, Philip J. Poole, Guocheng Liu, Khan Zeb, and Pedro Barrios
Advanced Elect. and Photonics Research Centre, National Research Council Canada, Ottawa, ON, Canada
Tel.: + 613-993-7331
E-mail: youxin.mao@nrc-cnrc.gc.ca

Summary: We present high performance semiconductor quantum dot (QDot) or dash (QDash) passively mode-locked multi-wavelength lasers (ML-MWL) fabricated in NRC Canada. The characterizations from C-band InAs/InP Fabry-Pérot Qdot and Qdash ML-MWLs with repetition rate of 10-90 GHz in buried hetero- and ridge-structures are demonstrated. Phase noise and timing jitter from these lasers have been theoretically analyzed and experimentally measured in detail. The performances of the lasers are also evaluated in an over ten-Terabit/s aggregate data transmission system and a Millimeter-Wave-over-Fiber fronthaul wireless link at 5G New Radio with high order QAM data formats.

Keywords: Quantum dot, Quantum dash, Mode-locked laser, Buried hetero-structure semiconductor laser, Phase noise, Timing jitter, Terabit/s transmissions, Radio-over-fiber, Fronthaul wireless networks.

1. Introduction

Quantum-Dot and Quantum-Dash (QDot/Dash) chip-scale mode-locked based optical frequency comb (OFC) are promising compact solutions to generate high power, low timing jitter, and high spectrum efficient optical pulses for applications in high capacity optical networks using WDM with advanced modulation formats and 5G New Radio MMW fronthaul wireless links [1]. In this presentation, we demonstrate InAs/InP QDot/Dash C-band single-section passively, i.e., Fabry-Pérot (F-P), mode-locked lasers with mode spacings of 10-90 GHz. The performances of lasers are investigated in detail, including RIN, phase noise (PN), and timing jitter (TJ). The applications of Terabit/s data transmission and real-time broadband optical heterodyne synthesizer based millimeter-wave-over-fiber (MMW-o-F) wireless links are presented. These results are obtained without any form of feedback to control the laser linewidths. These capabilities indicate that QDot/Dash ML-MWLs are promising in state-of-the-art optical and wireless networks.

2. Materials

The laser structure was grown on a 3" (001) oriented n-type InP substrate with a p-n cladding and InGaAsP core by chemical beam epitaxy. This core structure provides both carrier and optical confinement. By choosing appropriate growth conditions, we could create either InAs QDot or QDash layers as the gain medium [2] in the waveguide core. For the lasers presented here, we grew five-stacked-layers of QDots or QDash in the center, forming the active region. 2-2.5 μm wide single mode ridge waveguides are developed for both surface ridge and buried hetero-structures, as shown in Fig. 1(a). An F-P cavity is formed by cleaving 0.5-4 mm long devices providing mode spacing of 10-90 GHz, as shown in Fig. 1(b). No facet coatings are applied.

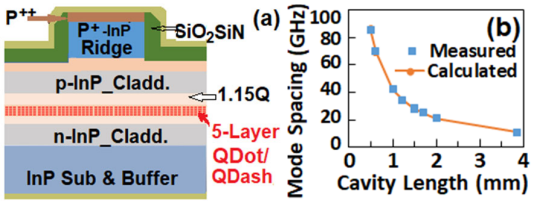

Fig. 1. (a) Schematic cross-sectional diagram of the ridge-waveguide InAs/InP QDot or QDash lasers. (b) Mode spacing vs. cavity length of InAs/InP Qdot and Qdash layers.

3. Theory

The TJ, caused mainly by PN, is critical for a QDot/Dash F-P ML-MWL for high-capacity networks. We demonstrate the theory of pulse-to-pulse and pulse-to-clock (integrated) TJs and the relationships of TJ, RF linewidth, and PN regarding the lasers for TJ characterizations [3].

4. Results and Discussion

Fig. 2 shows laser performances of RIN (a), optical mode linewidth, i.e., optical phase noise (b), phase noise spectrum (c), and the linewidth of RF beat note (d) for both QDot and Qdash lasers. Summarised

results for the two lasers and the two structures are shown in Tables 1 and 2, respectively. The phase noise is less than 2.0 MHz for all modes in 13.0 and 10.4 nm bandwidth for our QDot and Qdash lasers, respectively. By comparison, the performance from a similar laser in ref [4] is shown in the last raw in Table 1. Extreme low phase noise induces the narrow RF linewidth compared to what was reported from [4] shown in Fig. 2(d), therefore, this is attributed to the ultra-small timing jitter for our Qdot and Qdash lasers as shown in Table 1.

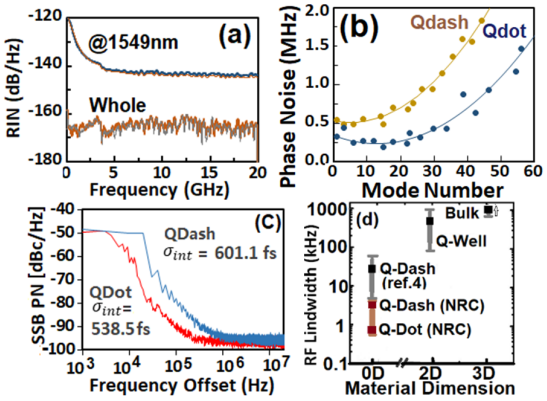

Fig. 2. Measured RIN spectra (a), PN vs. mode # with parabolic fit (b), single side band PN spectrum L(f) showing obtained integrated TJ values (c), and RF linewidth dependence on gain material dimensionality (d) for QDot and Qdash ML-MWL. All results were measured at 400 mA and a temperature of 18°C.

5. Applications

The performance of high-capacity networks highly depends on the properties of the OFC source, such as the number and power of comb lines, OSNR, PN, and TJ. Fig. 3(a) shows the dependence of BER evaluation on received optical power obtained with DP 16-QAM 28-GBd over 100-km SSMF by employing a 28 GHz QDot ML-MWL. An aggregate data transmission capacity of 12.5 Terabit/s is demonstrated with 56 wavelength channels as optical carriers.

The performance of buried heterostructures (BH) QDash ML-MWL is evaluated in broadband optical heterodyne based MMW-o-F fronthaul wireless links at 5G New Radio of around 25 GHz with a bit rate of 16-Gb/s, as shown in Fig. 4.

6. Conclusions

High performance QDot and QDash ML-MWLs are demonstrated with extremely low phase noise and timing jitter. By employing these high quality lasers, over ten-Terabit/s aggregate data transmission capacity (16QAM 56×28-GBd PDM) optical network and real-time broadband optical heterodyne synthesizer based MMW-o-F wireless links featuring multi-Gb/s data rates with a maximum data capacity of 16 Gb/s (16-QAM×4-GBaud) are achieved. These results may lead to an important step towards small size, cost-efficient, low noise, low timing jitter, and a high number of multi-channel light sources for advanced systems of next-generation optical and wireless communication networks.

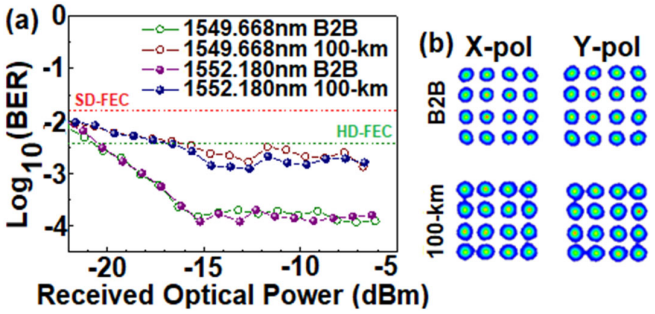

Fig. 3. (a) BER evaluation over the received optical power at the two mode wavelengths for B2B and after 100-km of SSMF transmission. The BER obtained from all the selected channels are below the SD-FEC limit (BER = 2.0×10^{-2}) and HD-FEC limit (BER = 3.8×10^{-3}). (b) Constellation diagram obtained for a selected channel at 1552.180 nm for both *X*- and *Y*-polarization after B2B and 100-km of SSMF transmission. The color indicates the relative density of symbols detected in the complex plane, with red indicating a higher density and blue a lower density.

Table 1. Summary for 28.4 GHz Qdot & Qdash ML-MWL by comparing to the Ref. [4].

Lasers (GHz)	3dB Optica Spectrum Bandwidth & CH#		Avg. RIN whole CH	Phase Noise Range in Bandwidth	3dB RF BW	p-p Timing Jitter	Integrated Timing Jitter	Frequency Range
	nm	CH #	dB/Hz	MHz (nm)	kHz	fs	fs	MHz
Qdot (28.4)	9.34	42	-164.38	0.19-1.47 (13.0)	0.65	2.13	538.5	1.0-20
Qdash (28.4)	10.88	49	-165.05	0.49-1.84 (10.4)	3.15	4.93	601.1	1.0-20
Qdash[Ref] (39.7)	13.0	40	-157.00	5.0-35.0 (9.64)	30.00	8.75	860.0	1.0-20

Table 2. Comparison of RF spectrum linewidth $\Delta\upsilon_{RF1}$, pulse-to pulse and integrated TJs for each 25 GHz QDash F-P ML-MWL with buried heterostructure and surface ridge structures (Parabolic fit as described in Ref. [3]).

Laser Structure	*Fit from Phase noise vs. Mode #*			*Pulsed Timing Jitter (fs)*	*Integrated Timing Jitter (ps)*
	$\Delta\upsilon_{min}$ *(MHz)*	n_{min}	$\Delta\upsilon_{RF1}$ *(kHz)*		
Ridge	0.968	5.6	3.57	6.03	1.90
BH	0.133	18.1	0.512	2.28	0.48

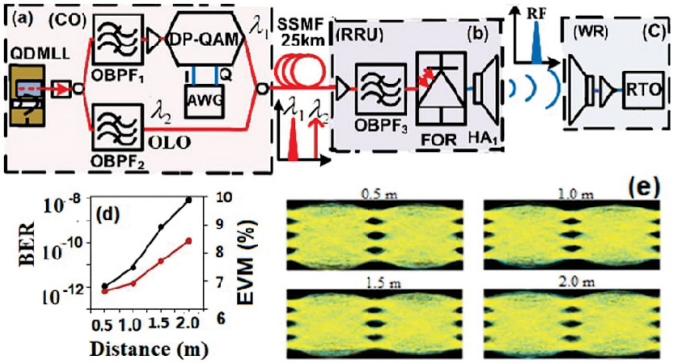

Fig. 4. Schematic of the experimental setups of Central Office (a), Remote Radio Unit (b), and Wireless Receiver (c) for photonics-assisted MMW-o-F RF signal generation, data transmission, and detection using two optical channels (data channel λ_1, and optical LO λ_2). Transmission performance (d) shows BER (left) and EVM (right) in photonics-assisted 16-Gb/s (4-Gbaud × 16 QAM) wireless links at 25 GHz 5G NR over 0.5 m to 2 m RF link distance through 25 km SSMF, and (e) shows corresponding eye diagrams by using an InAs/InP QDash ML-MWL with BH structure.

Acknowledgements

The authors would like to acknowledge the support of National Research Council Canada's High Throughput and Secure Networks (HTSN) challenge research program.

References

[1]. Z. G. Lu, et al, QDash multi-wavelength lasers for Tbit/s coherent communications and 5G wireless networks, *J. of Europ. Optical Society-Rapid Publications,* Vol. 17, Issue 9, 2021, pp. 1-7.

[2]. P. J. Poole, InP-based quantum dot lasers, in Advances in Semiconductor Lasers (J. J. Coleman, et al., Eds.), *Academic Press*, 2012, pp. 419-453.

[3]. Y. Mao, et al., Timing jitter in Fabry-Pérot quantum dash mode-locked lasers for the next-generation networks, in Advances in Optics, Vol. 6, Chapter 4, 2022, *IFSA Publishing*, pp. 71-106.

[4]. R. Rosales, et al., InAs/InP QD passively mode-locked lasers for 1.55-μm applications, *IEEE Journal of Selected Topics in Quantum Electronics*, Vol. 17, Issue 5, 2011, pp. 1292-1301.

(4379)

Semiconductor Laser Driver Based on Step Recovery Diode for Gain-switching Operation

P. Grześ, M. Michalska and J. Świderski
Military University of Technology, Institute of Optoelectronics,
2 S. Kaliskiego St., 00-908 Warsaw, Poland
Tel.: + 48261837075
E-mail: pawel.grzes@wat.edu.pl

Summary: A laser diode driver based on a step recovery diode, capable to generate short current pulses suitable for gain-switching operation, is presented. To define the requirements for the electronic circuit numerical simulations were performed using a rate equations model. The prototype consists of three separate boards, two signal conditioners and one main pulse generator board. The driver produces square pulses with sharp edges, electronically tunable amplitude and variable duration. The pulses can be generated on demand using an external trigger signal. Using a commercially off-the-shelf laser diode, the gain-switched laser pulses with duration of 13.87 ps and peak power of 39.87 mW were achieved. It is worth emphasizing that the performance of the circuit was limited by the apparatus. Shorter and more powerful pulses can be obtained.

Keywords: Semiconductor laser, Laser diode, Laser driver, Step recovery diode, Gain-switching.

1. Introduction

To generate short optical pulses using off-the-shelf semiconductor lasers (SL) a gain-switching (GS) technique can be used. In this scheme, a short current pulse pumps the medium above the threshold and the energy is then released in the form of a very short and powerful laser pulse. This method allows generating optical pulses with duration in order of tens or hundreds of picoseconds [1]. Even if the described scheme is straightforward, the most challenging task is to provide an appropriate pumping current pulse. To achieve a clear GS pulse the electronic driver has to generate a high-current pulse with subnanosecond or even picosecond duration.

In this paper we describe a prototype of a low-cost semiconductor laser electronic driver based on a step recovery diode (SRD) monostable pulse generator. The design allows tuning the output pulse amplitude and duration easily. Every pulse is triggered externally and independently providing pulse-on-demand operation. The experiment with the high-speed laser diode shows that the device can generate gain-switched pulses with duration less than 15 ps.

2. Gain-switching in Semiconductor Laser

The gain-switching technique can be modeled by solving rate equations. In case of a single-mode semiconductor lasers they take the form of a non-linear system of two differential equations, one for carrier density and one for photon density. To recognize the requirements for the pumping pulse parameters these equations were solved numerically assuming the rectangular current pulse shape. The qualitative results are presented in Fig. 1.

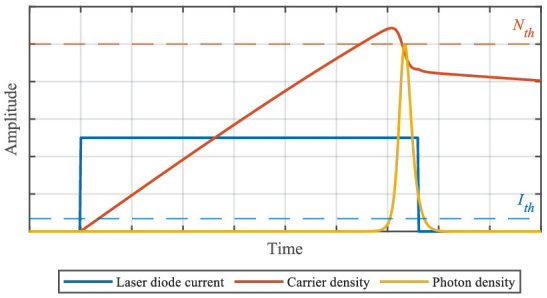

Fig. 1. Gain-switching in semiconductor laser (simulation).

Analyzing the obtained waveforms it can be noticed that there is a delay between the current pulse and the output signal resulting from the laser pulse build-up time. In effect, the current pulse can be much longer than the expected laser pulse. For a longer pumping pulse the carrier density rises above the threshold again and the second pulse appears. The higher amplitude of the current pulse speeds up the carrier density rise time, which reduces the delay. In this case, the pumping pulse duration must be shortened for an optimal operation [2]. Additionally, as long as the photon density is low and the stimulated emission term can be neglected, the carrier density is proportional to the integral of the current waveform, and therefore, the pulse shape has a secondary importance.

3. The Circuit Description

To meet the requirements for a GS operation in a semiconductor laser the electronic laser diode driver generating subnanosecond current pulses must be designed. To extend the functionality of the device the

pulse amplitude and duration tuning capabilities should be available. It will allow us to find the optimal pumping pulse parameters for the specific laser diode without significant interference into the circuit.

The short current pulse generator with tuning capabilities based on SRD was designed, built and tested. The prototype consists of three modules fabricated on separate boards (Fig. 2). The first module is the transistor-based monostable multivibrator responsible for the short rise time pulse generation (on the right in Fig. 2). The second stage is the amplifier which spreads the signal levels as wide as possible. After that, the signal goes to the main board with the SRD, the delay line and the bias circuit.

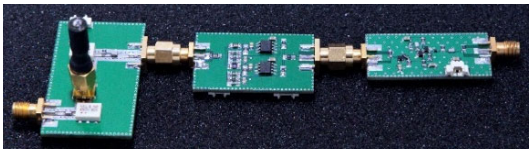

Fig. 2. The circuit of laser diode driver based on SRD.

The SRD has a capability to store the charge when it is forward biased. When the input signal polarization changes the diode is still conducting until the whole collected charge is removed. After that, the diode goes to a cut-off state rapidly with picosecond transition time and it produces a signal with a very sharp edge. Further, the signal propagates to the T-junction where it splits in half. One part goes directly to the output and it becomes a rising edge of the output current pulse. Second half travels through the shorted coaxial line. When it reaches the end of the line it bounces back with reversed polarity. The back-propagating signal reaches the T-junction again and it becomes a falling edge of the output signal [3, 4].

The output pulse duration is equal to the doubled propagation time through the attached coaxial line. The both edges are very sharp thanks to the fast transitions of the SRD. The pulse amplitude depends on the bias current and it can be easily changed electronically.

4. Experimental Results

The prototype was tested in the time domain using a high-speed ultrawideband oscilloscope. The electrical measurements on 50 Ω load show that pulses with duration down to 120 ps can be achieved. The peak current was 160 mA reached under 60 mA bias. Some distortions and oscillations in the signal were observed, but they should not affect the laser pulse generation process.

Using an off-the-shelf 1550 nm laser module with 4 GHz analog bandwidth and 20 mW maximum continuous power the output optical pulses were measured. To observe the GS pulses the fixed length coaxial line was connected and the bias current was slowly increased. The best results were recorded with the 25 mm line (330 ps propagation time) and 20 mA bias current (Fig. 3). The output pulse duration was only 13.87 ps and the peak power was 39.31 mW.

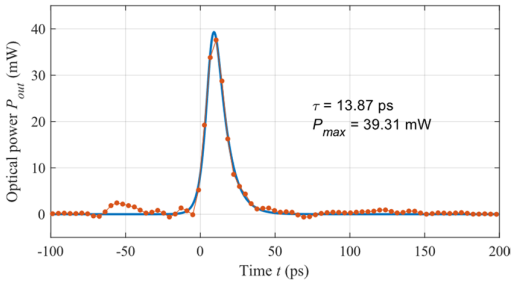

Fig. 3. Output laser pulse.

The presented results do not show the full capabilities of the driving circuit. The SRD bias current could not be increased any further in the experiment carried out, which results from the fact that the output optical power reached the photodetector saturation level (40 mW). Laser pulses with shorter duration and higher peak power can be achieved, but to measure their duration photodiode with higher damage threshold have to be used.

5. Conclusions

In summary, the paper describes a laser diode driver based on a step recovery diode capable to generate short current pulses suitable for gain-switching operation. The requirements were obtained using the numerical solutions of rate equations. The experiments with a commercially off-the-shelf laser diode show that the proposed setup is able to provide picosecond pulses with relatively high amplitude. Additionally, the circuit provides easy parameters tuning and pulse-on-demand operation, desired for many applications.

Acknowledgements

The authors would like to thank AM Technologies sp. z o. o. for lending the high-performance measuring equipment necessary for the research.

References

[1]. Z. Yang, X. Wu, D. O. Yang, *et al*., Highly stable adjustable gain-switched semiconductor pulsed seed source, *Optik*, Vol. 179, 2019, pp. 395-400.

[2]. P. P. Vasil'ev, I. H. White, J. Gowar, Fast phenomena in semiconductor lasers, *Reports on Progress in Physics*, Vol. 63, Issue 12, 2000, pp. 1997-2042.

[3]. C. Nguyen, J. Han, Time-Domain Ultra-Wideband Radar, Sensor and Components, *Springer*, 2014.

[4]. P. H. Binh, V. D. Trong, P. Renucci, X. Marie, 100 ps optical pulse generator using laser diodes for visible light communication applications, *Microwave and Optical Technology Letters*, Vol. 56, Issue 1, 2014, pp. 185-187.

(4452)

Wavelength-modulated Interferometer without Inter-axis Dependency

W. P. C. van de Sande [1], L. A. Cacace [1], J. P. Kappelhof [1], R. Hendrix [2] and M. Steinbuch [1]
[1] Eindhoven University of Technology, Control Systems Technology,
De Zaale. 5600MB Eindhoven, the Netherlands
[2] Prodrive Technologies, Science Park Eindhoven 5501, 5692 EM Son, the Netherlands
Tel.: + 31625728636
E-mail: w.p.c.v.d.sande@tue.nl

Summary: Quadrature detection by wavelength modulation can create a cost-efficient and compact displacement-measuring interferometer. Due to the required modulation depth adjustment, these interferometers typically have an inter-axis dependency. This paper presents a novel concept that removes the inter-axis dependency while using a single laser source. The novel interferometer incorporates a delay line in one arm. This delay line reduces the relative variation of the measured distance for a fixed measurement range, such that the wavelength modulation can be kept constant. As the wavelength modulation is constant, a single laser source can be used for independent multi-axes interferometry. A second interferometric measurement determines the drift of the delay line. Therefore the displacement measurement is corrected for thermal drift. The performance of the proposed interferometer has been analyzed through simulations, experimental verification of the low uncertainty has not yet been possible due to excessive noise from the available laser driver.

Keywords: Instruments, Interferometry, Displacement measurement, Wavelength modulation.

1. Introduction

Displacement-measuring interferometers (DMIs) are widely used in high-precision metrology applications and within motion control. These systems are typically characterized by low measurement uncertainty and complex and expensive components [1]. Furthermore, there is an increasing demand for compact fiber-fed sensors that can be integrated into hard-to-reach spaces or operate in harsh environments which may hinder the integration and alignment of free space beam delivery. To address these challenges, wavelength modulation interferometers (WMIs) have emerged as a promising alternative for enabling compact fiber-fed sensors at a lower cost. WMIs use wavelength modulation of a single-frequency laser diode, which allows for more straightforward fiber delivery and eliminates the need for costly components such as acousto optical modulators [2-4].

However, single source WMIs suffer from an inter-axis dependency due to a common wavelength modulation depth for all measurement axes. This dependency arises from the need to tune the wavelength modulation to the path length in the measurement axes to adjust to the varying phase modulation depth. It then leads to a varying phase modulation depth for the secondary axes which results in a varying measurement range for these axes. Therefore, addressing this issue will improve the applicability of WMIs.

2. Wavelength Modulation

Wavelength modulation in combination with a nonzero Optical Path Difference (OPD) results in phase modulation, this phase modulation is used to generate quadrature signals.

2.1. Modulation Depth

Using wavelength modulation to generate phase modulation introduces an OPD dependent phase modulation depth:

$$\delta\phi = \frac{2\pi\delta\lambda\Delta z}{\lambda^2}, \quad (1)$$

where $\delta\phi$ is the phase modulation depth, $\delta\lambda$ is the wavelength modulation depth, Δz is the OPD between the two interfering signals and λ is the wavelength.
The intensity measured at the detector can be described by:

$$I = I_{DC} + \cos(\phi + \delta\phi\cos(\Omega t)), \quad (2)$$

where I_{DC} is the DC part of the interference signal, ϕ is the phase difference, Ω is the modulation frequency and t is the time. As the DC signal is not phase dependent this will be omitted in the further derivation. Using the Jacobi-Anger expansion the observed intensity without offset can be described as:

$$I_{AC} = \sum_{\{k=-\infty\}}^{\infty} J_k(\delta\phi)\cos(\phi + k\Omega t), \quad (3)$$

where J_k is the k-th Bessel function of the first kind. As the Bessel functions are alternating odd and even, the signals after summation have either a sine or cosine response. Using demodulation, the different frequency bands in the modulated interference signal can be

isolated. The odd signals, after demodulation at their respective frequency, can be described by:

$$I_{k\Omega} = -J_{\mathrm{k}}(\delta\phi)\sin(\phi)[1+\cos(2k\Omega t)], \quad (4)$$

The even signals are then described by:

$$I_{\mathrm{k}\Omega} = J_{\mathrm{k}}(\delta\phi)\cos(\phi)[1+\cos(k\Omega t)], \quad (5)$$

Low pass filtering can be used to remove the remaining AC band resulting in two signals in quadrature.

The amplitude of the corresponding signal is proportional to the respective Bessel function. By controlling the phase modulation depth, the amplitude of the signals used can be maximized to achieve a sufficiently high Signal to Noise Ratio (SNR).

2.2. Inter-axis Dependency and Minimal Working Distance

For a sensor with multiple axes and a single laser source, the wavelength modulation depth is equal for all axes. However, if the OPD in these axes are independent of each other, the phase modulation depth can only be controlled for a single axis. A typical example is the displacement measurement of a multi-degree-of-freedom stage. This introduces 'blind spots' in the measurement range of the secondary axes as the SNR reduces significantly and the performance suffers up to the point that no position can be measured. Determining the optimal wavelength modulation for a combination of axis may partly alleviate this issue however, combinations of OPD in different axes still exist where the SNR will be insufficient. This inter-axis dependency severely limits the applicability of such a system in practical application.

Furthermore, such a system typically has a minimum working distance as there is a practical limitation on the maximum wavelength modulation depth as the required large current modulation introduces significant amplitude modulation of the laser diode which can harm the signal processing. This minimum working distance is not only disadvantageous for the space required to place the system but also introduces deadpath error.

3. Novel System

The novel system as will be presented here offers a solution to these limitations by introducing a fiber delay line. This approach creates a common path-length difference for all measurement axes. The light emitted by the laser is split into two paths, with one path consisting of a coiled fiber that introduces an optical path-length difference (OPD) with respect to the other. Both signals travel toward the sensor heads, where each signal is then split in two parts. Inside the sensor head, two interference measurements are performed. In each measurement, a part of the delayed signal is combined with a part of the undelayed signal, resulting in a common displacement between both measurements when a change is observed between the delayed and undelayed signal. To achieve non-common displacement, one part of the delayed signal is sent to a target mirror and one part of the signal travels a through a reference path. The noncommon measured displacement is then the difference between the reference path and the target path, which is the position measurement of interest. As a result of the common displacements, variations in the additional OPD due to environmental influences cancel out by subtracting the measured displacements.

All components except the sensor head are fiber-based reducing alignment and positional stability requirements for separate components and thus reducing the complexity of the system. Furthermore, all these components can be placed in a source unit remote from the measurement such that any heat generated by the laser and electronics does not influence the typically sensitive measurement environment.

A schematic layout of the system is shown in Fig. 1.

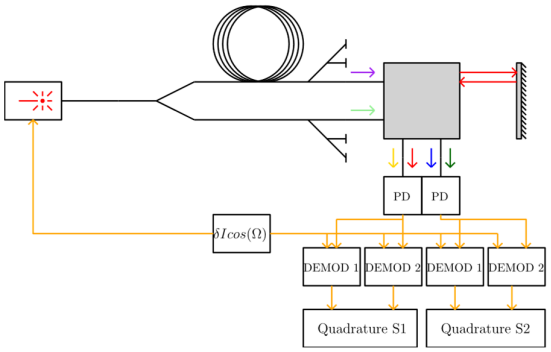

Fig. 1. Schematic layout of the system. In the sensor the purple signal is split in a red and blue signal, and the light green signal is split in dark green and yellow. Then two OPDs are measured, the red path compared to yellow and the blue compared to green measuring the target and delay OPD combined and only the delay OPD respectively. Multiple sensor heads can be connected by use of a fiber splitters. The yellow connections represent electrical signals present in the phase detection.

3.1. Sensor Heads

To ensure accurate and reliable measurements, suitable sensor heads must at least contain have two fiber signal inputs, an optical layout that accounts for all thermal expansion as part of the common displacement, have minimal parasitic interference signals, and have two signal pick-ups, e.g. two photodiodes (PDs).

To reduce the number of sources for parasitic interference signals, a single pass sensor head is preferred as these do not necessarily create a cavity

between the target and the retroreflector typically found in a double pass system. Furthermore, the signals traverse the optical interfaces non orthogonally by tilting the beamsplitter to reduce the contrast of the generated ghost signals.

In Fig. 2 a compact sensor head is shown schematically and a suitable differential sensor head is illustrated in Fig. 3.

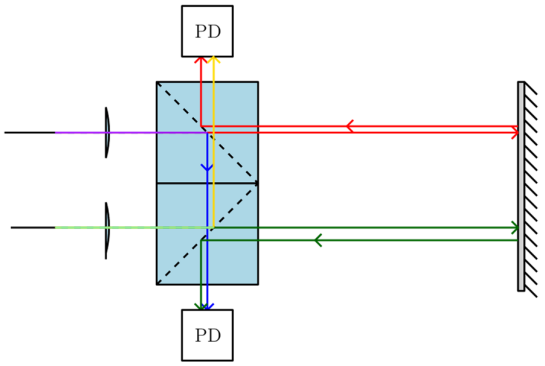

Fig. 2. Schematic layout of a sensor head. The purple (red and blue combined) signal travels through the delay line, and the light green (green and yellow combined) signal has no additional delay, the yellow signal interferes with the red and the green signal with the blue signal.

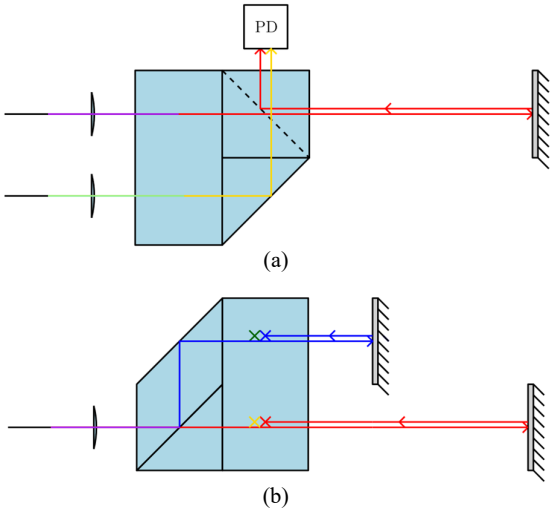

Fig. 3. Schematic layout of a sensor head. (a) depicts a horizontal section, showing only the paths of two of the four signals (b) depicts a vertical section, showing the separation of the blue and red signals. The purple (red and blue combined) signal travels through the delay line and to a target or reference mirror, and the light green (dark green and yellow combined) signal has no additional delay. The yellow signal interferes with the red and the green signal with the blue signal.

With the first layout a part of the undelayed signal and a part of the delayed signal travel toward the target mirror, as a result, the displacement of the target mirror is part of both measurements with an opposing sign. After subtraction, the measurement contains the target distance twice yielding an optical resolution increase from $\frac{1}{2}\lambda$ to $\frac{1}{4}\lambda$ similar to a double-pass interferometer. If the reflecting and transmissing paths inside both beamsplitters are equal, and the beamplitters are mounted against each other this optical layout is thermally balanced for homogenous heating.

In the differential optical layout, the paths inside the sensor head are balanced and parallel with each other to achieve minimal thermal sensitivity such that a non-common displacement results only from a relative displacement between both mirrors or certain thermal gradients in the glass. Both sensor heads consist of non-polarizing beam splitters, thus relaxing alignment tolerances and reducing the number and cost of components. However, a quarter of the intensity reaches the PD compared to a polarizing interferometer. This may be corrected for by using a more powerful laser.

4. Measurement Uncertainty

The novel design has some different contributions to the measurement uncertainty compared to other WMIs.

First, due to the longer OPD compared to typical interferometers wavelength noise in the laser has a higher gain factor compared to an interferometer with no additional OPD. However, phase drift over the OPD due to wavelength drift is common for both measurements, such that the difference in OPD between both measurements the gain is instead of the OPD in a single measurement.

Furthermore, as the wavelength modulation depth is for all target positions the SNR might be slightly lower than for a single axes WMI which optimizes the modulation depth for the current position. And the correction of some nonlinear errors is non-trivial due to the combination of the delay OPD and the target OPD. These effects will be discussed below.

4.1. Signal Strength

As the wavelength modulation depth is constant the ratio between the working range of the sensor and the length of the delay line determines the variation of the phase modulation. A longer delay line reduces the variation but increases the gain of wavelength noise. For the first sensor head, the relation between the range of modulation depths and the delay line length is given as:

$$\frac{\delta\phi_u - \delta\phi_l}{\delta\phi_l} = \frac{4l_{range}}{l_{del} - 2l_{range}}, \tag{6}$$

where $\delta\phi_u$ is the upper bound of the phase modulation depth, $\delta\phi_l$ is the lower bound of the phase modulation depth, l_{range} is the measurement range of the sensor and l_{del} is the length of the additional OPD.

For the second sensor head, the following relation holds:

$$\frac{\delta\phi_u - \delta\phi_l}{\delta\phi_l} = \frac{2l_{range}}{l_{del}} \quad (7)$$

The minimum signal strength over this range is given by the smallest of the used demodulated signals and is proportional to the respective Bessel function, to maximize the smallest signal over the measurement range the wavelength modulation depth should be chosen such that the following equation is satisfied:

$$J_n(\delta\phi_u) = J_{n+1}(\delta\phi_l), \quad (8)$$

where J_n is the lowest order used Bessel function and J_{n+1} is the second used Bessel function.

Due to the single-pass layout, a tilt of the target mirror reduces the interference contrast. The placement of an aperture in front of the photodiode reduces the phase variation seen by the detector. Using numerical simulation to determine the relationship between the target tilt, target distance and signal amplitude the angular working range for the interferometer can be predicted. In Fig. 4 the relative AC amplitude is shown for multiple combinations of mirror tilt and target distances. For a distance up to 1 m a target tilt of 0.3 mrad reduces the interference amplitude with a factor of 0.8.

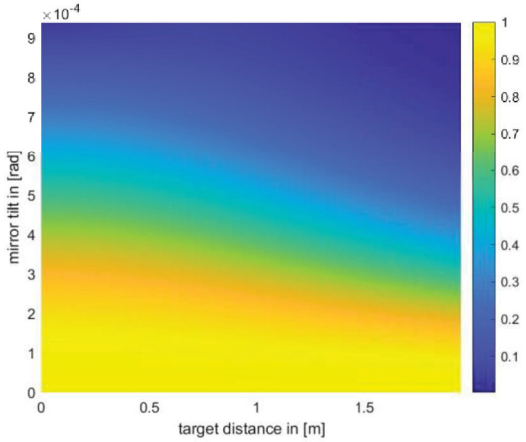

Fig. 4. Numerical calculation of the relative interference amplitude with respect to the target mirror tilt and target distance for a 1 mm aperture.

Using these results combined with a system consisting of a 10 mW laser diode divided over four channels, three for different sensor heads and one for a wavelength reference channel, a 10 m delay line and a measurement range of 1 m the relation between the acquisition noise and position noise can be simulated. In Fig. 5 the relation between the noise spectral density of the photodiode amplifiers and position error is shown.

For the laser driver a custom driver is being designed, this driver is anticipated to have noise power below 10 pA, and with the predicted driver noise the contribution to the position noise is predicted to be approximately 140 pm.

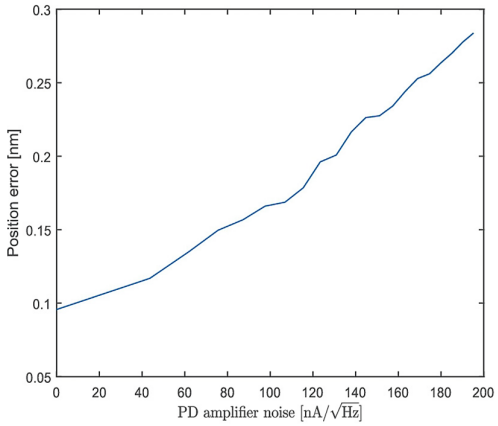

Fig. 5. Position error standard deviation with respect to PD amplifier noise in the absence of laser driver noise.

4.2. Nonlinear Error

In the proposed interferometer, the measurement signal consists not only of the target distance cavity but also of an additional delay length. As a result, not all nonlinear errors due to parasitic interference signals (PIS) can be corrected through ellipse fitting. The offset phase due to the delay can vary with environmental changes, which affects the PIS independently of the measured OPD. Therefore, the parasitic noise level (PNL) is divided into two classes. The first group includes PNL caused by ghost reflections inside the target cavity that reflect a second time from the target mirror and those caused by the ghost reflection of the front facet of the sensor, which does not reflect from the target mirror at all. These errors can not be corrected and therefore should be minimized in the design The other, second-order, ghost reflections produce a constant phase offset for the signal they originate from those changes slightly with the thermal expansion of the sensor. However, as the thermal expansion generates a much larger measured displacement, multiple fringes can be measured, and ellipse fitting can be used to continuously correct the variations in the phase offset. The second group of PNL has minimal effect and can be compensated by algorithms.

The effect of PIS on the phase can be linearized if the PIS is small compared to the main signal. An estimation of the maximum phase error is given by:

$$\Delta\phi_{PIS} = \frac{J_n(\delta\phi_{PIS})E_{PIS}}{J_n(\delta\phi)E_s}, \quad (9)$$

where the *n* is chosen from the two used signals in such a way that the ratio between is maximum, E_{PIS} is the electric field amplitude of the PIS and E_s the electric field strength of the desired signal.

Using an AR coating with a reflectivity of 0.25 % and a wedge of 1 mrad of the last surface of the sensor head to reduce both the amplitude and the contrast of the PIS the non-correctable nonlinear error reduces to 0.6 nm for a wavelength of 1550 nm.

5. Discussion

While the proposed interferometer has shown promising results through simulations, experimental verification is necessary to validate its performance. A first step has been made to validate the principle with available lab equipment, a displacement has been measured with this setup. However, this equipment was not suitable for verification of the measurement uncertainty as it produced excessive noise that affected the position measurement.

The excessive noise caused a significant amount of position noise. Furthermore, it led to the phase detection incidentally detecting non-existing 2 pi phase jumps. As a result, we were unable to accurately measure the phase difference and obtain the correct displacement measurements. Using a suitable laser driver with noise levels within specification is the next step in this research.

Despite this setback, we are confident that the proposed interferometer has the potential to provide nanometer-level precision with multiple independent axes measurements.

6. Conclusions

The proposed single source interferometer has the potential to achieve nanometer precision with multiple independent axes, making it suitable for a broad range of applications where high-precision measurement is crucial. Its ability to eliminate the inter-axis dependency while using wavelength modulation makes it a cost-effective alternative to complex heterodyne systems, with low measurement uncertainty and insensitivity to environmental influences. Additionally, there is no minimum required measurement distance, enabling sensor placement to minimize the death-path error.

With further optimization and experimental validation, this interferometer can become a valuable tool in various high-precision applications.

Acknowledgements

Authors acknowledge financial and material support from Prodrive Technologies.

References

[1]. V. G. Badami, P. J. de Groot, Displacement measuring Interferometry, in Handbook Of Optical Dimensional Metrology (K. Harding, Ed.), *CRC Press*, Boca Raton, 2016.

[2]. K. Thurner, F. P. Quacquarelli, P. F. Braun, C. Dal Salvio, K. Karrai. Fiber-based distance sensing interferometry, *Applied Optics*, Vol. 54, Issue 10, 2015, pp. 3051-3063.

[3]. O. Geberding, K. S. Isleif, Ghost beam suppression in deep frequency modulation interferometry for compact on-axis optical heads, *Sensors*, Vol. 21, Issue 5, 2021, 1708.

[4]. B. K. Nowakosski, D. T. Smith, S. T. Smith, Highly compact fiber Fabry-Perot interferometer: A new instrument design, *Review of Scientific Instruments*, Vol. 87, Issue 11, 2016, 115102.

(4546)

High-energy Few-optical-cycle Multispectral NIR-SWIR-MIR Laser Based on OPCPA and Stimulated Raman Scattering

A. Petrulėnas, P. Mackonis, A. Černeckytė and A. M. Rodin
Center for Physical Sciences and Technology, Solid State Laser laboratory,
Savanoriu 231, LT-02300 Vilnius, Lithuania
Tel.: +37067094170
E-mail: augustinas.petrulenas@ftmc.lt

Summary: The developed easily reproducible few-optical-cycle high-energy NIR-SWIR-MIR laser is well suited for driving secondary emission sources. It is based on the combination of optical parametric chirped pulse amplification (OPCPA) with transient stimulated Raman chirped-pulse amplification (TSRCPA). For pumping OPCPA and TSRCPA in the local spectral ranges, the same two-stage Yb:YAG chirped-pulse amplifier with ~1.2 ps, ~20 mJ output pulses at 1030 nm was used, which ensured internal synchronization by excitation of a multi-octave supercontinuum seed. TSRCPA in KGW exhibits a bandwidth of over ~40 nm and has proven itself as a possible replacement for OPCPA and as a complimentary technique for improving signal-to-idler conversion efficiency. Spectral extension beyond 2.5 μm is achieved due to the vibrational-rotational TSRCPA in H_2, N_2, SF_6 and their mixtures. Spectral ranges can be adapted on demand and in the current implementation correspond to ~1.1 μm, ~2.1 μm and >2.4 μm with energy of >2 mJ achieved in pulses compressed to ~38 fs with ~25 % pump-to-signal conversion efficiency.

Keywords: OPCPA, Supercontinuum, SRS, TSRCPA, SWIR, MIR, Pulse compression.

1. Introduction

Femtosecond laser sources in the short and mid-infrared (SWIR-MIR) wavelength range (2–3 μm) are in demand for a wide range of applications in molecular spectroscopy, strong-field physics, chemistry, biology, medicine, industry, remote sensing, and free-space communication. Increasing the efficiency of secondary THz and soft X-ray sources through the high harmonics generation (HHG) [1], as well as obtaining sub-cycle isolated attosecond pulses by waveforms synthesis, requires not only increasing the wavelength of high-energy few-cycle pulses, but also developing high-intensity multispectral driving lasers operating simultaneously in the NIR, SWIR, and MIR ranges with internal synchronization [2].

When developing few-cycle high-energy NIR-SWIR-MIR lasers, besides optical parametric chirped pulse amplification (OPCPA), an alternative approach based on transient stimulated Raman chirped-pulse amplification (TSRCPA) can also be used. In the transient regime ($\tau_P < T_2$) a much wider gain bandwidth becomes available. Indeed, OPCPA with a ~1 μm driving laser can reach mJ energy in few-cycle pulses. Usually, the seed pulses for SWIR OPCPA are obtained using the difference frequency generation (DFG). However, the direct use of a supercontinuum (SC) seed simplifies the SWIR OPCPA by eliminating the need for active synchronization between the seed and the pump lasers.

We describe an affordable and easily reproducible high-energy few-optical-cycle multispectral laser system based on OPCPA and TSRCPA with multi-octave SC seed source and a 1.2 ps Yb:YAG pump laser common to all stages. We have shown TSRCPA as a complementary approach to OPCPA for idler energy buildup. Experiments are discussed on the transfer of the laser radiation spectrum beyond 3 μm due to vibrational TSRCPA in gases.

2. Experiment Setup

The experimental setup of the NIR-SWIR-MIR laser system is shown in Fig. 1. A common pump source for SC, OPCPA, and TSRCPA is a self-made two-stage double-pass Yb:YAG chirped-pulse amplifier (CPA) providing transform-limited 1.2 ps pulses with an output energy of up to 20 mJ at 100 Hz [3]. SC seed pulses in the spectral range of 1050-2400 nm for both TSRCPA and OPCPA were generated in a YAG crystal using a small portion of the pump pulse. The NIR spectral range of SC was amplified in two successive TSRCPA stages based on KGW crystals, tuned to vibrational modes of 901 and 767 cm^{-1}, respectively, and the amplified pulses were compressed using SF11 prisms. The SWIR-MIR spectral range of SC at 1900–2400 nm was amplified in a three-stage noncollinear OPCPA based on BiBO crystals, and the amplified pulses were compressed in Suprasil-300 glass plates. These pulses were directed to a high-pressure gas cell filed with H_2, N_2, SF_6, and their mixtures in order to expand the spectrum in the MIR by excitation of the rotational TSRCPA.

To increase the idler energy, a collinear OPCPA with TSRCPA based on a KGW 45 mm long was used. Output pulses in the wavelength range ~1800-2000 nm for the signal and ~2100-2400 nm for the idler were used as pump and Stokes seed, respectively.

3. Results and Discussion

After TSRCPA, the largest spectral bandwidth (~40 nm) of amplified Stokes pulses with a positive chirp is sufficient for a transform-limited pulse width of ~50 fs (Fig. 2a). At the optimal pump energy, the maximum conversion efficiency after two KGW stages was 35 %. Compression of the amplified pulses was limited by the residual third-order dispersion (Fig. 2b).

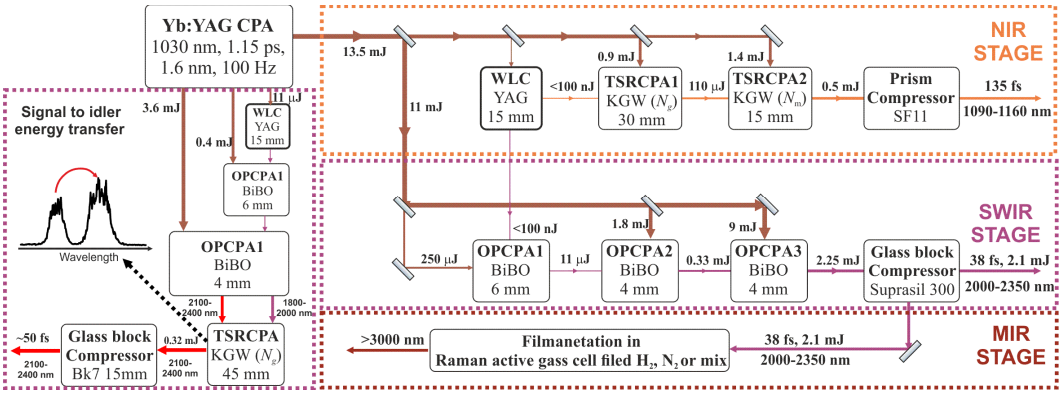

Fig. 1. Experimental setup of the NIR-SWIR-MIR laser system based on OPCPA and TSRCPA.

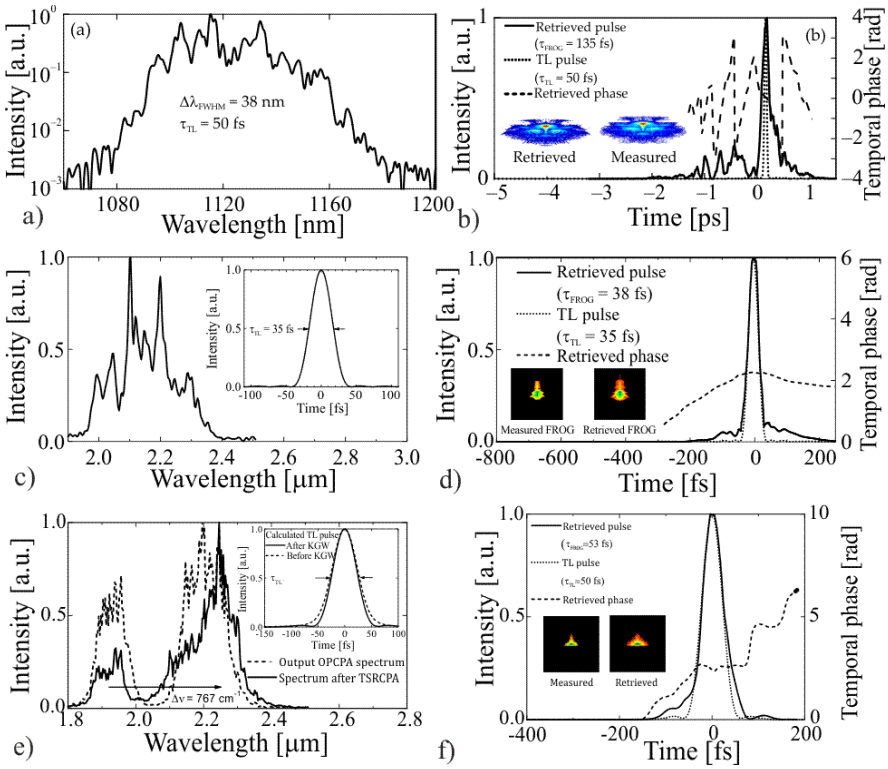

Fig. 2. a) TSRCPA output spectrum, and b) temporal shape and (solid) and phase (dashed) after compression; c) OPCPA output spectrum (Inset – transform-limited temporal shape calculated from the measured spectra), and d) temporal shape (solid) and phase (dashed line) of the compressed pulse; e) Idler spectra after (solid) and before (dashed) TSRCPA; f) temporal shape (solid) and phase (dashed) of compressed idler pulse.

OPCPA provides an output energy of 2.25 mJ with a pump-to-signal conversion efficiency of ~25 % at a pump intensity of ~30 GW/cm^2. The spectrum of amplified pulses spanned ~1.95–2.4 μm with a bandwidth corresponding to a transform-limited pulse width of 35 fs (Fig. 2c, inset), i.e., <5 cycles at 2.15 μm. After compression, the output energy reaches ~2.1 mJ at a pulse width of 38 fs, which corresponds to ~5 cycles at 2.15 μm (Fig. 2d) at a pulse intensity of 47 GW.

A significant increase in the idler pulse energy ~33 % and signal depletion were observed after

TSRCPA in SWIR-MIR spectral range (Fig. 2e) at an incident signal intensity of ~18 GW/cm^2. The amplified idler pulse was compressed in BK7 to 53 fs (Fig. 2f).

Compressed SWIR OPCPA pulses were directed to a high-pressure TSRCPA cell filled with hydrogen, which ensured spectrum expansion to the MIR spectral range by >200 nm and up to ~40 % Stokes conversion efficiency.

4. Conclusions

We have developed a NIR-SWIR-MIR laser system based on multi-octave generation of SC, OPCPA and TSRCPA with 1.2 ps Yb:YAG CPA as a common pump source. The TSRCPA stages based on KGW form a high-energy femtosecond laser source at a central wavelength of 1120 nm. Meanwhile BiBO-based OPCPA stages form a SWIR-MIR source of 38 fs laser pulses with output energy of ~2.1 mJ. The combination of OPCPA with TSRCPA significantly increases the idler pulse energy at the Stokes wavelength in the SWIR-MIR spectral range. Finally, additional opportunities for expanding the spectrum towards the MIR spectral range using a rotational TSRCPA in a high-pressure gas cell are demonstrated.

Acknowledgements

This research was funded by Research Council of Lithuania under contract S-MIP-23-74 and NATO Science for Peace and Security Programme under grant G5734.

References

[1]. S. Ghimire, A. D. DiChiara, E. Sistrunk, P. Agostini, L. F. DiMauro, D. A. Reis, Observation of high-order harmonic generation in a bulk crystal, *Nature Physics*, Vol. 7, 2011, pp. 138-141.

[2]. S. W. Huang, G. Cirmi, J. Moses, K. H. Hong, S. Bhardwaj, J. R. Birge, L. J. Chen, E. Li, B. J. Eggleton, G. Cerullo, F. X. Kartner, High-energy pulse synthesis with sub-cycle waveform control for strong-field physics. *Nature Photon*, Vol. 5, 2011, pp. 475-479.

[3]. P. Mackonis, A. M. Rodin, Laser with 1.2 ps, 20 mJ pulses at 100 Hz based on CPA with a low doping level Yb:YAG rods for seeding and pumping of OPCPA, *Optics Express*, Vol. 28, Issue 2, 2020, pp. 1261-1268.

(4547)

1D V- and U-shaped IP-Dip Structures for Surface-enhanced Raman Spectroscopy

I. Lettrichova, D. Pudis, D. Jandura and P. Gaso
University of Žilina, Dept. of Dept. of Physics, 1 Univerzitna, 010 26 Zilina, Slovakia
Tel.: + 421 41 513 23 20
E-mail: lettrichova@fyzika.uniza.sk

Summary: In this paper, we present gold-coated 1D structures patterned in the surface of IP-Dip polymer by direct laser polymerization. The 1D structure consists of parallel rods with two different profiles: V- and U-shape. The period of structure is 3 μm. Afterwards, an Au layer with 3 different thicknesses (5 nm, 10 nm and 20 nm) is evaporated. Transmission spectra were simulated and measured for characterization of prepared structures. Examination of absorption peaks in transmission spectra and their shift with Au thickness leads to definition of resonant wavelengths of localized surface plasmon polariton that can be present at the rod edges in metal-dielectric interface. Definition of such wavelength make these structures useful as Surface-enhanced Raman spectroscopy substrates.

Keywords: Polymer-based materials, IP-Dip, Surface-enhanced Raman spectroscopy, SERS substrate.

1. Introduction

For the development of selective and sensitive analytical procedures, the Surface-enhanced Raman spectroscopy (SERS) is very attractive [1]. It combines advantages of vibration-based Raman spectroscopy with signal enhancing techniques. As the energy spectrum of molecular vibrations serves as a characteristic and unique fingerprint for the chemical composition of a sample, the Raman spectroscopy provides fast and accurate identification and quantification. Although it requires little or no sample preparation and it is applicable to many types of hazardous materials, Raman scattering is an extremely week effect. For this reason, often signal enhancing techniques are employed for detection methods [2].

If the scattering molecule is placed near a roughened metal substrate, the magnitude of Raman scattering can be considerably enhanced [1]. Thanks to surface plasmon in nanoscale features of metal surface excited by visible light, strong electromagnetic fields are generated, what leads to enhancement in Raman signal. This enhancement factor is on the order of $10^6 – 10^7$, or in case of resonance as high as $10^{12} – 10^{14}$ [3]. The resonant frequency of the conduction electrons in a metal-dielectric nanostructure depends on the size, shape and material of nanoscale features.

A large variety of different SERS active substrates has been realized for different SERS applications introducing different planar and three dimensional (3D) technologies. Very promising alternative is single-step process based on direct laser polymerization in a volume of liquid polymers. It leads to exceptional variable designs of 3D structures with submicrometer resolution. In combination with metal deposition, effective SERS substrates can be prepared [4-6].

2. Experimental

We present gold-coated 1D structures patterned in the surface of IP-Dip polymer. Nanoscribe Photonic Professional GT laser lithographic system based on direct laser writing was used for structure fabrication. The laser focuses into the volume of IP-Dip photoresist, where two-photon polymerization process arises in the focal spot volume with lateral resolution achieving 200 nm and vertical resolution of 600 nm.

Prepared structures consists of parallel rods with two different profiles: V- and U-shape. The period of structure is defined by the rod basis dimension – 3 μm. The length of the rods is about 100 μm which is long enough to neglect the edge effect of the structure. In the next step, an Au layer with 3 different thicknesses (5 nm, 10 nm and 20 nm) is evaporated.

Transmission spectra were simulated and measured for characterization of prepared structures. Transmission spectrum was measured using halogen lamp coupled to a multimode optical fiber with core diameter of 50 μm. The optical fiber illuminated the structure surface in the central part of squared area of the structure. The transmitted light was collected by 100 μm optical fiber on the substrate side of the sample app. 0.5 mm from the substrate surface. As a reference spectrum, a transmission spectrum of corresponding (5 nm, 10 nm and 20 nm) thin gold layer on the glass substrate was considered.

3. Results

In the Fig. 1a and 1b, there are shown SEM images of prepared 1D V- and U-shaped IP-Dip structures, respectively.

1D structures consisting of rods with 3 μm base and 20 nm Au layer are shown. The V-shaped structure

simulates the commercial silicon-based SERS substrates. In order to create and control the possible hot spot, the U-shaped profile was proposed. At the edges of the rods, after Au evaporation, the sharpened metal profile is created, which can lead to localized surface plasmon polariton (LSPP) formation.

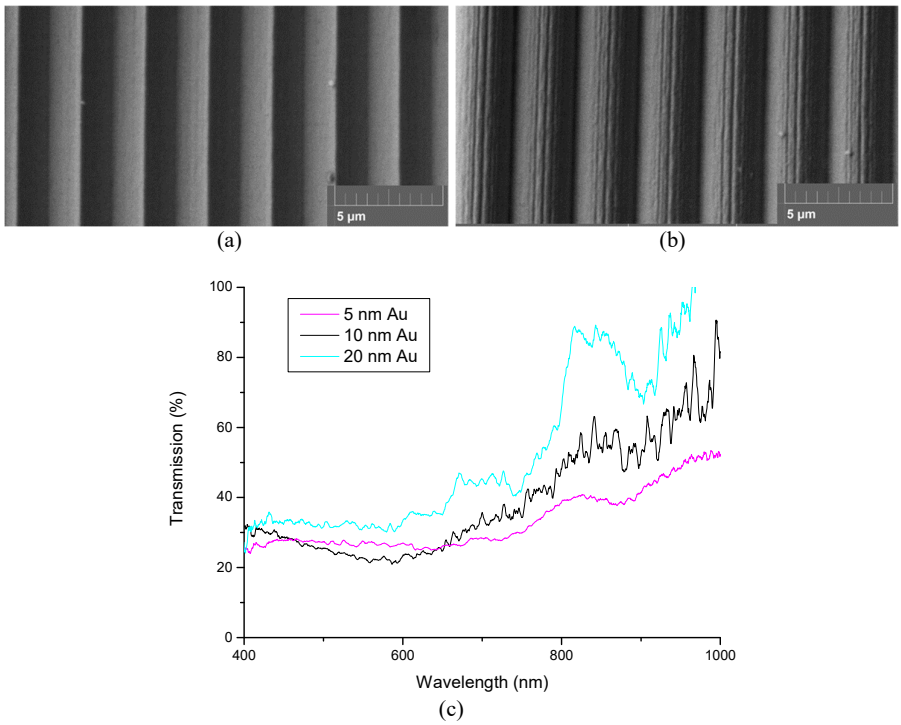

Fig. 1. Scanning electron microscope image of 1D a) V-shaped, and b) U-shaped IP-Dip polymer structure; c) Transmission spectra of the 1D U-shaped structure with 5 nm, 10 nm and 20 nm Au layer.

The detailed SEM image documents layer-by-layer technology process, where the structure slicing of app. 200 nm can be visible. According to Mu et al., it can lead to SPP resonance formation [7].

The measured transmission spectra of 1D U- shaped IP-Dip structures with three different gold thickness (5 nm, 10 nm and 20 nm) are shown in Fig. 1c. As the reference, the unpatterned glass substrate with corresponding Au layer was used. The transmission is a function of wavenumber with several local minima. Most of them derive from the diffraction on the 3 µm structure and they are shifted while scanning the surface of the sample. On the other hand, the minimum at app. 900 nm is not diffraction-based, and it is shifted with different Au layer thickness. For this reason, it is a potential candidate for the resonant wavelength of LSPP at metal-dielectric interface, what makes these structures useful as SERS substrates.

4. Conclusions

The transmission measurements of prepared structures show usability of prepared structures for SERS. Further simulation and investigation of rod profile has to be done in order to enhance the Raman signal for application in SERS.

Acknowledgements

This work was supported by grant agency of Ministry of Education, Science, Research and Sport of the Slovak Republic projects VEGA 1/0363/22, and APVV 20-0264. This publication was realized with support of Operational Program Integrated Infrastructure 2014-2020 of the project: Innovative Solutions for Propulsion, Power and Safety Components of Transport Vehicles, code ITMS 313011V334.

References

[1]. M. Fleischmann. P. J. Hendra, A. J. McQuillan, Raman spectra of pyridine adsorbed at a silver electrode, *Chemical Physics Letters*, Vol. 26, 1974, pp. 163-166.
[2]. P. L. Stiles, J. A. Dieringer, N. C. Shah, R. P. V. Duyne, Surface-enhanced Raman spectroscopy, *Annual Review of Analytical Chemistry*, Vol. 1, 2008, pp. 601-626.
[3]. S. Nie, S. R. Emory, Probing single molecules and single nanoparticles by surface enhanced Raman scattering, *Science*, Vol. 275, 1997, pp. 1102-1106.
[4]. S. Z. Oo, S. Siitonen, V. Kontturi, D. A. Eustace, M. D. B. Charlton, Disposable gold coated pyramidal SERS sensor on the plastic platform, *Optics Express*, Vol. 24, Issue 1, 2016, pp. 724-731.

[5]. W. Zhao, et al., Polymer nanopillar array with Au nanoparticle inlays as a flexible and transparent SERS substrate, *RSC Advances*, Vol. 6, 2016, pp. 35527-35531.
[6]. X. Zhao, et al., Flexible and stretchable SERS substrate based on a pyramidal PMMA structure hybridized with graphene oxide assivated AgNPs, *Applied Surface Science*, Vol. 455, 2018, pp. 1171-1178.
[7]. J. Mu, J. Li, W. Li, Q. Luo, Ch. Gu, Hollow metallic pyramid plasmonic structures fabricated by direct laser writing and electron beam evaporation, *Microelectronic Eng.*, Vol. 110, 2013, pp. 307-310.

(4600)

Detecting and Deflecting the Death Asteroid

C. Phipps
Photonic Associates, LLC, 200A Ojo de la Vaca, Santa Fe, NM, USA
Tel.: +1-215-358-4360, fax: +1-505-466-3877
E-mail: crphipps@aol.com

Summary: In this paper we claim that the most likely surprise visit from an epoch-ending NEO is one arriving radially from the Oort Cloud. We then propose using the Breakthrough Starshot laser to slow the object enough to avoid an epoch-ending collision with Earth, assuming that it has been funded and built. We show that the likely low reflectivity of a "dirty iceball" approaching Earth is so low that the NEO will not be detected until it has approached to within 0.35 AU from Earth, with a velocity that gives about 2 weeks to react. This detection depends on raster-scanning the sky. Given 100 GW from Breakthrough Starshot applied during that period, we show that a collision can be avoided, by slowing the NEO just enough that the Earth passes the collision point prior to predicted collision.

Keywords: Death asteroid, Breakthrough starshot, Laser propulsion, NEO.

1. Introduction

The work of Alvarez [1] used the presence of thin layers of iridium all around the Earth to show that a giant meteor strike caused the K-T extinction 66M years ago. This led to the collapse of ecosystems and the extinction of most terrestrial species. This work initiated a discussion of planetary defense. Since that point, NASA's Asteroid Terrestrial-impact Last Alert System (ATLAS) has been developed. It uses four telescopes to search the entire sky for hazardous NEO's (near Earth objects) every 24 hours. However, it is designed to detect near Earth objects (NEO's) that approach Earth closer than 2.6E-5 AU. If such a NEO is co-orbiting with Earth, that is useful information. However, if it is approaching radially, having begun in the Oort Cloud, this object will have a velocity of 40-60 km/s as it approaches Earth, giving us on Earth only a few days to react. The work of NASA has determined the orbit of 95 % of co-orbiting objects large enough to do damage. Over the past 20-years, NASA's Spaceguard Profram [2], including JPL"s Asteroid Watch program [3], NASA's NEOWISE space telescope [4] and Pan-STARRS[5] on Haleakala have collectively determined 95 % of the orbits of objects larger than 140 m that have orbits inside that of Jupiter [6]. By definition, because they are known, these co-orbiting objects are not the threat that will destroy us. On the contrary, it's obvious that an object approaching radially toward the sun, originating in the Oort Cloud at or beyond 10k AU, detected on first approach, will constitute the surprise. Such an object might be coming from the direction of the Sun, which would be a hopeless case for us on Earth. In this paper, we will address large objects coming in from the Oort Cloud opposite the Sun, and discuss how to detect and deflect them.

2. Detection

There are two different solid angles involved in detection of targets illuminated by the sun. First is background B,

$$B = B_\lambda(\pi d_s^2/4)(\Delta\lambda)(\pi D_b^2/4)/(\pi z^2), \qquad (1)$$

with background spectral intensity B_λ in units of W/(m^{2}sterrad-μm). Second is signal S, given by

$$S = R_\lambda I_\lambda(\pi D^2/4)(\Delta\lambda)(\pi D_b^2/4/(\pi z^2), \qquad (2)$$

with spectral reflectivity R_λ per sterradian-μm. In Eq. (2), I_λ = 1000 W/(m^{2}sterrad-μm), B_λ = 1E-6 W/(m^{2}sterrad-μm) [7], D_b is launch mirror diameter, D is target diameter, z is range and $\Delta\lambda$ is detector bandwidth in μm. d_s is the search aperture in the target plane, limited by apertures in the detector array. Combining Eqs. (1) and (2), the signal to background ratio is given by

$$S/B = \frac{R_\lambda I_\lambda D^2}{B_\lambda d_s^2}, \qquad (3)$$

depending solely on the ratio of target area to search area, R_λ, and the ratio I_λ/ B_λ.

Many incoming NEO's originating in the Oort Cloud will be "dirty iceballs", basically comet nuclei with spectral reflectivity R_λ as small as 0.03 [8]. Even if R_λ = 0.3, with I_λ and B_λ as above, a barely detectable object with S/B = 2 will require $d_s^2/D^2 \leq$ 3E6 in order to not be overwhelmed by the background. Search solid angle is

$$\Omega_s = (\pi/4)(d_s/z)^2 = \frac{\pi}{4}\frac{R_\lambda I_\lambda D^2}{B_\lambda (S/B) z^2} \qquad (4)$$

In terms of d_s/z, or, using Eq. (3), in terms of D/z.

Then, the number of searches to ensure detection as a function of detection range z and object diameter in a sky with solid angle 2π is

$$N = 2\pi/\Omega_s = 1.79E23\frac{B_\lambda(S/B)z_{AU}^2}{R_\lambda I_\lambda D^2}, \quad (5)$$

where we have recast z in astronomical units (AU). If the search rate is f spots/s the time to search the sky successfully is N/f,

$$T = 1.79E23\frac{B_\lambda(S/B)z_{AU}^2}{R_\lambda I_\lambda D^2 f} \quad (6)$$

Fig. 1 shows the time required by a single telescope to search the whole sky at f = 1000 spot/s and find the oncoming NEO as a function of its size and range on detection.

We note that even a 1 km diameter NEO will not be detected much further than 0.3 AU in a reasonable amount of time to react to it, because of the terrific approach speeds calculated in the "Urgency" section.

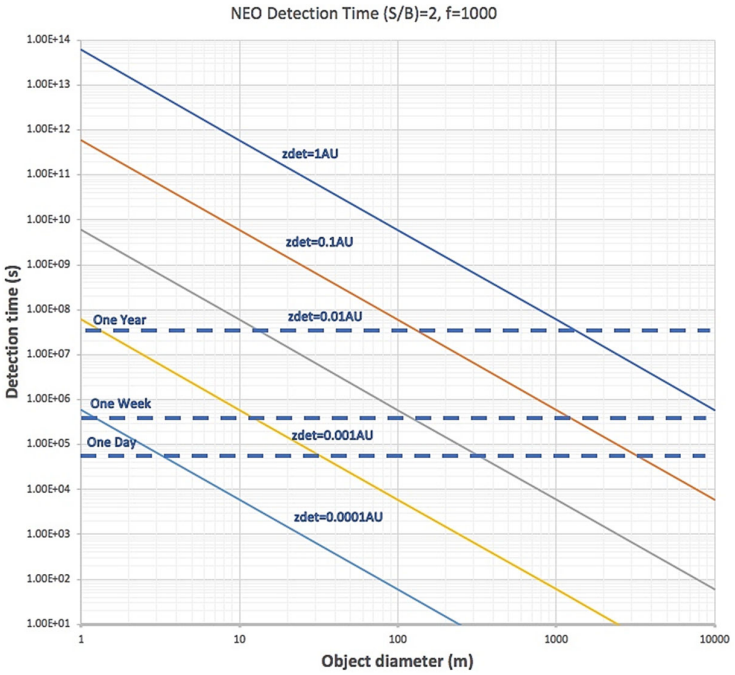

Fig. 1. Time for detection of the NEO as a function of its diameter and distance.

2.1. Photoelectron Count

There is a lower limit on f: we must detect enough photoelectrons to limit dark noise to a few percent. Basically, that means $N_{pe} > 1000$. We can calculate that, starting from S with λ = 1 μm, to find

$$N_{pe} = S/(hc/\lambda f) = 1.39E-4\frac{R_\lambda I_\lambda D^2 D_b^2}{z_{AU}^2 f} \quad (7)$$

Picking values that will be of interest to u s, with R_λ = 0.3, I_λ = 1000, Eq. (7) gives $N_{pe} = 0.042(D^2D_b^2/(z_{AU}^2 f)$, which reduces to $N_{pe} = 1000$ at $fz_{AU}^2/(DD_b)^2 = 4.16E\text{-}5$. For example, if D = 1 km, D_b = 3 m and z_{AU} = 0.35 we have f ≤ 3060. Such a scanning speed can be achieved with an electro-optic scanner. Large f is important to give reasonable values of T. f is achieved by raster-scanning across the sky.

2.2. Urgency

To give an idea of the urgency of action after detection, we present what will be a typical scenario for an Oort object arriving at Earth in Fig. 2. The so-called *vis viva* equation gives the velocities for an object orbiting a fixed point in a lossless orbit, in this case, the Sun

$$v^2 = \mu(2/r - 1/a) \quad (8)$$

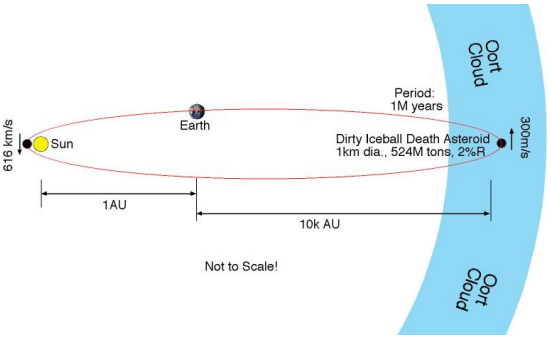

Fig. 2. Orbit of the Oort cloud object (not to scale).

In Eq. (8), μ is the gravitational constant, GM, M is the sun's mass, r is the heliocentric radius of the orbit and a is the aphelion. We take the object's velocity in the Oort cloud to be 300 m/s, due to a nudge by some other object which sends it toward Earth. Its new

orbital period is 1M years. Its velocity in the vicinity of Earth is 42 km/s and at the Sun 616 km/s. If we detect it at 0.35 AU, for example, we have only 14.4 days to react before it hits (Fig. 3).

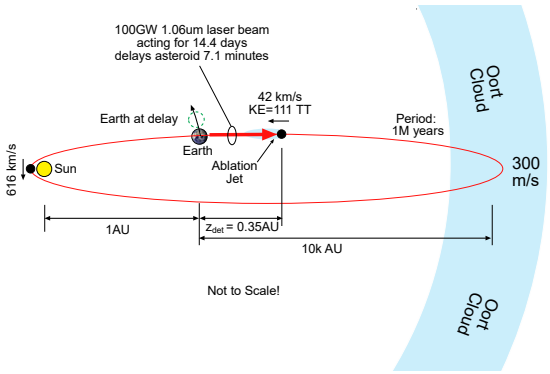

Fig. 3. Limited time to react.

The kinetic energy of this 1 km diameter NEO as it approaches Earth is 1.11E14 tons explosive equivalent, or 1.11E8 megatons, well above the threshold defined by Morrison, Chapman and Slovic [9] for irreversible global catastrophe.

3. Deflection Methods

Several methods have been suggested to deflect an oncoming epoch-ending NEO. These are 1) a standoff nuclear explosion [10], 2) a direct hit by a high velocity spacecraft [11] and 3) gentle slowing of the object by a high power laser [12].

At 42 km/s, there is no way that current rocket technology could fly up, reverse, and match its speed to that of the NEO in order to deflect it with a standoff nuclear explosion. That would require 126 km/s propulsion capability. Even if you could, you would not have a second chance. Fig. 3 showed the kinetic energy of a 1 km diameter iceball is 111teratons explosive equivalent, equal to more than a million 100 MT nuclear weapons.

In October, 2022, NASA made a lot of news by deliberately hitting a stony asteroid with a high speed spacecraft. This was advertised as “planetary defense.” However, striking a dirty iceball with a cannon ball is exactly what you don’t want to do. Doing this would create a dispersed cloud of high speed objects re-entering the atmosphere and cooking us in a 2000 K oven. This is what happened at the dinosaur extinction. In that case, the asteroid blasted a cloud of pieces out of the Earth, which re-entered all over the planet and cooked lifer on Earth for ten hours.

Reference [12] featured a high power pulsed laser. Here we consider instead the effects of a 100 GW CW laser on Earth such as that proposed by the Breakthrough Starshot program [13]. We will show that applying 100 GW (suitably focused to produce ablation on the NEO) for 14.4 days will decelerate the 1 km diameter NEO sufficiently to delay its arrival by 420 seconds. In this interval, the Earth moves 2 Earth radii, avoiding collision with the NEO. To maintain continuous illumination of the NEO will require three Breakthrough Starshot lasers on Earth. The laser is far too large to be based in space.

References

[1]. L. W. Alvarez, F. Asaro, H. V. Michel, Extraterrestrial cause for the Cretaceous-Tertiary extinction, *Science*, Vol. 208, 1980, pp. 1095-1108.
[2]. Spaceguard, https://en.wikipedia.org/wiki/Spaceguard
[3]. Asteroid Watch: Keeping an Eye on Near-Earth Objects, https://www.jpl.nasa.gov/asteroid-watch
[4]. NEOWISE, https://www.jpl.nasa.gov/missions/neowise
[5]. Pan-STARRS, https://en.wikipedia.org/wiki/Pan-STARRS
[6]. Twenty Years of Tracking Near-Earth Objects, https://www.jpl.nasa.gov/news/twenty-years-of-tracking-near-earth-objects
[7]. C. W. Allen, Astrophysical Quantities, *Athlone*, London, 1973.
[8]. C. Phipps, Can lasers play a rôle in planetary defense?, *AIP Conference Proceedings*, Vol. 1278, 2010, pp. 502-508.
[9]. D. Morrison, C. Chapman, P. Slovic, The impact hazard, in Hazards due to Comets and Asteroids, *U. of Arizona Press*, 1994.
[10]. V. Gadzgieva, V. Nogin, O. Shubin, V. Simonenko, Effect of nuclear burst on asteroids, in *Proceedings of the Livermore Planetary Defense Workshop*, 22-26 May 1995, pp. 371-376.
[11]. NASA DART Mission, https://www.nasa.gov/press-release/nasa-confirms-dart-mission-impact-changed-asteroid-s-motion-in-space
[12]. C. Phipps, Lasers can play an important role in planetary defense, in *Proceedings of the Livermore Planetary Defense Workshop*, 22-26 May 1995, pp. 325-331.
[13]. K. Parkin, The breakthrough starshot system model, *Acta Astronautica*, Vol. 152, 2018, pp. 370-384.

(4618)

Integration of the Three Dimensional GaP Nanocone onto Single Mode Optical Fibre

J. Novák [1], A. Rosova [1], D. Pudis [2], S, Hasenohrl [1] P. Elias [1], I. Lettrichová [2]
[1] Institute of Electrical Engineering, Slovak Academy of Sciences, 84104 Bratislava, Slovakia
[2] Department of Physics, University of Žilina, Univerzitna 1, 01026 Žilina, Slovakia
Tel.: + 4212 5922 2468, fax: + 4212 5477 5816
E-mail: eleknova@savba.sk

Summary: This paper is focused on a novel and nonconventional design and realization of nano-optical probes prepared using the 3D shaped gallium phosphide (GaP) semiconductor nanocones (NCs) deposited onto single mode optical fiber. These NCs were prepared by metal organic vapor phase epitaxy and transferred onto single mode optical fiber using Focused Ion Beam (FIB) technique. Nano-optical probes using this novel treatments and nano-fabrication promises a low-cost, high-throughput, and reproducible manufacturing leading to unique near-field probes.

Keywords: Nanocone, Optical sensor, Near field probe, Focused ion beam technique.

1. Introduction

The widespread adoption of plasmonic and nano-optical devices in real-life applications is the difficulty to mass-fabricate nano-optical probes in reproducible fashion, and the capability to precisely place these probes into real devices with nanometer-scale precision [1]. On the other hand, the near-field probes are key element of the near-field microscopy achieving subwavelength resolution of optical fields. Majority of these probes is based on metal-dielectric interface and mostly they were prepared or integrated at the facet or end of optical fibers [2, 3].

2. Experimental

NCs were grown on p-type Zn doped GaP<111>B substrates by a combination of standard 2D growth with a vapour-liquid-solid technique (VLS) using 30 nm gold particles as seeds. These seeds were deposited on the substrate at a density lower than one nanoparticle per 1000 μm^2 from a water-based colloid. The distances between such low-density nanoparticles ranged from 50 to 100 μm. The shape of typical NC consists of a hexagonal base (determined by substrate orientation) with diameter between 800 and 2000 nm and six triangular sidewalls. Typical height of NCs used in this study was from 5 to 8 μm. Because of core diameter of a single mode optical fibre is 9 μm, NCs with dimensions as described above are very convenient for integration onto its top. With aim to obtain special samples for SERS study a part of some NCs samples was covered by Ag nanoparticles. Thin Ag layers with nominal thickness between 5 and 40 nm were deposited on the substrates. The formation of Ag nanoparticles on the nanocones was finished by subsequent in-situ annealing of the Ag layers at a temperature of 200 °C [4].

To prevent a deteriorate influence of optical absorption in the GaP substrate under nanocones we decided to decrease its thickness under 30 μm.

We developed a special method for thinning of GaP substrate under NCs. It consists of backside grinding and polishing while NCs are prevented before damaging by deep dipping into a thermal glue.

Focused ion beam (FIB) method was applied for separation of individual NCs from the sample. The typical device shape is square-like with side size close to 50 μm with NC in the middle. Fig. 2 presents this typical device view. To prevent contamination of nanocone surface by aggressive waste produced during the cutting process it is necessary make such cutting far from the nanocone: To our best experience such sufficient safety distance is higher as 10 micrometers.

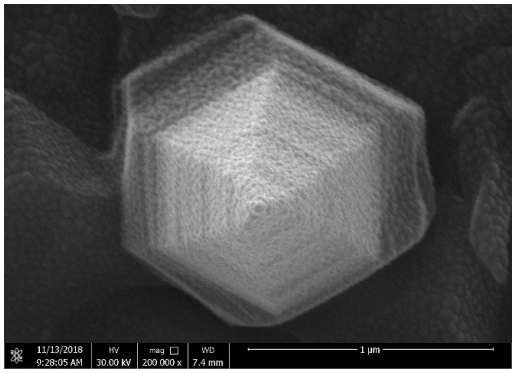

Fig. 1. SEM top view on GaP nanocone covered by 10 nm silver photonic nanoparticles.

For a detailed analysis of GaP NC and their ability to locally enhance the electromagnetic wave, we focused on the near-field properties of GaP NC's. [5]. The idea was to measure the local response of the individual NC on a transmitting and exciting light. The NSOM measurements (see Fig. 3) could characterize

local emission and plasmonic properties of a single NC mounted on the top of the single mode fiber.

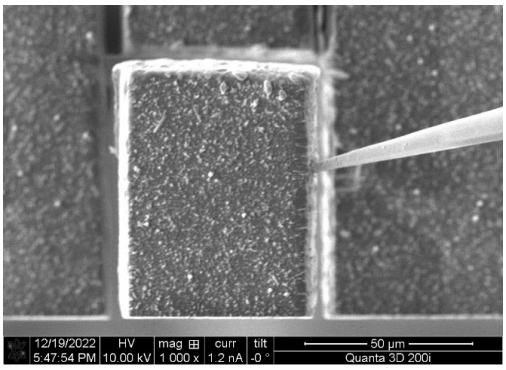

Fig. 2. SEM top view on GaP nanocone on FIB holder after separation from the basic GaP wafer. Separation is proved by unsharpness of the wafer in comparison to the probe on the needle holder.

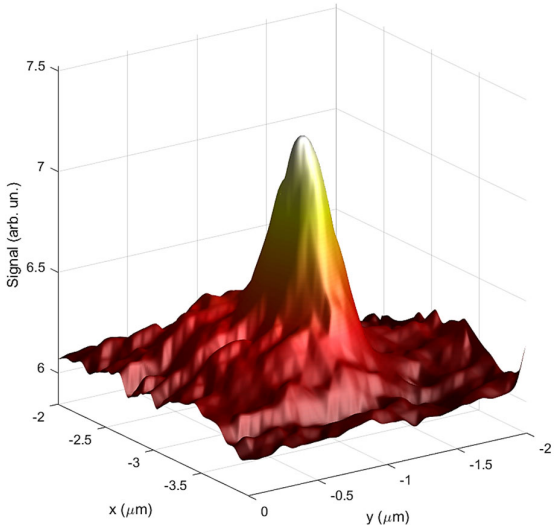

Fig. 3. NSOM scan of the GaP nanocone.

3. Conclusions

In summary, we studied preparation and properties of nanocone probes consisted from GaP nanocone deposited on central part of single mode fibre. FIM technique was used for NC cutting of from the GaP wafer. Crucial point of this experiment is backside thinning and polishing. Undesirable scattering and absorption may be suppressed to acceptable value. Final quality of backside polishing is very important but very hard mission.

Finally, we present results of optical characterisation of the GaP nanoprobes in both illumination and collection regime. At first, the device is illuminated from the bottom side through the optical fiber and the nanoprobe optical field is characterised in the near field. Secondly, nanoprobe scans small defined optical source and light is captured by nanocone.

Acknowledgement:

This research was supported by the Science and Technology Assistance Agency under grant APVV-20-0264 and APVV-20-0437.

References

[1]. M. H. Jiang, T. J. Yen, Ch. Chen, D. Z. Lin, H. Chou, J. Y. Chu, Near-field plasmonic probe with super resolution and high throughput and signal-to-noise ratio, *Nano Letters*, Vol. 18, Issue 2, 2018, pp. 881-885.

[2]. S. Kim, et al., High external-efficiency nanofocusing for lens-free near-field optical nanoscopy, *Nature Photonics*, Vol. 13, 2019, pp. 636-643.

[3]. Q. Yuxuan, C. Kuang, X. Liu, L. Tang, Single-molecule surface enhanced Raman spectroscopy, *Sensors,* Vol. 22, 2022, 4889.

[4]. J. Novák**,** P. Eliáš, S. Hasenöhrl, A. Laurenčíková, J. Kováč Jr., P. Urbancová, D. Pudiš, Twinned nanoparticle structures for surface enhanced Raman scattering, *Applied Surface Science*, Vol. 528, 2020, 146548.

[5]. D. Pudiš, P. Urbancová, J. Novák**,** A Kuzma, I. Lettrichová, M. Goraus, P. Eliáš, A. Laurenčíková, D. Jandura, Ľ. Šušlik, S. Hasenöhrl, Near-field analysis of GaP nanocones, *Applied Surface Science*, Vol. 539, 2021, 148213.

(4754)

3DTIPs based on IP-dip Polymer for Scanning Probe Microscopy

D. Pudis [1,2], P. Gaso [1], S. Bulatov [1] and D. Jandura [1]
[1] Dept. of Physics, Faculty of Electrical Engineering and Information Technology,
University of Žilina, Univerzitná 1, 010 26 Žilina, Slovakia
[2] University Science Park of the University of Zilina, Zilina, Slovakia
Tel.: + 4215132300
E-mail: dusan.pudis@feit.uniza.sk

Summary: We present a concept of probes for scanning force microscopy fabricated be three-dimensional (3D) laser lithography. We proposed two main designs based on probe printed on standard Si cantilever and fully printed probe with cantilever prepared from IP-Dip polymer. We achieved high-quality probes which can be used in scanning force microscopy. The probe printed on Si cantilever was used for measurement of calibration grating. The achieved results favor this technique for fabrication of cellular architectured probes with controlled stiffness. The obtained results are promising for fabrication of polymer based 3D probes for direct integration on standard cantilevers.

Keywords: Scanning probe microscopy, Probes, 3D laser lithography, IP-dip polymer.

1. Introduction

Atomic force microscopy (AFM) technology allows scientists to observe, measure, and manipulate samples at micro and nanoscale with unique precision. Modern AFM are able to scan different materials as the properties of probes can be tuned. Also on commercial basis the wide variety of AFM probes was developed as: AFM probes with sphere, colloids, functionalized and chemical tips and different metallic and magnetic material probes. The performance of scanning-probe microscopy systems significantly depends on the shape, size, and composition of the probing tip. In practically all cases, the tip radius should be as small as possible to obtain a high lateral resolution. Also the overall shape of the tip is frequently also important [1].

Moreover, not only the tip but also the cantilever is a significant part affecting the behavior of the probe. Different spring constants of the cantilever are typically used depending on whether the system is operated in contact or dynamic mode and also depending on the material stiffness [2].

Generally, the shape of the AFM probes is limited by crystal properties and materials patterning. Modern treatments in scanning probe microscopies have achieved new kind of AFM probes in true three-dimensional shapes called 3DTIPs [2, 3]. The novel 3DTIPs use tailored 3D design using single-step 3D printing process and create new platform utilized for a wider variety of applications than standard Si-based probes. This advanced additive manufacturing single-step process in microscale create also new class of artificial cellular microarchitectures, referred to as controlled microstructural architectured (CMA) probes [4]. The CMA probes can be structurally programmed with a controllable geometry and spatial configuration for advantageous size dependent metamechanical properties, such as low density but strong robustness, high stiffness-to-weight ratio, excellent resilience, mechanical tunability, and in particular, energy absorption. The CMA cellular hierarchy improves tip itself and, reduces the tip-sample interaction [5].

Our experiences with the three-dimensional (3D) fabrication of submicrometer structures for near-field probes based on the nanocone design leaded to preparation novel design of AFM 3D TIPs by introducing submicrometer three-dimensional lithography. The nanoprobes based on IP-Dip polymer were designed, prepared by 3D laser lithography and experimentally verified in AFM imaging.

2. Experimental and Results

There are two main treatments in the 3D fabrication of AFM probes: i) probes printed on Si cantilever and ii) probes printed together with cantilever (Fig. 1). In this contribution, we proposed simple nanoconical structure in both designs. The basis of nanocone was 30 µm and height of 80 µm.

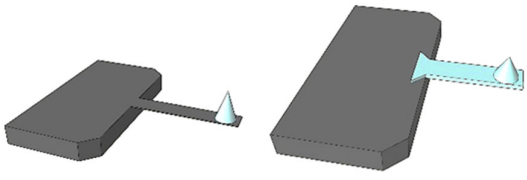

Fig. 1. Probe in shape of nanocone a) printed directly on Si cantilever and b) nanocone on polymer cantilever.

For the fabrication of the nanoprobes, we used a commercial 3D laser lithography system Photonic Professional GT from Nanoscribe GmbH working on principle of two-photon absorption in the volume of polymer. As a dielectric polymer material IP-Dip (n = 1.52 at 780 nm unexposed) was used. High

quality nanoprobes were prepared and documented by scanning electron microscope (SEM) (Figs. 2 and 3).

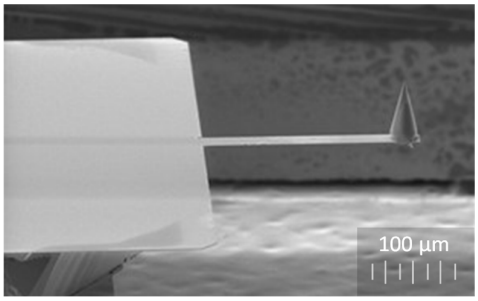

Fig. 2. SEM image of nanoprobe printed directly on Si cantilever – side view.

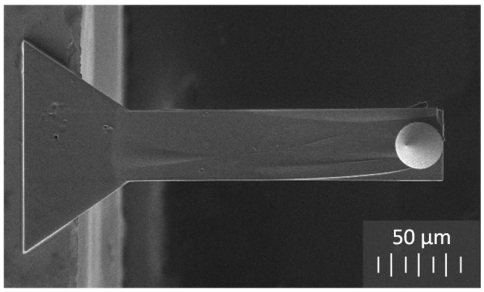

Fig. 3. SEM image of nanocone on polymer cantilever fixed on Si substrate – top view.

The probe printed on Si cantilever was examined in standard scanning force microscope in contact mode (Fig. 4). We obtained an AFM image of standard calibrating grating AppNano SHS – 0.1 with depth of 100 nm showing a submicrometer lateral resolution. The line profile documents the 100 nm grating depth (Fig. 5). Mechanical and stiffness properties as well the spring constant will be investigated in forthcoming experiments.

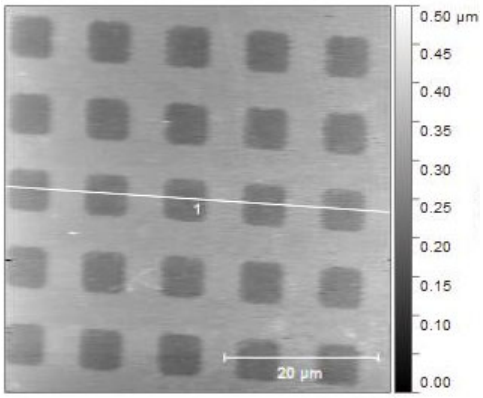

Fig. 4. AFM image obtained in contact mode.

3. Conclusions

We presented concept of fabrication of probes for scanning force microscopy based on 3D laser lithography. We proposed two main designs based on probe printed on standard Si cantilever and printed probe with cantilever prepared from IP-Dip polymer. We achieved high-quality probes which can be used in AFM scanning. The probe printed on Si cantilever was used for measurement of calibration grating. We achieved results which favors this technique for fabrication of probes with more complicated cellular architecture. The obtained results are promising for fabrication of polymer based 3D probes for direct integration on standard scanning probes.

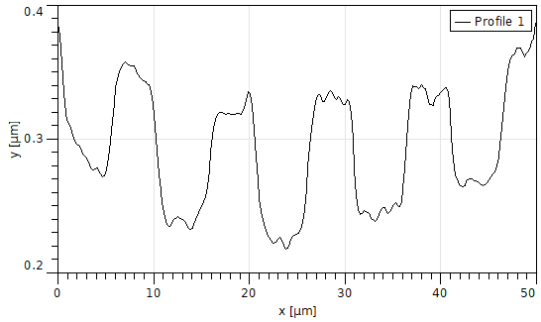

Fig. 5. AFM line profile obtained from Fig. 4 (line 1).

Acknowledgements

This work was supported by grant agency of Ministry of Education, Science, Research and Sport of the Slovak Republic projects VEGA 1/0363/22, and APVV 20-0264. This publication was realized with support of Operational Program Integrated Infrastructure 2014 - 2020 of the project: Innovative Solutions for Propulsion, Power and Safety Components of Transport Vehicles, code ITMS 313011V334, co-financed by the European Regional Development Fund and Independent research and development of technological kits based on wearable electronics products, as tools for raising hygienic standards in a society exposed to the virus causing the COVID-19 disease, ITMS2014+ code 313011ASK8.

References

[1]. N. Alsharif, et al., Design and realization of 3D printed AFM probes, *Small*, Vol. 14, 2018, 1800162.
[2]. J. D. Adams, et al., Harnessing the damping properties of materials for high-speed atomic force microscopy, *Nature Nanotechnology*, Vol. 11, 2016, pp. 147-151.
[3]. G. Göring, et al., Tailored probes for atomic force microscopy fabricated by two-photon polymerization, *Applied Physics Letters*, Vol. 109, 2016, 063101.
[4]. A. Glia, et al., 3D Generation of Multipurpose Atomic Force Microscopy Tips, *Advanced Science*, Vol. 9, 2022, 2201489.
[5]. H. Ding, et al., Controlled microstructural architectures based on smart fabrication strategies, *Advanced Functional Materials*, Vol. 30, 2019, 1901760.
[6]. L. Sun, et al., 3D-printed cellular tips for tuning fork atomic force microscopy in shear mode, *Nature Communications*, Vol. 11, 2020, 5732.

(4833)

Optical Characteristics of Very Diluted Aqueous Solutions of Sucrose

Dilbar Bozorova [1], Shukur Gofurov [4], Mavlonbek Ziyayev [5], Kakhkharov Abdulmutllib [1] and Oksana Ismailova [1, 2, 3, 4]

[1] Institute of Ion-plasma and laser technologies, 100125, 33 Durmon yuli street, Uzbekistan
[2] Turin Polytechnic University in Tashkent, 100195, Almazar district,
17 Kichik Khalka yuli street, Uzbekistan
[3] Uzbekistan-Japan Innovation Center of Youth, 100195, 2B Universitet street, Uzbekistan
[4] National University of Uzbekistan named after Mirzo Ulugbek, 100174,
4 Universitet street, Tashkent, Uzbekistan
[5] Namangan State University, 160107, 316 Uychi street, Namangan, Uzbekistan
Tel.: + 998909194890, fax: + 998712030022
E-mail: oismailova56@gmail.com

Summary: The work is devoted to optical studies of the concentration-dependent properties of very diluted aqueous solutions of sucrose. The results of refractometry and Raman spectroscopy combined with the method of molecular dynamics of diluted aqueous solutions at concentrations of 0.05, 0.06, 0.09, 0.10 and 0.12 mol/L of sucrose are presented. The analysis of the dynamics of sucrose complexes formed in water is presented. It is shown that at the concentration of 0.06 mol/L of sucrose, the refractive index has the lowest value, associated with the largest number of hydrogen bonds in the mixture. Information on the nonlinear change in the hydrogen bond strength of the mixtures was obtained from the analysis of the valence OH-band contour. The strongest hydrogen bond strength is shown for a system with a concentration of 0.06 mol/L of sucrose. It was shown that the refractometry method is informative for detecting sucrose complexes formed in diluted aqueous solutions. A new approach has been proposed to study the concentration dependences of optical characteristics of low-diluted sucrose solutions based on the combined application of methods: refractometry, Raman spectroscopy and molecular dynamics.

Keywords: Refractometry, Raman spectroscopy, Hydrogen bonds, Molecular dynamics method.

1. Introduction

There are numerous experimental data indicating that aqueous systems containing dissolved substances of different nature in the low concentration range have a number of nonlinearly dependent physicochemical properties [1-4]. Therefore, understanding of the dissolution processes and their connection with the physicochemical properties of the system is not entirely clear. Studies of the complex formation of molecular structures in aqueous medium consisting of heterocyclic compounds are of particular interest. In this regard, the study of self-organization, physicochemical properties of aqueous mixtures of sucrose are an important objective at present. This work is aimed at studying the effect of sucrose concentration on the nonlinear concentration dependence of the physicochemical properties of solutions in the low concentration range of sucrose in water.

2. Experiment and Molecular Dynamics

2.1. Sample Preparation

Sucrose (Sigma-Aldrich, USA, ≥99.5 %) powder has been used for aqueous solutions of Sucrose. Different amount of sucrose was dissolved in 5 ml pure distilled water to make 0.01 to 0.12 mol/L sucrose concentration in water.

2.2. Refractometry Method

Refractometry was used to reveal the concentration-dependent optical properties of aqueous solutions of components and to study the role of hydrogen bonds in the formation of various types of associates [12-16]. The measured values of the refractive indices are presented in the concentration range of 0÷0.12 mol/L with an increment of 0.01 mol/L (Fig. 1). The highest value of the refractive index corresponds to a concentration of 0.12 mol/L. It can be seen that the nonlinear dependence of the refractive index value on sucrose concentration is observed in the concentration range of 0÷0.1 mol/L. The maximum value of refractive index prohibits at the concentration of 0.05 mol/L, minimum values correspond to 0.06 mol/L and 0.09 mol/L, afterwards it suddenly increases. To explain the nonlinear dependencies of refractive indices of aqueous solutions of sucrose we have chosen 0.05, 0.06, 0.09, 0.10 and ~0.12 mol/L samples for further consideration by other methods. The process of dissolution of 'guest' molecules in real systems has peculiarities due to dynamic phenomena. Direct study of the processes occurring in solutions is usually a nontrivial task because of their complex dynamics. Direct experimental investigation of the solvation process in solutions is a complex multiparameter problem. In this connection, indirect methods of studying this phenomenon are used.

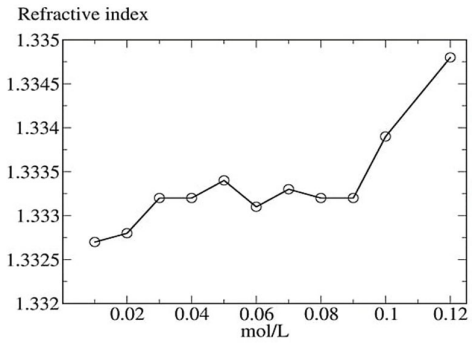

Fig. 1. Refractive indices of aqueous solutions of sucrose at 0.01-0.12 mol/L range concentrations.

2.3. Raman Spectroscopy

Among such indirect methods, spectroscopic approach should be singled out, which allows identifying a significant number of parameters of the sorption process, correlating them with the recorded data. Molecular spectroscopy is one of the most important physical methods of learning the structure of matter. This is due to the specificity of each molecule's spectrum and its high sensitivity to various kinds of perturbations of both the molecule as a whole and individual atomic groups. Modern theoretical spectroscopy is the spectroscopy of isolated molecules. Therefore, to explain the mechanisms of self-aggregation of sucrose molecules, we have used the Raman spectroscopy method.

For Raman spectra, the same solutions as for measuring the refractive index of aqueous solutions with sucrose concentrations of ~0.05, 0.06, 0.09, 0.10 and ~0.12 mol/L were used. The water spectrum was obtained by us early [13]. Raman spectra were obtained by Renishaw InVia Raman spectrometer using an excitation neodymium-doped yttrium aluminum garnet (Nd:YAG) laser source of 532 nm and in wavenumber range 400-4000 cm^{-1} with resolution 1 cm^{-1} [13]. Fig. 2 shows the Raman spectra of aqueous-sucrose solutions in the wave number region of 2800-3800 cm^{-1}. From a comparison of the spectra of pure water and aqueous solutions of sucrose, it can be seen that the addition of a small amount of sucrose into the water, the intensity of the spectra of mixtures increases markedly in the wave number range of 700÷2800 cm^{-1}. The increase of peak intensity is nonlinear: the highest intensity is observed at 0.06 mol/L of sucrose, and further decreases in the following sequence: 0.09, 0.05, 0.12, and 0.10 mol/L.

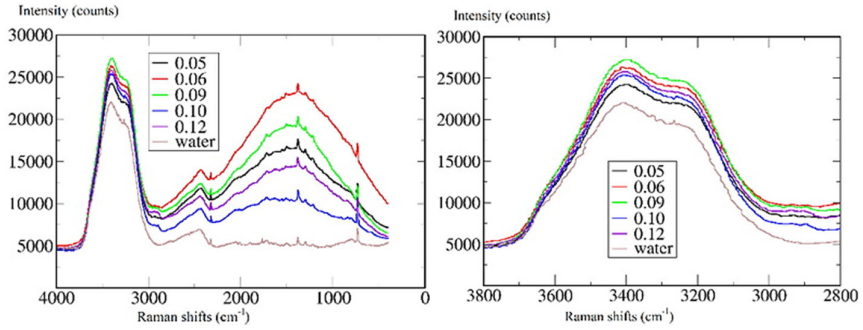

Fig. 2. Raman spectra of aqueous solutions of sucrose at sucrose concentration of 0.05, 0.06, 0.09, 0.10, 0.12 mol/L, whole region (left) and 3800-2800 cm^{-1} (right). The spectrum of water, shown in brown, is taken with the permission of authors from [14].

2.4. Molecular Dynamics

We used the molecular dynamics method to investigate self-organization processes of sucrose molecules in water. The systems were modeled in such a way that the number of sucrose and water molecules corresponded to their experimental values of concentrations in solutions. The calculations were performed using the GROMACS (Groningen Machine for Chemical Simulations) software package [17] version 5.0.2. The energy of the created systems was minimized by the gradient descent method. The integration of Newton's equations of motion was carried out using the leap-frog algorithm. All calculations were performed in an isobaric-isothermal NPT ensemble and a Parinello-Rachmann barostat [18] at a pressure of 1 bar and a temperature of 300 K in a time interval of 40 ns with a step of 1 fs. The bond lengths were fixed using the LINCS (decode) algorithm [19]. The Particle Mesh Ewald method (PME) with Fourier intervals of 0.12 nm [20] and a cut off radius of 1.1 nm [21] was used to calculate long-range electrostatic interactions. SPC/E model [22] was used for water, which has been used quite successfully to describe the formation of heterostructures in binary [11, 12, 14] and multicomponent solutions [13]. The OPLS- AA force field was used for sucrose molecules, the structure of which is shown in Fig. 3.

3. Results and Discussion

The widespread usage of mixed solvents in various nanotechnological processes requires the establishment of a relationship between the

physicochemical properties of individual components and the structure and composition of their binary and multicomponent systems. However, in dilute solutions, the strong absorption of water exceeds the limited dynamic range of the detection system and thus allows only a very short optical path length and limited concentration sensitivity. Therefore, we used the molecular dynamics method to determine the structure of the clusters formed.

The smallest number of sucrose clusters is formed at a concentration of 0.06 mol/L and the largest for 0.12 mol/L. It should be noted that dynamic cluster formation for a time interval of 5 ps is observed at concentrations of 0.06, 0.10, and 0.12 mol/L, and static at 0.05 and 0.09 mol/L (Fig. 4). The Fig. 5 shows a structure clusters of sucrose formed at the concentration of 0.06 and 0.12 mol/L with number of 4 and 6 correspondingly presented at diagram Fig. 4.

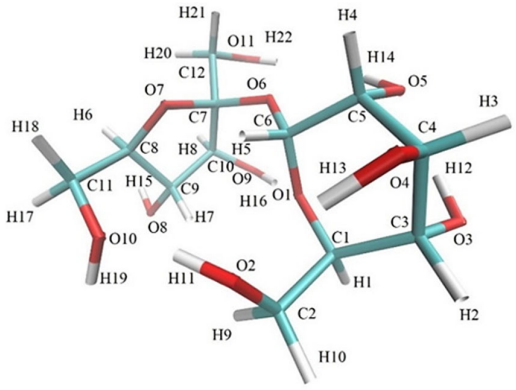

Fig. 3. Chemical structure of sucrose molecule in water.

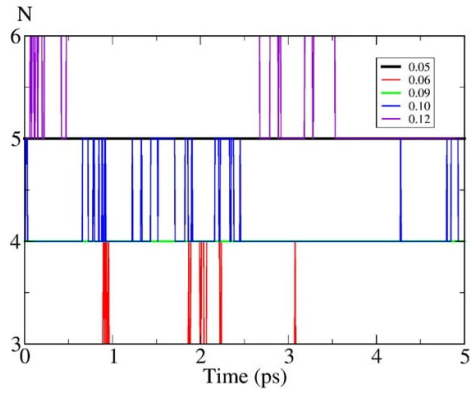

Fig. 4. Number of sucrose clusters in aqueous solution.

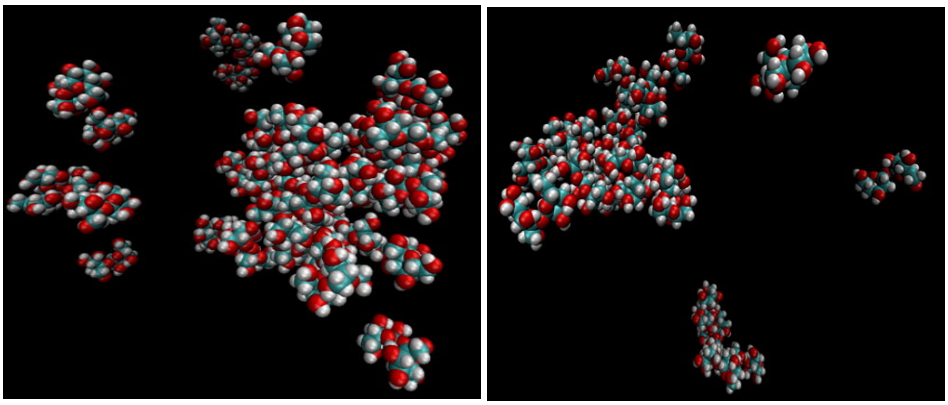

Fig. 5. Sucrose clusters formed in aqueous solutions with a concentration of 0.06 mol/L (left) and with a concentration of 0.12 mol/L (right).

For the convenience of comparing the calculated and experimental data, the refractive index and the number of formed clusters as function of concentration are shown in Fig. 6. This figure shows that the refractive index (red) is inversely proportional to the number of formed sucrose complexes (blue). The lowest refractive index value corresponds to aqueous sucrose solutions at a concentration of 0.06 mol/L. This is due to the fact that the formed clusters have the highest conformational stability presented as an analysis of Root mean square deviation (RMSD) and the lowest value of Root Mean Square fluctuation (RMSF) (Fig. 7). Based on RMSD and RMSF. We can conclude that clusters formed in mixtures at a concentration of 0.06 mol/L are very stable. The lowest conformational stability and the highest fluctuations are characteristic of sucrose clusters formed at a concentration of 0.10 mol/L. The RMSD was calculated for a time interval of 40 ns.

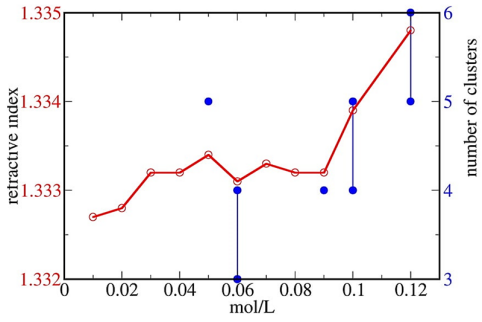

Fig. 6. Refractive index (red) and number of formed clusters (blue) as function of sucrose at 0.01-0.12 mol/L concentration range.

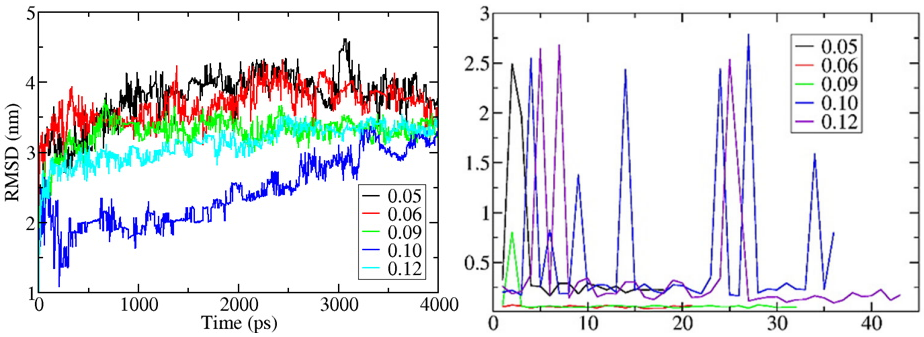

Fig. 7. Root mean square deviation (left) and Root Mean Square fluctuation (right) of sucrose molecules.

The processes of cluster formation are influenced by specific interactions manifested during solvation of molecules, in particular hydrogen bonding (H-bonding), since their presence often determines the stability of the system. To investigate the stability of the system, we analyzed the behavior of the OH valence band in water-sucrose solutions because the contour of this band is significantly affected by hydrogen bonding. Parameter χ12 was calculated as the ratio of the intensity of the low-frequency arm of the valence band (I = 3200 cm^{-1}) to the intensity of the high-frequency arm of the valence band (I = 3250 cm^{-1}) [13]. The valence band of I = 3200 cm^{-1} interpreted as the OH stretching band for gas clathrates [23, 24], while I = 3250 cm^{-1} corresponds to the formation of aggregates through hydrogen bonding, which have a structure similar to the tetragonal structure of water [25], and coherent vibrational energy transfer of water molecules represented in vibrational spectra [26, 27]. Dependence of the ratio I3200/I3250 on sucrose concentration for the Raman spectra is shown in Fig. 8. As can be seen, the ratio has maximum values at a concentration of 0.06 mol/L. The maximum value of this parameter indicates the maximum number of OH groups with strong hydrogen bonds relative to the number of OH groups with weak bonds [28]. We interpret these results as the realization of the maximum number of hydrogen bonds in the system [24].

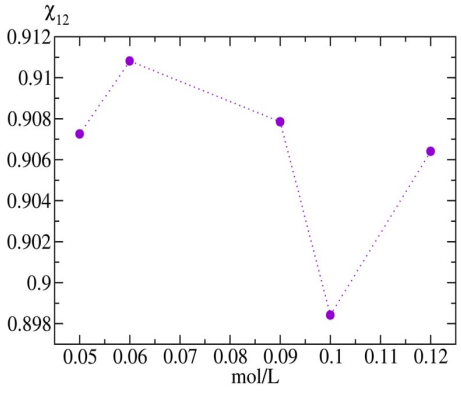

Fig. 8. Dependence of the ratio of absorption band peaks (χ12 parameter) on sucrose at 0.01-0.12 mol/L concentration range for Raman spectra.

4. Conclusions

Unlike other methods of research, Raman spectroscopy, having relative simplicity and accessibility, allows us to reliably establish the main features of the structure of solutions. In the present work, the Raman scattering method in combination with refractometry and the molecular dynamics method were applied to study the structure of diluted aqueous solutions of sucrose. At a concentration of 0.06 mol/L, the system exhibits the maximum realization of hydrogen bonds, affecting the smallest number of formed sucrose complexes.

Acknowledgments

This work was financially supported by the Basic Research Grant of the Academy of Sciences of the Republic of Uzbekistan, Grant No. UZB-IND-2021-83 of the Ministry of Science and Technology of the Republic of Uzbekistan and MIRAI Grant.

References

[1]. B. Long, S. Chen, Z. Li, Y. Ding, Solubility of ammonium fluoride in aqueous sodium fluoride solutions of various concentrations from dilute to saturated at 298.15 K for fluorine recovery from wet-process phosphoric acid, *Journal of Molecular Liquids*, Vol. 299, 2020, 112247.

[2]. K. M. Schockman, R. H. Byrne, A hybrid conductometric/spectrophotometric method for determining ionic strength of dilute aqueous solutions, *Analytica Chimica Acta*, Vol. 1220, 2022, 340008.

[3]. J. Zhang, D. Zou, S. Zhai, Y. Yan, H. Yang, Ch. He, Y. Ke, S. Singh, Enhancing the interaction between cellulose and dilute aqueous ionic liquid solutions and its implication to ionic liquid recycling and reuse, *Carbohydrate Polymers*, Vol. 277, 2022, 118848.

[4]. R. Fan, C. Chen, J. Lin, J. Tzeng, C. Huang, C. Dong, P. Huang, Adsorption characteristics of ammonium ion onto hydrous biochars in dilute aqueous solutions, *Bioresourse Technology*, Vol. 272, 2019, pp. 465-472.

[5]. J. Yao, L. Li, W. H. Benjamin Wong, C. Tan, D. Dong, H. Wang, Formation of ZIF-8 membranes and crystals in a diluted aqueous solution, *Materials Chemistry and Physics*, Vol. 139, 2013, pp. 1003-1008.

[6]. M. Kamli, M. Guettari, T. Tajouri, Structure of polyvinylpyrrolidone aqueous solution in semi-dilute regime: Roles of polymer-surfactant complexation, *Journal of Molecular Structure*, Vol. 1196, 2019, pp. 176-185.

[7]. J. Demangeat, Water proton NMR relaxation revisited: Ultrahighly diluted aqueous solutions beyond Avogadro's limit prepared by iterative centesimal dilution under shaking cannot be considered as pure solvent, *Journal of Molecular Liquids*, Vol. 360, 2022, 119500.

[8]. A. B. Brizuela, L. C. Bichara, E. Romano, A. Yurquina, S. Locatelli, S. A. Brandán, A complete characterization of the vibrational spectra of sucrose, *Carbohydrate Research*, Vol. 361, 2012, pp. 212-218.

[9]. M. Mothlouthi, D. V. Luu, Laser-Raman spectra of D-glucose and sucrose in aqueous solution, Carbohydrate Research, Vol. 81, 1980, pp. 203-212.

[10]. J. Max, C. Chapados, Sucrose hydrates in aqueous solution by IR spectroscopy, *The Journal of Physical Chemistry A*, Vol. 105, 2001, pp. 10681-10688.

[11]. S. Gofurov, U. Makhmanov, A. Kokhkharov, O. B. Ismailova, Structural and optical characteristics of aqueous solutions of acetic acid, *Applied Spectroscopy*, Vol. 73, Issue 5, 2019, pp. 503-510.

[12]. D. T. Bozorova, S. P. Gofurov, A. M. Kokhkharov, Terahertz spectroscopy of aqueous solutions of acetic acid, O. B. Ismailova, *Journal of Applied Spectroscopy*, Vol. 88, Issue 4, 2021, pp. 719-722.

[13]. I. V. Plastinin, S. A. Burikov, S. P. Gofurov, Y. A. Mirgorod, T. A Dolenko, Features of self-organization of sodium dodecyl sulfate in water-ethanol solutions: Theory and vibrational spectroscopy, *Journal of Molecular Liquids*, Vol. 298, 2020, 112053.

[14]. D. Razzokov, O. B. Ismailova, Sh. I. Mamatkulov, O. V. Trunilina, A. M. Kokhkharov, Heteromolecular structures in aqueous solutions of dimethylformamide and tetrahydrofuran, according to molecular dynamics data, *Russian Journal of Physical Chemistry A*, Vol. 88, Issue 9, 2014, pp. 1500-1506.

[15]. J. C. Reis, I. M. Lampreia, A. F. Santos, Refractive Index of Liquid Mixtures: Theory and Experiment, *Chemphyschem*. Vol. 11(17), 2010, pp. 3722-3733.

[16]. D. T. Bozorova, Sh. P. Gofurov, A. M. Kokhkharov, M. A. Ziyayev, F. T. Umarova, O. B. Ismailova, The excess refractive indices of some organic and inorganic components, in Advanced Materials and Nano Systems: Theory and Experiment (Part-1)*, Bentham Science Publisher*, 2022, pp. 108-119.

[17]. B. Hess, C. Kutzner, D. van der Spoel, E. Lindahl, Algorithms for highly efficient, load-balanced, and scalable molecular simulation, *Journal of Chemical Theory and Computation*, Vol. 4, 2008, pp. 435-447.

[18]. M. Parrinello, A. Rahman, Polymorphic transitions in single crystals: A new molecular dynamics method, *Journal of Applied Physics*, Vol. 52, 1981, pp. 7182-7190.

[19]. B. Hess, H. Bekker, H. J. C. Berendsen, J. G. E. M. Fraaije, LINCS: a linear constraint solver for molecular simulations, *Journal of Computational Chemistry*, Vol. 18, Issue 12, 1997, pp. 1463-1472.

[20]. U. Essmann, L. Perera, M. L. Berkowitz, et al., A smooth particle mesh Ewald method, *The Journal of Chemical Physics*, Vol. 103, 1995, pp. 8577-8593.

[21]. S. J. Marrink, D. P. Tielemann, A. E. Mark, Molecular dynamics simulation of the kinetics of spontaneous micelle formation, *The Journal of Physical Chemistry B*, Vol. 104, Issue 51, 2000, pp. 12165-12173.

[22]. H. J. C. Berendsen, J. R. Grigera, T. P. J. Straatsma, The missing term in effective pair potentials*, The Journal of Physical Chemistry*, Vol. 91, 1987, pp. 6269-6271.

[23]. J. M. Schics, J. Erzinger, M. A. Zieman, Raman spectra of gas hydrates – Differences and analogies to ice 1h and (gas saturated) water, *Spectrochimica Acta Part A*, Vol. 61, 2005, pp. 2399-2403.

[24]. T. Dolenko, S. Burikova, M. Hojob, S. Patsaevaa, V. Yuzhakova, Hydrogen bonding in aqueous ethanol solutions studied by Raman spectroscopy, *Proceedings of SPIE*, Vol. 7376, 2010, 73761B.

[25]. G. E. Walrafen, Y. C. Chu, Linearity between structural correlation length and correlated-proton Raman intensity from amorphous ice and supercooled water up to dense supercritical steam, *The Journal of Physical Chemistry*, Vol. 99, 1995, 11225.

[26]. M. Yang, J. L. Skinner, Signatures of coherent vibrational energy transfer in IR and Raman line shapes for liquid water, *Physical Chemistry Chemical Physics*, Vol. 12, 2010, pp. 982-991.

[27]. H. J. Bakker, J. L. Skinner, Vibrational spectroscopy as a probe of structure and dynamics in liquid water, *Chemical Reviews*, Vol. 110, Issue 3, 2010, pp. 1498-1517.

[28]. T. A. Dolenko, S. A. Burikov, S. A. Dolenko, A. O. Efitorov, I. V. Plastinin, V. I. Yuzhakov, S. V. Patsaeva, Raman spectroscopy of water-ethanol solutions: The estimation of hydrogen bonding energy and the appearance of clathrate -like structures in solutions, *The Journal of Physical Chemistry A*, Vol. 119, 2015, pp. 10806-10815.

(4925)

Structural Mapping of Mechanically Flexible Photoluminescent and Photodynamic Molecular Crystals

S. Bhandary [1], A. M. Kaczmarek [2] and K. Van Hecke [1]
[1] Ghent University, XStruct, Krijgslaan 281-S3, B-9000 Ghent, Belgium
[2] Ghent University, NanoSensing Group, Krijgslaan 281-S3, B-9000 Ghent, Belgium
Tel.: + 3292644870
E-mail: kristof.vanhecke@ugent.be

Summary: Mechanically flexible luminescent organic crystals have become an essential part of modern technologies like optoelectronics, while photoluminescent crystals, able to transform light energy into mechanical motions, are a promising choice for actuating and photonic devices. Here, we present our findings on how quantitative structural mapping can rationalize the change in phosphorescence emission, as a function of the flexibility of elastic single crystals of dibenzothiophene and its brominated derivate. The dibenzothiophene crystals show dual fluorescence (FL) and room temperature phosphorescence (RTP), while the bromo derivative only shows RTP. We further present how the photosalient behavior of room temperature phosphorescent molecular crystals, based on organoboron containing Lewis acid-base adducts, can be explained by crystal-to-crystal [2+2] cycloaddition reactions as the driving force. The latter crystals display short-lived room temperature phosphorescence, while the photodynamic events are accompanied by enhancement of their phosphorescence intensity.

Keywords: Photoluminescent, Photodynamic, Flexible crystals, Phosphorescence, [2+2] cycloaddition reaction.

1. Introduction

Organic crystals have become an essential part of modern technology including optoelectronics, solar cells, semiconductors, etc. [1]. The main obstacle with organic crystalline materials is that they are generally known as brittle and inelastic, which limits specific practical applications. The inherent advantage of organic molecular materials lies in their long-range structural order, small defects, easy to functionalize, low-cost and sustainable characteristics [2]. In fact, molecular organic crystals, able to respond to external mechanical force and reconfigure their shape by deformation have become an emerging field in materials science [2]. Organic flexible molecular crystals, equipped with deformation capabilities, can bridge *hard* inorganic and *soft* polymeric materials.

In that regard, organic light-emitting (luminescent) single crystals that are also mechanically flexible, could be a smart choice of materials for modern flexible displays and mechanosensors [1]. Recently, room temperature phosphorescent (RTP) organic crystalline materials have gained interest for emerging photonic applications owing to their higher lifetimes of emission in comparison to the fluorescent materials [3] (Fig. 1). RTP crystals which can change their emission properties (color, lifetime, or peak positions) by adopting different crystal shapes under external mechanical stress, are hence of extreme relevance [4].

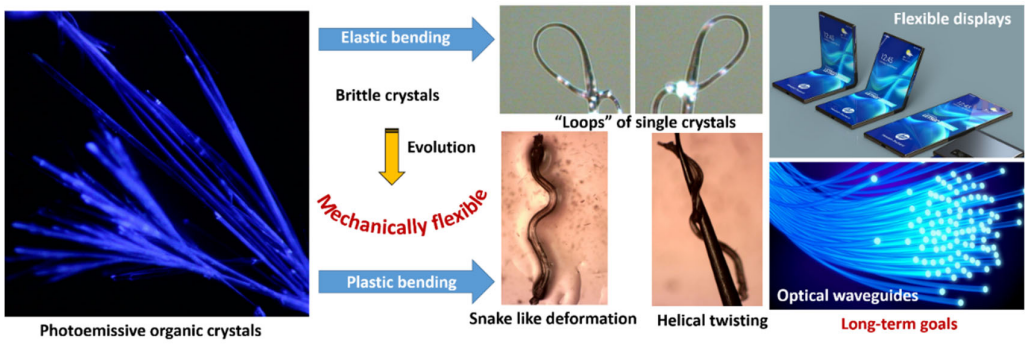

Fig. 1. Schematic representation of different flexible molecular crystals (elastic and plastic) with efficient luminescence properties for potential applications in modern smart devices.

Besides flexible crystals, stimuli-responsive crystalline materials are able to convert light energy into mechanical motions and also find applications in flexible electronics, actuating devices, sensors etc. [5].

Such photodynamic crystals often exhibit various photosalient motions like bending, expanding, splitting, twisting, and popping effects. The driving force is related to perturbations at the molecular level

caused by the applied light and has been observed in chemical reactions with e.g. azobenzenes, diarethenes etc. [5]. Regarding olefins, the mechanical response of molecular crystals can be induced by a topochemical [2+2] photocycloaddition reaction, when the olefin cores are in a *ready-to-react* arrangement. Despite the versatility offered in terms of structure design, only a very limited number of olefin-containing single crystals show visible photomechanical motions [6].

Following our continuing efforts toward the synthesis of functional and flexible crystals [4, 6], we present our findings on how quantitative structural mapping can rationalize the change in phosphorescence emission, as a function of the flexibility of elastic single (organic) crystals and how the photosalient behavior of room temperature phosphorescent (organoboron-based) crystals, is revealed in terms of crystal-to-crystal [2+2] cycloaddition reactions as the driving force.

2. Experimental

Crystallization of both compounds dibenzothiophene and its brominated derivative (DBS and DBS-Br), in various organic solvents, resulted in acicular, straight, as well as naturally deformed, flexible crystals [4]. The organoboron-based adduct (BN1) was synthesized via mechanochemical methods using 2:2 mol equiv of *para*-CF_3 substituted triphenylboroxine and 1,2-di(4-pyridyl)ethylene and fully characterized [6]. Structural mapping was performed using (synchrotron) single-crystal X-ray diffraction analyses and ^{1}H NMR spectroscopy [4, 6].

3. Results and Discussion

The DBS crystals are elastically 2D flexible organic crystals and can be macroscopically bent, by applying external force. The crystals of the bromo derivative (DBS-Br) can be deformed from one direction on the major crystal face (1D flexible). However, when stress is applied on a lateral face, they become brittle. Photoluminescence (PL) characterization of a straight DBS single crystal show dual fluorescence (FL) (peak at 365 nm) and RTP (peak at 563 nm; lifetime of 11.6 ms), while the bromo derivative DBS-Br only shows RTP (peak at 441 nm; lifetime of 8.7 ms). Interestingly, a blue shifting occurs (563 nm to 543 nm) in the emission of an elastically deformed crystal, when compared to straight and naturally bent crystals.

To investigate the effect of mechanical force on the RTP change, structural mapping was performed on pristine straight, elastically bent and naturally bent crystals, enabling to quantify its origin in terms of supramolecular topology [4]. As such, we were able to establish that chalcogen-centered weak interactions are essential regarding the elasticity and RTP properties in both materials, while the RTP blue shift in the elastically bent DBS is due to the weakening of S-π bonds during bending [4].

Regarding the organoboron-based crystals (BN1), bending and subsequent shape recovery was observed as photodynamic responses when irradiated with a 375 nm continuous wave (CW) UV laser source [6]. In addition to the flexible bending, these single crystals exhibit several photosalient effects (fast splitting, popping/jumping, delamination, expansion), while, remarkably, maintaining their single crystallinity. Further, single crystals of BN1 emit blue in color when excited (max. at 437 nm). Upon irradiation (few sec.) with a 375 nm CW laser, visible cracks are observed, while the emission intensity increases. Importantly, the emission lifetimes of BN1 crystals, before and after UV laser irradiation, were determined to be 7.2 and 12.3 μs, respectively, which clearly show that BN1 crystals are short-lived room temperature phosphorescent. To build an understanding of the origin of the light-driven mechanical motions of BN1 single crystals and associated RTP, we again performed extensive structural mapping. Apparently, the photosalient events in the crystals happen with intensity enhancement of their phosphorescence emission in a response to prompt light-induced [2+2] cycloaddition reaction, while preserving the 3D arrangement of the crystal lattice [6].

4. Conclusions

First, we reported 1D/2D elastic bendability in dibenzothiophene derivative crystals, including the first finding of a flexible crystal showing a mechanophosphorescence effect upon bending, while structural mapping established the relationship between chalcogen-interactions and the elasticity and RTP properties. Second, photodynamic crystals of an organoboron-based adduct are reported, which feature both short-lived RTP and diverse mechanical (photosalient) motions as response to prompt light-induced [2+2] cycloaddition reactions, while preserving their 3D crystal lattice. Our results disclose the rational design of RTP *soft* crystals for potential photonic applications and as smart and energy-transducing materials.

References

[1]. Y. Wang, L. Sun, C. Wang, et al., Organic crystalline materials in flexible electronics, *Chemical Society Reviews*, Vol. 48, 2019, pp. 1492-1530.

[2]. D. P. Karothu, J. Mahmoud Halabi, E. Ahmed, R. Ferreira, P. R. Spackman, M. A. Spackman, P. Naumov, Global analysis of the mechanical properties of organic crystals, *Angewandte Chemie Int. Ed*., Vol. 61, 2022, e202113988.

[3]. M. Godumala, A. V. Kumar, R. Chandrasekar, Room-temperature phosphorescent organic materials for optical waveguides, *Journal of Materials Chemistry C*, Vol. 9, 2021, 14115.

[4]. S. Bhandary, R. Van Deun, A. M. Kaczmarek, K. Van Hecke, Deformation-induced phosphorescence shift in a 2D elastically flexible organic single crystal: Role of chalcogen-centered weak interactions, *Chemical Science*, Vol. 13, 2022, pp. 10308-10314.

[5]. P. Naumov, D. P. Karothu, E. Ahmed, L. Catalano, P. Commins, J. Mahmoud Halabi, M. B. Al-Handawi, L. Li, The rise of the dynamic crystals, *Journal of the American Chemical Society*, Vol. 142, 2020, pp. 13256-13272.

[6]. S. Bhandary, M. Beliš, A. M. Kaczmarek, K. Van Hecke, Photomechanical motions in organo-boron based phosphorescent molecular crystals driven by a crystal state [2+2] cycloaddition reaction, *Journal of the American Chemical Society*, Vol. 144, 2022, pp. 22051-22058.

(4981)

Laser with SBS-compression and Phase-conjugation in Perfluorooctane for Interference Patterning

A. Černeckytė [1], P. Mackonis [1], A. M. Rodin [1] and O. Myronyuk [2]
[1] Center for Physical Sciences and Technology, Solid State Laser Laboratory,
231 Savanoriu Ave, 02300 Vilnius, Lithuania
[2] Igor Sikorsky, Kyiv Polytechnic Institute, Department of Chemical Technology
of Composite Materials, Peremohy Ave. 37, 03056 Kyiv, Ukraine
Tel.:+37067025050
E-mail: paulius.mackonis@ftmc.lt

Summary: Self-seeded configuration of a perfluorooctane SBS-compressor with a double-pass phase-conjugated Nd:YAG amplifier provides up to ~50 mJ, 94 ps output pulses using a commercial 1.1 ns, ~2 mJ mini-laser. These short, transform-limited pulses ensure high-contrast fringes for high-throughput interference patterning of metal surfaces in order to impart water-repellent properties. The developed laser layout is also well suited for laser dermatology due to smooth diffraction-free output beams and the use of a non-toxic compressor substance.

Keywords: Stimulated Brillouin scattering, Injection seeding, Pulse compression, Perfluorooctane, Carbon tetrachloride, Interference patterning, Laser dermatology.

1. Introduction

Pulse compression based on stimulated Brillouin scattering (SBS) [1] makes it possible to achieve a pulse width of ~110 ps in liquids such as perfluorooctane C_8F_{18} [2] and carbon tetrachloride CCl_4 [3], as well as ~180 ps in fused quartz [4]. However, the most studied CCl_4 is toxic for use in medical lasers and is not suitable for phase conjugation in double-pass amplifiers, since it is prone to optical breakdown and has a low reflectivity ~40 % of the SBS-mirror. In contrast, the safety of C_8F_{18} has been proven by its use as a coolant, tamponade in eye surgery and as a breathable fluid. The high breakdown threshold and reflectance above 90 % allow it to be used in high-energy >200 mJ double-pass phase-conjugated amplifiers [2]. Self-seeding of the SBS-compressor with CCl_4 allows to improve energy stability, reduce jitter, and achieve shorter pulses [3], however with an energy limited to ~1 mJ.

The goal of this study was to define a self-seeded SBS-compressor layout providing ~90 ps high-energy pulses with a smooth diffraction-free beam suitable for both interference patterning and laser dermatology.

2. Experiment

Input pulses of ~2 mJ, ~1.1 ns at 10 Hz from a commercial TEM_{00} SLM mini-laser were amplified (Fig. 1) in a 50 mm side-pumped Nd:YAG gain module (AMP). A Faraday isolator (FI) protected the laser source from backward amplified and compressed pulses. Output pulses were decoupled after the second pass using a quarter-wave retardation plate (λ/4) and a thin-film polarizer (TFP). Various SBS-compression configurations have been experimentally studied: with a focusing lens (F3) and a flat mirror (PM) returning the pump radiation passed through a C_8F_{18} SBS-cell 20 cm long (Fig. 1a), with a spherical mirror (SM) (Fig. 1b) and with variable splitting of the pulse into seed and pump, followed by their spatial overlap in the SBS-cell and tuning of the relative delay (Fig. 1c). The optimal layout of SBS-compressor layout was determined by the highest output energy and the shortest pulse width. The temporal shape of the SBS-compressed pulses was measured using a 20 GHz oscilloscope (Teledyne LeCroy SDA 820ZI-B) with an InGaAs PIN photodetector (Discovery Semiconductors DSC10ER-39-FC/APC-V-2).

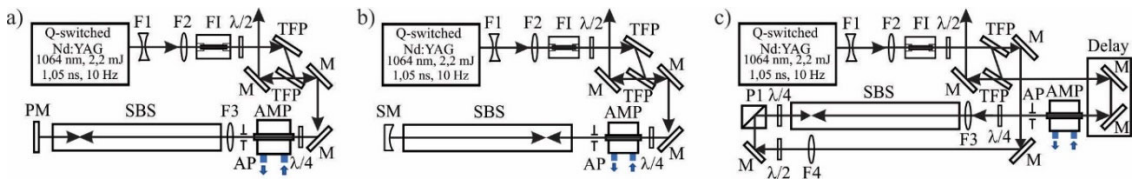

Fig. 1. SBS-compression schemes a – c: FI – Faraday isolator, F1,2 – beam expanding telescope, F3 – focusing lens, λ/2 and λ/4 – half-wave and quarter-wave retardation plates, PM – plane mirror, SM – spherical mirror, TFP – double thin-film polarizer, AMP – double-pass side diode-pumped phase-conjugated Nd:YAG amplifier, AP – aperture.

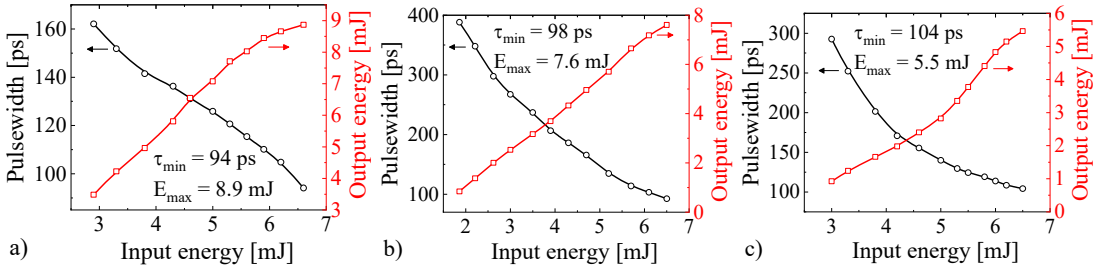

Fig. 2. Pulse width (black line) and energy (red line) of an SBS-compressed pulse as a function of the input energy in self-seeding configurations: a) with a flat mirror, b) with a spherical mirror and c) with variable pulse splitting into seed and pump.

3. Results

In any of the investigated SBS-compression configurations, self-seeding lowered the SBS threshold and improved the reflectivity. In a self-seeding SBS-compressor using a flat mirror (PM) and a lens (F3) with an optimal focal length of $f = 250$ mm (Fig. 1a) the highest energy of ~9 mJ (Fig. 2a) and the shortest pulse width of ~94 ps (Fig. 3) was obtained for compressed Stokes pulses.

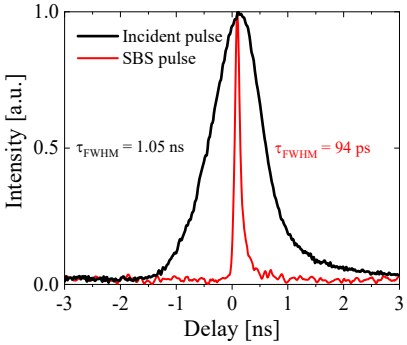

Fig. 3. Temporal shapes of the SBS-compressed (red line) and the incident laser pulse (black line).

For the second configuration (Fig. 1b), there was no significant advantage in terms of pulse width or output energy compared to the case shown in Fig. 1a. The optimum radius of curvature of a spherical mirror (SM) turned out to be $R = 500$ mm. The shortest compressed pulse width of 98 ps and the maximum output energy of 7.6 mJ were achieved (Fig. 2b).

For a more complex scheme (Fig. 1c) the optimal seed pulse energy was 0.2 mJ. It has also been observed that choosing the correct delay between the seed and incident pulses is critical. The shortest pulse width of 104 ps was obtained after compression with an energy of 5.5 mJ (Fig. 2c). Thus, despite the complexity of such a scheme and in contrast to [3] it does not provide a significant advantage over the configurations shown in Fig. 1a, b.

In a flat-mirror scheme, using two consecutive phase-conjugated Nd:YAG gain modules, the output energy of SBS-compressed pulses can reach 50 mJ, while maintaining the high quality of the diffraction-free beam (Fig. 4). The quality of the output beam after the SBS-compressor–amplifier $M^2 = 1.3$ practically did not differ from the quality of the output beam of the mini-laser.

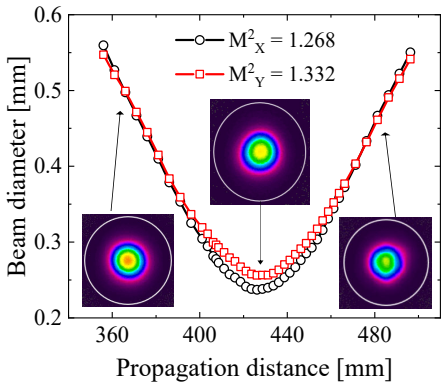

Fig. 4. M^2 measurement of the SBS-compressed pulse in a flat-mirror scheme using two consecutive phase-conjugated Nd:YAG gain modules. Insets: beam intensity profiles in three positions from waist location.

The layout of the laser currently fits into the size of 700×250 mm^2 and a further twofold reduction is possible when designing a compact prototype. The high energy and picosecond pulse width, together with the smooth, diffraction-free beam profile reflected from the SBS-mirror, are suitable for better tattoo removal compared to nanosecond Nd:YAG lasers [5].

For further studies of the surface patterning of aluminum [6] and stainless steel, the laser beam will be divided into two beams interfering in the area of the processed sample, which leads to intensity modulation given by the $\cos^2(\theta)$ distribution. The pattern period d can be varied by the angle of incidence θ, where $d = \lambda/(2\sin\theta)$ with the laser wavelength λ.

Fig. 5 shows an experimental setup consisting of a 50:50 beam splitter (BS), two high-reflection mirrors (HR) and a combination of a half-wave retardation plate (λ/2) with a thin-film polarizer (TFP) to smoothly control the laser pulse energy. The calculated intensity distribution on the sample, which is a convolution of a nearly Gaussian laser pulse intensity distribution, is shown in the inset. The achievable periods in our experiment will be in the range from 0.75 μm to 2 μm, which will allow us to form microtextured surfaces, as in direct laser writing [6], but with a much higher throughput.

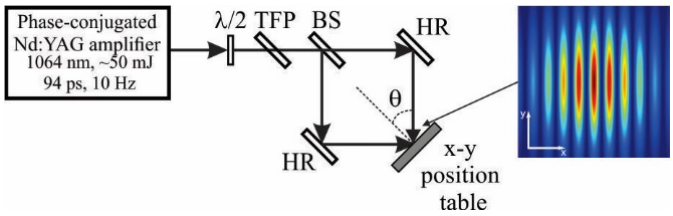

Fig. 5. Setup for a two-beam interference patterning with the calculated intensity distribution of the laser beam. λ/2 – half-wave retardation plate, TFP – thin-film polarizer HR – high reflectivity mirrors, BS – 50:50 beamsplitter, θ – incident angle.

4. Conclusion

Contrary to expectations associated with more complex seed injection configurations, the shortest pulse width and the highest energy of compressed Stokes pulses were obtained in the simplest SBS-compression scheme with a flat mirror. When two consecutive phase-conjugated Nd:YAG gain modules are used, the output energy of compressed pulses can reach ~50 mJ at a pulse width of ~100 ps with a diffraction-free smooth output beam. Transform-limited ~90 ps pulses provide high-contrast interference patterns at high throughput, and phase conjugation ensures smooth, diffraction-free beams for dermatology.

Acknowledgements

This project received partial funding from the Research Council of Lithuania, agreement S-LU-22-3 and Ministry of Education and Science of Ukraine, agreement No. 28, reg. No. 0122U002645.

References

[1]. C. Cao, Y. Wang, Z. Ba, Y. Li, Y. Yu, Z. Lu, Developments of picosecond lasers based on stimulated Brillouin scattering pulse compression, *Frontiers in Physics*, Vol. 9, 2021, 747272.

[2]. N. F. Andreev, E. A. Grishin, O. Kulagin, A. Rodin, Picosecond lasers with Brillouin and Raman pulse compression, in *Proceedings of the International Conference High Power Laser Beams (HPLB'06)*, Nizhny Novgorod, Russia, 2006.

[3]. A. S. Dement'ev, I. Demin, E. Murauskas, S. Slavinskis, Compression of pulses during their amplification in the field of a focused counterpropagating pump pulse of the same frequency and width in media with electrostriction nonlinearity, *Quantum Electronics*, Vol. 41, Issue 2, 2011, pp. 153-159.

[4]. G. Marcus, S. Pearl, G. Pasmanik, Stimulated Brillouin scattering pulse compression to 175 ps in a fused quartz at 1064 nm, *Journal of Applied Physics*, Vol. 103, Issue 10, 2008, pp. 103-105.

[5]. K. Sardana, R. Ranjan, S. Ghunawat, Optimising laser tattoo removal, *Journal of Cutaneous and Aesthetic Surgery*, Vol. 8, Issue 10, 2015; pp. 16-24.

[6]. O. Myronyuk, D. Baklan, G. S. Vasilyev, A. M. Rodin, E. Vanagas, Wetting patterns of liquid-repellent femtosecond laser textured aluminum surfaces, *Coatings*, Vol. 12, Issue 12, 2022, 1852.

(6059)

Current Dependent Emission Properties of Random Laser Diodes

A. Consoli [1,2], P. D. García [2] and C. Lopez [2]
[1] Escuela de Ingeniería de Fuenlabrada, Universidad Rey Juan Carlos,
Camino del Molino 5, 28942 Fuenlabrada, Madrid, Spain
[2] Instituto de Ciencia de Materiales de Madrid, Consejo Superior de Investigaciones Científicas,
C. Sor Juana de la Cruz 3, 28049, Madrid, Spain
Tel.: + 34 913 34 90 00
E-mail: antonio.consoli@csic.es

Summary: Random lasers are based on feedback provided by scattering materials and optical amplification given by pumped active media. Typical architecture of random lasers is based on distributed feedback in which diffusive elements are spatially distributed at random positions inside the active medium. Alternatively, non-distributed feedback geometry consists of a gain medium enclosed between diffusive elements. Recently, we proposed and demonstrated a mixed architecture, in which a mirror and a disordered surface enclose the active medium, i.e. the multi quantum wells of a single transverse mode, Fabry-Perot laser diode. In the present work, we apply our technique to a multi transverse mode Fabry-Perot laser diode, and we provide a detailed characterization of the modified device at different currents. We observe strong variations of the output beam intensity and of the spatially resolved emission spectrum with current and we attribute this behavior to strong modal competition. In general, the presented work reports new results on the behavior of these novel devices with several potential applications.

Keywords: Random lasers, Semiconductor lasers, Laser diodes, Scattering, Pulsed laser ablation.

1. Introduction

Classical optical cavities are based on mirrors, as in Fabry-Perot (FP) lasers, or periodic modulation of refractive index, as in photonic crystals and distributed feedback lasers. Differently, confinement of light due to scattering events provide the diffusive feedback required for lasing action in random lasers (RLs) [1]. RLs can be fabricated with different materials: solid and liquid dye mixed with scattering particles, powders of gain media, active optical fibers with Rayleigh scattering [2]. Emission of RLs is characterized by a multi-mode spectrum with frequency peaks which vary randomly in number and position and by tunable spatial coherence of the output beam depending on the number of transverse modes. These characteristics make RLs attractive for different applications, as imaging and lighting with low spatial coherence and laser-like energy conversion efficiency, spectral analysis with super resolution, networks, signal processing and anti-counterfeiting [3].

Feedback in RLs is provided by scattering elements, that can be placed in random positions inside the active medium or enclosing it, resulting in spatially distributed or non-distributed feedback architectures, respectively. We recently proposed a mixed architecture in which the active medium, consisting of the multi quantum wells of a laser diode (LD), were enclosed between a mirror and a rough surface [4]. This was obtained after pulsed laser ablation of the output mirror of a commercially available, single transverse mode FP LD emitting at 635 nm, with nominal output power of 5 mW.

In this work, we apply our fabrication method to a multi transverse mode FP LD. We first describe the modification process and characterization results of the modified LD. We finally analyze the results and briefly draw some conclusions.

2. Results

The original device is a FP LD emitting at 637 nm (Thorlabs HL6388MG), with measured maximum output power of 190 mW at 350 mA, threshold current of 90 mA and efficiency slope of 0.8 W/A.

The output mirror of the original LD is subject to pulsed laser ablation with a high energy picosecond laser (Ekspla, 30 ps, 10 Hz at 532 nm). The ablating beam has a diameter of 50 μm and 100 μJ per pulse energy. The beam is swept along the active area of the output mirror of the device by moving the LD with a computer-controlled translation stage at 60 μm/s. In Fig. 1(a), a scanning electron microscope (SEM) image is presented of the obtained random laser diode (RLD): the area of the mirror which is not hit by the ablating beam is darker than the disordered surface induced by the ablation process.

Power and spectral measurements of the RLD as a function of current are shown in Fig. 1(b). Threshold current increases to 110 mA and maximum output power and efficiency slope decrease to 200 μW and 0.003 W/A, respectively. These measurements agree with previous results and are attributed to deterioration of the cavity as the ablation process introduces additional losses [4]. Linewidth of 15 nm below threshold decreases abruptly when current is increased above threshold.

Spectrally resolved emission profiles are obtained at different currents by scanning the collimated output beam with an optical fiber connected to a spectrometer and acquiring a spectrum at each point. The intensity

distributions obtained by integrating the collected spectra over the entire wavelength range, are shown in Fig. 2(a-c) for different currents. The intensity profile consists of local maxima and minima randomly placed which vary their distribution with bias current. This is attributed to the variation of the spatial distribution of gain inside the cavity with current and competition between different modes. Full emission spectra for different currents are shown in Fig. 2(d). Spectral profiles change with current and single or multiple peak spectra are observed.

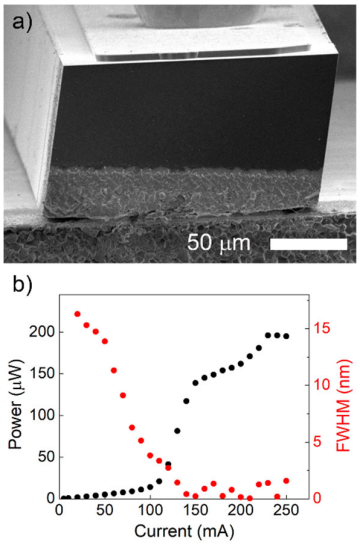

Fig. 1. Scanning electron microscope image of the modified device (a). Output power, left axis, black dots, and full width at half maximum (FWHM) spectral linewidth, right axis, red dots, as a function of current (b).

Spectra collected at different angles differ and lasing frequencies emit along different directions, as shown in Fig. 2(e) for 180 mA.

3. Conclusions

We present here the characterization of a RLD obtained from a multi transverse mode FP LD by pulsed laser ablation of its output mirror. The measured spectrally resolved beam profiles show that lasing modes emit in different directions. Results indicate that emission profile and spectral signature change with current. This is attributed to the current dependent spatial distribution of gain inside the cavity and mode competition. Our work contributes to the study of RLDs which are still novel and not yet fully understood devices with a rich potential for multiple applications.

Acknowledgements

This work was supported by the Spanish Minister of Science and Innovation via the projects PID2021-124814NB-C21 (SPhAM) and PDC2022-133418-I00 (RanLaD).

References

[1]. D. Wiersma, The physics and applications of random lasers, *Nature Physics*, Vol. 4, 2008, pp. 359-367.
[2]. A. S. L. Gomes, A. L. Moura, C. B. de Araújo, E. P. Raposo, Recent advances and applications of random lasers and random fiber lasers *Progress in Quantum Electronics*, Vol. 78, 2021, 100343.
[3]. D. Ni, M. Späth, F. Klämpfl, M. Hohman, Properties and applications of random lasers as emerging light sources and optical sensors: A review, *Sensors*, Vol. 23, Issue 1, 2023, 247.
[4]. A. Consoli, N. Caselli, C. López, Electrically driven random lasing from a modified Fabry-Pérot laser diode, *Nature Photonics*, Vol. 16, 2022, pp. 219-225.

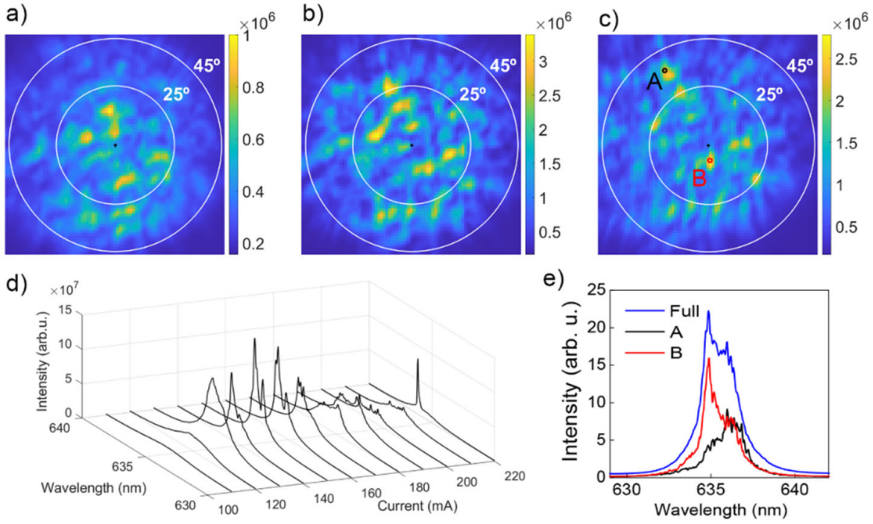

Fig. 2. Beam profiles at 110 mA (a), 150 mA (b) and 180 mA (c). Emission spectra for different currents (d). Spectra obtained at 180 mA (e): full spectrum (blue line) and spectra collected at point A (black line) and B (red line) in (c).

(6202)

NSOM Characterization of Polymer Inverted Refractive-index-contrast Grating Prepared by Laser Lithography on Si Substrate

D. Jandura [1], J. Suffczyński [2], T. Czyszanowski [3] and D. Pudis [1, 4]
[1] Department of Physics, Faculty of Electrical Engineering and Information Technology, University of Zilina, Univerzitna 1, 01026 Zilina, Slovakia,
[2] Institute of Experimental Physics, Faculty of Physics, University of Warsaw, ul. Pasteura 5, 02-093 Warsaw, Poland,
[3] Photonics Group, Institute of Physics, Lodz University of Technology, 90-924 Łódź, Poland
[4] University Science Park of the University of Zilina, Univerzitna 1, 01026 Zilina, Slovakia
E-mail: jandura@fyzika.uniza.sk

Summary: In this paper, we present the preparation and characterization in IP-Dip material of a polymer grating, which is used as a highly reflective and spectrally selective mirror based on Inverted Refractive-Index-Contrast Grating (ICG) geometry. We prepared the grating structure in IP-Dip material using three-dimensional (3D) laser lithography according the proposed theoretical design. We optimized the preparation process for the silicon substrate, the ring arrangement and the geometrical parameters. The morphology of the prepared structures was analyzed using a confocal microscope. Finally, the highly resolved near-field scanning optical microscope (NSOM) for the optical field distribution over the grating structure was used. NSOM in transmission mode was used for the precise characterization and comparison of the near-field profiles of gratings with different period.

Keywords: Grating, Polymer photonics, 3D laser lithography, IP-Dip polymer.

1. Introduction

For decades, nanophotonic devices use a light-matter interaction that leads to an impressive improvement in optical properties. This is typically done by using optical cavities, which trap photons for many cycles before they are released. This allows, for instance, a photon to interact with an active optical material for a longer time, which is advantageous for many applications [1]. A new type of planar optics has recently been discovered, which features a subwavelength grating surrounded by an area with a significantly lower refractive index. This is referred to as high-contrast gratings (HCGs) [2]. It can be designed to produce a nearly perfect reflection or transmission of light over a broad range of wavelengths and angles of incidence [3]. We focused on a specific concept of the grating with the inverted arrangement of refractive index contrast with respect to HCG, known as Inverted Refractive-Index-Contrast Grating (ICG) [4]. Recent attention has been given to polymeric materials due to the development of more advanced 3D printing techniques. 3D Laser lithography has achieved a resolution better than 200 nm allowing the preparation of 3D photonic crystals [5]. In this paper, we focus on the experimental demonstration of the near-field optical properties of polymer grating in IP-Dip material based on ICG geometry using the 3D laser lithography process.

2. Fabrication and Analysis of ICG Grating

For preparation, we used a laser lithography system Photonic Professional GT from Nanoscribe GmbH. A femtosecond laser is focused on the volume of an IP-Dip photoresist, where the two-photon polymerization process occurs in the volume focal spot (voxel). In the fabrication process, the IP-Dip photoresist was deposited on top of the silicon substrate and polymerization by laser writing was realized layer by layer in a single-step process. As the IP-Dip material exhibits a shrinkage effect after polymerization and the development process, the designed dimensions were appropriately oversized. A confocal microscope image of prepared IP-Dip surface grating on a silicon substrate with defined parameters is shown in Fig. 1. We prepared a set of different periods ranging from 1316-1608 nm with the step of 73 nm.

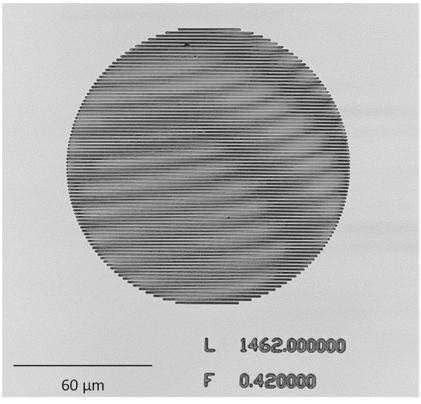

Fig. 1. Confocal microscope top view of IP-Dip surface grating with real parameters: L = 1462 nm, F = 0.42.

3. NSOM Analysis

For the near-field investigation of prepared grating structures, we arranged the experimental setup shown in Fig. 2. The setup consists of a laser source, multimode optical fiber, fused silica sample with the grating structures, and the near-field scanning optical microscope (NSOM) including the tapered optical fiber tip, the precise piezo stages, and InGaAs detector. We prepared very precise optical fiber tapers for the highly resolved vertical characterization. The near-field distribution in the proximity (< 200 nm) of the grating was measured in transmission mode using a 1550 nm light emitting diode (LED) source and the final 3D NSOM image can be seen in Fig. 3a. From this figure, we can see a homogeneous near-field map with a horizontally modulated optical field across the grating structure.

A comparison of NSOM line profiles of the gratings with a slightly different period (1389 nm and 1462 nm) is shown in Fig. 3b. Near-field profile reflects well the ICG period as was measured from confocal laser microscope.

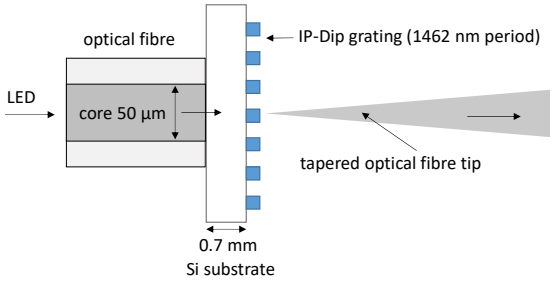

Fig. 2. Illustration of experimental setup for NSOM investigation of prepared grating structures.

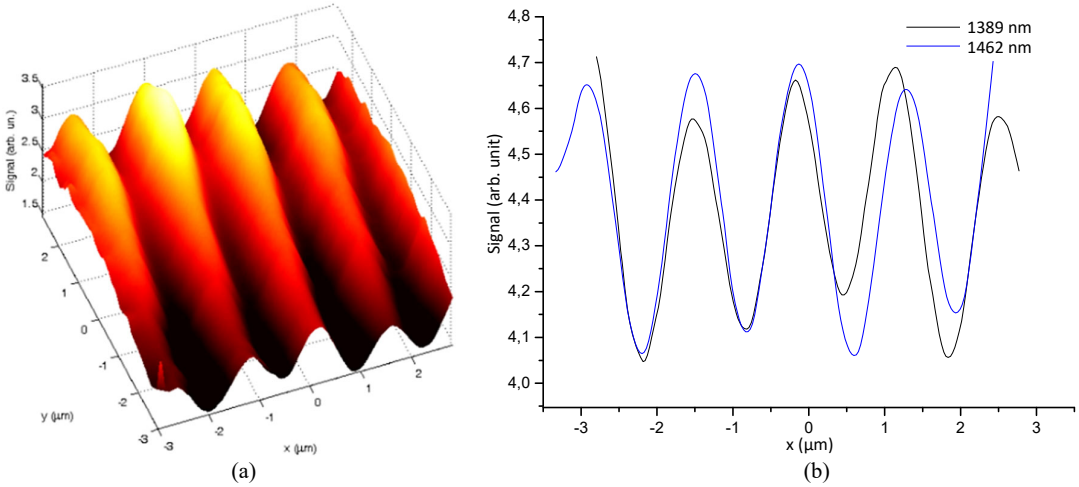

Fig. 3. a) Near-field map of light intensity distribution over the prepared ICG structure with L = 1462 nm illuminated with 1550 nm LED and b) comparison of near-field profiles of two gratings with different period.

4. Conclusions

In this paper, we have presented the preparation and NSOM analysis of the polymer based ICG structure. We experimentally demonstrated highly resolved near-field scanning optical microscope (NSOM) for the optical field distribution over the grating structure. Presented results favors the potential of the NSOM analysis for the complex characterizations of grating structures. The main advantage of the polymer grating compared with semiconductor ICG could be very fast and less demanding preparation and simple application to various hybrid photonic devices, while maintaining such properties as high reflectance, polarization selectivity and a possibility of phase control of the light.

Acknowledgements

This work was supported by the Slovak National Grant Agency under project No. VEGA 1/0363/22 and the Slovak Research and Development Agency under the project No. APVV-20-0264, as well as the Polish National Science Centre within the projects OPUS 2020/39/B/ST7/03502. This paper was supported under the project of Operational Programme Integrated Infrastructure: Independent research and development of technological kits based on wearable electronics products, as tools for raising hygienic standards in a society exposed to the virus causing the COVID-19 disease, ITMS2014+ code 313011ASK8. The project is co-funding by European Regional Development Fund.

References

[1]. A. C. Overvig, S. Shrestha, N. Yu, Dimerized high contrast gratings, *Nanophotonics*, Vol. 7, 2018, pp. 1157-1168.

[2]. C. J. Chang-Hasnain, W. Yang, High-contrast gratings for integrated optoelectronics, *Advances in Optics and Photonics*, Vol. 4, 2012, pp. 379-440.

[3]. M Gębski, M. Dems, A. Szerling, M. Motyka, et al., Monolithic high-index contrast grating: A material independent high-reflectance VCSEL mirror, *Optics Express,* Vol. 23, 2015, pp. 11674-11686.

[4]. E. Pruszyńska-Karbownik, et al., Concept of inverted refractive-index-contrast grating mirror and exemplary fabrication by 3d microprinting, *arXiv Prepress*, 2023, arXiv:2302.06950.

[5]. P. Urbancová, et al., IP-Dip-based woodpile structures for VIS and NIR spectral range: Complex PBG analysis, *Optical Material Express,* Vol. 9, 2019, pp. 4307-4317.

(6224)

Topological Phase Transition in C_6 Photonic Crystals

D. Borges-Silva [1,2], C. G. Bezerra [1] and C. H. O. Costa [3]
[1] Universidade Federal do Rio Grande do Norte, Natal, Rio Grande do Norte, Brazil
[2] Instituto Federal de Educação, Ciência e Tecnologia do Ceará, Cedro, Ceará, Brazil
[3] Universidade Federal do Ceará, Russas, Ceará, Brazil
E-mail: daniel.silva@ifce.edu.br

Summary: Topological photonic crystals have become an interesting topic over the last years because of their potential technological applications and the possibility to mimic quantum phenomena by using classical waves. In this work, we propose a photonic system with C_6 symmetry that allows a topological phase. We consider a triangular lattice composed of six dielectric American football ball-shaped rods in an air matrix. The topological phase is induced by an angular perturbative parameter. We notice that the nonzero perturbative parameter induces a complete bandgap in the Brillouin zone by breaking the double degenerescence at Γ point which is associated to the pseudospin states. We found two different phases: a trivial one and a topological one, according to the value of the perturbative parameter. Since the system presents two different topological phases, light is topologically protected against disorder and defects and it can be used in technological implementations based on the Bulk-Edge correspondence.

Keywords: Photonic crystal, Topology, Chern number, C_6 symmetry.

1. Introduction

The study of topological photonic crystals (TPCs) has become a great research field in physics and engineering. These devices have been attracting interest in nanoscience from both: a basic science and a technological point of view. This is because of their unusual properties which allow to study phenomena such as the quantum spin Hall effect (QSHE), beyond they present a large range of technological applications. In this work we propose a TPC with C_6 point symmetry that supports the photonic analogous of the QSHE. We investigate the conditions to induce a topological phase in the system, as well as its main features.

2. The Photonic Crystals

Let us consider a triangular lattice composed of six dielectric rods ($\varepsilon = 13$) surrounded by an air matrix, with $a = 1$ μm as illustrated in Fig. 1(a). The unit cell is composed with six dielectric American football ball-shaped rods (AFB rods). The AFB rods are built taking into account two cylindrical rods of radius $r = 0.17a$. Then, these cylindrical rods are shifted by a distance $d = \pm a/15$. After that, we consider the intersection area between the shifted cylindrical rods. Finally, the final shapes are placed in their locations which are distant $R = a/3$ from the unit cell's center in order to create a structure with C_6 point symmetry group.

Each AFB rod in the unit cell can be rotated around its respective center by the orientation angle Φ_i, as illustrated in Fig. 1(a). The rods present an anisotropic geometry and their angular orientation can spatially vary. Therefore, we may expect that an angular perturbation will lead to topological phase transitions from trivial to non-trivial domain [1]. A perturbation is introduced in the orientation angle Φ_i so that we can write the orientation angle of the i-th AFB rod as $\Phi_i = (2i-1)\pi/6 + \phi_0 + \phi$. Here $i = 1,2,\ldots,6$ is the rod index, ϕ_0 is the initial unperturbed angle and ϕ is the angular perturbation introduced in our system which has a period π, i.e., given a value of the perturbation ϕ, another value $\phi + \pi$ induces in the system the same topological behavior corresponding to the ϕ. Here we assume $\phi_0 = 29\pi/120$ (see Fig. 1(a)).

It is well-known from the literature that triangular lattices with six artificial atoms have two two-dimensional irreducible representations in the C_6 point symmetry group which are associated with the symmetry of the triangular lattice [2]. Because of that, a doubly degenerate Dirac cone appears at Brillouin zone center [3] and degenerated bands are pseudospin states, which are related to p_x (p_y) and d_{xy} ($d_{x^2-y^2}$) orbitals, corresponding to odd and even parity in the real space, respectively [4]. Taking into account the real space distribution of the fields, these orbitals present dipole and quadrupole distributions and they are related to pseudospin states as $p_\pm = 1/2\left(p_x \pm ip_y\right)$ and $d_\pm = 1/2\left(d_{xy} \pm id_{x^2-y^2}\right)$ [1]. Here, the positive signal is labeled as pseudospin-up states and the negative signal is labeled as pseudospin-down states. They are labeled in this way because the phases of the electromagnetic field related to them present windings, with corresponding rotations in opposite directions. In another words, while the pseudospin-up present an anti-clockwise circular polarization, the pseudospin-down present a clockwise circular polarization [4].

Taking into account the unperturbed Photonic Crystal ($\phi = 0$), we calculate the Band Structure for

the TM modes ($E_z, H_x, H_y \neq 0$) by using COMSOL Multiphysics software [5], as we can see on Fig. 1(b). Observe that, because of C_6 symmetry group, a doubly degenerated Dirac point is created at Γ point between the second and fifth bands. In Fig. 1(c) we plot the Electric Field along z-direction (E_z) at the Dirac point, and we found four states that are related to dipoles modes and quadrupoles modes: p_x and p_y orbitals are dipole modes, while d_{xy} and $d_{x^2-y^2}$ orbitals are quadrupole modes.

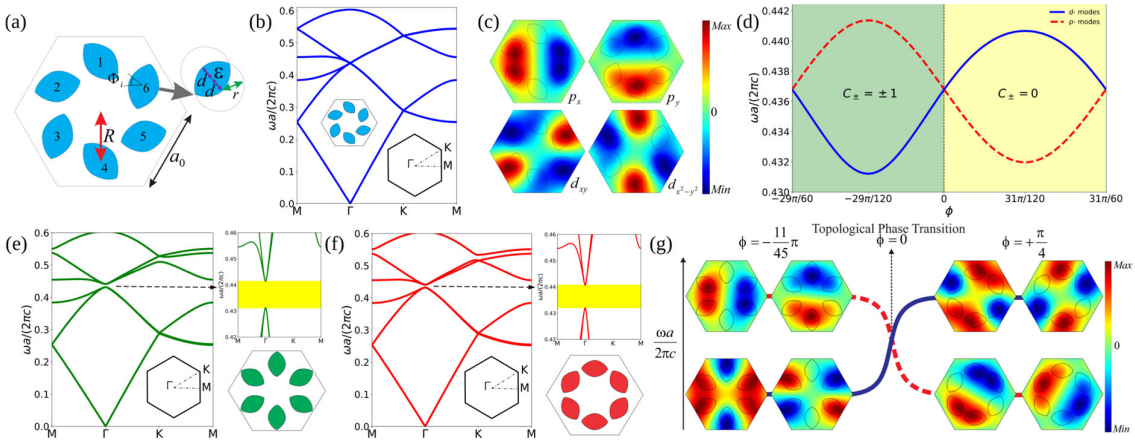

Fig. 1. (a) Scheme of the unit cell for the unperturbed two-dimensional Photonic Crystal ($\phi_0 = 0$), with $a_0 = a/\sqrt{3}$. (b) Band structure for the TM modes of the crystal with $\phi = 0$. There is a double degenerate Dirac point at the Γ point with $\omega\, a/(2\pi c) = 0.437$. (c) Profile of E_z at the Dirac point for $\phi = 0$. (d) Effect of ϕ on the TM band structure for the second, third, fourth and fifth bands at the Γ point. (e) Band structure for the TM modes for the negative case ($\phi = -11\,\pi/45$) and (f) for the positive case ($\phi = \pi/4$). The bandgap is highlighted by the yellow area. (g) Profile of the electric field E_z. We easily can see the inversion of bands between positive and negative photonic crystals with the topological phase transition happening at $\phi = 0$ (where there is the double degenerated Dirac cone).

3. Topological Phase Transition

In order to study the opening of the bandgap at the Γ point we consider a nonzero perturbation in the rods' orientation angle ϕ and evaluate $\omega\, a/(2\pi c)$ *vs* ϕ for the second, third, fourth and fifth bands, as we can see in Fig. 1(d). We can observe that as $|\phi|$ increases from 0, the bandgap width monotonically increases, reaching its maximum at $\phi = -29\,\pi/120$ and $\phi = 30\,\pi/120$. On the contrary, as $|\phi|$ increases from $\phi = -29\,\pi/120$ and $\phi = 30\,\pi/120$, the bandgap width monotonically decreases, until the double Dirac cone is recovered at $\phi = -29\,\pi/60$ and $\phi = 30\,\pi/60$. This is a consequence, as mentioned before, of the perturbation's period π.

To exemplify those two bandgaps, Fig. 1(e) and Fig. 1 (f) show the band structure for the negative ($\phi = -11\,\pi/45$) and positive ($\phi = \pi/4$) perturbed photonic crystal. The perturbation opens a gap between $\omega\, a/(2\pi c) = 0.432$ and $\omega\, a/(2\pi c) = 0.4408$, for the positive perturbation case; and between $\omega\, a/(2\pi c) = 0.431$ and $\omega\, a/(2\pi c) = 0.4415$, for the negative perturbation case, corresponding to a gap-midgap ratio [6] of $\Delta\,\omega/\omega_m = 0.0202$ and $\Delta\,\omega/\omega_m = 0.0241$, respectively. Since the bandgap is opened, edge states can appear inside the gap and these states may present interesting features.

With a view to study the topological behaviour close to the Γ point, we can write an effective Hamiltonian by using the k.p perturbed model and the Chern number becomes $C_\pm = \pm 1/2\,(Sign[B] + Sign[M])$[4]. Here B is the diagonal term of the effective Hamiltonian close to the Γ point which is essentially negative. Also, $M = (\omega_d - \omega_p)/2$, where ω_d and ω_p are the eigenvalues of orbital *d* and orbital *p*, respectively [7]. The eigenvalue ω_p is related to the degenerate dipole states of $p_\pm$, while ω_d is related to the degenerate quadrupole states of $d_\pm$ [8]. If $\omega_p < \omega_d$ then $M > 0$, hence $C_\pm = 0$ and the Photonic Crystal is topologically trivial. However, if $\omega_p > \omega_d$ then $M < 0$, hence $C_\pm = \pm 1$ and the photonic crystal is in a topological phase. Thus, the inversion of the bands between the degenerated modes at the Γ point promotes the topological phase transition [9].

For this work, we consider the inversion of the bands that occurs between $\phi = -11\,\pi/45$ and $\phi = \pi/4$ for the degenerated modes, as shown in Fig. 1(g). We can observe that, for the positive case, the frequency of the dipole modes is lower than the frequency of the quadrupole modes, while for the negative case, the frequency of the dipole modes is higher than the frequency of the quadrupole modes. The inversion of the bands happens at $\phi = 0$. Therefore, for $\phi = \pi/4$ we obtain $C_\pm = 0$, which corresponds to a trivial photonic crystal, and for the case $\phi = -11\,\pi/45$ we obtain $C_\pm = \pm 1$, which corresponds to a topological photonic crystal. Since we have a topological phase, edge states are going to emerge in a finite sample, and these edge states must present the same pseudospin behaviour as mentioned before, i.e., a pseudosip-up edge state and a pseudospin-down edge state [7].

4. Conclusions

We have proposed a photonic system that supports two different topological phases. The system present C_6 symmetry group and we induce the topological phase by introducing an angular perturbation. We notice that the unperturbed system presents a double Dirac cone at Γ point. On the other hand, for nonzero values of the perturbation, a complete bandgap is opened for both cases, positive and negative perturbation angle. Those cases have different topological invariants, the negative perturbation induces the system to a topological phase, while the positive perturbation induces the system to a trivial phase. Our results allow the possibility of building devices composed, simultaneously, of crystals with positive and negative perturbations, i.e., trivial and topological ones. Thus, robust and confined edge states can be founded in this composed system because of Bulk-Edge correspondence [10].

References

[1]. H. Huang, S. Huo, J. Chen, reconfigurable topological phases in two-dimensional dielectric photonic crystals, *Crystals*, Vol. 9, Issue 4, 2019, pp. 221-230.

[2]. M. S. Dresselhaus, G. Dresselhaus, A. Jorio, Group Theory: Application to the Physics of Condensed Matter, *Springer-Verlag,* 2008.

[3]. Y. Yang, Y. F. Xu, T. Xu, H.-X. Wang, J.-H. Jiang, X. Hu, Z. H. Hang, Visualization of a unidirectional electromagnetic waveguide using topological photonic crystals made of dielectric materials, *Phys. Rev. Lett.*, Vol. 120, Issue 21, 2018, 217401.

[4]. L.-H. Wu, X. Hu, Scheme for achieving a topological photonic crystal by using dielectric material, *Phys. Rev. Lett.*, Vol. 114, Issue 22, 2015, 223901.

[5]. COMSOL Multiphysics, www.comsol.com

[6]. R. Meade, J. N. Winn, J. Joannopoulos, Photonic Crystals: Molding the Flow of Light, *Princeton Univ. Press*, 1995.

[7]. Y. Peng, B. Yan, J. Xie, E. Liu, H. Li, R. Ge, F. Gao, J. Liu, Variation of topological edge states of 2D honeycomb lattice photonic crystals, *Phys. Status Solidi RRL,* Vol. 14, Issue 8, 2020, 200020.

[8]. Y. Fang, Z. Wang, Highly confined topological edge states from two simple triangular lattices with reversed materials, *Opt. Commun*., Vol. 479, 2021, 126451.

[9]. Z. Li, H.-C. Chan, Y. Xiang, Fragile topology based helical edge states in two-dimensional moon-shaped photonic crystals, *Phys. Rev. B,* Vol. 102, Issue 24, 2020, 245149.

[10]. A. B. Khanikaev, G. Shvets, Two-dimensional topological photonics, *Nat. Photonics,* Vol. 11, 2017, pp. 763-773.

(6265)

Compression of Femtosecond Laser Pulses using Self-phase Modulation: from Kilowatts to Petawatts over 40 Years

E. A. Khazanov
Institute of Applied Physics of the Russian Academy of Sciences, 46 Ulyanov St, N. Novgorod, Russia
E-mail: efimkhazanov@gmail.com

Summary: The pulse duration at the output of femtosecond lasers is usually close to the Fourier limit and may be shortened by increasing the spectral width. To this end, use is made of self-phase modulation when a pulse propagates in a medium with cubic nonlinearity. Then, the pulse with a chirp (frequency dependence of the spectrum phase) is compressed by a linear dispersion element, which introduces a chirp of the same modulus but opposite sign. This pulse post-compression, known since the 1960s, has been widely used and is being developed up to the present for pulses with energies from fractions of a nJ to tens of J. The review is devoted to the theoretical foundations of this method, problems of energy scaling, and a discussion of the results of more than 150 experimental studies.

Keywords: Post-compression, TFC, CafCA, Femtosecond lasers, Kerr nonlinearity.

1. Introduction

From the advent of lasers to the present day, one of the main goals of research has been to obtain the shortest possible laser pulses. There are three reasons why short pulses are of interest. Firstly, it is a tool for studying ultrafast processes in physics, chemistry, and biology. Secondly, under certain conditions, short pulses open the way to experiments that are inaccessible for longer pulses. Thirdly, in the field of ultra-high power lasers and ultra-intense fields, the pulse duration also plays a key role, since the power depends only on the pulse energy and duration. An increase in the energy of such lasers is associated with an increase in the number of amplifiers, which greatly increases the already significant size and cost of lasers. Moreover, the radiation power of modern lasers is not limited by laser pulse amplification. Actually, it is limited by the fact that after amplification it cannot be compressed, since diffraction gratings have a low damage threshold, which limits the power. Thus, the only way to multiply the power of such lasers in practice is to shorten the output pulse after the diffraction grating compressor.

2. Basic Idea of Pulse Post-compression

The pulse duration at the output of femtosecond lasers usually slightly exceeds the Fourier limit, and for multiple pulse shortening its spectrum should be stretched by at least the same factor. For this, selfphase modulation (SPM) of the laser pulse is used during its propagation in a medium with cubic (Kerr) nonlinearity. This key idea was proposed [1] in 1969. At the output of a nonlinear element, the pulse becomes chirped, which must be compensated for by adding the phase equal in magnitude but opposite in sign. This is done by means of chirped mirrors or other linear devices. This method of nonlinear compression of laser pulses (see Fig. 1) is usually called postcompression. In application to high-power lasers, the term TFC (Thin Film Compression) or CafCA (Compression after Compressor Approach) is used.

Post-compression is the subject of several reviews [27] focused on certain methods of its implementation and the corresponding ranges of pulse intensity. The purpose of this talk is to summarise the main experimental results obtained over the past 40 years.

3. Post-compression Geometries

Fig. 1 schematically shows eight variants of the geometry of a nonlinear medium. To begin with, the waveguide and the free propagation of the beam should be separated. As concerns the waveguide, a beam as close as possible to the mode (usually the lowest one) of the corresponding waveguide is formed at its input. The main disadvantage of waveguides is the small size of the mode, which limits the power. Their undoubted advantage is their large length, which provides a large B-integral even at a low intensity.

The simplest waveguide is a single-mode fibre (SMF), in which the field is retained either due to total internal reflection (SMF-TIR) or to photonic crystal fibres (SMF-PCF).

The pulse power may be increased significantly by abandoning SMF in favour of gas-filled capillaries, i.e., hollow-core fibres (HCFs). The principal feature of a capillary is its multimodal nature and also the fact that it is the grazing angles of incidence on the walls of the capillary rather than the

total internal reflection that prevent the beam from transverse spreading. Both of these circumstances are significant drawbacks. The length of a conventional rigid thick-walled hollowcore fibre (TW-HCF) does not exceed 1 m, since it is impossible to ensure the required quality of the inner wall at longer lengths. The fact is that losses are significant even with minimal bends (distortions) of the core. A stretched flexible thin-walled hollow core fibre (SF-HCF) can have a significantly longer length.

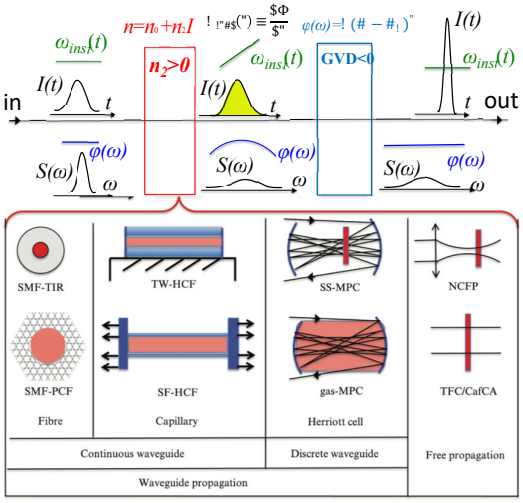

Fig. 1. Principles of post-compression and geometries of nonlinear element.

Instead of continuous waveguides discrete ones can be employed. The beam propagates in free space, and diffraction is compensated for by periodically located lenses or mirrors, between which there are waists. Such devices are called multipass cells (MPC); the radiation passes through them dozens of times. Solid-state-based multipass cells (SS-MPCs) as well as gas-filled multipass cells (gas-MPCs) are used. In both cases, SFM, while remaining small per pass, accumulates per many passes. The laser power is limited by ionization in the focal waist; increasing the waist requires a huge MPC size (the best result is obtained with an 8-meter cell).

An alternative to waveguides is a bulk solid-state nonlinear element in which the laser beam propagates freely. The use of gases in this case is problematic due to their low nonlinearity. For a solid-state nonlinear medium, to avoid breakdown at a high radiation power, the beam diameter must be large enough: for multiterawatt and petawatt power, from 1 to 10 cm or more. Thus, the geometry of the nonlinear medium changes radically – from a long cylinder to a thin disk. The first works were devoted to noncollinear free propagation (NCFP) of a focused beam, but the most exciting results are obtained with a collimated beam (TFC/CafCA).

The results of the experiments implemented over 40 years and published in more than 150 papers are summurized in Figs. 2, 3.

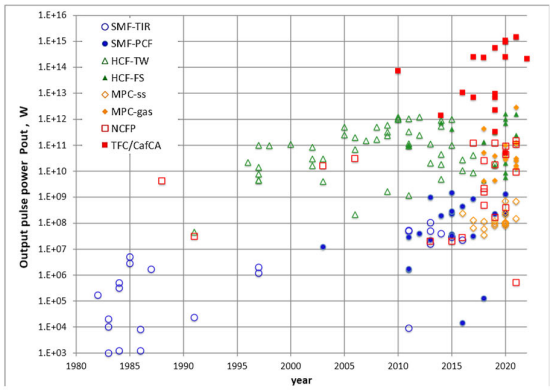

Fig. 2. History of post-compression.

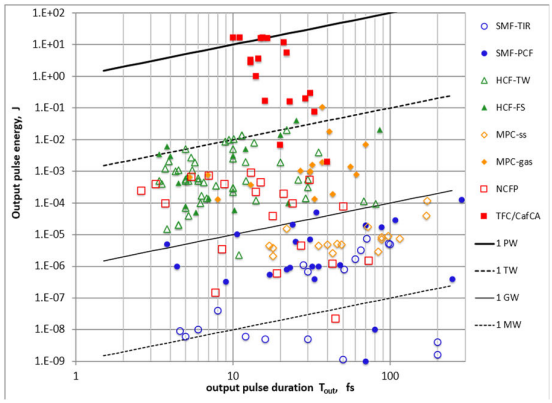

Fig. 3. Experimental results on the 'output pulse duration–output pulse energy' plane.

Conclusions

Fig. 2 shows that the most dynamically developing post-compression variants are currently SF-HCF, gas-MPC and TFC/CafCA. It is in these variants of geometry that further progress should be expected in the coming years. One can see from Figs. 2 and 3 that, as applied to ultra-high power lasers, the use of TFC/CafCA is the only option for pulse compression. It is also important to note that although this is the cheapest and simplest technology (see Fig. 1), it has virtually no power limit.

References

[1]. R. A. Fisher, P. L. Kelley and T. K. Gustajson. Subpicosecond pulse generation using the optical Kerr effect, *Applied Physics Letters*, Vol. 14, Issue 4, 1969, pp. 140-143.

[2]. T. Brabec and F. Krausz, Intense few-cycle laser fields: Frontiers of nonlinear optics, *Reviews of Modern Physics*, Vol. 72, 2000, Issue 2, pp. 545-591.

[3]. S. De Silvestri, M. Nisoli, G. Sansone, S. Stagira and O. Svelto, Few-cycle pulses by external compression, *Topics in Applied Physics*, Vol. 95, 2004, pp. 137-177.

[4]. E. A. Khazanov, S. Y. Mironov and G. Mourou, Nonlinear compression of high-power laser pulses: compression after compressor approach, *PhysicsUspekhi*, Vol. 62, Issue 11, 2019, pp. 1096-1124.

[5]. T. Nagy, P. Simon and L. Veisz, High-energy few-cycle pulses: post-compression techniques, *Advances in Physics X*, Vol. 6, Issue 1, 2020, Article 1845795.

[6]. M. Hanna, F. Guichard, N. Daher, Q. Bournet, X. Delen and P. Georges, Nonlinear Optics in Multipass Cells, *Laser & Photonics Reviews*, 15, 12, 2021, p. 2100220.

[7]. E. A. Khazanov, Post-compression of femtosecond laser pulses using self-phase modulation: from kilowatts to petawatts in 40 years, *Quantum Electronics*, Vol. 52, Issue 3, 2022, pp. 208-226.

(6463)

Time-resolved Volumetric Modification in Fused Silica Reveals Ultrafast Electron Dynamics and Shielding

M. Zukerstein [1], V. P. Zhukov [1, 2, 3] and N. M. Bulgakova [1]
[1] HiLASE Centre, Institute of Physics ASCR, Za Radnicí 828, Dolní Břežany, Czech Republic
[2] Federal Research Center for Information and Computational Technologies, 6 Lavrentyev Ave., Novosibirsk, Russia
[3] Novosibirsk State Technical University, 20 Karl Marx Ave., Novosibirsk, Russia
Tel.: + 420314007754
E-mail: zukerstein@fzu.cz

Abstract: Volumetric modification of dielectrics is a complex and dynamic process involving many nonlinear phenomena. The modification level is directly related to the local density of the absorbed energy of the laser radiation. Thanks to time-resolved experiments and numerical simulations, we can observe the effect of various dynamic processes on the modification and control it. We show that the generated electron plasma causes a shielding effect with a characteristic duration of 600 fs. Additionally, the use of a weaker pre-pulse affects the modification level of the second pulse due to shielding and absorption on long-lived self-trapped excitons generated by multiphoton absorption. Experimental results are supported by numerical simulations of pulse propagation in non-linear media using Maxwell's equations.

Keywords: Volumetric modification, femtosecond laser pulses, laser processing, fused silica, double-pulse experiment.

1. Introduction

Laser materials processing is one of the most important areas of laser physics. Among various applications in this field, volumetric modification of transparent crystals and glasses is a key technology for inscription of three-dimensional structures with perspectives of novel developments in photonics and optoelectronics [1]. Optimization of 3D direct laser writing technique is of high demand in this research area that in particular includes spatiotemporal laser beam manipulation for achieving high quality of structural modification.

In this experimental and theoretical work, we study the volumetric modification with two Gaussian pulses depending on time separation between them. Our experiments allow us to follow the evolution of the electron plasma, which causes shielding and delocalization of the absorbed energy. At the same time, we can observe the influence of long-lived electronic states (self-trapped excitons) on the investigated modification level of the material.

The experimental results were compared with numerical simulations based on the propagation of laser pulses in a nonlinear media by axially symmetric Maxwell's equations [2].

2. Experimental

In the experiment we use the Ti:sapphire laser Astrella (Coherent) as a light source, operating at a central wavelength of $\lambda_0 = 800$ nm and $\tau_{\mathrm{FWHM}} \approx$ 40 fs. The laser beam is divided by a beam-splitter into two parts, one arm is guided through a delay line to introduce a time delay between the two pulses. Both arms are combined into collinear beams and focused with an objective (10× magnification with $NA = 0.25$) on the fused silica plate.

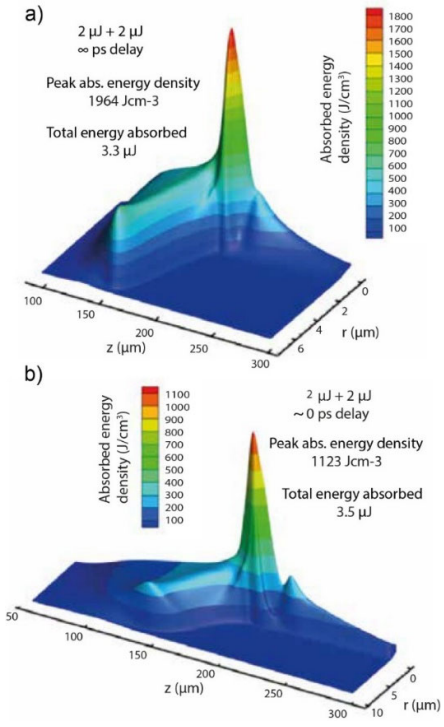

Fig. 1. Calculated energy density distribution of two pulses with energies of $E_{\mathrm{P}} = 2$ µJ with time delays a) $\tau = \infty$ ps (two separate pulses), and b) $\tau \approx 0$ ps.

3. Theory

Propagation in a nonlinear medium is described by axially symmetric Maxwell's equations [2]. The distribution of absorbed laser energy density

$$E_{\mathrm{ab}} = \int_{-t_0}^{\infty} \left(\frac{\boldsymbol{jE^* + j^* E}}{4} + \alpha \hbar\omega W_{\mathrm{PI}} + \alpha_{\mathrm{STE}} \hbar\omega W_{\mathrm{PI}}^{\mathrm{STE}} \right) \mathrm{d}t \quad (1)$$

is a main purpose of the nonlinear calculations [2]. This value determines the residual modifications of the glass. W_{PI} is multiphoton ionization rate, $\alpha = 6$ (the bandgap $E_{\mathrm{g0}} = 9$ eV). $W_{\mathrm{PI}}^{\mathrm{STE}}$, $\alpha_{\mathrm{STE}} = 4$ correspond to the self-trapped excitons (STE) with the bandgap $E_{\mathrm{g0}}^{\mathrm{STE}} = 5.5$ eV.

Fig. 1 shows the calculated energy density distribution of two pulses with $E_{\mathrm{P}} = 2$ μJ with time delays $\tau = \infty$ ps (two separate pulses) and $\tau \approx 0$ ps.

4. Results and Discussion

We show that two almost overlapping pulses in time cause a significantly smaller volumetric modification than the two time-separated pulses (two pulses with a large time delay). Based on experimental measurements of the dependence of the volumetric modification on the time delay between two pulses, we estimate the duration of the electron plasma shielding effect of $\tau_{\mathrm{plasma}} \approx 600$ fs (see Fig. 2). Modification level was obtained by grayscale analysis of in-plane microscopic images of the modified region.

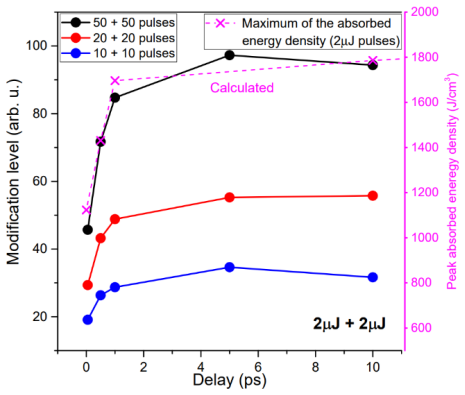

Fig. 2. The data on experimentally obtained modification with 2 pulses (accumulation of 10, 20 and 50 pairs of pulses) at $\lambda_0 = 800$ nm and $E_{\mathrm{P}} = 2$ μJ depending on their time delay. By pink crosses the calculated data on maximum of the absorbed energy density are presented for one pair of pulses at the energy $E_{\mathrm{P}} = 2$ μJ each.

Based on asymmetric experiments (two pulses with different energy), we also show that, for larger volumetric modification, it is advantageous to use a weak pre-pulse followed by a stronger pulse (see Fig. 3). This can be explained by screening of the focus by self-trapped exciton population in the focal area [3].

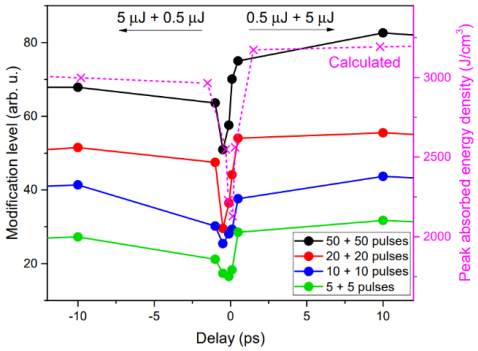

Fig. 3. The data on experimentally obtained modification with 2 pulses (accumulation of 5, 10, 20 and 50 pairs of pulses) at $\lambda_0 = 800$ nm with energies of $E_{\mathrm{P}} = 0.5$ μJ and 5 μJ depending on their time delay. By pink crosses, the calculated data on the maximum of the absorbed energy density are given for one pair of pulses for these particular experimental conditions. The self-trapped exciton decay time $\tau_{\mathrm{STE}} \approx 34$ ps in the theoretical calculations was used.

5. Conclusion

In this work, we investigated the shielding effect and electron dynamics by observing the bulk modification in fused silica. We show that two almost overlapping pulses in time cause a significantly smaller volumetric modification than the two separate pulses (two pulses with a large time delay).

Furthermore, we explain the mechanisms taking place on picosecond time scales and we show that long-lasting self-trapped excitons have a great impact on volumetric modification. These self-trapped exciton states then primarily cause additional shielding when the second pulse is applied.

Acknowledgements

This work was supported by the European Regional Development Fund and the state budget of the Czech Republic (project BIATRI: No. CZ.02.1.01/0.0/0.0/15_003/0000445).

References

[1]. R. Stoian, Volume photoinscription of glasses: three-dimensional micro- and nanostructuring with ultrashort laser pulses, *Applied Physics A*, Vol. 126, 2020, Article 438.

[2]. N. M. Bulgakova, V. P. Zhukov, S. V. Sonina, and Y. P. Meshcheryakov, Modification of transparent materials with ultrashort laser pulses: What is energetically and mechanically meaningful?, *Journal of Applied Physics*, Vol. 118, Issue 23, 2015, pp. 233108.

[3]. N. M. Bulgakova, V. P. Zhukov, Y. P. Meshcheryakov, L. Gemini, J. Brajer, D. Rostohar, and T. Mocek, Pulsed laser modification of transparent dielectrics: what can be foreseen and predicted by numerical simulations?, *Journal of the Optical Society of America B*, Vol. 31, Issue 11, 2014. pp C8-C14.

(6727)

Optimization of Multiplexed Wide-angle Solar Concentrators with High Diffraction Efficiency

T. Lloret [1,2], M. Morales-Vidal [1,3], B. Nieto [1], J. C. García-Vazquez [3], M. G. Ramírez [3], S. Gallego [3] and I. Pascual [1,3]

[1] Dept. de Óptica, Farmacología y Anatomía, Universidad de Alicante, 03690 San Vicent del Raspeig, Spain

[2] Materials Science & Engineering, University of Colorado, Boulder, Colorado 80303, USA

[3] Instituto Universitario de Física Aplicada a las Ciencias y las Tecnologías, Universidad de Alicante, 03690 San Vicente del Raspeig, Spain

E-mail: tomas.lloret@ua.es

Summary: The main objective of the work was to obtain a versatile holographic element to concentrate sunlight from different relative positions of the Sun during the day, avoiding the need for expensive tracking systems. For this purpose, symmetric and asymmetric holographic lenses of negative focal length were stored using peristrophic holographic multiplexing techniques to obtain holographic optical elements of width angular response and high diffraction efficiency. For this purpose, a low-toxicity photopolymer called Biophotopol whose dye was photosensitive at the recording wavelength of 473 nm was used. The holographic behavior of the solar concentrators (HSC) was studied by measuring the angular diffraction efficiency at 633 nm (near the maximum response of silicon cells). The efficiency of the complete HSC-solar cell system has been studied in short-circuit under solar illumination, using a solar simulator, at different incidence angles. In addition, the relationship between the angular separation between multiplexed HLs and the efficiency of the complete system has also been studied.

Keywords: Holographic solar concentrators, Photovoltaic energy, Photopolymers, Diffraction efficiency.

1. Introduction

Low-cost and environmentally friendly solar concentrator systems represent an important challenge in our society to obtain competitive photovoltaic (PV) energy. The study and development of applied optical systems to generate clean and renewable energy is one of the most important lines of research today and is known as Green Photonics. This includes solar concentrators, solar cells, and low toxicity recording materials.

Sunlight can be concentrated with conventional refractive lenses, such as Fresnel lenses [1], or with reflective elements [2]. Fresnel lenses are widely used as traditional concentrators, but they have a small acceptance angle and reflective elements need continuous maintenance of surface reflectivity. In addition, conventional solar concentrators also require cooling [3] and expensive tracking systems to follow the Sun's trajectory. Holographic optical elements (HOE) are optical elements obtained using the holographic technique and can be an alternative to conventional lenses because they are cheaper and versatile. They provide an enlarged focusing area which helps to protect solar cells from heating damage [4]. The first HOE as a wide-angle solar concentrator was proposed by Ludman in 1982 [5]. During the last few years HOEs are widely used as solar concentrators, researchers have described high [6] and low [7] spatial frequency holographic concentrators, with a range of operating angles from 12° to 30°. Different types of holographic lenses, spherical [6, 7] and cylindrical [7], have also been developed for solar applications, operating at high or low photometric conditions. Kostuk et al. and Zhao et al. describe the characteristics of transmission [8] and reflection [9] holographic lenses for solar concentrators.

One of the most important aspects when fabricating a holographic solar concentrator (HSC) is the material used to etch it. Photopolymers [7] are excellent holographic materials with the ability to modulate their refractive index, with high spatial resolution, high diffraction efficiency, and low scattering. There is also a commercial photopolymer material, Bayfol HX, which is widely used in holographic applications [6].

In this work, to obtain cost-effective tracking and light concentration systems, low-toxicity holographic solar concentrators (HSCs) obtained from five peristrophic multiplexed symmetric and asymmetric negative holographic lenses with different parameters and recorded in 150 μm layers of Biophotopol are shown.

2. Materials and Methods

2.1. Recording Material

Volume phase transmission HSCs were recorded in a Biophotopol photopolymer, a low-toxicity hydrophilic material made-up of one or more monomers in a binder, an electron donor, and a dye sensitizer. Biophotopol composition was developed using sodium acrylate (NaAO) as the monomer, water as a unique solvent, triethanolamine (TEA) serving as the initiator and plasticizer, riboflavin

5'-monophosphate sodium salt (RF) serving as a dye, and polyvinyl alcohol (PVA). Table 1 shows the recording material component quantities.

Table 1. Optimized concentrations.

PVA	NaAO	TEA	RF
wt/V(%)	M	M	M
13.3	0.44	$10 \cdot 10^{-3}$	$1.4 \cdot 10^{-3}$

2.2. Experimental Setup

The experimental setup used in the recording stage is a typical holographic setup. While a laser emitting at a wavelength of 473 nm was used for the recording stage, an unexpanded Helium-Neon laser emitting at a wavelength of 633 nm, to which the recording material is not sensitive, was used for the control (monitoring) and reconstruction stage. In addition, the experimental setup used to reconstruct the HSCs with the solar simulator can be seen in ref [10].

3. Results

The results obtained in this work are shown in Fig. 1. The diffraction efficiency has been plotted as a function of the reconstruction angle for a wavelength of 633 nm since this wavelength has the greatest influence on Si photovoltaic cells (Fig. 1a).

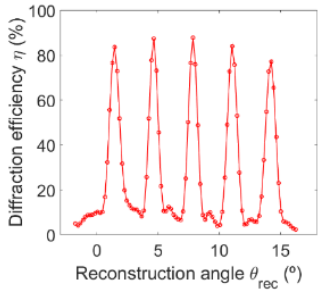

(a)

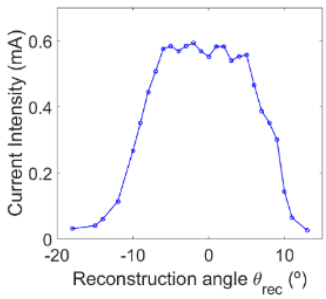

(b)

Fig. 1. Angular reconstruction for $\Delta\theta = 3°$ under (a) 633 nm laser (b) Solar light.

In addition, the efficiency of the complete HSC-solar cell system in short-circuit under solar illumination at different angles of incidence has been studied in Fig. 1b. The smaller the angle between peaks, the larger the enveloped area in the curve. Interestingly, despite obtaining good performance in diffraction and current intensity, angular width is reduced. Therefore, the optimization of the HSCs will depend on the system in which they are to be implemented.

4. Conclusions

This work presents holographic solar concentrators as a low-cost solution to the current tracking systems used in photovoltaic energy. This solar concentrator with high diffraction efficiency is obtained from 5 multiplexed holographic lenses.

Acknowledgments

This research was funded by Universidad de Alicante (UAFPU20-23), by Ministerio de Ciencia e Innovación (PID2019-106601RB-I00, PID2021-123124OB-I00), and by Generalitat Valenciana (CDEIGENT/2018/024, CIDEXG/2022/60, IDIFEDER/2021/014, PROMETEO/2021/006).

References

[1]. W. T. Xie, *et al.*, Concentrated solar energy applications using Fresnel lenses: A review, *Renewable and Sustainable Energy Reviews*, Vol. 15, Issue 6, 2011, pp. 2588-2606.
[2]. C. A. Arancibia-Bulnes, *et al.*, A survey of methods for the evaluation of reflective solar concentrator optics, *Renewable and Sustainable Energy Reviews,* Vol. 69, 2017, pp. 673-684.
[3]. N. Xu, *et al.*, Numerical simulation and experimental validation of a high concentration photovoltaic/thermal module based on point-focus Fresnel lens, *Applied Energy,* Vol. 168, 2016, pp. 269-281.
[4]. A. G. Imenes, *et al.*, Spectral beam splitting technology for increased conversion efficiency in solar concentrating systems: A review, *Solar Energy Materials and Solar Cells,* Vol. 84, 2004, pp. 19-69.
[5]. J. E. Ludman, Holographic solar concentrator, *Applied Optics,* Vol. 21, Issue 17, 1982, pp. 3057-3058.
[6]. H. Kao, *et al.*, Crosstalk-reduced double-layer half-divided volume holographic concentrator for solar energy concentration, *Sensors*, Vol. 20, Issue 23, 2020, 6903.
[7]. H. Akbari, *et al.*, Development and testing of low spatial frequency holographic concentrator elements for collection of solar energy, *Solar Energy*, Vol. 155, 2017, pp. 103-109.
[8]. R. K. Kostuk, *et al.*, Holographic low concentration ratio solar concentrators, in *Proceedings of the Frontiers in Optics Conference*, San Jose, California United States, 11-15 October 2009, p. FMB3.
[9]. J. Zhao, *et al.*, Holographic low concentration optical system increasing light collection efficiency of regular solar panels, *J. Photon. Energy*, Vol. 11, Issue 02, 2021, 027002.
[10]. M. Morales-Vidal, *et al.*, Green and wide acceptance angle solar concentrators, *Optics Express*, Vol. 30, 2022, pp. 25366-25379.

(7063)

Fabrication of Bioinspired Surface Structures Using the Oblique-angle Deposition Technique for Applications in the Field of Optics

R. J. Martín-Palma [1,2], A. Lakhtakia [3] and V. Torres-Costa [1]
[1] Universidad Autónoma de Madrid, Departamento de Física Aplicada,
Campus de Cantoblanco, 28049 Madrid, Spain
[2] The Pennsylvania State University, Department of Materials Science and Engineering,
University Park, Pennsylvania 16802, USA
[3] The Pennsylvania State University, Department of Materials Engineering Science
and Mechanics, University Park, Pennsylvania 16802, USA
Tel.: + 34 497 4028, fax: + 34 91 497 3969
E-mail: rauljose.martin@uam.es

Summary: The oblique angle deposition technique, based on directing a vapor flux towards a substrate with the trajectory of adatoms not parallel to the substrate normal, has been demonstrated as a method capable of generating nanostructured thin films. Sequential substrate movements can be used to shape the morphology of the thin films. The conformal-evaporated-film-by-rotation technique, which has evolved from the oblique angle deposition technique, was initially developed to fabricate high-fidelity replicas of biotemplates with features on the micron- and nanoscales distributed over a curved surface. This technique has been demonstrated to be effective in several fields ranging from optics to forensics.

Keywords: Bioinspiration, Bioreplication, Oblique angle deposition, Fly eye, Butterfly wing.

1. Introduction

Biological species are endowed with multiscale structures which provide them with very specific functionalities. These structures range from the nano- to micro- to macroscales. Ina broad sense, it can be established that the objective of engineered biomimicry is to reproduce the outcome of a particular functionality of a given species.

Although humans have long been imitating biological structures to serve their particular purposes, only a few decades ago engineered biomimicry began to be considered a technoscientific discipline with a great problem-solving potential.

Within this context, the oblique-angle deposition (OAD) technique has been used to replicate the surface structure of several biotemplates aiming at reproducing their optical functionalities.

2. Fabrication Technique

A variant of OAD, termed the conformal-evaporated-film-by-rotation (CEFR) technique, was formulated to rapidly replicate the surface structure of biotemplates with high fidelity.

In this technique, the biotemplate is mounted on a planar substrate that is rapidly rotated about an axis passing normally through it, while a thermally generated vapor flux of a chosen material is directed obliquely, at a fixed angle (close to 0º) with respect to the substrate plane. The attractive features of the CEFR technique are that (i) deposition occurs near the ambient temperature, (ii) the deposition rate can be several $nm \cdot s^{-1}$, and (iii) no chemicals are present so that the original biotemplate is not altered during deposition.

Furthermore, self-supporting surface replicas can be obtained if the coatings formed on the biotemplates are separated from them. Accordingly, this technique has a great potential to make inorganic replicas that exhibit greater chemical and mechanical robustness than the original biotemplates.

Till date, the CEFR technique has been applied for replicating several parts of insects, including the compound eyes of tephritid flies and the wings of butterflies, without compromising their optical characteristics that are due to nanoscale (<100 nm) structural features. Other applications already demonstrated include the mass replication of visual decoys for pest control, devices with improved angular light emission, and forensics.

3. Reproduction of the Surface Morphology of Parts of Insects

Evolutionary processes have ensured that biologic species possess diverse structures with very specific optical performance to simultaneously fulfill such requirements as either high or low reflectance in a particular spectral regime, or to diffuse incident light in a wide angular sector. These specific optical functionalities serve in camouflage, territorial assertion, and courtship, all of which can be responsible for the enhancement of reproductive success.

Insects provide many examples of optical micro- and nanostructures to enable iridescence and/or to appear metallic. As such, initial research on the

CEFR technique for bioreplication was centered on the reproduction of the surface morphology and, therefore, the optical behavior of exoskeletal structures of various insects. In this line, Fig. 1 shows the top view of a wing of a butterfly coated with a ~500 nm-thick film of $Ge_{28}Sb_{12}Ge_{60}$ chalcogenide glass.

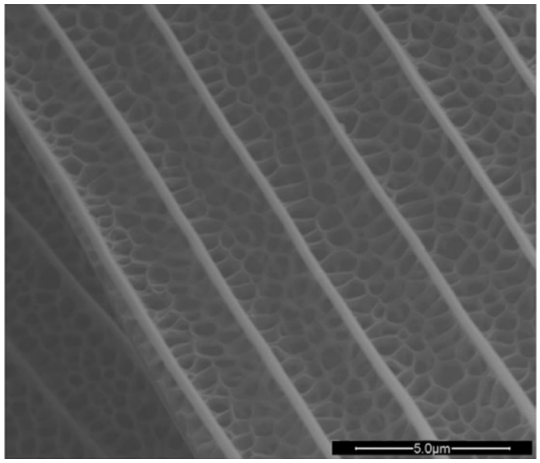

Fig. 1. Scanning-electron microscope image of a wing of the butterfly Battus philenor coated with a ~500 nm thick $Ge_{28}Sb_{12}Ge_{60}$ film using the CEFR technique.

The similar reflectance characteristics of the uncoated and coated wings confirm that use of the CEFR technique resulted in faithful replication of the surface morphology of the biotemplate.

4. Light Emission with Improved Angular Response

The compound eyes in insects of many species provide them a wide angular field of view, making these natural optical structures attractive for the development of bioreplicated sources of light. With this objective in mind, corneas of compound eyes of the common blowfly (*E. lilea*) were conformally coated with Alq3, as shown in Fig. 2, and illuminated with ultraviolet light.

The angular distribution of light emitted by coated corneas was compared with that emitted by flat surfaces. The experimental results showed that the conformally coated cornea has a notable weaker angular dependence of emission than the flat surface. This initial demonstration should impact the development of bioreplicated light-emitting and light-detecting devices.

5. Conclusions

A specific functionality of a biologic structure emerges, in many cases, from its morphology at the nanometer, micrometer, and/or macroscopic length scales. The OAD technique evolved into the CEFR technique to replicate the surface features of biotemplates for several application beyond optics.

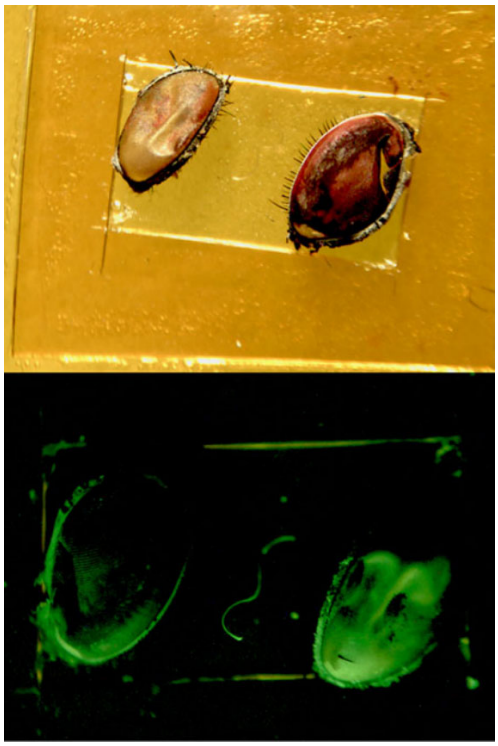

Fig. 2. Photographs of two blowfly corneas mounted on a glass slide, (top) before and (bottom) after being coated with Alq3. The top photograph was taken under normal illumination, but the bottom one was taken under shortwave-ultraviolet illumination.

Acknowledgements

This research was in part sponsored by the NATO Science for Peace and Security Programme under grant G5734 and the Community of Madrid within the framework of the agreement with Universidad Autónoma de Madrid in item “Excellence of University Professorate”.

References

[1]. A. Lakhtakia, R. J. Martín-Palma, Engineered Biomimicry, *Elsevier*, 2013.
[2]. R. J. Martín-Palma, A. Lakhtakia, Bioreplication for optical applications, *MRS Communications*, Vol. 8, Issue 2, 2018, pp. 220-225.
[3]. R. J. Martín-Palma, A. Lakhtakia, Progress on bioinspired, biomimetic, and bioreplication routes to harvest solar energy, *Applied Physics Reviews*, Vol. 4, 2017, 021103.
[4]. M. J. Domingue, A. Lakhtakia, D. P. Pulsifer, et al., Bioreplicated visual features of nanofabricated buprestid beetle decoys evoke stereotypical male mating flights, *Proceedings of the National Academy of Sciences of the United States of America*, Vol. 111, Issue 39, 2014, pp. 14106-14111.

(7553)

The Effect of Skull Thickness on Acousto-Optic Sensing

M. Wainberg, R. Shechter and M. Balberg
Holon Institute of Technology, 52 Golomb st. 5810502 Holon, Israel
Tel.: +97235026812, fax: + 87654321
E-mail: balbergm@hit.ac.il

Summary: Acousto-optic (AO) modulation of light enables localized, non-invasive measurement of the brain's vasculature, through the skull. When low-frequency ultrasound (1MHz) is applied, the AO signal is attenuated by the skull. We investigate the effect of the thickness of the skull on the SNR of AO signals using both Monte-Carlo simulations and tissue-mimicking phantoms. We demonstrate that the SNR is reduced as the thickness of the skull increases, for different source-detector (SD) separations. We also show that the phase distribution of the collected photons is broadened as the SD separation increases.

Keywords: Acousto-optics, Brain, Cerebral blood flow, Monte-Carlo.

1. Introduction

Non-invasive optical monitoring of changes in cerebral blood flow is critical to assess brain's health during critical conditions [1]. Acousto-optics (AO) is an optical technology that integrates coherent light illumination with ultrasonic modulation of the light. The modulated signal provides an improved depth-selectivity of the optical measurement [2], and improves the sensitivity of the measurement to the brain's vasculature.

An AO sensor applies a pressure wave, using a piezoelectric transducer, into the same tissue volume that is illuminated with coherent light. When applied through the skull, this pressure wave is attenuated. Therefore, we expect that differences in skull thickness will affect the modulation of light in soft-tissue (i.e. in the brain).

The human skull is not a homogeneous spherical shell, its thickness ranges between 6-9 mm, and depends on ethnicity and gender and increases with age. Consequently, the effect of the skull's thickness on the SNR of the measurement may affect the efficiency of AO brain monitoring.

In this work we analyze the effect of the skull's thickness on the SNR of AO sensing using Monte-Carlo simulations and a tissue-mimicking phantom.

2. Methods

2.1. Monte-Carlo Simulations

An AO Monte-Carlo (AOMC) model was constructed in order to investigate the effect of skull thickness and source-detector separation on the acousto-optic modulation ratio. The model is based on a parallel MC algorithm [3] using a three layer tissue structure (skin, skull, grey-matter) with one source, and 3 detectors as shown in Fig. 1. The thickness of the layers was 2.25 mm for the skin layer, 6-8.25 mm for the skull layer and 12 mm for the brain layer.

The effect of the acoustic modulation on the phase of the photons was simulated in the AOMC model by using both scattering and refractive index modulation [4]. The optical properties of the tissue layers were taken from [6]. The average phase and the number of photons reaching each detector were calculated at three different conditions. The following conditions were simulated: No ultrasound, ultrasound phase 1 and ultrasound phase 2, where the difference between the two phases was π.

The ultrasound modulation results in a change of the refractive index and in movement of the scattering centers only within the soft tissue (we assume that the skull is not compressible). The refractive index is modulated in a binary way within the volume of the cylinder in Fig. 1. For a pressure amplitude that corresponds to the maximal permissible acoustic power in brain tissue (I_{sppa}=190 W/m^2), we set Δn=0.02, as derived from empirical measurements [5].

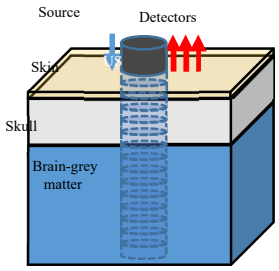

Fig. 1. 3D MC model. Layers' thickness and locations of source and detectors are not to scale (US=ultrasound transducer).

The sum of the amplitude and phase of all photons was calculated according to [2] with both scattering and refractive index modulation contributions as described in [4]. The SNR was defined by dividing the signal obtained with ultrasound on (for the two phases) to that obtained without ultrasound.

2.2. Tissue Mimicking Phantom

A phantom consisting of three layers was constructed. The "brain" was made from RTV (thickness 10 cm), the "skull" was 3D printed from white PLA (thickness 6 & 8 mm), and the "skin" was a hydrogen adhesive (2 mm). The ultrasound transducer's frequency was 1 MHz. Light at 808 nm, from a single-mode laser diode (IPS, USA) was introduced using an optical fiber (62.5 µm diameter), and was collected using a fiber bundle (1 mm diameter) and detected by an avalanche photodiode (APD) (Hamamatsu, Japan). The detected signal was digitized by a high speed (50 MSample/s) sampling card (NI, USA). The distances of the collecting fiber were 15, 20 & 25 mm from the emitting fiber. For each thickness of the "skull" and for each location of the collecting fiber, the peak of the power spectrum (PS) of the detected light, at 1MHz was measured, and divided by the average amplitude of the PS at the range of 900-920 kHz and 1100-1120 kHz, to calculate the SNR.

3. Results

3.1. Monte-Carlo Simulations

The effect of the AO modulation on the phase of the collected photons is presented in Fig. 2 for each source-detector (SD) distance, for a skull thickness of 6 mm.

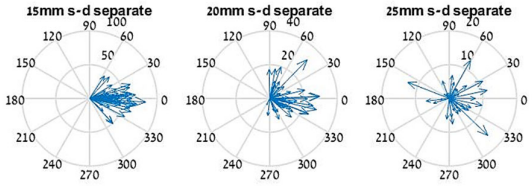

Fig. 2. Phase diagrames of the phase (angle) of the detected photons when ultrasound is applied.

The SNR dependence on the SD distance is presented in Fig. 3. Three "skull" thicknesses – 6, 7.5 and 8.25 mm were chosen for the model.

3.2. Tissue Mimicking Phantom

For the phantom, the SNR dependence on the SD distance is presented in Fig. 4. Two "skull" thicknesses: 6, and 8mm were chosen for the model and compared to a "no skull" condition.

4. Discussion and Conclusions

As demonstrated by the MC simulations and the phantom measurements, AO modulation through the skull is attenuated by the skull. As the thickness increases, the SNR is reduced for all SD distances. In addition, as demonstrated in Fig. 2, the phase of the collected photons is more uniform for a short SD separation (15 mm) than for a longer one (25 mm). As the distance increases, the phase distribution is broadened, resulting in a lower constructive interference at the collecting aperture, thus reducing the amplitude of the modulated signal.

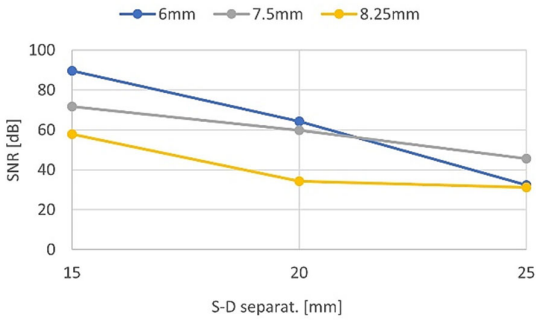

Fig. 3. SNR of simulated AO signals for different skull thicknesses.

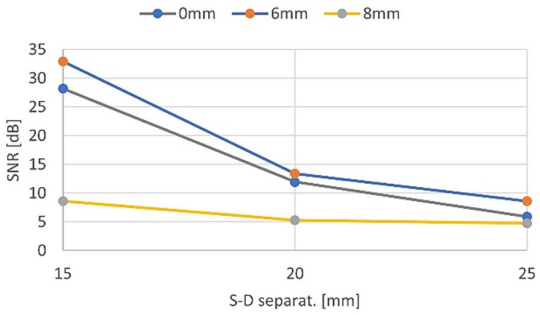

Fig. 4. SNR of experimental AO signals for different skull thicknesses.

Acknowledgements

This work was funded by the Binational US Israel Foundation (BSF) grant 2015193.

References

[1]. S. Fantini *et. al.,* "Cerebral blood flow and autoregulation: current measurement techniques and prospects for noninvasive optical methods, *Neurophotonics*, Vol. 3, No. 3, 2016, p. 031411.

[2]. A. Tsalach *et al.*, Depth selective acousto-optic flow measurement, *Biomedical Optic Express*, Vol. 6, No. 12, 2015, p. 4871.

[3]. Q. Fang *et al.*, Monte Carlo Simulation of Photon Migration in 3D Turbid Media Accelerated by Graphics Processing Units, *Optics Express,* Vol. 17, No. 22, 2009, pp. 20178–20190.

[4]. L. V Wang, Mechanisms of ultrasonic modulation of multiply scattered coherent light: a Monte Carlo model., *Optics Letters*, Vol. 26, No. 15, 2001, pp. 1191–1193.

[5]. J. Wang *et al.*, Study of dynamic pressure-induced refractive index change using derivative total reflection method, *Journal of Biomedical Optics*, Vol. 18, No. 11, 2013 p. 117005.

[6]. Q.Fang *et al.*, Mesh-based Monte Carlo method using fast ray-tracing in Plucker coordinates, *Biomedical Optics Express*, Vol. 1, No. 1,2010, p. 165-175.

(7571)

Infrared Spectroscopy of Leukocytes for Rapid Diagnosis of the Etiology of Patients' Infections as Bacterial or Viral

S. Mordechai [1], G. Beck [2], U. Sharaha [3,4], Y. D. Eshel [2], G. Cohen-Logasi [5], J. Kapelushnik [2], A. H. Agbaria [1], I. Lapidot [6,7], M. Huleihel [3] and A. Salman [8]

[1] Ben-Gurion University, Department of Physics, 84105 Beer-Sheva, Israel
[2] Soroka University Medical Center, Department of Hematology and Oncology, Saban Pediatric Medical Center, 84105 Beer-Sheva, Israel
[3] Ben-Gurion University, Department of Microbiology, Immunology, and Genetics, 84105 Beer-Sheva, Israel
[4] Hebron University, Department of Biology, Science and Technology College, P760 Hebron, Palestine
[5] SCE-Sami Shamoon College of Engineering, Department of Green Engineering, 84100 Beer-Sheva, Israel
[6] Afeka Tel-Aviv Academic College of Engineering, Department of Electrical and Electronics Engineering, ACLP-Afeka Center for Language Processing, 69107 Tel-Aviv, Israel
[7] LIA Avignon Université, 339 Chemin des Meinajaries, 84000, Avignon, France
[8] SCE-Sami Shamoon College of Engineering, Department of Physics, 84100 Beer-Sheva, Israel
Tel.: + 972-8-6461749; E-mail: shaulm@bgu.ac.il

Summary: It is possible to diagnose the etiology of infection as bacterial or viral by monitoring the immune system's response. Peripheral blood samples were collected and the leukocytes were separated and measured by an infrared spectrometer. The recorded spectra were analyzed by a support vector machine (SVM) classifier. The classifier was trained using the accessible infection data, which served as the gold standard and were used to predict the etiology of inaccessible infections. It was possible to diagnose the etiology of infection for both accessible and inaccessible infections as bacterial or viral with >94 % sensitivity and > 90 % specificity within one hour after the collection of the blood sample.

Keywords: Infectious diseases, Bacterial infections, Viral infections, Accessible infections, Inaccessible infections, Immune system, Machine learning.

1. Introduction

Infectious diseases have long been one of the major causes of human morbidity and mortality [1]. The symptoms of these illnesses are the same regardless of how the immune system reacts to the bacterial or viral infection types.

Current etiology-diagnosis techniques take 2-4 days and are objective for accessible infections, but they are useless for inaccessible infections.

As a result, based solely on symptoms, their experience, and medical measures, doctors frequently diagnose subjectively whether an infection is viral or bacterial in all cases for inaccessible infections and frequently for accessible infections, and in many cases, they begin unnecessary antibiotic treatment.

Thus, for determining, the etiology of infections for both accessible and inaccessible infections, sensitive, specific, and quick new approaches are needed.

All of the aforementioned characteristics of Fourier transform infrared (FTIR) spectroscopy in conjunction with machine learning algorithms make it a valuable diagnostic tool in the medical field [2].

We hypothesize that the ability to identify small changes in WBC cells together with larger changes in these cells due to various immune system responses to viral/bacterial infections is present here as well [3, 4].

In this study, we assessed the possibility of the mid-infrared spectroscopy technique for simple peripheral blood samples-based rapid and accurate diagnosis of bacterial and viral illnesses.

2. Methodology

Peripheral blood samples from 0-18 years of fever illness patients as detailed in Table 1, were collected. The leukocytes' blood components were separated and measured using an infrared spectrometer.

Table 1. Details of the samples included in this study.

Category description	No. of patients (spectra)
Accessible sites which had positive cultures.	32 (512)
Accessible sites. Diagnosed as viral using RT-PCR	12 (192)
Inaccessible sites. Diagnosed by a physician as bacterial.	37 (592)
Inaccessible sites. Diagnosed by a physician as viral.	24 (384)
Controls 'with no infections	93 (1488)

A classification procedure consisting of four stages was used to analyze the data: a) data extraction, b) data pre-processing, c) feature selection d) classifiers training and prediction.

A binary classification was performed in two distinct steps; in the first step, the classification was between controls versus infected patients (which includes both viral and bacterial samples). The second classification was between the viral versus bacterial infection samples.

A five-fold cross-validation approach was used to evaluate the performances of the SVM classifier.

3. Results and Discussions

The average infrared absorption spectra of leukocytes from bacterial, viral, and control samples are shown in Fig. 1 for the 900–1800 cm^{-1} range.

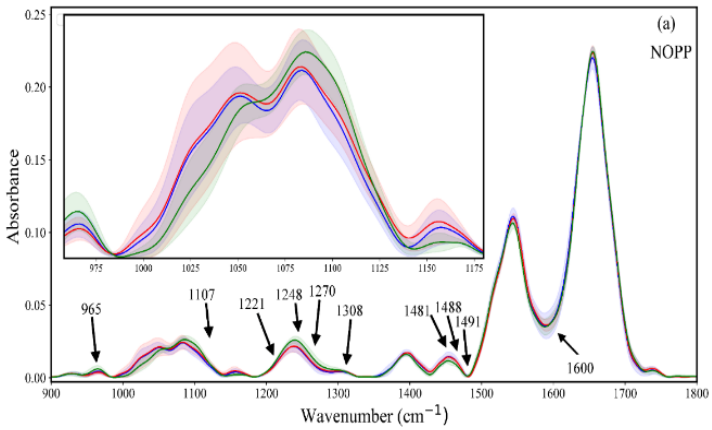

Fig. 1. Infrared absorption spectra in the 900-1800 cm^{-1} wavenumber region.

The figure includes labels for the principal absorption bands. Protein vibrations are primarily responsible for the contributions to the amide I (C = O) and amide II (C-N stretching and H-N-C bending) bands. The carbohydrates contributed primarily in the 900–1200 cm^{-1} range, while the amide III bands are centered at 1252 cm^{-1}.

Since the individual spectra overlapped with just slight variations in shapes and intensities, we employed various machine-learning techniques to separate the different groups into infected patients vs. controls and viral versus bacterial infections, respectively.

The effectiveness of the classifier is quantified by calculating the area under the curve of the receiver operating characteristic curves (AUROC) in correctly identifying the category of the tested sample.

The performance of the classifier in the different classification experiments is summarized in Table 2.

As can be seen from Table 2d, the physicians' misdiagnosis of the etiology of infection in numerous cases. Thus, the inaccessible cases were labeled according to the predicted categories by our approach, then the classification was performed for both accessible and inaccessible infections. The classification performance is summarized in Table 3.

4. Conclusions

Using a mid-infrared spectroscopy based-machine learning algorithms approach, a high infection etiology diagnosis success rate is attainable within 70 minutes of acquiring the blood samples. It is applicable for both accessible and inaccessible infections, for which microbiological lab tests are frequently useless. As a result, it might be a crucial and impartial diagnostic tool that enables doctors to pinpoint the cause of the illnesses more precisely, particularly in the case of diseases that are challenging to cure.

Table 2. Performances of the SVM classifier with linear kernel in percentage for the classification.

AUROC	Acc	SE	SP	PPV	NPV
(a) Control-infected					
0.97	95	99	92	99	92
(b) Bacterial versus viral (accessible and inaccessible)					
0.93	91	95	82	91	90
(c) Bacterial versus viral (accessible)					
0.96	93	94	90	96	85
(d) Estimated evaluations of the physicians' diagnosis in percentage for the inaccessible infections. The classifier was trained using accessible infection cases and the categories of inaccessible infection cases were predicted.					
-	75	89	54	75	76

Table 3. Performances of the SVM classifier for the classification between truly bacterial and truly viral.

AUROC	Acc	SE	SP	PPV	NPV
0.92	93	95	87	95	87

Acknowledgments

This research was supported by the ISRAEL SCIENCE FOUNDATION (grant No. 1087/20).

References

[1]. H. Nair, W.A. Brooks, M. Katz, et al., Global burden of respiratory infections due to seasonal influenza in young children: a systematic review and meta-analysis, *Lancet* (London, England), Vol. 378, 2011, pp. 1917-1930.

[2]. M. J. Baker, J. Trevisan, P. Bassan, et al., Using Fourier transform IR spectroscopy to analyze biological materials, *Nature Protocols*, Vol. 9, 2014, pp. 1771-1791.

[3]. A. H. Agbaria, G. Beck Rosen, I. Lapidot, et al., Differential diagnosis of the etiologies of bacterial and viral infections using infrared microscopy of peripheral human blood samples and multivariate analysis, *Analytical Chemistry*, Vol. 90, Issue 13, 2018, pp. 7888-7895.

[4]. A. H. Agbaria, G. Beck, I. Lapidot, et al., Diagnosis of inaccessible infections using infrared microscopy of white blood cells and machine learning algorithms, *Analyst*, Vol. 145, Issue 22, 2020, pp. 6955-6967.

(7760)

Hydrogen Bonding in Diluted Solutions of Tetrahydrofuran + Water and Tetrahydrofuran + Ethanol: An Experimental FTIR and Molecular Dynamics Study

Dilbar Bozorova [1], Shukur Gofurov [2,4] and Oksana Ismailova [1, 3, 4, 5]
[1] Institute of Ion-plasma and laser technologies, 100125, 33 Durmon yuli street, Uzbekistan
[2] University of Tsukuba, Tennodai 1-1-1, Ibaraki-shi, Japan
[3] Turin Polytechnic University in Tashkent, 100195, Almazar district,
17 Kichik Khalka yuli street, Uzbekistan
[4] Uzbekistan-Japan Innovation Center of Youth, 100195, 2B Universitet street, Uzbekistan
[5] National University of Uzbekistan named after Mirzo Ulugbek, 100174,
4 Universitet street, Tashkent, Uzbekistan
Tel.: + 998909194890, fax: + 998712030022
E-mail: oismailova56@gmail.com

Summary: The dynamics of hydrogen-bonded network in tetrahydrofuran+water and tetrahydrofuran+ethanol systems was studied using Fourier-transform infrared (FTIR) spectroscopy and molecular dynamics. Spectra for the diluted tetrahydrofuran solutions were recorded in the concentration range of 0.01-0.09 in 0.01 mole fraction increments. A comparative analysis of hydrogen bonds in aqueous and ethanol mixtures of tetrahydrofuran was performed. It was shown that in aqueous solutions of tetrahydrofuran at a concentration of 0.04 mole fraction, water molecules create a clathrate-like structure around the tetrahydrofuran molecules. Whereas in ethanol mixtures at concentrations of 0.06 and 0.08 mole fractions of tetrahydrofuran, the saturation of hydrogen bonds between ethanol molecules occurs.

Keywords: Fourier-transform infrared spectroscopy (FTIR) transmittance, Molecular dynamics, Clathrate like structure.

1. Introduction

Molecular spectroscopy, due to the specificity of each molecule's spectrum and high sensitivity to various perturbations of both the molecule as a whole and the individual atomic group, is one of the informative methods for determining the intensity of functional groups manifested in mixtures. Molecular spectra can provide valuable information on the nature and properties of intermolecular and dipole-dipole interactions. The study of the effect of solvation processes of individual molecules and the resulting clusters is important both from a theoretical and practical point of view [1-6]. The availability and simplicity of infrared absorption spectra allow for a reliable interpretation of the experiment, the sensitivity of vibrational parameters to various types of perturbations. They contain information on CO-, CH-, OH- functional groups whose vibrational frequencies are fully determined by the structure of nearby groups. Therefore, we chose tetrahydrofuran solutions in aqueous and ethanol mixtures as objects of study. Aqueous and alcoholic systems are of particular interest because a particular type of interaction can predominate depending on the concentration of the dissolved component. The present work is devoted to the study of spectral properties and the type of intermolecular hydrogen bonding between tetrahydrofuran molecules in aqueous and ethanol solutions, based on the combined use of Fourier IR spectroscopy and molecular dynamics methods with classical force fields.

2. Materials and Method

2.1. Sample Preparation

Double distilled water, ethyl alcohol, and tetrahydrofuran (99.9 %, Sigma-Aldrich, USA). Aqueous and alcoholic solutions of tetrahydrofuran in the concentration range of 0-0.09 with an interval of 0.01 mole fractions were prepared by conductometric method at room temperature as described in [7] and studied by Fourier IR spectroscopy.

2.2. Fourier-Transform Infrared (FTIR) Spectroscopy

FTIR spectra (Perkin Elmer Spectrum Two series spectrophotometer) were recorded using a $LiTaO_3$ detector with a signal-to-noise ratio of 9300:1 and a resolution of 0.5 cm^{-1}.

2.3. Molecular Dynamics

The calculations were performed in a concentration range of tetrahydrofuran 0-0.09 in increments of 0.01 mole fraction of tetrahydrofuran in water and ethanol using the GROMACS software package [8] version 5.0.4. An isobaric-isothermal ensemble and a Parinello-Rachmann barostat were studied at a pressure of 1 bar and at room temperature in the time interval of 40 ns with 2 fs time increment. The SPC/E

model [9] was used for water, which describes quite well the radial distribution function of oxygen atoms [10], the dielectric permittivity of water [11], and the structural and thermodynamic properties of the water-alcohol binary mixture [12].

3. Results and Discussion

Dilute solutions of aqueous systems have recently attracted the attention of many scientists. The interest is caused by the fact that at a certain concentration value or in a narrow concentration range, water molecules are structured in a way that is completely different from others, namely, water molecules form clathrate-like structures.

Figs. 1, 2 and 3 show the IR spectra of both aqueous and ethanol solution of tetrahydrofuran at concentration range 0.01÷0.09 mole fraction and pure water and ethanol. At 1030 cm^{-1} and 1133 cm^{-1}, which characterizes the ring strain of tetrahydrofuran and C-C-H vibrational assignment [13], strongest shift with the highest intensity occurs for the concentration of 0.04 mole fraction. With decreasing concentrations of tetrahydrofuran in aqueous solutions, a shift of the peak in the 1640 cm^{-1} absorption band to the region of low wave numbers is observed. As can be seen from the Fig. 3 for aqueous solution (left part), the lowest position of the hydrogen bond intensity corresponds to 0.04 mole fraction, which indicating weak interactions between different type of molecules. Similar effects have been observed for aqueous solutions of ethanol [14], tertiary butanol [15], methylenediamine [16].

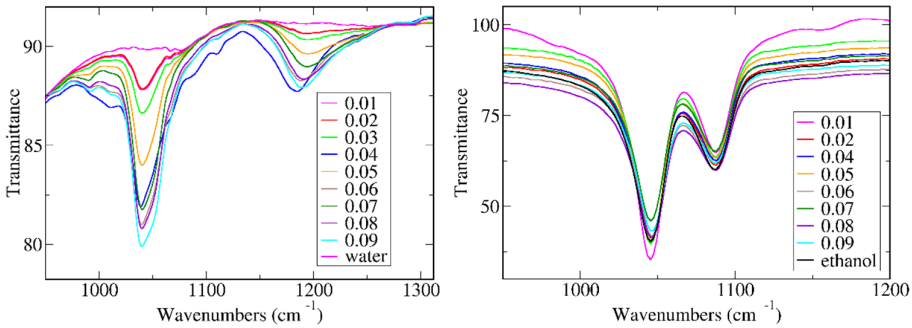

Fig. 1. Fourier transform IR fingerprint spectra for aqueous solutions (left part) and ethanol solution (right part) of tetrahydrofuran**.**

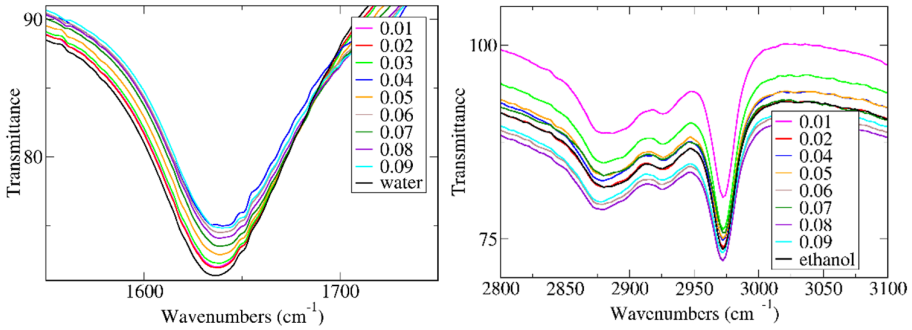

Fig. 2. Fourier transform IR spectra of HOH band of aqueous solutions (left part) and C-H band of ethanol solution (right part) of tetrahydrofuran**.**

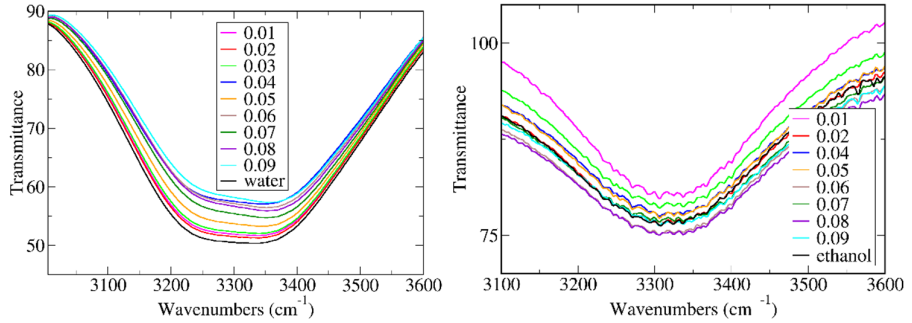

Fig. 3. Fourier transform IR spectra of OH band for both aqueous solutions (left part) and ethanol solution (right part) of tetrahydrofuran**.**

It was shown that the formation of aqueous tetrahydrofuran mixture leads to a decrease in the volume of the mixture due to increased interactions between its components [16]. It was shown that the partial molar volumes of water decrease with increasing mole fraction of tetrahydrofuran in the mixture under study. It was shown that, at a tetrahydrofuran concentration of ≈0.04 mole fraction, the maximum disappears with an increase in temperature. The authors [14, 17] reported that this dependence is related to the complete destruction of water clusters. A similar effect with a pronounced maximum in the region of low solvent concentrations is observed in all aqueous nonelectrolytes [14, 17].

As can been seen from Fig. 1 (right part) for ethanol solutions,, the strongest C-O vibrational mode at 1046 cm^{-1} occurs for 0.01 mole fraction. The strong hydrogen bond between molecules is characterized by the C-O band at 1092 cm^{-1}, C-H band at 2980 cm^{-1} (right part of Fig. 2) and O-H band at 3366 cm-1(right part of Fig. 3) prohibit their maximum for 0.06 and 0.08 mole fraction It explained by the fact that all these band for 0.06 and 0.08 mole fraction have intensity higher than for pure ethanol [18].

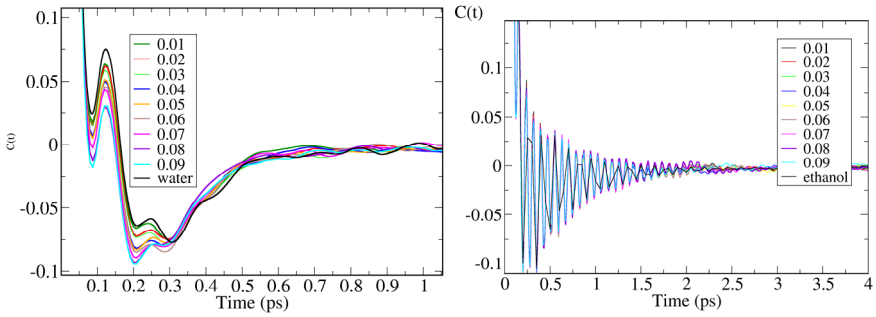

Fig. 4. Autocorrelation velocity function of O atom for both water (left part) and ethanol molecules.

The molecular dynamics method was used to study the intermolecular bonds between molecules.

The shape of the autocorrelation function curves for the oxygen atom velocity of water molecules shows that the first minimum corresponds to 88 fs and the maximum to 125 fs. A linear dependence of the behavior of the maximum and minimum intensities depending on the concentrations of the dissolved component is observed. The value of the second minimum is observed at 200 fs, and the maximum at 250 fs. With increasing concentrations, the intensity of the maxima changes nonlinearly in the region of concentrations of 0.03-0.09 m. f. of tetrahydrofuran.

With increasing concentrations, the third minimum located at 290 fs is characteristic for 0.06 region. The minimum for the concentration of 0.04 m. f. is located lower than that for 0.05 m. f., characterizing the strong bonding with ethanol molecules.

The figure shows the autocorrelation functions of the oxygen atom velocity of ethanol molecules in tetrahydrofuran+ethanol mixtures. The relaxation process for the water molecule occurs at 1.2 ps, and for the reference at 2.5 ps. The maxima and minima of the peaks are typical for the concentration range of 0.06-0.08 m. f. of tetrahydrofuran. This fact indicates that ethanol molecules are bound to each other through weak and strong hydrogen bonds.

4. Conclusions

The study of the dynamics of hydrogen bonded network in the tetrahydrofuran+water and tetrahydrofuran+ethanol systems by Fourier transform infrared spectroscopy (FTIR) and molecular dynamics showed a nonlinear dependence of formation/destruction of hydrogen bonds depending on tetrahydrofuran concentrations. It was shown that at a concentration of 0.04 m. f., tetrahydrofuran molecules, embedded in the hydrogen network of water, lead to a rearrangement of water molecules with the formation of clathrate-like structure. For ethanol solutions, an increase in the intensity of hydrogen bonds in the concentration range 0.06-0.08 m. f. of tetrahydrofuran is observed.

Acknowledgments

This study was financially supported by the Foundation for Basic Research of the Academy of Sciences of Uzbekistan and the Ministry of Innovative Development of the Republic of Uzbekistan (grant No. UZB-Ind-2021-83) and Mirai Foundation.

References

[1]. Z. Song, Z. Wang, J. Ma, J. Sun, C. Li, X. Xu, C. Chen, Z. Chen, B. Xu, Y. Jiang, J. Kumirska, E M. Siedlecka, A. Ikhlaq, F. Qi, O. Ismailova, Molecular levels unveil the mebrane fouling mitigation mechanism of a superpotent N-rGO catalytic ozonation membrane: Interfacial catalytic reaction pathway and induced EfOM transformation reactions, *Applied Catalysis B: Environmental,* Vol. 319, 2022, 121943.

[2]. O. B. Ismailova, T. Kh. Akhmedov, Kh. T. Igamberdiev, Sh. I. Mamatkulov, A. A. Saidov, Sh. O. Tursunov, P. K. Khabibullaev, Heat-capacity anomaly in a wide vicinity of the critical point of the

triethylamine-water phase transition, *Journal of Engineering Physics and Thermophysics*, Vol. 78, 2005, pp. 1040-1045.

[3]. I. V. Plastinin, S. A. Burikov, S. P. Gofurov, O. B. Ismailova, Y. A. Mirgorod, T. A. Dolenko, Features of self-organization of sodium dodecyl sulfate in water-ethanol solutions: Theory and vibrational spectroscopy, *Journal of Molecular Liquids,* Vol. 298*,* 2020, 112053.

[4]. D. T. Bozorova, S. P. Gofurov, A. M. Kokhkharov, O. B. Ismailova, Terahertz spectroscopy of aqueous solutions of acetic acid, *Journal of Applied Spectroscopy*, Vol. 88, Issue 4, 2021, pp. 719-722.

[5]. D. Razzokov, O. B. Ismailova, Sh. I. Mamatkulov, O. V. Trunilina, A. M. Kokhkharov, Heteromolecular structures in aqueous solutions of dimethylformamide and tetrahydrofuran, according to molecular dynamics data, *Russian Journal of Physical Chemistry A*, Vol. 88, Issue 9, 2014, pp. 1500-1506.

[6]. D. T. Bozorova, Sh. P. Gofurov, A. M. Kokhkharov, M. A. Ziyayev, F. T. Umarova, O. B. Ismailova, The excess refractive indices of some organic and inorganic components, in Advanced Materials and Nano Systems: Theory and Experiment (Part-1)*, Bentham Science Publisher*, 2022, pp. 108-119.

[7]. Sh. Gofurov, O. Ismailova, U. Makhmanov, A. Kokhkharov, Heteromolecular structure formation in aqueous solutions of ethanol, tetrahydrofuran and dimethylformamide, *Int. J. Chem. Mol. Eng*., Vol. 11, Issue 4, 2017, pp. 330-333.

[8]. D. Van Der Spoel, E. Lindahl, B. Hess, G. Groenhof, A. E. Mark, H. J. C. J. Berendsen, GROMACS: fast, flexible, and free, *Comput. Chem*., Vol. 26, Issue 16, 2005, pp. 1701-1718.

[9]. O. Ismailova, A. Berezin, M. Probst, R. R. Nazmutdinov, Interfacial bond-breaking electron transfer in mixed water-ethylene glycol solutions: Reorganization energy and interplay between different solvent modes, *J. Phys. Chem. B*, Vol. 117, 2013, pp. 8793-8801.

[10]. D. T. Bozorova, Sh. P. Gofurov, M. A. Ziyayev, O. Ismailova, *Chemistry and Chemical Engineering*, Vol. 2021, Issue 1, 2021, pp. 44-47.

[11]. H. J. C. Berendsen, R. J. Grigera, T. P. Straatsma, The missing term in effective pair potentials, *J. Phys. Chem*., Vol. 91, 1987, pp. 6269-6271.

[12]. E. Tombari, S. Presto, G. Salvetti, Heat capacity of tetrahydrofuran clathrate hydrate and of its components, and the clathrate formation from supercooled melt, *J. Chem. Phys*., Vol. 124, 2006, pp. 154507-154516.

[13]. A. Dwivedi, V. Baboo, A. Bajpai, Fukui function analysis and optical, electronic, and vibrational properties of tetrahydrofuran and its derivatives, *Journal of Theoretical Chemistry,* Vol. 2015, 2015, 345234

[14]. G. I. Egorov, D. M. Makarov, Densities and volume properties of (water+tert-butanol) over the temperature range of (274.15 to 348.15) K at pressure of 0.1 MPa, *The Journal of Chemical Thermodynamics*, Vol. 43, Issue 3, 2011, pp. 430-441.

[15]. G. I. Egorov, D. M. Makarov, Volumetric properties of the water + tetramethylurea mixture over the temperature range from 274.15 to 333.15 K at atmospheric pressure, *Journal of Molecular Liquids*, Vol. 278, 2019, pp. 279-289.

[16]. W. Hayduk, H. Laudie, O. H. Smith, Viscosity, freezing point, vapor-liquid equilibria, and other properties of aqueous-tetrahydrofuran solutions, *Journal of Chemical & Engineering Data*, Vol. 18, 1973, pp. 373-376.

[17]. G. I. Egorov, D. M. Makarov, Densities and molar isobaric thermal expansions of the water + formamide mixture over the temperature range from 274.15 to 333.15 K at atmospheric pressure*, Journal of Chemical & Engineering Data*, Vol. 62, 2017, pp. 1247-1256.

[18]. G. I. Egorov, D. M. Makarov, Densities and molar isobaric thermal expansions of the water + formamide mixture over the temperature range from 274.15 to 333.15 K at atmospheric pressure*, Journal of Chemical & Engineering Data*, Vol. 62, 2017, pp. 1247-1256.

(8617)

All-silica Optics with Extreme Resistivity to Laser Radiation

T. Tolenis [1,2], R. Buzelis [1], G. Dolmantaitė [1] and L. Ramalis [1]
[1] Center for Physical Sciences and Technology, Savanorių ave. 231, LT-02300, Vilnius, Lithuania
[2] ELI Beamlines, ELI-ERIC, Za Radnicí 835, Dolní Břežany, Czech Republic
Tel.: + 420 722 994 889,
E-mail: tomas.tolenis@ftmc.lt

Summary: Optical resistivity of coatings is determined by thin film materials and multilayer designs, all of which limits the overall performance of optical elements and all laser systems. Coatings, consisting of high band-gap materials and capable of withstanding extreme laser power under the multiple pulse irradiation, could substantially expand the current capabilities of generated laser power in major laser facilities. Currently, the glancing angle deposition has demonstrated the capability to form multilayer coatings using only silica material. Several optical components, such as mirrors, zero-angle polarizers and waveplates, were developed to reach high laser induced damage thresholds, which suffered instabilities due to high porosity of the coatings. In our current research we investigated a procedure to reach the stable extreme resistivity to laser radiation by ramping the irradiation energy using ns pulses. As a result, high reflectivity mirrors with 174 J/cm^2 damage threshold were achieved at the 355 nm using 2 ns pulsed laser.

Keywords: Glancing angle deposition, Sculptured thin films, Optical coatings, Laser damage, Nano-structures.

1. Introduction

Optical resistivity is one of the essential properties of optical components, namely coatings, determining the output power of the laser systems. Any shortcomings of elements capability to withstand the energy of incoming laser radiation is compensated by increasing the beam diameter, therefore, the size of the system itself. As a consequence, major laser facilities (NIF, LMJ, ELI, etc.) implement meter-size optics and lower the irradiation power flux on the coating accordingly [1].

For the past five years, the development of all-silica coatings have been focused on establishing new type of components, including high and low reflectivity coatings [2, 3], multilayers for polarization control [4], etc. All coatings indicated extremely high optical resistivity, which was limited by defects within the films and strong dependency on testing conditions.

In this work we present the investigation of laser conditioning of all-silica mirrors using ns pulsed UV laser radiation. A set of high reflectivity mirrors have been manufactured using only silica material and Glancing Angle Deposition (GLAD) method. All of the samples have been tested using different laser conditioning protocols, which allowed to improve the LIDT of the coatings up to the ~200 J/cm^2 using pulsed ns Nd:YAG laser system. The results are repeated several times and additionally supported by optical and structural investigation.

2. Methods

GLAD method was applied to combine multilayer structure of nanostructured porous and dense silica (effective refractive indexes of 1.25 and 1.43 at 355 nm wavelength, respectively) in order to form highly reflective (>99%) all-silica Bragg mirrors. Coating design consisted of 53 quarter wavelength optical thickness (QWOT) layers with triple QWOT layer of dense silica on the top. Vacuum chamber „Sidrabe" (Latvia), equipped with two stepper motors substrate holder system and electron beam source, was used for mirrors formation. Fused silica substrates were prepared by cleaning the surface in an ultrasonic bath, which is held in ISO 5 standard compatible clean room, to reduce any contamination. During deposition process, thin film growth rate was maintained at 5 Å/s, pressure of the vacuum chamber was held at 8×10^{-5} Torr. After the deposition process samples were placed in sealed polyethylene terephthalate glycol (PET-G) boxes and filled with argon gases.

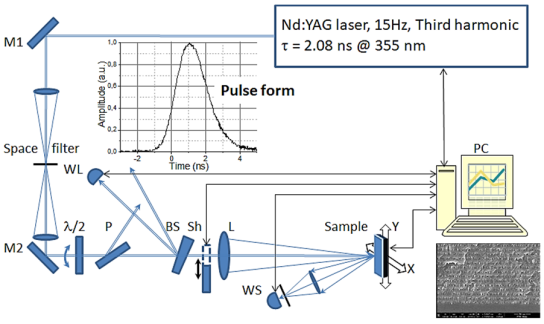

Fig. 1. Experimental setup for LIDT tests.

The pulsed Nd:YAG laser (model Ekspla NL 120) was used for conditioning and LIDT measurements of all samples. Experimental setup is shown in Fig. 1. Third harmonic single mode space filtered Gaussian beam pulses with repetition rate of 15 Hz were controlled by an attenuator (λ/2 and P) and focused by the lens L onto the surface of the sample. The energy

of the incident laser beam was measured by a detector WL. These readings were calibrated by measuring the radiation, which passed the lens L with a certified energy meter. The following parameters of laser radiation were used in the measurements: wavelength - 355 nm; pulse duration – 2.08 ns; beam diameter on the surface of the sample – 61 µm. LIDT measurements were performed according to the procedure of the International Standard. By changing the position of the sample, new spot was exposed with each pulse, and the scattered radiation was recorded by the detector WS.

3. Results

The reflectivity of the prepared coatings is 99.1 % and most of the electric field intensity is distributed in outer layers, which is common in quarter based mirrors. The transmittance of the component is ~0.4 %, which indicates 0.5 % losses. Such losses include absorption and the optical scattering. Scattering is considered as the main candidate due to our previous optical scattering investigation [2].

Initially, 1-on-1 test method of LIDT has been performed in order to determine the base optical resistivity of all-silica HR coatings. The threshold values with zero probability of damage reached 24.6 J/cm^2 and increased up to 56.6 J/cm^2, with probability of damage up to 50% as an indicator of intrinsic optical resistivity of the coatings [5]. Defect initiated damage is observed, which is common in e-beam based optical coatings [6].

Afterwards, different laser conditioning protocols have been tested in order to improve the optical resistivity of all-silica HR coatings (Fig. 2). Changing the rate of energy increase per pulse (J/cm^2 per pulse) in the same spot of surface, different optical resistivities have been obtained. Rapid increase in irradiated energy results in LIDT ranging from 50 J/cm^2 to 80 J/cm^2 of all-silica mirrors. This resistivity maintains in interval of energy increase rate between 4 J/cm^2 per pulse to 32 J/cm^2 per pulse. Therefore, even rapid increase in energy gives better results than standard 1-on-1 test. Reducing the energy increments to the level of <0.25 J/cm^2 per pulse, optical resistivity of the coatings increases even further, up to the level of ~200 J/cm^2. The LIDT fluctuates between 170 J/cm^2 and 200 J/cm^2, if the energy increment is kept below this level. Increasing the laser conditioning time, optical resistivity was increased by almost three times compared to fast conditioning and eight times compared to unconditioned sample using 1-on-1 test method. Within the range of energy increments between 0.25 J/cm^2 and 4 J/cm^2 per pulse, the optical resistivity changes rapidly from 50 J/cm^2 and 200 J/cm^2, respectively. To our knowledge, the largest LIDT in pulsed ns regime at the wavelength of 355 nm for silica material has been reported in Optics Express journal by Huang et al. - ~90 J/cm^2 [7].

Additionally, longevity of the coatings has been tested as well after the laser conditioning using the ramping rate of 0.13 J/cm^2 per pulse. Each site was irradiated by ramping the energy to the specific intensity and this intensity maintained until damage was initiated. The maximum number of pulses was held at 10 000. When the energy was raised to the level of 180 J/cm^2, coatings were able to withstand several thousands of pulses, but did not reached 10 000. The coatings were able to withstand at least 10 000 shots when the pulse intensity did not exceed the threshold of 174 J/cm^2 as shown in Fig. 2.

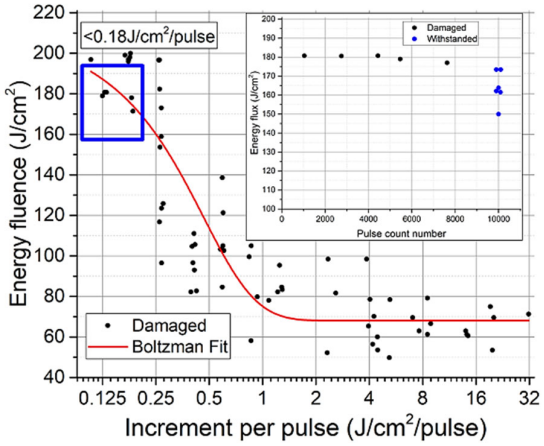

Fig. 2. Laser conditioning results and longevity of laser conditioned sample.

4. Conclusions

Current research presents the development in laser conditioning of all-silica mirrors at the wavelength of 355 nm. Different conditioning protocols have resulted in LIDT of 180 J/cm^2 and such resistivity maintained for several thousands of pulses. Optical resistivity exceeded 10 000 pulses with the irradiated energy flux of 174 J/cm^2. Such development opens new capabilities in industrial high power laser systems and major laser facilities.

Acknowledgements

Authors are grateful for the research funding from Lietuvos Mokslo Taryba ((LMTLT) Project No. S-M-ERA.NET-20-2).

References

[1]. C. N. Danson, et al., Petawatt and exawatt class lasers worldwide, *High Power Laser Science and Engineering*, Vol. 7, 2019, E54.

[2]. T. Tolenis, *et.al.,* Next generation highly resistant mirrors featuring all-silica layers, *Scientific Reports,* Vol. 7, 2017, Nr. 10898.

[3]. T. Tolenis, *et.al.*, Sculptured anti-reflection coatings for high power lasers, *Optical Materials Express*, Vol. 7, 2017, pp. 1249-1258.

[4]. L. Grinevičiūtė, *et.al.*, Highly Resistant Zero-Order Waveplates Based on All-Silica Multilayer Coatings, *Physica Status Solidi (A),* Vol. 214, 2017, 1700764.
[5]. M. Mende, *et.al.*, Laser-induced damage of pure and mixture material high reflectors for 355 nm and 1064 nm wavelength, *Advances in Optical Thin Films IV*, Vol. 8168, 2011, 816821.
[6]. S. Papernov and A. W. Schmid, Correlations between embedded single gold nanoparticles in SiO_2 thin film and nanoscale crater formation induced by pulsed-laser radiation, *Journal of Applied Physics,* Vol. 92, 2002, pp. 5720–5728.
[7]. J. Huang, *et.al.*, Influence of bulk defects on bulk damage performance of fused silica optics at 355 nm nanosecond pulse laser, *Optics Express,* Vol. 25, 2017, pp. 33416-33428.

(8684)

Laser Micro-processing of Functional Surfaces

A. Žemaitis, S. Steponavičiūtė, U. Gudauskytė, P. Gečys and M. Gedvilas
Department of Laser Technologies (LTS), Center for Physical Sciences and Technology (FTMC),
Savanoriu Ave. 231, 02300 Vilnius, Lithuania
E-mail: andrius.zemaitis@ftmc.lt

Summary: Utilisation of pulsed lasers for the fabrication of functional surfaces was demonstrated. Highly hydrophilic and superhydrophobic surfaces were created due to laser-induced self-organised structures with varied characteristic sizes. Direct laser ablation was optimised by two methods, which do not compromise the maximum average laser power. The pulse repetition rate and the number of pulses per burst were varied to locate the optimum point for the highest ablation efficiency. The highest efficiency of 4.2 $\mu m^3/\mu J$ was measured for copper ablation by ultrashort pulses.

Keywords: Pulsed laser, Ablation efficiency, Surface texturing, Burst, Wettability, Superhydrophobic.

1. Introduction

Fabricating bio-inspired (or biomimetic) functional surfaces is one of the burgeoning fields where laser processing is being used [1]. For species to survive, functional surfaces have evolved over millions of years. As a result, humankind has a strong urge to replicate and manufacture these surfaces artificially. Many animals, insects, and plants in nature have surfaces with special capabilities. These kinds of surfaces are constructed of micro- and nano-scale complex patterns that enable beneficial characteristics, including water repellence, drag reduction, adhesion, antireflection, structural coloration, self-cleaning, and antibacterial. As laser processing can be applied to both micrometer and nanometer scales, it is an ideal technique for the production of functional surfaces [2-4]. The nano-scale texturing of surfaces can be realised via self-organised structures like laser-induced periodic surface structures. By using material ablation, laser surface structuring in the micrometer range can be accomplished. Also, the ablation process has to be time and energy efficient to transfer the technology from the laboratory to the industry [5]. The beam size optimisation method allows to find the optimum fluence for the highest material removal rate (e.g. mm^3/s) and the highest ablation efficiency (e.g. $\mu m^3/\mu J$) simultaneously [6]. Furthermore, the increase in efficiency can be realised by the introduction of MHz bursts. Compared to a conventional pulsed laser, the individual energy of one pulse within a burst is lower as many times as there are intra-burst pulses and could be used to bring the pulse fluence closer to the optimum [7]. The removal of material using an ablation-cooled GHz burst processing was introduced as revolutionising [8]. The authors claimed the increase in ablation efficiency due to the removal of excess thermal energy from the interaction zone with the successive pulses. After systematic studies, the high efficiency of GHz bursts was linked with the long (100's and 1000's of pulses) bursts only [9, 10], while tens of pulses within GHz burst produce low ablation efficiency [11, 12]. Nevertheless, the utilisation of GHz bursts shows promising results in polishing applications [13].

This work was dedicated to the optimisation of ablation efficiency and the exploration of pulsed laser applications for the fabrication of functional surfaces.

2. Experiment

Ultrashort ($\tau < 10$ ps) and short ($\tau < 10$ ns) pulse lasers at $\lambda \approx 1$ µm wavelength were utilised in the laser processing experiments. Galvanometer scanners coupled with an F-theta lens were used to scan and focus the laser beam, while the beam waist location and precise sample positioning were performed by linear *Z*- and *XY*-stages. For ablation efficiency calculation cavities with dimensions of 2×1 mm^2 were milled into metals. Various laser processing parameters like pulse repetition rate, burst configuration, pulse energy, beam size, scanning speed, and hatch, were varied to find the optimum point for ablation or surface functionalisation.

Characterisation of samples was performed by scanning electron microscope (SEM) (JSM-6490LV, JEOL), 3D optical profiler (S neox, Sensofar), stylus profiler (Dektak 150, Veeco), contact angle measuring and contour analysis system (OCA 15EC, Data-Physics Instruments GmbH).

3. Results and Discussion

Two ablation optimisation strategies were applied for copper processing by ultrashort pulses. The first one, pulse repetition rate optimisation, allows to find the highest ablation efficiency by varying the pulse repetition rate (as well as pulse fluence) while maintaining the average laser power at maximum (Fig. 1a). The highest available power ensures that the ablation rate is not compromised. The second method, MHz burst optimisation, allows to find the highest

ablation efficiency by varying the number of pulses per burst (Fig. 1b). Therefore, laser energy is divided to bring the individual pulse fluence closer to the optimum.

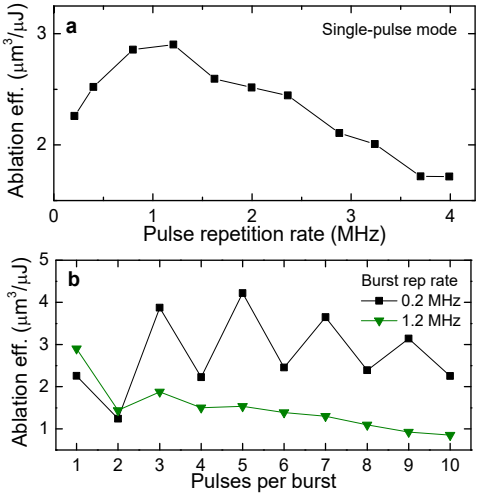

Fig. 1. Laser ablation efficiency of copper. (a) Optimisation by pulse repetition rate. (b) Optimisation by number of pulses within MHz burst. Processing parameters: pulse duration τ = 320 fs, wavelength λ = 1030 nm, average power $P \approx 17 - 22$ W (pulse repetition rate dependent), intra-burst repetition rate f_p = 50 MHz.

The interesting oscillation of ablation efficiency for an odd and even number of pulses per burst was recorded. Low ablation efficiency for an odd number of pulses can be explained by shielding. The first pulse causes gas and liquid phase material ejection (phase explosion) from the interaction area above the surface which does not dissipate until the second pulse arrives after 20 ns. Therefore, the second pulse is absorbed by the ablation cloud and causes re-ignition of plasma clearing the way for the third pulse [14].

Laser texturing by self-organisation was applied on copper samples to alter the surface wettability (Fig. 2). Hydrophobic surface was changed to both hydrophilic (Fig. 2a) and superhydrophobic (Fig. 2b) by laser irradiation. The differences in resulting patterns and sizes of self-organized structures were responsible for the wettability state of copper surface.

4. Conclusions

Pulse repetition rate and burst mode optimisation methods helped to locate the most efficient ablation point with preserved maximum laser power. Pulsed laser irradiation is suitable for wettability control of surfaces.

Acknowledgements

This project has received funding from European Regional Development Fund (project No. 01.2.2-LMT-K-718-03-0050) under grant agreement with the Research Council of Lithuania (LMTLT).

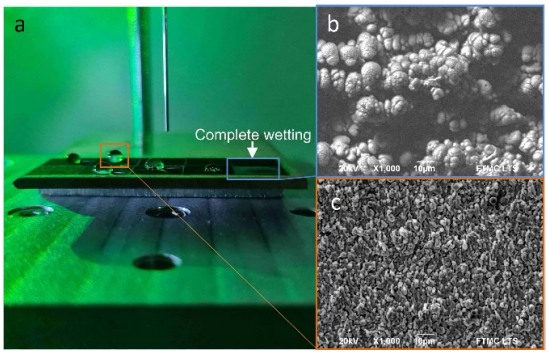

Fig. 2. Laser structured copper surface. (a) Image of different states of wettability achieved by laser structuring. (b) Complete wetting – highly hydrophilic surface. (c) Water repellence – superhydrophobic surface. Processing parameters: pulse duration τ = 10 ns, wavelength λ = 1064 nm, power P = 11.7 W, rep. rate f_p = 10 kHz.

References

[1]. J. Bonse, S. Höhm, S. V Kirner, A. Rosenfeld, J. Krüger, Laser-induced periodic surface structures – A scientific evergreen, *IEEE Journal of Selected Topics in Quantum Electronics*, Vol. 23, Issue 3, 2017, 9000615.

[2]. A. Žemaitis, J. Mikšys, M. Gaidys, P. Gečys, M. Gedvilas, High-efficiency laser fabrication of drag reducing riblet surfaces on pre-heated Teflon. *Materials Research Express*, Vol. 6, Issue 6, 2019, 065309.

[3]. A. Žemaitis, A. Mimidis, A. Papadopoulos, *et al*., Controlling the wettability of stainless steel from highly-hydrophilic to super-hydrophobic by femtosecond laser-induced ripples and nanospikes. *RSC Advances*, Vol. 10, Issue 62, 2020, pp. 37956-37961.

[4]. A. Papadopoulos, E. Skoulas, A. Mimidis, et al., Biomimetic omnidirectional antireflective glass via direct ultrafast laser nanostructuring, *Advanced Materials*, Vol. 31, Issue 32, 2019, 1901123.

[5]. A. Žemaitis, M. Gaidys, M. Brikas, P. Gečys, G. Račiukaitis, M. Gedvilas, Advanced laser scanning for highly- efficient ablation and ultrafast surface structuring: Experiment and model, *Scientific Reports*, Vol. 8, 2018, 17376.

[6]. A. Žemaitis, M. Gaidys, P. Gečys, G. Račiukaitis, M. Gedvilas, Rapid high-quality 3D micro-machining by optimised efficient ultrashort laser ablation, *Optics and Lasers in Engineering*, Vol. 114, 2019, pp. 83-89.

[7]. A. Žemaitis, P. Gečys, M. Barkauskas, G. Račiukaitis, M. Gedvilas, Highly-efficient laser ablation of copper by bursts of ultrashort tuneable (fs-ps) pulses, *Scientific Reports*, Vol. 9, Issue 1, 2019, 12280.

[8]. C. Kerse, H. Kalaycıoğlu, P. Elahi, et al., Ablation-cooled material removal with ultrafast bursts of pulses,. *Nature*, Vol. 537, 2016, pp. 84-88.

[9]. G. Bonamis, K. Mishchick, E. Audouard, et al., High efficiency femtosecond laser ablation with gigahertz level bursts, *Journal of Laser Applications*, Vol. 31, Issue 2, 2019, 22205.

[10]. D. J. Förster, B. Jäggi, A. Michalowski, B. Neuenschwander, Review on experimental and theoretical investigations of ultra-short pulsed laser ablation of metals with burst pulses, *Materials*, Vol. 14, Issue 12, 2021, 3331.

[11]. G. Bonamis, E. Audouard, C. Hönninger, et al., Systematic study of laser ablation with GHz bursts of femtosecond pulses, *Optics Express*, Vol. 28, Issue 19, 2020, pp. 27702-27714.

[12]. A. Žemaitis, M. Gaidys, P. Gečys, M. Barkauskas, M. Gedvilas, Femtosecond laser ablation by bibursts in the MHz and GHz pulse repetition rates, *Optics Express*, Vol. 29, Issue 5, 2021, pp. 7641-7653.

[13]. M. Gaidys, A. Žemaitis, P. Gečys, M. Gedvilas, Efficient surface polishing using burst and biburst mode ultrafast laser irradiation, *RSC Advances*, Vol. 13, Issue 6, 2023, pp. 3586-3591.

[14]. D. J. Förster, S. Faas, S. Gröninger, et al., Shielding effects and re-deposition of material during processing of metals with bursts of ultra-short laser pulses, *Applied Surface Science*, Vol. 440, 2018, pp. 926-931.

(8750)

Study of the Strongly Coupled Tamm-plasmon Polariton States in the Surface Lattice Array of Gold Nano-bumps

Justina Anulytė [1], Ernesta Bužavaitė-Vertelienė [1] and Zigmas Balevičius [1, 2]
[1] Plasmonics and nanophotonics lab., Department of Laser Technology, State Research Institute Center for Physical Sciences and Technology, Saulėtekio ave. 3, LT-10257, Vilnius, Lithuania
[2] Department of Computer Science and Communications Technologies, Faculty of Electronics, VilniusTech, Sauletekio ave. 11, LT-10223, Vilnius, Lithuania
E-mail: justina.anulyte@ftmc.lt

Summary: The strong coupling between the Tamm and surface plasmon polariton (SPP) in 1D photonic crystals (PCs) with gold lattice array was investigated by total internal reflection ellipsometry (TIRE). An optical dispersion and propagation characteristics of plasmons in 1D PCs with uniform gold layer and lattice array were studied using two coupled oscillator model. The assessed propagation length for SPP and TPP components in the hybrid polaritonic mode for nanostructures with a uniform gold layer was $\delta_{SPP} \approx$ 5.5-6.5 μm and $\delta_{TPP} \approx$ 6.5-9.5 μm, respectively. Meanwhile, the periodic gold surface lattice showed longer propagation length for the SPP component ($\delta_{SPPlattice} \approx$ 7-10.5 μm), and a shorter length for TPP ($\delta_{TPPlattice} \approx$ 5.5-8.5 μm). When surface lattice resonances are used in conjunction with the strong coupling regime, losses are reduced, resulting in increased propagation length and better coherence properties of such plasmonic excitations.

Keywords: Hybrid lattice plasmonic resonance, Strong coupling, Tamm plasmons.

1. Introduction

The attempts to apply metal nanostructures for various photonic devices usually reach their limits due to high losses [1]. Various metallic nanostructures such as grating arrays have recently been used to reduce the energy losses in metals. In contrast with the propagated surface plasmon resonances or metal nanoparticles, the metallic lattices have rather narrow plasmonic resonances [2]. The uses of nanophotonic – plasmonic nanostructures that may sustain prolonged coherence characteristics under strong coupling have drawn attention for potential applications such as plasmonic lasing [3] or enhanced bio-sensing [4]. One of the more widely investigated plasmonic system for enhanced biosensing is the surface plasmon polariton (SPP). The SPPs are collective charge oscillations associated to an electromagnetic field traveling at the interface between a metal and a dielectric. Due to the mismatch of the wave vectors of SPP and light wave in vacuum, a prism or grating coupler is needed. Another plasmonic mode that can be generated between metal and dielectric is the Tamm plasmon polariton (TPP), appearing between the metal and 1D photonic crystal. The Tamm plasmon polaritons are non-propagating optical states, which contrary to the SPPs, does not require a prism or grating coupler for excitation, because their wave vector is always smaller than the wave vector of light in vacuum. Compared with the SPP, the Tamm plasmon has a higher resonance quality factor (Q), due to smaller energy losses for the TPP mode. However, the Q-factor of the resonance can be further increased and the propagation length of the plasmon increased by introducing periodic nanoparticle structures [1].

One of such nanostructures that are presented in this research modifying the resonance propagation length is the gold microbump lattices produced on 1D PC. Here, optical response of two structures – 1D PC with thin gold layer and 1D PC with gold micro-bumps – are investigated and compared.

2. Methods

The total internal reflection ellipsometry (TIRE) method was used to excite and examine the strong coupling between the two plasmonic modes – the Tamm plasmon polariton (TPP) and surface plasmon polariton (SPP) – generated in nanophotonic structures consisting of 1D photonic crystal (PC) with a lattice of gold nano-bumps array on top. The hybrid TPP-SPP mode excitation sample was made up of a 1D PC and a thin metal layer of gold nano-bumps (50 nm) generated by direct laser writing. Ion beam sputtering was used to form five bilayers of TiO_2 (99.95 % purity) (110 nm) and SiO_2 (99.99 % purity) (200 nm) in alternate orientations to a BK-7 glass substrate through the optical contact. The Au (99.99 % purity) layer was formed on PC using magnetron sputtering, and the gold nano-bumps were created by employing second-harmonic (515 nm) 300-fs laser pulses generated by a Yb:KGW based fs-laser (Pharos, Light Conversion Ltd.) (Fig. 1).

3. Results and Discussion

Recent research has demonstrated that the gold nanobump lattice caused the creation of an extra Bragg mode, related to the lattice period, which is not implicated in the strong coupling of the hybrid TPP-SPP polaritonic mode. The additional

investigation revealed that the propagation length of the SPP grew while the TPP reduced due to the creation of an extra Bragg mode. By using a two linked oscillator model and wave-vector vs. energy broadening, it was possible to analyze the optical dispersion and propagation characteristics of plasmons in a 1D PC with a uniform gold layer and a lattice of gold nano-bumps. The assessed propagation lengths for the SPP and TPP components in the hybrid polaritonic mode for nanostructures with homogeneous gold layers were δSPP = 5.5-6.5 μm and δTPP = 6.5-9.5 μm, respectively (Fig. 2).

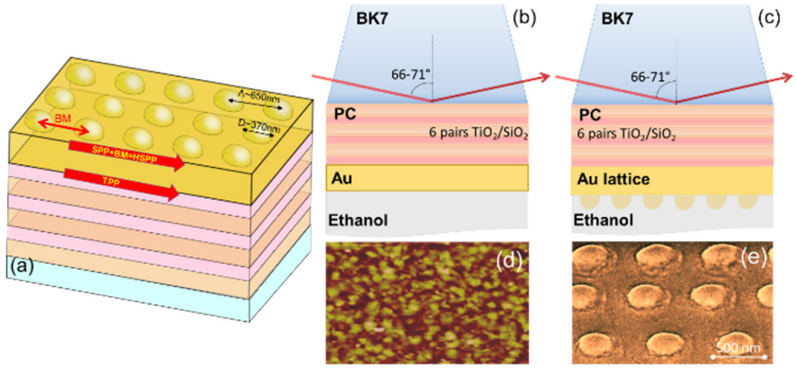

Fig. 1. (a) Structure geometry consisting of a gold nano-bumps lattice with a diameter of ~370 nm and a period of B652 nm. Scheme of excitation configurations for the (b) hybrid TPP–SPP mode and (c) SPP–HSPP structures. SEM micrograph of (d) a uniform (50 nm) Au layer and (e) a nano-bumps lattice array on the same thin gold layer [5].

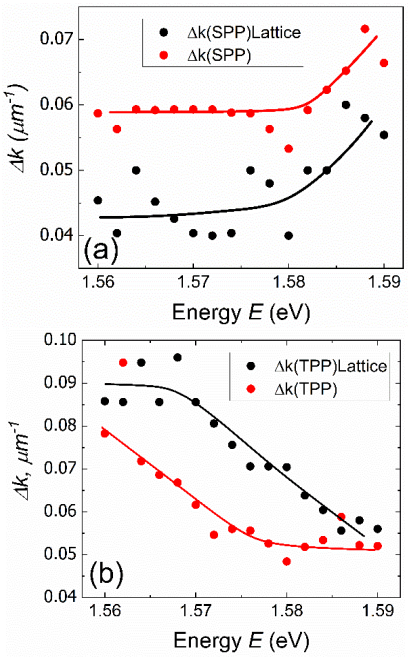

Fig. 2. Evolution of Δk in the vicinity of strong coupling for (a) SPP (red circles – uniform layer; black circles – lattice array) and (b) TPP (red circles– uniform layer; black circles –lattice array) components in the uniform gold layer and lattice array of gold nano-bumps. Δk was evaluated from the dispersion map at FWHM as a function of wave vector vs. energy. The solid black and red lines represent the evolution of Δk at the FWHM [5].

The periodic gold surface lattice has caused alterations that result in greater propagation lengths for the SPP component (SPPlattice) and shorter propagation lengths for the TPP (TPPlattice), which range from 5.5 to 8.5 m. The obtained results provide a unique method for controlling and modifying the propagation length between TPP and SPP components in the hybrid plasmonic mode utilizing surface lattice arrays. The developed nanophotonic-plasmonic structures demonstrate the direct laser writing technique's (DLW) promise as a quick, large-area, cost-effective way for producing integrated photonic devices with desired attributes, in this case by modifying the propagation length and coherence characteristics in the hybrid plasmonic mode.

4. Conclusions

We find that the DLW approach has the ability to produce nanophotonic-plasmonic structures with desired features, in this example by modifying the propagation length between TPP and SPP components in the hybrid plasmonic mode. When surface lattice resonances are used in combination with a strong coupling regime, losses are reduced, therefore increases the propagation length and improves the coherence characteristics of such plasmonic excitations, which in turn promises advanced properties for plasmonic-based coherent emission nanosources.

References

[1]. V. G. Kravets, F. Schedin, A. N. Grigorenko, Extremely narrow plasmon resonances based on diffraction coupling of localized plasmons in arrays of metallic nanoparticles, *Physical Review Letters*, Vol. 101, Issue 8, 2008, 087403.

[2]. T. K. Hakala, A. J. Moilanen, A. I. Väkeväinen, et.al., Bose-Einstein condensation in a plasmonic lattice, *Nature Physics*, Vol. 14, Issue 7, 2018, pp. 739-744.

[3]. A. Paulauskas, S. Tumenas, A. Selskis, et. al., Hybrid Tamm-surface plasmon polaritons mode for detection of mercury adsorption on 1D photonic crystal/gold nanostructures by total internal reflection ellipsometry, *Optics Express*, Vol. 26, Issue 23, 2018, pp. 30400-30408.

[4]. B. Auguié, W. L. Barnes, Diffractive coupling in gold nanoparticle arrays and the effect of disorder, *Optics Letter*s, Vol. 34, Issue 4, 2009, pp. 401-403.

[5]. J. Anulytė, E. Bužavaite-Verteliene, V. Vertelis, et. al., Influence of a gold nano-bumps surface lattice array on the propagation length of strongly coupled Tamm and surface plasmon polaritons, *Journal of Materials Chemistry C*, Vol. 10, 2022, pp. 13234-13241.

(9125)

Effect of WO_3 Addition on the Structure and Luminescent Properties of $ZnO\text{-}B_2O_3:Eu^{3+}$ Glass

L. Aleksandrov [1], A. Yordanova [1], M. Milanova [1], R. Iordanova [1] P. Petrova [2] and N. Nedyalkov [3]

[1] Institute of General and Inorganic Chemistry, Bulgarian Academy of Sciences, G. Bonchev, str. bld. 11, 1113 Sofia, Bulgaria
[2] Institute of Optical Materials and Technologies "Acad. Jordan Malinowski", blvd. Akad. G. Bonchev 109, Sofia 1113, Bulgaria
[3] Institute of Electronics, Bulgarian Academy of Sciences, 72, Tsarigradsko Chaussee Blvd., 1784 Sofia, Bulgaria
Tel.: +3592979 3588, fax: +3592870 50 24
E-mail: lubomirivov@gmail.com

Summary: Glasses with the composition in mol% of $50ZnO:(50\text{-}x)B_2O_3:0.5Eu_2O_3:xWO_3$, x = 0, 1, 3, 5 were obtained by applying the melt-quenching method and investigated by infrared (IR) and Raman spectroscopies, DSC analysis and photoluminescence spectroscopy (PL). Physical properties like density, molar volume, oxygen molar volume and oxygen packing density were also determined. IR spectra revealed that WO_3 modify borate network resulting in a decrease of $[BØ_4]^-$ units and favoring formation of pyroborate dimers, $[B_2O_5]^{4-}$. Tungstate ions incorporate into base zinc-borate glass as tetrahedral $[WO_4]^{2-}$ groups, and octahedral $[WØ_4O_2]^{2-}$ species with four bridging and two non-bridging oxygen atoms. The emission intensity of the Eu^{3+} ion increases with increasing WO_3 content due to the occurrence of non-radiative energy transfer from the tungstate groups to the active ion. The most intense luminescence peak observed at 612 nm suggest that the glasses are potential materials for red emission.

Keywords: Glasses, Structure, Europium, IR spectra, Density.

1. Introduction

Tungsten ions are well known for their unusual influence on optical and electrochemical properties of glasses [1, 2]. Due the high polarizability, WO_3 could contribute in a great extent to the obtaining of high refractive index glasses and enhanced non-linear optical properties and improved luminescent properties of RE ions [1]. In our recent paper, we have been established that the addition of 10 mol% WO_3 suppresses the phase separation of the zinc-borate glass at high rare earth doping concentrations (up to 10 mol%) and improves Eu^{3+} luminescence emission [3]. Motivated by these results, in this work we investigate the effect the addition of smaller amount of WO_3 (up to 5 mol%) on the structure and luminescent properties of $ZnO\text{-}B_2O_3$ glass doped with 0.5 mol % Eu_2O_3 by using of IR spectroscopy, density measurements and photoluminescent spectroscopy. The aim is to gain a structural information and to check its possible use for visible red emission application.

2. Experimental

Glasses with nominal compositions of $50ZnO:(50\text{-}x)B_2O_3:0.5Eu_2O_3:xWO_3$, (x = 0, 1, 3 and 5 mol %) were prepared by melt quenching method and studied by X-ray diffraction (XRD), differential scanning calorimetry (DSC), infrared (IR) spectroscopy and photoluminescence (PL) spectroscopy.

3. Results and Discussion

Bulk, transparent colourless glasses, (insets, Fig. 1) were obtained in this study. The measured X-ray diffraction patterns are shown in Fig. 1 and confirm the amorphous nature of the prepared materials.

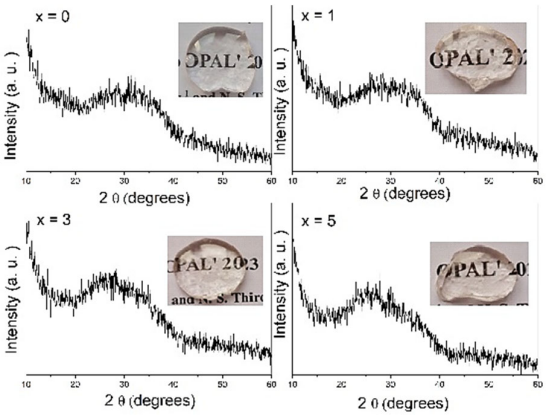

Fig. 1. XRD patterns and photographs (insets) of glasses $50ZnO:(50\text{-}x)B_2O_3:xWO_3:0.5Eu_2O_3$, (x = 0, 1, 3 and 5 mol %).

The structure of the glasses was studied by IR and Raman spectroscopies. IR spectra (Fig. 2) revealed that tungsten ions incorporate into the base zinc borate glass as $[WO_4]^{2-}$ tethahedral (IR band at 480 cm^{-1}, ν_4) and octahedral $[WØ_4O_2]^{2-}$ species with four bridging

and two non-bridging oxygen atoms (bands at 870 cm^{-1} and 840 cm^{-1}, $\nu_s(WO_2)$ and $\nu_{as}(WO^2)$ vibrations of terminal WO_2 units). The two strong bands at 680 and 630 cm^{-1} are connected with the asymmetric stretching vibrations of two-oxygen bridges (W_2O_2) in octahedral $[W\O_4O_2]^{2-}$ species, overlapping with the vibrations of borate oxygen network [3, 4].

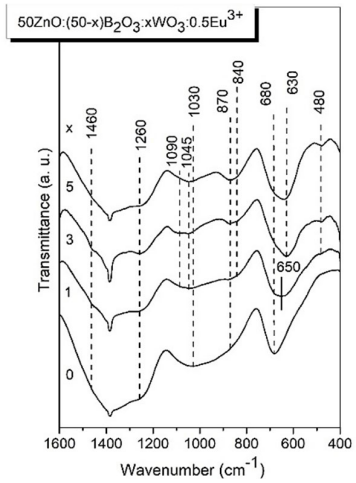

Fig. 2. Infrared spectra of glasses 50ZnO:(50-x)B_2O_3: xWO_3:0.5Eu_2O_3, (x = 0, 1, 3 and 5 mol %.

IR bands in the 1500 - 1000 cm^{-1} frequency range are connected with the vibrations of $[B\O_2O]^-$ (shoulder at 1460 cm^{-1},$\nu(B–O^-)$ stretch) and $[B\O_4]^-$ (band at 1090 cm^{-1}, ν_{as}) metaborate groups (Ø = bridging oxygen, O^- = nonbridging oxygen). IR band at 1260 cm^{-1} is assigned to the stretching vibration of $B\O_3$ triangles involved in various types of superstructural borate groups [3]. The decreasing intensity of the 1090 cm^{-1} peak and the growth of new IR feature at ca. 1045 cm^{-1} due to the ν_{as}(B-O-B) vibration of pyroborate dimers, $[B_2O_5]^{4-}$with increasing WO_3 content, indicate that the inclusion of WO_3 results in a decrease in $[B\O_4]^-$ units and increasing amount of BO_3 groups with non-bridging oxygens (NBOs) [3].

The simultaneous presence of $[WO_4]^{2-}$ tethahedral and octahedral $[W\O_4O_2]^{2-}$ species in the networks of the studied glasses is also revealed by Raman analysis. Raman spectra shown in Fig. 3, contain strong band at 970 cm^{-1} due to ν_1 symmetric vibration and bands at 300 and 400 cm^{-1} due to ν_2 and ν_4 modes of $[WO_4]^{2-}$ tethahedra respectively. Raman band at 846-865 cm^{-1} is connected with $\nu_s(WO_2)$ vibration of terminal WO_2 units, while the band at 660 and 695 cm^{-1} are related with the asymmetric stretching vibrations of two-oxygen bridges (W_2O_2) in octahedral $[W\O_4O_2]^{2-}$ species [3]. From the Raman spectra present here it is difficult to obtain information for the borate oxygen units present in the structure of these glasses, as the Raman spectra are dominated by the bands of tungstate structural units due to their higher Raman scattering ability and thereafter a stronger band intensity in comparison with borate related bands [5].

The depolimerization of the glass structure of base zinc borate glass (increasing NBOs) when WO_3 is added established by IR analysis is also confirmed by the observed increasing density, molar volume and oxygen molar volume, and lowering OPD values of WO_3-containing glasses with increasing WO_3 content [3].

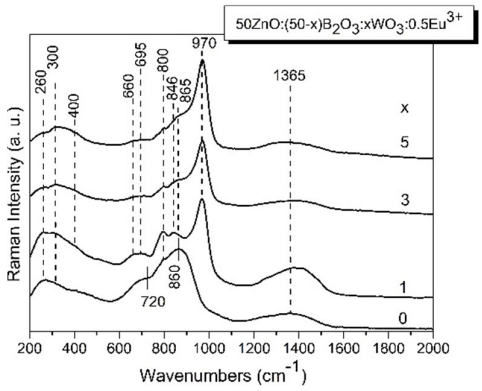

Fig. 3. Raman spectra of glasses 50ZnO: (50-x)B_2O_3:xWO_3:0.5Eu_2O_3:, x = 0, 1, 3 and 5 mol%.

The luminescent spectra of glasses (excited by wavelength of 395 nm), shown in Fig. 4 consist of several narrow lines originating from the intra-configurational transitions of excited states $^5D_0$ to the ground states $^7F_0$ (578 nm), $^7F_1$ (591 nm), $^7F_2$ (612 nm), $^7F_3$ (651 nm), $^7F_4$ (700 nm) in the $^4F_6$ configuration of Eu^{3+} [6].

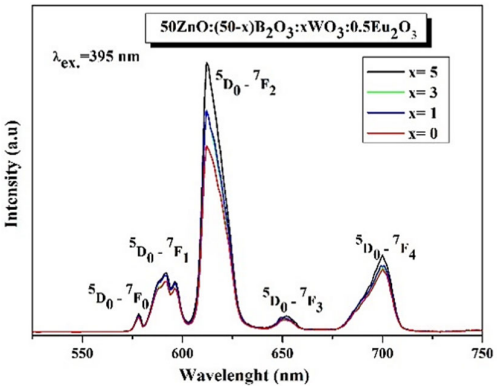

Fig. 4. Emission spectra of glasses 50ZnO: (50-x)B_2O_3:xWO_3:0.5Eu_2O_3:, x = 0, 1, 3 and 5 mol%.

The absence of host emission band originating from WO_n groups in the spectra when excited with Eu^{3+} energy (394 nm) suggests that efficient energy transfer from host matrix to Eu^{3+} ions has occurred. Comparing the luminescence spectra of the zinc borate glass without WO_3 (red line) and the zinc borate glasses containing 1÷5 mol% WO_3, an increase in the luminescent intensity is observed in presence of WO_3 that was found to be the most intense for host glass composition having 5 mol% WO_3.

4. Conclusions

The effect the addition of WO_3 (up to 5 mol%) on the structure and luminescent properties of $ZnO\text{-}B_2O_3$ glass doped with 0.5 mol % Eu_2O_3 was investigated. IR and Raman spectra revealed that the glass network consists of $[BØ_2O]^-$ and $[BØ_4]$- metaborate groups, $[B_2O_5]^{4-}$ pyroborate dimmers, $[WO_4]^{2-}$ tetrahedral, and octahedral $[WØ_4O_2]^{2-}$ species with four bridging and two non-bridging oxygen atoms. The glasses obtained presented strong 612 nm red luminescence with excitation at 395 nm. The positive effect of WO_3 on the luminescence intensity of the Eu^{3+} doped zinc borate glass was established.

Acknowledgements

This work is supported by European Regional Development Fund within the framework of OP "Science and Education for Smart Growth 2014-2020", Project CoE "National center of mechatronics and clean technologies", No.BG05M2OP001-1.001-0008-C01 and the Bulgarian National Science Fund at the Ministry of Education and Science under project КП-06-Н29/7.

References

[1]. M. Reza Dousti, G. Y. Poirier, A. Simone Stucchide Camargo, Structural and spectroscopic characteristics of Eu^{3+}-doped tungsten phosphate glasses, *Optical Materials*, Vol. 45, 2015, pp. 185-190.

[2]. M. Ataalla, A. S. Afify, M. Hassan, M. Abdallah, Margarita Milanova, H. Y. Aboul-Enein, A. Mohamed, Tungsten-based glasses for photochromic, electrochromic, gas sensors, and related applications: A review, *Journal of Non-Crystalline Solids*, Vol. 491, 2018, pp. 43-54.

[3]. M. Milanova, L. Aleksandrov, A. Yordanova, R. Iordanova, N. S. Tagiara, A. Herrmann, G. Gao, L. Wondraczek, E. I. Kamitsos, Structural and luminescence behavior of Eu^{3+} ions in $ZnO\text{-}B_2O_3\text{-}WO_3$ glasses, *Journal of Non-Crystalline Solids*, Vol. 600, 2023, 122006.

[4]. M. Mancheva, R. Iordanova, Y. Dimitriev, Mechanochemical synthesis of nanocrystalline $ZnWO_4$ at room temperature, *J. Alloys Compound*., Vol. 509, 2011, pp. 15-20.

[5]. D. Moncke, E.I. Kamitsos, D. Palles, R. Limbach, A. Winterstein-Beckmann, T. Honma, Z. Yao, T. Rouxel, L. Wondraczek, Transition and post-transition metal ions in borate glasses: Borate ligand speciation, cluster formation, and their effect on glass transition and mechanical properties, *Journal of Chemical Physics*, Vol. 145, 2016, pp. 124-501.

[6]. K. Binnemans, Interpretation of europium (III) spectra, *Coordination Chemistry Reviews,* Vol. 295, 2015, pp. 1-45.

(9497)

Simultaneous Multipoint Guided Elastic Wave Measurements Using FBG Based Multi-channel Dynamic Interrogation System

K. Aananth, S. Kishore Kumar and Balaji Srinivasan
FiLS Group, Department of Electrical Engineering, Indian Institute of Technology Madras,
Chennai 600036, India
E-mail: balajis@ee.iitm.ac.in

Summary: We experimentally demonstrate a Multi-Channel Dynamic Interrogation System with 8 channels (MCDIS-8) developed for simultaneous multipoint guided elastic wave sensing using fiber Bragg grating (FBG) sensor. Our matched filter based dynamic interrogator uses Wavelength Division Multiplexing (WDM) in combination with Time Domain Multiplexing (TDM) for supporting multiple channels of measurements. In this work, guided elastic waves at 8 different locations in a Al sample plate were simultaneously measured using MCDIS-8 and surface mounted sensor FBGs. 3D numerical simulations were conducted on a model identical to the test sample used in experiments for comparison. Experimental results obtained from time of flight (ToF) studies are in agreement with 3D FAE simulations. The number of channels in MCDIS can be further scaled up using WDM and TDM techniques.

Keywords: Structural Health Monitoring, Guided elastic wave sensing, FBG Dynamic interrogation

1. Motivation

Periodic inspection of capital intensive structures such as airplanes, dams, bridges etc. helps to prolong its lifespan. Structural Health Monitoring (SHM) allows identification of destructive events of least severity, that when unattended may lead to a catastrophic failure of the structure/system [1, 2]. Ultrasonic guided wave-based SHM with its ability for long range inspections [3] has evolved as a popular technique in recent years. Specifically, Fiber Bragg Grating (FBG) sensors for guided wave measurements have enabled in-situ monitoring of structures in a minimally invasive manner. In addition, matched filter interrogation of FBGs for detecting the guided elastic waves has been previously demonstrated [4-6]. However, such a technique needs to be extended to multiple channels for practical SHM applications. In this work, we demonstrate interrogation of eight FBG sensors surface bonded to a 4 mm thick Aluminum plate using our 8-channel Dynamic Interrogation System (MCDIS-8) through coarse Wavelength Division Multiplexing (WDM) [8], and Time Division Multiplexing (TDM) techniques. The results obtained are confirmed through Time of Flight (ToF) data obtained experimentally and comparing it with results from 3D FEA simulations.

2. Eight Channel Interrogation using TDM

The MCDIS-8 unit, whose schematic diagram is presented in Fig. 1(a) is an enhanced version of our previously demonstrated 4-channel Dynamic Interrogation System (MCDIS-4) [8]. An optical broadband light source (BBS) connected to port 1 of circulator is used for illuminating 4 sensor FBGs cascaded into a single fiber connected to port 2 of the circulator through an 1×2 optical switch. The optical switch enables time domain multiplexing of sensors by selecting a port at any instance for simultaneous 4-channel interrogation. At a given instance, reflections from the 4 cascaded FBG sensors on selected port gets split into four individual channels for interrogation through a 20 nm spaced Coarse Wavelength Division Multiplexer (CWDM). These individual channels are then coupled to corresponding matched interrogation FBGs of similar Bragg wavelength pasted on voltage controlled PZTs. These PZTs, driven by PZT drivers, help to align the interrogation FBG suitably with sensor FBGs and enable wavelength to intensity demodulation.

The proportionate change in intensity available at the transmission side of the interrogator FBG undergoes voltage conversion and measurement through our data acquisition system as discussed in [7]. Suitable upgrades were made to MCDIS-4, both at the hardware level and in the Graphical User Interface (GUI) for supporting eight channel interrogation through two consecutive 4-channel (simultaneous) interrogation at successive time instances. Above-mentioned upgrades in MCDIS-8 enables fast and reliable measurements, comparable to conventional ultrasonic guided wave measurement systems using PZTs.

3. Experiments

In order to demonstrate the capability of the 8-channel interrogation unit, an Al plate of dimension 43 cm × 30 cm × 4 mm, consisting of four

through-hole defects D1 to D4 as illustrated in Fig. 2 was selected as the test sample. Locations P1 to P4 in the plate are chosen for excitation of ultrasonic guided waves and eight FBG sensors with Bragg wavelengths of 1530 nm (F1, F5), 1550 nm (F2, F6), 1570 nm (F3, F7), and 1590 nm (F4, F8) were surface bonded at locations F1 to F8 respectively for probing guided waves from the structure. The two sets of cascaded FBGs F1 to F4 and F5 to F8 are connected to ports 1 and 2 of MCDIS-8 respectively.

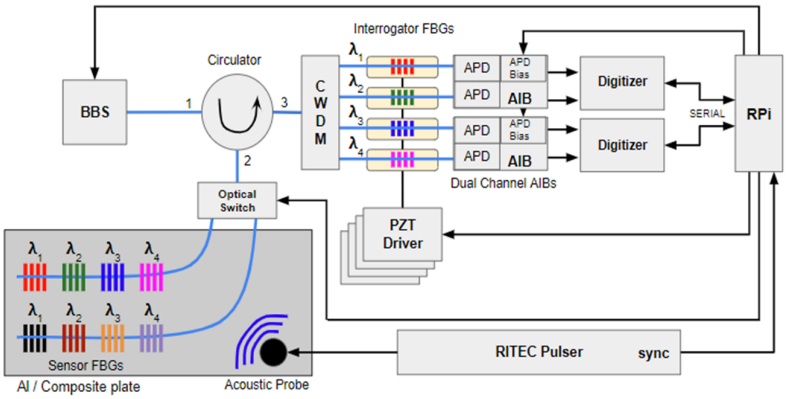

Fig. 1. Schematic representation of 8-channel dynamic interrogation system. Broadband light source (BBS), Analog Interrogation Board (AIB).

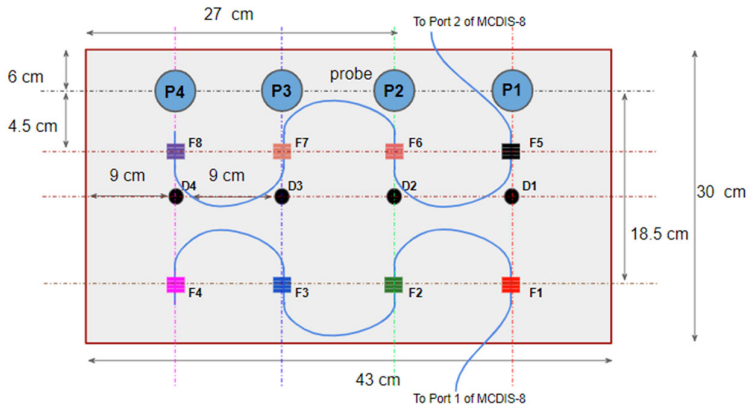

Fig. 2. Experimental setup for 8 channel dynamic interrogation.

The test sample was excited using a 250 kHz, 5 cycle tone burst generated from a commercial pulse excitation source (Ritec) in sync with MCDIS-8. Excitation pulses generated at 50 Hz pulse repetition rate were applied to SP-5H Piezo discs pasted at location P2. All the eight FBG channels are interrogated, four channels simultaneously at an instance for a duration of 200 µs at a sample rate of 5 MHz with 1024 averages. Signals measured from the sensor FBGs on the test sample were bandpass filtered and the results are shown in Fig. 3.

4. Results and Discussion

3D numerical simulations were conducted using commercially available Abaqus FEA software on a model identical to the test sample used in experiments to visualize the Lamb wave propagation in the structure. A 250 kHz, 5 cycle tone burst at location P2 (radial excitation) was used as the excitation signal. Normalized displacements at locations F1 to F8 along Y axis (U2) identical to direction of the surface-bonded sensor FBGs were simulated. The results obtained were bandpass filtered and compared with experimental results in the time domain shown in Fig. 3.

The Time of Flight (ToF) results measured from the sensor FBGs on the test sample were found to be consistent with the results obtained from 3D FEA simulations. Specifically, the wave packets arriving at identical time instances in channels (1,3) and (5,7) as highlighted illustrates the consistency of the measurements with inherent symmetry among these pairs from the exciter location P2. Similarly, the FBG closest to P2 i.e., F6 measured in channel 6 has the shortest time of flight, as predicted by the simulations.

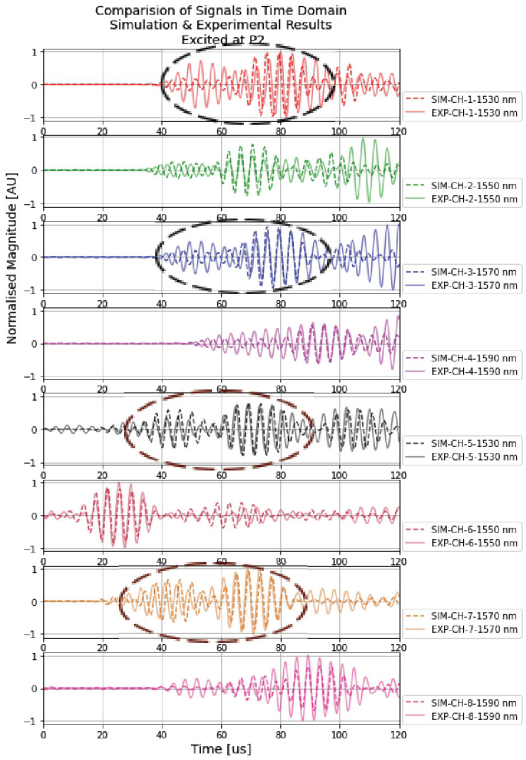

Fig. 3. Comparison of ToF measurements obtained from simulations and MCDIS-8 in time domain.

5. Conclusions

In this paper, we have demonstrated eight-channel dynamic interrogation of FBG sensors using matched-filter configuration for measurement of ultrasonic guided elastic waves in structures. Proceeding further the number of channels in MCDIS can be scaled up using wavelength division multiplexing and time division multiplexing techniques.

Acknowledgements

Authors acknowledge Gobi Rakkiannan R., Uma Sankar P., Vidya M. for their technical support. Aananth K., would like to acknowledge Samsung India and IITM Pravartak for their Fellowship support.

References

[1]. J. Krautkrämer, H.t Krautkrämer, Ultrasonic Testing of Materials, *Springer Science & Business Media*, 2013.

[2]. J. L. Tabjula, et al., Outlier analysis for defect detection using sparse sampling in guided wave structural health monitoring, *Structural Control and Health Monitoring*, Vol. 28, Issue 3, 2021, e2690.

[3]. J. L. Rose, Ultrasonic Guided Waves in Solid Media, *Cambridge University Press*, 2014.

[4]. P. Ray, et al., Feature-guided wave-based health monitoring of bent plates using fiber Bragg gratings, *Journal of Intelligent Material Systems and Structures*, Vol. 28, Issue 9, 2016, pp. 1211-1220.

[5]. T. L. Jagadeeshwar, P. Rajagopal, B. Srinivasan, Detection of guided waves in a composite plate using surface bonded fiber Bragg gratings sensor, in *Proceedings of the IEEE SENSORS Conference*, 2018, pp. 1-4.

[6]. A.V. Harish, et al., Dynamic interrogator for elastic wave sensing using Fabry Perot filters based on fiber Bragg gratings, *Ultrasonics*, Vol. 60, 2015, pp. 103-108.

[7]. K. Aananth, T. L. Jagadeeshwar, B. Srinivasan, Demonstration of a multi-channel dynamic interrogation system based on matched filters for elastic wave sensing, in *Proceedings of the Conference on Frontiers in Optics + Laser Science*, 2021, p. JTu1A.5.

[8]. K. Aananth, A. Hood, B. Srinivasan, Anomaly detection in aluminum structures using multi-channel dynamic interrogation system, in *Proceedings of the Conference on Frontiers in Optics + Laser Science*, 2022, p. JTu4B.67.

(9626)

Silica-based Optical Fibers with Low Attenuation in the Mid-infrared

W. Belardi [1], A. Pastre [1], L. Bigot [1], G. Bouwmans [1], P. Jaworki [2] and K. Krzempek [2]
[1] Université de Lille, CNRS, UMR 8523 –PhLAM – Physique des Lasers,
Atomes et Molécules, F-59000 Lille, France
[2] Laser & Fiber Electronics Group, Faculty of Electronics, Wroclaw University of Science and Technology,
50-370 Wroclaw, Poland
Tel.: +33362531617
E-mail: walter.belardi@univ-lille.fr

Summary: Despite the important practical advantages of using silica as the basic material for conventional optical fibers, these can guide light only up to the near-infrared spectral range. Indeed, silica absorption becomes too high at operating wavelengths above 2 microns. This is why, normally "soft glass" optical fibers are generally employed in the mid-infrared spectral range. In this work, we demonstrate silica-based hollow core optical fibers with a minimum attenuation as low as 0.22 dB/m at 4.6 μm and propose novel optical fiber designs with less than 1 dB/m attenuation above 5 μm. As a result, these can be used in specific optical detection systems, capable of sensing hazardous gases (e.g., NO [8]), with high sensitivity.

Keywords: Fiber design and fabrication, Fiber properties, Microstructured fibers.

1. Introduction

The last few years have seen tremendous progress in the area of hollow core optical fibers based on a simple optical design, which are easy to fabricate and have been demonstrated to have a very low overlap between the light travelling within the fiber and the silica forming the cladding. This novel form of optical waveguide is known as the Anti-Resonant Hollow Core Fiber (ARF) [1-4]. It has been demonstrated numerically [3] and experimentally [2] that a modification of the curvature of the core boundary of ARFs can significantly decrease fiber attenuation. By adopting a large fiber core, these fibers have allowed a level of overlap of the guided light with the silica cladding material of <0.01 % [3].

These novel and peculiar characteristics of ARFs have driven recent scientific innovations and technological applications in optical beam delivery (higher damage threshold due to the low light/glass overlap), increased optical transmission in the ultraviolet as well as lower latency for optical communication systems transmission links, due to the decreased effective index of guidance [1].

ARFs have been already successfully employed in the 3-4 μm spectral wavelength [2], with relatively low attenuation (100 dB/km) and bending loss, which were used for the realization of the first mid-infrared electrically pumped gas fiber amplifier at 3.5 μm [5] and the first optically pumped gas laser at 3.12 μm [6]. However, the optical attenuation of ARFs in the mid-infrared rapidly increases at longer wavelengths, due to the increased absorption of silica glass, particularly above 4.5 μm [7]. It reaches values exceeding 50000 dB/m at wavelengths above 5 μm.

We demonstrate silica-based hollow core optical fibers with a record minimum attenuation of 0.22 dB/m at 4.6 μm and propose novel optical designs with less than 1 dB/m attenuation above the 5 μm wavelength range. As a result, these can be used in specific optical detection systems, capable of sensing more than one hazardous gas (e.g. NO [8]), with high sensitivity.

2. Record Attenuation in the Mid-infrared

The hollow core optical fiber shown in the inset of Fig. 1 has been fabricated at the University of Lille. Its geometric characteristics have been designed for optimal transmission in the mid-infrared spectral range. The fiber has a large core size of 162 μm, a silica core boundary thickness of 1.3 μm and an overall fiber size of 376 μm. Its attenuation spectrum is shown in Fig. 1(a) and it can show a minimum loss of 0.22 dB/m at 4.6 μm, the minimum value ever reported at this wavelength.

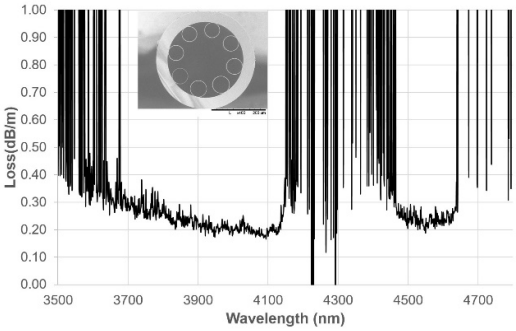

Fig. 1. Record attenuation in the mid-infrared for the hollow core fiber shown in the inset.

In order to further improve the attenuation of this fiber type at even longer wavelength (i.e., above 5 μm) a novel design for hollow antiresonant fibers is proposed in Fig. 2 (inset in blue). As compared to other

conventional antiresonant hollow core fibers (inset in red), this fiber structure can largely reduce the power overlap between the optical mode travelling within the fibre and the silica struts of the core boundary, i.e. reducing the impact of material attenuation on the overall fiber losses (blue line). Fig. 2 shows how, theoretically, it could be possible to achieve optical attenuations below 1 dB/m in silica based hollow core fibers, even above the 6 µm wavelength range.

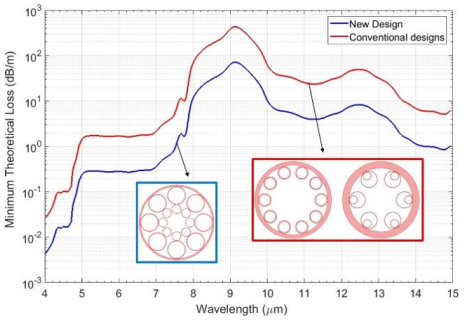

Fig. 2. Novel design for hollow core optical fibers with record attenuation beyond 5 µm.

3. Novel Optical Design for High Performance Hollow Core Optical Fibers

The hollow core optical fiber described above has been incorporated within the detection optical system described in Fig. 3. Thanks to the inscription of a series micro-channels along the lateral section of the hollow core fiber, up to date, the sensing system has allowed the detection of nitrous oxide at 5.26 µm with a minimum detection limit of 11 ppbv for an integration time of 144 s.

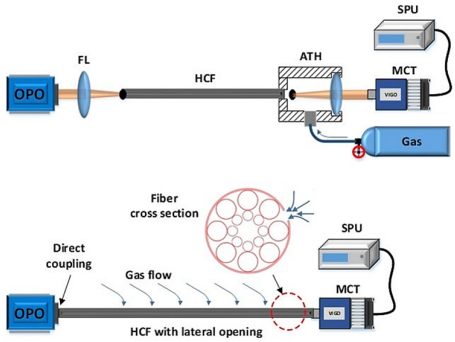

Fig. 3. (Top) Setup of a broadband detection optical system employing an hollow core optical fiber. (Down) Evolution of the system for high compactness.

4. Conclusions

We have discussed the fabrication of a hollow core optical fiber with a record minimum attenuation of 0.22 dB/m at 4.6 µm, his implementation in an optical NO detection system with very high sensitivity, the design of novel hollow core fibers with improved performances in the mid-infrared and the developments of improved broadband sensing systems with high compactness.

Acknowledgements

This work is supported by the European M-ERA.NET project GADEIRE.

References

[1]. W. Belardi, Hollow Core Optical Fibers, *MDPI*, 2019.
[2]. W. Belardi, J. C. Knight, Hollow antiresonant fibers with low bending loss, *Optics Express,* Vol. 22, Issue 8, 2014, pp. 10091-10096.
[3]. W. Belardi, J. C. Knight, Effect of core boundary curvature on the confinement losses of hollow antiresonant fibers, *Optics Express,* Vol. 21, Issue 19, 2013, pp. 21912-21917.
[4]. N. M. Litchinitser, A. K. Abeeluck, C. Headley, B. J. Eggleton, Antiresonant reflecting photonic crystal optical waveguides, *Optics Letters,* Vol. 27, Issue 18, 2002, pp. 1592-1594.
[5]. S. A. Bateman, W. Belardi, F. Yu, C. E. Webb, W. Wadsworth, Gain from Helium-Xenon discharges in Hollow optical fibres at 3 to 3.5 µm, in *Proceedings of the CLEO Conference,* 2014, p. STh5C.
[6]. Z. Wang, W. Belardi, F. Yu, W. J. Wadsworth, J. C. Knight, Efficient diode-pumped mid-infrared emission from acetylene-filled hollow-core fiber, *Opt. Express,* Vol. 22, Issue 18, 2014, pp. 21872-21878.
[7]. R. Kitamura, L. Pilon, M. Jonasz, Optical constants of silica glass from extreme ultraviolet to far infrared at near room temperature, *Applied Optics,* Vol. 46, Issue 33, 2007, pp. 8118-8133.
[8]. K. Krzempek, P. Koziol, P. Jaworki, W. Belardi, Antiresonant hollow core fiber-assisted photothermal spectroscopy of nitric oxide at 5.26 µm with parts-per-billion sensitivity, *Sensors and Actuators B: Chemical,* Vol. 345, 2021, 130374.

(9652)

UV Light Emitters based on AlGaN Resonant Tunneling Diodes

E. R. Brown [1, 2], W-D. Zhang [1, 2] and A. Al-Khalidi [3]
[1] Wright State University, Department of Physics, 3640 Col. Glenn Hwy, Dayton OH, 45434, USA
[2] Terapico, LLC, 2565 Vayview Drive, Beavercreek OH, 45431, USA
[3] University of Glasgow, James Watt School of Engineering, Oakfield Avenue, Glasgow, G12 8LT, UK
E-mail: elliott.brown@wright.edu

Summary: We describe a design methodology and supporting experimental data for a recent type of room-temperature light emitter based on double-barrier electron resonant-tunneling diodes made from GaN or its AlGaN alloys. The light emission is made possible because of hole generation within the active region by interband (Zener) tunneling or impact ionization – both of which are quite probable in the typically-high-E-field profile of RTDs. Lacking p-type doping, the so-called RTD-LED could mitigate the light-efficiency and reliability issues associated with the p-type doping in p-n AlGaN LEDs.

Keywords: Double-barrier resonant-tunneling diodes (RTDs), AlGaN/AlN RTDs, Hole generation by interband tunneling and impact ionization, UV-C light emission, 265 nm sterilization band.

1. Introduction

Since the first demonstration by Akasaki et al. of the bright, blue semiconductor LED in the early 1990s [1], there has been great interest in GaN and its AlGaN alloys for creating efficient light emitters in the UV portion of the spectrum, particularly in the UV-C region (λ = 100 to 265 nm) where there are many applications, such as surface and water sterilization, and free-space communications. However, the scaling from blue to UV-C wavelengths has not been easy. A major problem has been the An p-type doping (usually Mg) required to make traditional p-n junction light emitters. The p-type dopants have introduced optical losses that increase as the wavelength is reduced, leading to "current droop" in the L-V efficiency. Worse yet, the *reliability* of AlGaN light emitters is often compromised because of contaminants (e.g., hydrogen) that p-type dopants (e.g., Mg) introduce [2].

This paper concerns an alternative approach to achieving strong UV light emission from AlGaN heterostructures, and that requires *no p-type doping*. It entails an AlGaN/AlN double-barrier heterostructure designed as an electron resonant tunneling diode (RTD). GaN/AlN RTDs had been investigated unsuccessfully for many years, but a breakthrough occurred in 2016 with the realization of repeatable negative-differential resistance NDR (the telltale sign of strong resonant tunneling) in RTDs at room temperature [3], as shown in Fig. 1(a). This was followed by the serendipitous observation of bright near-UV light emission [Fig. 1(b)] from the same RTD structure [4].

2. Hole Generation in n-type GaN/AlN RTDs

The emission spectrum in Fig. 1(b) displays a peak at 360 nm, close to the accepted bandgap wavelength of GaN at room temperature. This suggests that the emission mechanism is cross-gap electron-hole recombination, just like in conventional p-n LED emitters. But where are the holes coming from ?

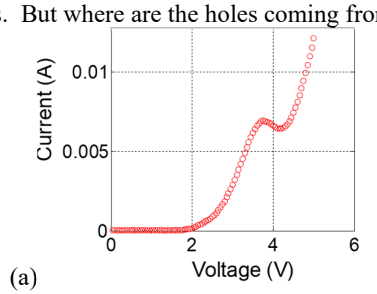

(a)

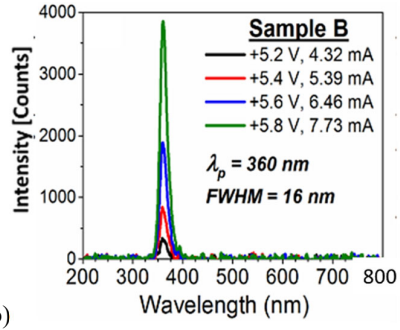

(b)

Fig. 1. (a) I-V curve, and (b) light emission spectrum of GaN/AlN RTD at room temperature [Refs. 3 and 4].

Rigorous simulations of the transport mechanisms in GaN RTDs have been carried out using non-equilibrium Green's functions (NEGFs) [4]. In addition, analytic quantum-transport simulations have been carried out for hole generation in separate $In_{0.53}Ga_{0.47}As$/AlAs RTDs emitting near 1630 nm [5] – a much simpler material system than GaN/AlN. The associated band-bending diagrams for the GaN/AlN RTD is are in Fig. 2. The key result from all these simulations is that holes can be generated in resonant tunneling structures by two separate mechanisms: (1) interband (Zener) tunneling between the valence and conduction bands on the collector side; and (2) impact ionization on the collector side. Double-barrier RTD

structures naturally support both mechanisms because of their high internal electric fields, and their "quasi-ballistic" electron transport through the double-barrier structure and across the collector side. And this is one of the few known devices in which two forms of quantum transport – resonant and interband tunneling – are occurring simultaneously.

Furthermore, once holes are generated on the collector side, they drift "uphill" to the double-barrier structure where transmission to the emitter side can occur by resonant tunneling with high probability. Upon reaching the emitter side, they recombine radiatively with the ample population of electrons on that side. This "bipolar" resonant tunneling mechanism is a new and fascinating aspect of RTDs.

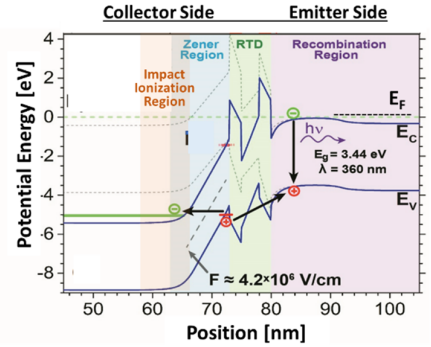

Fig. 2. GaN/AlN RTD structure at 5.0 V bias.

3. Extension to UV-C Emission

3.1. Bandgap Engineering

With the goal of extending the RTD light emission to the sterilization band (λ ≈ 255 to 285 nm), we have a first design of an $Al_XGa_{1-X}N$/AlN double-barrier RTD for 265 nm – the peak λ of sterilization effectiveness. The first issue is AlGaN composition. Using optically determined values for the AlGaN direct-bandgap energy vs Al fraction [6], Fig 3 shows that for a bandgap λ of 265 nm (E_G = 4.68 eV), X should be ≈0.58. Since the AlN barriers have a bandgap of 6.2 eV, there should still be usefully high AlN barriers since typically about 60% of the bandgap difference occurs for the electron barrier, and the remainder for the hole barrier.

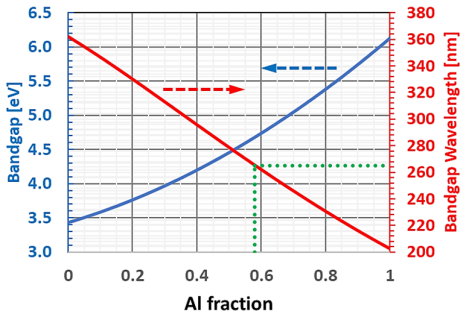

Fig. 3. Room-temperature bandgap energy and wavelength for the $Al_XGa_{1-X}N$ alloy vs Al fraction X.

3.2. Photonic Engineering

In GaN and most other direct bandgap semiconductors, the emission is omnidirectional and strongest along the growth axis (c axis in Fig. 4) of the semiconductor active layer. Total-internal-reflection reduces the amount of radiation that transmits through the top air-semiconductor interface, but there is still significant escaped power. Of course, light can be transmitted through the sidewalls too, and modern LEDs are designed to collect both.

In $Al_XGa_{1-X}N$, the emission properties change dramatically mostly because of peculiarities in the valence band structure [7]. As X increases, more and more of the emission propagates in-plane and must be collected out the edges. Our optical coupling approach, shown in Fig. 4, is a cup-like design similar to that used in many LEDs. The edge emission is collected by Al mirrors micromachined into silicon substrates. Fortunately, Al has high reflectance at λ = 265 and even shorter UV-C wavelengths

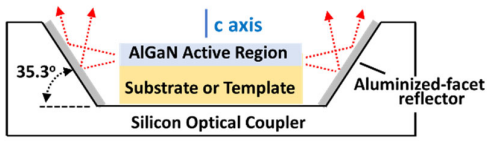

Fig. 4. RTD-LED chip embedded in a silicon optical coupler for efficient operation in UV-C.

3.3. Epitaxial Growth and Substrates

The third and most daunting issue is epitaxial material quality. Molecular beam epitaxy is the logical research growth technique for GaN and its AlGaN alloys, but the material quality often suffers from dislocations created by lattice mismatch to the substrate. This is especially true for bipolar devices, such as light emitters. Recently, crystal growers have developed AlGaN "templates" on sapphire substrates, which appear to be well suited to our UV-C RTD-LED approach. More on this will be discussed in the paper.

4. Conclusion

The extension of AlGaN-based LEDs to the UV-C region around λ = 265 nm (sterilization band) poses many challenges. The n-type AlGaN/AlN RTD-LED – a recent type of quantum-transport-based light emitter – appears capable of meeting these challenges.

References

[1]. I. Akasaki and H. Amano, Breakthroughs in Improving Crystal Quality of GaN and Invention of p-n Junction Blue-Light-Emitting Diode, *Jap. J. Appl. Phys.*, 45, 12, 2006, pp. 9001–9010.

[2]. Z. Ma, et al., Degradation and failure mechanism of AlGaN-based UVC-LEDs, *Solid State Electronics,* 156, 2019, pp. 92-96.

[3]. T. A. Growden, D. F. Storm, W-D. Zhang, E. R. Brown, et al., Highly repeatable room temperature negative differential resistance in AlN/GaN resonant tunneling diodes, *Appl. Phys. Lett.*, 109, 2016, 083504.

[4] T. A. Growden, W-D. Zhang, E. R. Brown et al., Near-UV Electroluminescence in Unipolar-Doped, Bipolar-Tunneling GaN/AlN Heterostructures, *Nature Light: Science & Appl*., 7, 2018, 17150.

[5]. E. R. Brown, W-D. Zhang, T. A. Growden, et al., Electroluminescence in unipolar-doped $In_{0.53}Ga_{0.47}As$/AlAs resonant-tunneling diodes: A competition between interband tunneling and impact ionization, *Phys. Rev. Appl.*, 16, 5, 2021, 054008.

[6]. D. Brunner, et al, Optical Constants of Epitaxial AlGaN Films and Their Temperature Dependence, *J. Appl. Phys*., 82, 1997, 5090.

[7]. K. B. Nam et al, Unique optical properties of AlGaN alloys and related ultraviolet emitters, *Appl. Phys Lett*., 84, 2004, pp. 5264–5266.